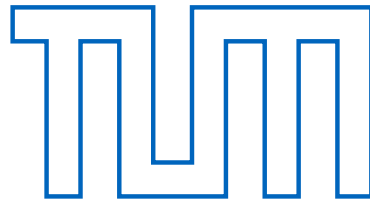


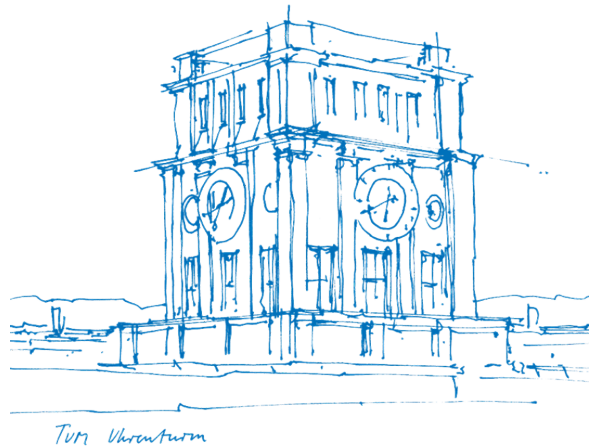
Technical University of Munich



# Functional biomacromolecules on medical polymer surfaces

a thesis  
presented by

Benjamin Winkeljann



Munich School of Bioengineering and Department of Mechanical Engineering  
Biomechanics and Biointerfaces Lab



Technische Universität München

Fakultät für Maschinenwesen

Professur für Biomechanik

# Functional biomacromolecules on medical polymer surfaces

Benjamin Winkeljann

Vollständiger Abdruck der von der Fakultät für Maschinenwesen der  
Technischen Universität München zur Erlangung des akademischen Grades  
eines

Doktor-Ingenieurs (Dr.-Ing.)

genehmigten Dissertation.

Vorsitzender: Prof. Dr.-Ing. Karsten Stahl

Prüfer der Dissertation:

1. Prof. Dr. rer. nat. Oliver Lieleg
2. Prof. dr. ir. Daniel J. Rixen
3. Prof. Thomas Crouzier, Ph.D.

Die Dissertation wurde am 08.06.2020 bei der Technischen Universität  
München eingereicht und durch die Fakultät für Maschinenwesen am  
28.10.2020 angenommen.



## Abstract

An artificial, foreign material which is inserted into the human body while surgery or diagnostics always bears the risk of causing complications: those not only include mechanically induced inflammations and damage, but also foreign body reactions or device-associated exogenous infections from temporary clinical implants such as urinal and vascular catheters or tracheal tubes. The latter, according to the World Health Organization (WHO) – alone in the EU – cause annually about three billion euro of community expenses reflecting six million days of additional hospital stay. For patients, the side-effects caused by medical devices and implants reach from simple inconvenience to chronic inflammations and further to severe, life-threatening complications such as pneumonia, bacteremia, or sepsis. In this thesis, a three-headed strategy is presented that aims at simultaneously tackling different roots of health care-associated inflammations and infections. First, by employing hydrated biomacromolecules as lubricious coatings for medical devices, friction-induced tissue damage and inflammatory responses are reduced. Furthermore, those polymer-bush coatings are shown to have intrinsic anti-biofouling properties, thus reducing the unwanted deposition of proteins, bacteria and cells. In the third and last step, this strategy is extended by an active component: A smart mechanism is designed, that allows for the liberation of two independent antibiotic doses to overcome both, immediate postoperative and recurring infections. All strategy aspects applied here can be achieved in several ways, *e.g.* using different macromolecules on different substrates or different drugs, thus rendering these approaches extremely versatile. Therefore, the findings of this thesis hold great potential to go beyond the borders of academic research to provide real benefits in daily clinical practice, and thus to improve real peoples' lives.



# Content

<b>1</b>	<b>Outline</b> .....	<b>1</b>
<b>2</b>	<b>Materials and methods</b> .....	<b>7</b>
2.1	Macromolecules.....	7
2.2	Coupling strategy for macromolecular coatings.....	12
2.3	Polymer materials used in clinical applications.....	14
2.4	Macrorheology.....	17
2.5	Biotribology.....	18
2.6	Fluorescence techniques.....	23
2.7	Liposomes.....	24
2.8	Drug release experiments from macromolecular coatings.....	26
2.9	Adsorption measurements using quartz crystal microbalance with dissipation monitoring (QCM-D).....	30
2.10	Surface topography analysis.....	32
2.11	Data analysis and graphical representation.....	34
<b>3</b>	<b>Biomacromolecule enriched aqueous solutions as high-performance lubricants</b> .....	<b>37</b>
3.1	Development of an oscillatory tribology setup.....	37
3.1.1	Versatility of the custom-made measuring system.....	38
3.1.2	Tribology on lateral material interfaces.....	43
3.2	Friction and wear on articular cartilage lubricated with different biopolymer solutions.....	45
3.3	Lubricity of mucin in varying physiological conditions.....	48
3.3.1	Effect of mucin concentration.....	49
3.3.2	Influence of pH conditions and salt concentrations.....	52
3.3.3	Interactions of small proteins with mucin molecules.....	55
<b>4</b>	<b>Covalently coupled macromolecules on clinically used polymer materials</b> ..	<b>57</b>
4.1	Covalent coatings with enhanced stability and surface lubricity.....	57
4.1.1	Mucin coatings: lubricity and mechanical stability.....	59
4.1.2	Thermal and chemical stability of covalent mucin coatings.....	59

4.1.3	Lubricity of covalent PEG and PLL coatings .....	63
4.2	Coating-lubricant interactions affect lubricity.....	64
4.3	Macromolecular coatings improve wear resistance .....	68
4.4	Applicability of the coating protocol to other polymers .....	71
<b>5</b>	<b>Biopolymer coatings with tunable functionalities .....</b>	<b>75</b>
5.1	Macromolecular coatings enable selective binding.....	75
5.1.1	Selective filtering through electrostatic interactions .....	76
5.1.2	Site-specific binding .....	78
5.1.3	Enzyme immobilization.....	79
5.2	Covalent mucin coatings reduce the initial stages of biofouling .....	80
5.2.1	Reduction of particle and protein adhesion .....	81
5.2.2	Reduction of prokaryotic and eukaryotic cell adhesion .....	83
5.3	Switchable biopolymer-based coatings as smart drug delivery systems .....	86
5.3.1	Reversible condensation of mucins into nanoparticles.....	87
5.3.2	DNA mediated drug release from a surface-bound mucin layer.....	89
5.3.3	A physiologically compatible trigger for large scale applications .....	92
5.3.4	Variation of coating polymers and stabilizing ions .....	95
5.3.5	Controlled two-step release from a mucin multilayer construct .....	98
<b>6</b>	<b>Summary and outlook.....</b>	<b>105</b>
	<b>Appendix.....</b>	<b>109</b>
Appendix A	: Purified porcine gastric mucin .....	109
Appendix B	: Additional methods .....	117
Appendix C	: Supplementary data .....	129
	<b>Bibliography .....</b>	<b>145</b>
	<b>Acknowledgements .....</b>	<b>179</b>
	<b>Author Contributions.....</b>	<b>183</b>
	<b>List of publications .....</b>	<b>187</b>
	<b>List of patents .....</b>	<b>189</b>

# 1 Outline

According to the definition of the *International Union of Pure and Applied Chemistry* (IUPAC), the term macromolecule refers to a relatively large molecule, which comprises multiple repetitions of smaller base-units, called monomers<sup>1</sup>. Macromolecules are typically divided into synthetic or biological macromolecules. Biomacromolecules include biopolymers, such as nucleic acids, proteins or carbohydrates, and non-polymeric molecules, *e.g.* lipids, which all fulfil crucial functions in the human body. Different from synthetic polymers, biopolymers are typically produced by animals, plants, bacteria or fungi, which often gives biomacromolecules superior biocompatibility.

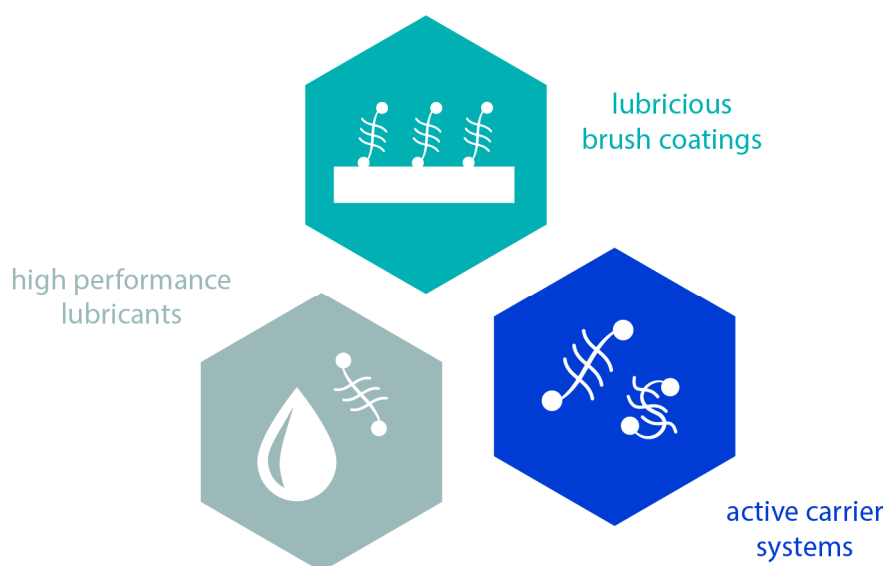


**Figure 1: Biomedical applications for macromolecular systems.** Macromolecules, such as Mucin or PEG offer a wide range for possible (bio)-medical applications, including high-performance lubricants, lubricious polymer brush coatings or dynamic carrier systems for a controlled drug release.

In different body fluids, such as saliva, the tear film, the vaginal or synovial fluid, biomacromolecules are responsible for the excellent lubricity of those body fluids<sup>2-6</sup>. Especially in the context of joint lubrication, a remarkable amount of research was

---

\* This section follows in part the review article Song *et al.*, *Advanced Materials Interfaces* (2020)

conducted in the last decades to investigate the underlying mechanisms of this astonishing lubricity<sup>2,7-12</sup>. A more detailed and deeper understanding of the nature of biopolymer-based lubrication and the involved microscopic mechanisms could help to create a new generation of bio-inspired high-performance lubricants (**Figure 1**, grey). Such bio-lubricants are particularly interesting for a broad range of medical applications as they could be used as eye drops, mouth sprays, artificial synovial fluid or lubes.

Physiologically, biomacromolecules not only exist in a solubilized form as component of different body fluids but are also present in surface bound forms where they fulfill crucial functions, *e.g.* as selective barriers for nutrients and pathogens or as mediators for cell signaling<sup>13-16</sup>. Inspired by the biological role model, immobilized macromolecules are also employed for a variety of biomedical applications. Most of those strategies share a common objective, *i.e.* they aim at gaining control over molecular and cellular binding towards the coated surface. The term '*control*' here is dependent on the particular application, and includes either the promotion of binding, the inhibition of binding, or selective binding of molecules or cells (**Figure 2**).

Strongly hydrated macromolecules, *i.e.* macromolecules that efficiently bind water molecules, for example can be used to generate lubricious coatings (**Figure 1**, cyan), as those coatings can supply a thin water film on the substrate's surface<sup>17-19</sup> (**Figure 2**). There are several studies where biological or synthetic macromolecules have been immobilized to technical surfaces to improve their lubricity<sup>20-24</sup>. However, many of those approaches used coating methods based on passive adsorption. Such coatings based on passive adsorption can not only be generated using simply hydrophobic or electrostatic interactions between coating molecule and surface but also by employing more complex strategies such as catechol mediated immobilization<sup>25-30</sup>. Compared to covalent coupling strategies, the deposition of macromolecules *via* physical forces entails lower mechanical stability and thus the range of possible applications is very limited.

Whereas binding water to a surface is often advantageous for biomedical applications, the adhesion of other molecules is mostly considered an unwanted side effect. For many medical implants, *e.g.* catheters, endotracheal tubes, stents, artificial heart valves or shunts, the unwanted deposition of proteins, pathogens or cells are a major cause for device associated infections and can further lead to total implant failure<sup>31-33</sup>. Consequently, preventing these so-called biofouling events is an important concern in the development of these products (**Figure 2**). In the last

decades, several studies have shown how biopolymer coatings can be used to improve the anti-biofouling properties of technical surfaces<sup>34-36</sup>. The mechanisms that govern these antifouling properties are dependent on the particular chemistry of the coating molecule and identifying specific antifouling properties brought about by a certain strategy is often based on empirical investigations. Whereas technical antifouling surfaces often employ toxic coatings to suppress the adhesion of living organisms<sup>37,38</sup>, the developers of biomedical implants have to take another route: here controlling the wettability of the surface plays a major role, but also charge effects or specific motifs that hinder binding contribute to the fouling resistance of a surface<sup>31,39</sup>.

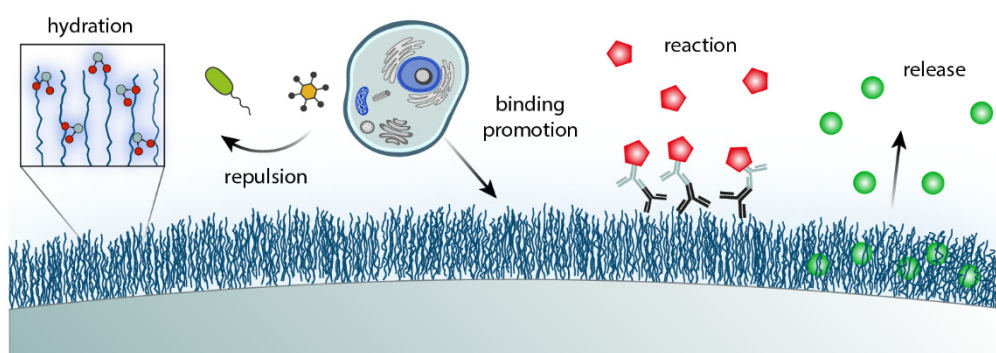


**Figure 2: Functionality of macromolecular coatings.** To gain control over binding of molecules and cells towards a surface is the main purpose of most coating strategies that are applied in biomedical applications. These “control” strategies may also include the release of previously bound molecules for drug delivery applications. Some applications, *e.g.* biosensors, further use surface bound macromolecules to perform chemical reactions.

For other applications, however, it may be desired to actually improve the binding towards a surface; not only of simple molecules but also of more complicated subjects such as cells (**Figure 2**). The control over cellular binding is particularly important - or actually the key point - in all tissue engineering strategies: here, biomacromolecules have shown to be a promising and versatile tool to achieve a controlled integration of scaffolds and implants into the body environment<sup>40-43</sup>. This is usually achieved by immobilizing cell-adhesive or growth factor-binding moieties to improve the cell-adhesive characteristics of those implants or to actively induce cell migration, proliferation, and differentiation<sup>44-46</sup>. Typical application areas for such tissue engineering constructs include skin patches<sup>47,48</sup>, bone and cartilage replacements<sup>49-52</sup>, dental implants<sup>41,53-55</sup>, scaffolds for nerve repair<sup>44</sup> or vascular grafts<sup>56-58</sup>. Furthermore, also many biological sensors are based on the principle that

specific molecules bind to a substrate to become detectable<sup>59-61</sup>. Such high selectivity is often achieved by immobilizing antibodies onto the substrates (**Figure 2**). The most common example for such an antibody-based biological sensor is certainly the pregnancy test. Similar mechanisms are employed in other sensor applications to test for specific target molecules or gene expression<sup>62,63</sup>. For sensory applications, however, coatings are not only used to immobilize targets but can further be used to perform chemical reactions with target molecules (**Figure 2**). Such chemical reactions can either be used to create a color signal (*e.g.* by enzymatic conversion of a substrate) or a electrochemical signal (*e.g.* through oxidizing reactions) and those signals which can further be quantified by suitable analytical detection methods<sup>60,61,64-66</sup>.

In analogy to cell signaling processes, macromolecular coatings are also used to actively modulate immune reactions. Such immunomodulating coatings can be used to reduce the foreign body response towards artificial materials or implants<sup>67-69</sup>. Furthermore, by reducing the immune response, stealth surfaces can be generated which are used to improve the blood circulation time of therapeutic nanoparticles<sup>70</sup>. Other immunomodulating coatings are used to specifically target particles towards disease sites by improving their “recognition” through the target cells<sup>71-74</sup> or to develop new vaccinations<sup>75,76</sup>.

The control over binding and subsequent unbinding of molecules from coated surfaces further allows to access another application area: the field of controlled drug delivery (**Figure 2**). Drug loaded coatings are especially interesting for implant coatings to overcome early stage infections, reduce the foreign body response or improve integration in the surrounding tissue by supplying growth factors. Yet, most of those strategies lack specificity and the release of the active component is often passive only. Macromolecular coatings are only employed in these systems to control the time span of the release event - by either acting as a diffusive barrier or by serving as a degradable drug reservoir<sup>77-81</sup>.

In this thesis, the application of macromolecules will be investigated in three different categories. Starting with macromolecules as high-performance bio-lubricants, this study will identify the underlying lubrication mechanisms and focus on chances and limitations of their use (**Figure 1**, grey). In the second part, lubricious macromolecules will be immobilized onto medically relevant polymer surfaces. Three aspects, *i.e.* the lubricity, mechanical and chemical stability, and interactions of polymer-brush coatings with macromolecular lubricants will be investigated (**Figure 1**, cyan). In the final chapter, the field of biotribology will be

left and the focus will be shifted to more specific and active properties of macromolecular coatings. It will be shown how different macromolecular coatings can provide a versatile platform for selective binding and filtering and how they can be used to perform chemical reactions on a surface. As a special, application orientated case of selective binding, the ability of mucin-based coatings to suppress bacterial and cellular adhesion onto a substrate will be analyzed. In the last step, this mucin coating will be rendered smart: using a multilayer approach, this coating will gain the ability to supply a controlled, trigger-induced release of two independent antibiotic doses (**Figure 1**, blue).



## 2 Materials and methods

### 2.1 Macromolecules

The studies within this thesis were mainly performed with five different macromolecules: porcine gastric mucin, lubricin, hyaluronic acid, polyethylene glycol, and poly-L-lysine. The sources, purification procedures and properties are summarized in this section.

#### Mucin

Mucins are a group of large glycoproteins with molecular weights of up to a few MDa.<sup>82</sup> They are the main functional component of mucus, which covers all wet epithelia in the human body, including the corneal surface<sup>83</sup>, the gastrointestinal tract<sup>84</sup>, and the female reproductive system<sup>85</sup>. The mucus layer protects the underlying epithelial cells from dehydration. Furthermore, mucus has unique selective properties, that on the one hand allow nutrients to pass, but on the other hand trap or repel pathogens, such as viruses or bacteria<sup>86-88</sup>. Owing to their ability to bind many water molecules<sup>18</sup> and to adsorb to various surfaces<sup>82,89</sup>, mucins also serve as excellent lubricants and thus protect the sensitive cellular surface from mechanical damage.

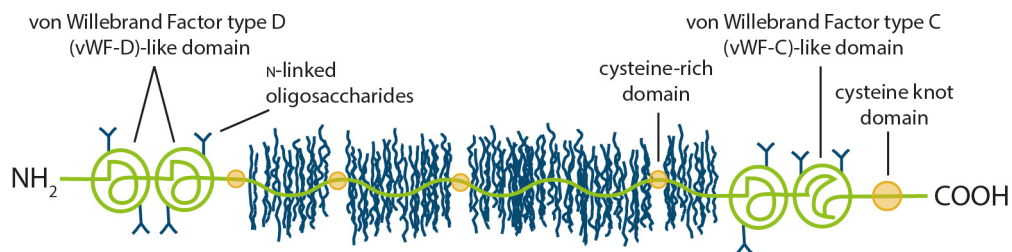


**Figure 3: Structure of gastric mucins.** The backbone of the mucin molecule consists of a large polypeptide backbone. Its terminal ends are partially folded, whereas the central region is highly glycosylated. These sugars make up to about two-thirds of the molar mass of the molecule. Some of these sugars contain negatively charged sulfate and sialic acid groups which render the mucin molecule polyanionic.

To date, around 20 mucin genes have been identified. The mucins discovered so far can be divided into three groups: secreted gel-forming mucins, secreted non-gel-forming mucins, and mucins which are attached to the cell membrane. Secreted gel-forming mucins, *i.e.*, MUC2, MUC5AC, MUC5B, MUC6, and MUC19, are the

major constituents of mucus. Depending on the specific mucus localization and function, the mucin concentration can vary between 1 and 5 %. Secreted gel-forming mucins are produced by specialized epithelial cells and by glands located in the submucosal connective tissues.

Mucins comprise a linear, mostly unfolded polypeptide chain consisting of several thousand amino acids and a molecular weight of 500-700 kDa<sup>90</sup>. The central region is highly O-glycosylated and makes up to 80 % of the total mass of the mucin molecule. The high glycosylation density of mucins is probably a key factor that suppresses polypeptide folding and contributes to the bottle-brush-like structure of the glycoprotein. This glycosylated area is flanked by cysteine-rich regions and *von-Willebrand factor*-like domains at both termini of the macromolecule (**Figure 3**).

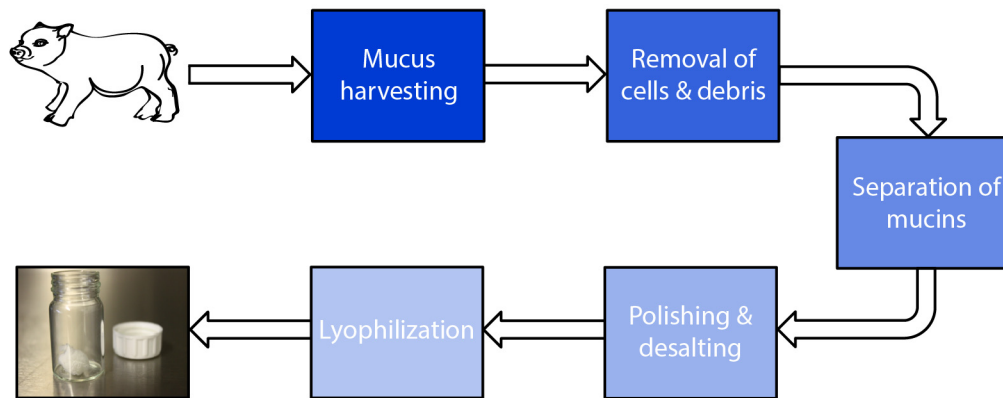


**Figure 4: Purification of porcine gastric mucin.** The process for the purification of functional mucins comprises five steps: Mucus is harvested from animal tissues to obtain crude mucin containing material that can be further processed. The removal of cells and cellular debris is followed by a technique that isolates the mucin glycoproteins from most molecular impurities. Afterwards, mucins are typically desalted and further purified to remove remaining molecular contaminants. Finally, lyophilization yields a protein powder which can be stored for extended time periods.

The C-terminal cysteine knot domain is thought to contribute to the dimer formation of the glycoprotein *via* cystine (S-S) disulfide bonds, and these dimers can further polymerize into larger oligomers. This assembly process increases the molecular weight from 2-3 MDa for monomeric mucins up to 50 MDa for oligomers. Whereas the central region is almost exclusively constituted by polar amino acids (and rich in serine and threonine as required for O-glycosylation), the non-glycosylated termini exhibit a rather hydrophobic character. For research purposes, porcine gastric mucins, as well as bovine submaxillary mucins, are

available from different commercial distributors. Furthermore, also some mucin-based medical products already exist on the market. However, all these commercially available mucins have been altered in their structure or are still contaminated which results in a loss of their native functionality<sup>91-94</sup>. Thus, here exclusively manually purified mucins were used. To allow for a constant quality with reproducible characteristics the manual purification protocols as described by Celli *et al.*<sup>95</sup> and Schömig *et al.*<sup>93</sup> were further developed (see *Appendix A* for details): Briefly, mucus was obtained from gently rinsed pig stomachs by manual scraping the surface of the gastric tissue. The collected mucus was diluted 5-fold in 10 mM sodium phosphate buffer (pH = 7.0) containing 170 mM NaCl and 0.04 % Sodium azide (Carl Roth, Karlsruhe, Germany) and stirred at 4 °C overnight. Cellular debris in the liquid phase was removed *via* filtration through a tea filter and a single ultracentrifugation step (150,000g at 4 °C for 1 h). Subsequently, the mucins were separated from other macromolecules by size exclusion chromatography using an ÄKTA purifier system (GE Healthcare, Munich, Germany) and a XK50/100 column packed with Sepharose 6FF. The obtained mucin fractions were pooled, and the sodium chloride concentration increased to 2 M. Then, the solutions were dialyzed against ultrapure water and concentrated by crossflow filtration. Finally, the concentrate was lyophilized and stored at -80 °C until further use (**Figure 4**).

### Lubricin

Lubricin, a mucinous glycoprotein, is one of the two main components in the synovial fluid of articular joints.

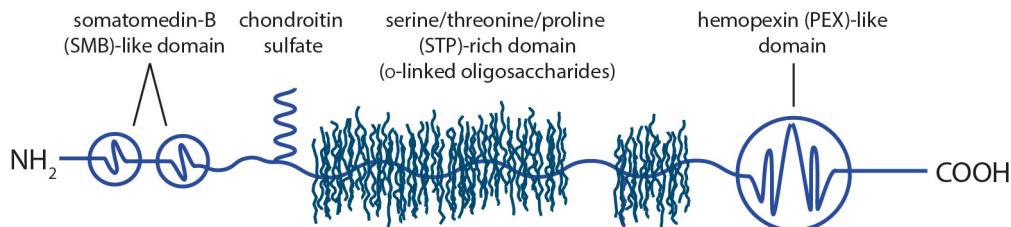


**Figure 5: Lubricin Structure.** Similar to the mucin molecule, lubricin comprises a polypeptide backbone that is partially folded in the terminal regions and highly glycosylated in the central part<sup>96</sup>. In contrast, however, the lubricin backbone is with a molecular weight of approximately 300 kDa<sup>7</sup> comparably smaller.

Here, in interplay with other components such as hyaluronic acid, lubricin is responsible for the outstanding tribological performance in joint movement and guarantees astonishing low friction with almost no wear formation over decades.

Lubricin, quite similar to mucin<sup>97,98</sup>, comprises a linear polypeptide backbone with partially folded termini and a densely glycosylated central region<sup>96</sup> (**Figure 5**). Compared to mucin, lubricin is a bit smaller. The lubricin protein backbone has a molecular weight of approximately 300 kDa<sup>7</sup>. Purification of lubricin is rather expensive, time-consuming and the purification efficacy is rather low.

Here, purified lubricin from the Schmidt Lab (University of Calgary, CA) was used, which they purified from bovine knee joints, according to their protocol from 2007<sup>3</sup>. In brief, cartilage discs were cultured in Dulbecco's Modified Eagle's Medium and purified using salt gradient diethylaminoethanol anion exchange chromatography. The purity of the solution was confirmed using a 3–8 % Tris-Acetate SDS page followed by *Simply Blue* protein stain and densitometry analysis.

### Hyaluronic acid (HA)

HA is a glycosaminoglycan (GAG), a biological macromolecule, which naturally occurs in all mammalian joints both, as a component of cartilage tissue and the synovial fluid<sup>99</sup>. GAGs are linear polysaccharides based on a repeating disaccharide unit (**Figure 6**). HA is the only GAG with no sulfate groups and is highly negatively charged due to the large amounts of carboxyl groups.

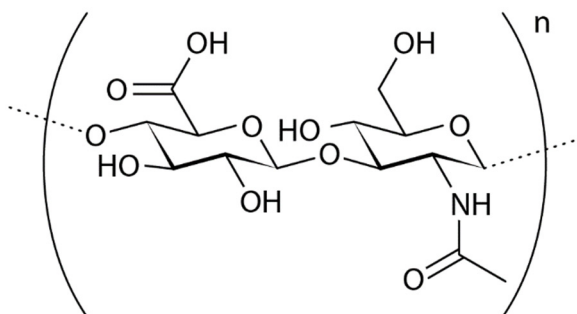


**Figure 6: Structure of hyaluronic acid.** The anionic, non-sulfated glycosaminoglycan hyaluronic acid consists of D-glucuronic acid and N-acetyl-D-glucosamine, which are linked by glycosidic bonds.

In joints, surface-bound HA and free HA in the synovial fluid act synergistically together with the glycoprotein lubricin and other smaller molecules to achieve the outstandingly low friction values observed on articular cartilage<sup>100-102</sup>. HA has been used extensively in medical applications. For example, HA has been used for more than 20 years in artificial teardrops for dry eye syndrome therapy. Although hyaluronic acid is not part of the natural tear fluid, its ability to bind water and

retard tear film evaporation substantiates its use for therapeutical issues in ocular medicine. Furthermore, hyaluronic acid has positive effects on cell migration<sup>103</sup> and corneal wound healing<sup>104,105</sup> which makes it even more interesting for clinical applications.

Here, HA from two different sources was used: One pure, high molecular weight version (2 – 2.4 MDa from *Streptococcus equi*, Sigma Aldrich) and an HA-based artificial synovial fluid, which contains 1.6 % (w/v) of hyaluronic acid in a preserved buffer system (Sinovial HighVisc, Humantis GmbH, Iserlohn, Germany).

### **Polyethylene glycol (PEG)**

Polyethylene glycol (PEG), depending on the molecular weight sometimes also referred to as polyethylene oxide (PEO) is a synthetic polymer with the repeating unit ethylene oxide. Due to its (bio)inert character, PEG has been particularly interesting for clinical research and is to date already used in different applications, e.g. in drug formulations or as passivation coatings for devices or particles<sup>106-115</sup>. Owing to its rapid degradation in aqueous physiological environments<sup>116-122</sup>, the use of PEG, however, is limited to short time applications,

Here, PEG was used to compare different parameters in the coating process as well as lubricant interactions with the macromolecules. As lubricants, two different products were used - one low molecular weight PEG (10 kDa, Merck KGaA, Darmstadt, Germany) and one high molecular weight PEO (1 MDa, Sigma Aldrich). To be able to couple PEG *via* a carbodiimide reaction in aqueous solution, an amine end-functionalized molecule was chosen. To reduce the probability of unwanted side reactions, the chosen PEG derivate contains only one primary (alpha) amine and an (omega) methyl group (mPEGa, 20 kDa, Rapp Polymere GmbH, Tübingen, Germany).

### **Poly-L-lysine (PLL)**

PLL is a cationic homopolymer, mostly of synthetic origin. It is often used to improve cell adhesion<sup>123</sup>, an attribute which is based on electrostatic interactions with negative charges from proteins and cell membranes. Furthermore, as PLL exhibits a rather high charge density, it is frequently used to form stable complexes with anionic macromolecules, e.g. to form multilayered coatings<sup>123-125</sup> or for the preparation of microcapsules as drug delivery vesicles<sup>126,127</sup>. However, PLL is also known to be immunogenic<sup>128</sup> and cytotoxic to several cell lines<sup>129</sup>, which is why the

use of PLL-containing products in a medical context requires careful investigation of the biocompatibility.

Here, two types of PLL were used; First, a solution containing 0.1 % (w/v) PLL with a molecular weight in the range between 150 and 300 kDa (Sigma Aldrich) and, second, an end-functionalized alkynyl-poly-L-lysine (aPLL, Alamanda Polymers, Inc., Huntsville, AL, U.S.A.) with a molecular weight of 21 kDa.

## 2.2 Coupling strategy for macromolecular coatings

To generate covalently coupled polymer layers on different substrates, a multi-step coating process was developed that is based on silane chemistry and carbodiimide coupling (**Figure 7**).

### Surface activation and silanization of polymeric surfaces

Briefly, the polymeric samples were treated with O<sub>2</sub> plasma at 0.4 mbar pressure and an intensity of 30 W for 90 s. The plasma treatment replaces the methoxy groups on the polymer surface with hydroxyl groups, which enable a covalent attachment of silane molecules.

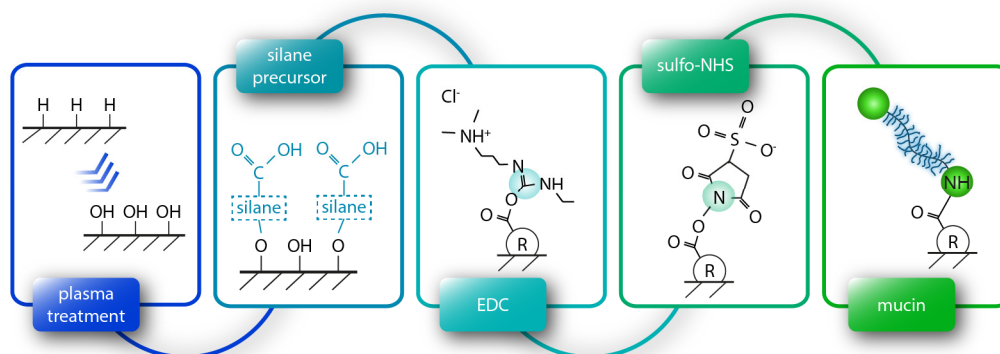


**Figure 7: Coating process for porcine gastric mucin.** To functionalize the PDMS substrate, the O<sub>2</sub>-plasma-activated surface first is pre-coated with a silane-based precursor. Afterwards, porcine gastric mucin (MUC5AC) can be covalently linked to the surface by carbodiimide chemistry.

The silane was used as a coupling agent to further allow for attaching amine-containing/functionalized macromolecules, *e.g.* porcine gastric mucin to the surface *via* carbodiimide coupling or azide-functionalized PLL *via* 1,3-dipolar cycloaddition. The silanization protocol used here was adapted from Zhang and

Srinivasan<sup>130</sup> and optimized for this project. To obtain carboxylated surfaces for the final macromolecular coating, the coupling agent *N*-[(3-trimethoxysilyl)propyl]ethylenediamine triacetic acid trisodium salt (TMS-EDTA, abcr GmbH, Karlsruhe, Germany) was used. The azide modified surface for “click”-chemistry was generated by covalently bonding 6-azidosulfonyl-hexyltriethoxysilane (ASH-TES, abcr GmbH) to the activated surface. TMS-EDTA was diluted to a final concentration of 0.1 % (w/v) in 10 mM acetate buffer (HOAc, pH = 4.5) containing 0.37 g/L sodium acetate anhydrous and 0.33 g/L acetic acid (Carl Roth). ASH-TES was diluted to 0.13 % (v/v) in methanol (MeOH, > 99.9 %, Carl Roth) and acetate buffer (pH = 4.5) was slowly added to obtain a 3:1 (MeOH:HOAc) solution with a final ASH-TES concentration of 0.1 % (v/v). To allow the different silanes to react with the activated polymer surface, the samples were incubated in the silane solution at an increased temperature of 60 °C for 5 h. Afterwards, the silane-modified samples were removed from the solutions, dipped into 2-propanol (IPA, > 99.5 %, Carl Roth, Karlsruhe, Germany) and washed in 96 % ethanol (EtOH, Carl Roth) on a rolling shaker (RS-TR 05, Phoenix Instrument GmbH, Garbsen, Germany) at 70 rpm for 1 h to remove unbound residues. Subsequently, the samples were again placed into the oven and stored at 110 °C for 1 h to further stabilize the siloxane bond.

### Macromolecular coupling to silanized surfaces

To covalently bind purified MUC5AC or commercial amine functionalized polyethylene glycol (mPEGa, in the main text, always referred to as PEG) to carboxylated PDMS surfaces, an amide coupling reaction was chosen. To activate the carboxyl groups, the precoated polymer samples were immersed in 100 mM 2-(*N*-morpholino)ethanesulfonic acid (MES, Applichem GmbH, Darmstadt, Germany) buffer (pH = 5) containing 5 mM 1-ethyl-3-(3-dimethyl-amino-propyl)carbodiimide-hydrochloride (EDC, Carl Roth, Karlsruhe, Germany) and 5 mM *N*-hydroxysulfosuccinimide (sulfo-NHS, abcr GmbH) and placed onto a shaker at room temperature (RT) for 30 min (as outlined in Sam *et al.*<sup>131</sup>).

Afterwards, the EDC-NHS solution was exchanged with a commercial Dulbecco’s phosphate-buffered saline solution (DPBS, pH = 7.4, Lonza, Verviers, Belgium) containing the desired macromolecule. For  $\alpha$ -methoxy- $\omega$ -amino polyethylene glycol (mPEGa, MW = 20 kDa, Rapp Polymere GmbH), the macromolecule concentration in the DPBS solution was set to 0.4 % (w/v), and for porcine gastric mucin to 0.1 % (w/v). The reaction was allowed to take place for either 0.5 h (for mPEGa) or 12 h (for purified mucin), respectively. In principle, also PLL could

easily be attached to the carboxylated PDMS surface *via* carbodiimide coupling. However, compared to mPEGa (which only carries a single amine group at its terminal end) and mucin (where the amine groups are also more easily accessible at its non-glycosylated termini<sup>89</sup>) PLL carries a multitude of amine groups all along the macromolecule. Thus, it is likely, that binding PLL to the silanized surface by means of carbodiimide coupling would lead to a rather flat, uneven layer and not a polymer-brush coating as desired here.

Thus, to generate a comparable coating pattern with PLL as for mPEGa and mucin, an end-functionalized alkynyl-poly(L-lysine hydrobromide) molecule (aPLL, Alamanda Polymers), is used. To covalently attach aPLL to the PDMS surface, 1,3-dipolar cycloaddition was used, which has emerged as one of the most popular methods to employ the principle of “click”-chemistry<sup>132</sup>. Although the 1,3-dipolar cycloaddition typically requires elevated temperatures, a rather long reaction time, and provides poor selectivity towards the reaction products, these restrictions have been remedied by employing a copper-(I)-catalyzed reaction scheme (CuAAC)<sup>133</sup>. In this modified form, the reaction is especially useful for bioconjugation at RT<sup>134</sup>.

Here, a mixture of 1,4-diazabicyclo-[2,2,2]-octane (DABCO), glacial acetic acid (AcOH), and Cu(I) ions were prepared according to Sarode *et al.*<sup>135</sup>. Therefore, 0.03 mmol copper sulfate pentahydrate (CuSO<sub>4</sub> x 5H<sub>2</sub>O), 0.12 mmol sodium ascorbate (NaAsc), and 0.06 mmol 1,4-diazabicyclo[2.2.2]octane (DABCO, Carl Roth) were dissolved in 2 mL ultrapure water. Then, 0.06 mmol AcOH were added to the mixture and 5 mg aPLL were added to this solution to obtain an aPLL concentration of 0.1 %. As before, the reaction was allowed to take place at RT for 0.5 h. Finally, all samples were washed in ethanol and stored in DPBS until further use.

### 2.3 Polymer materials used in clinical applications

Additional to silicone-based materials such as PDMS, there are many other polymer materials that are commonly used in clinical applications. For example, polyethylene (PE) is used in total joint replacements or as a material for catheters; polypropylene (PP) is often the basis for finger joint prostheses or non-degradable sutures; intraocular lenses, tooth replacements, and artificial tendons/ligaments are frequently made of polymethylmethacrylate (PMMA) or polyethylene terephthalate (PET); polyurethane (PU) and polyvinylchloride (PVC) are probably the most common materials for medical tubings, and PU is used as a biocompatible, soft coating for titan-based stents (**Table 1**). As all polymer materials used here

contain accessible hydrogen groups, they can be activated by oxygen plasma in a similar manner as PDMS.

**Table 1: Structure and application of medical polymers**

Name	Monomer Structure	Medical Application
Polymethyl-Methacrylate (PMMA)	$\left[ \begin{array}{c} \text{CH}_3 \\   \\ \cdots\text{CH}_2 - \text{C} \cdots \\   \\ \text{C} \\   \\ \text{O} \\   \\ \text{CH}_3 \end{array} \right]_n$	Tooth fillings & Replacements, intraocular lenses, Bone cement <sup>136,137</sup>
Polyethylene-Terephthalate (PET)	$\left[ \text{O} - \text{CH}_2 - \text{CH}_2 - \text{O} - \text{C}(=\text{O}) - \text{C}_6\text{H}_4 - \text{C}(=\text{O}) \right]_n$	Artificial vessels, replacements for tendons & ligaments, surgical suture material <sup>136,138</sup>
Polyvinyl-carbonate (PVC)	$\left[ \begin{array}{c} \text{Cl} \\   \\ \cdots\text{CH} - \text{CH}_2 \cdots \end{array} \right]_n$	Tubings, catheters, blood pouches <sup>136,139</sup>
Polyethylene (PE)	$\left[ \begin{array}{cc} \text{H} & \text{H} \\   &   \\ \cdots\text{C} & - \text{C} \cdots \\   &   \\ \text{H} & \text{H} \end{array} \right]_n$	Medical containers, catheters, artificial tendons, total joint replacements <sup>136,138,140</sup>
Polyurethane (PU)	$\left[ \text{R} - \text{O} - \text{C}(=\text{O}) - \text{NH} - \text{R} - \text{NH} - \text{C}(=\text{O}) - \text{O} \right]_n$	Artificial cardiac valves, balloon catheters, tubings, skin replacement, cardiac pacemakers, vascular grafts, long term implants <sup>136,140</sup>
Polypropylene (PP)	$\left[ \begin{array}{c} \text{CH}_3 \\   \\ \cdots\text{CH} - \text{CH}_2 \cdots \end{array} \right]_n$	Finger joint prothesis, grafts, non-degradable sutures <sup>138,140</sup>
Polydimethyl-Siloxane (PDMS)	$\left[ \begin{array}{c} \text{CH}_3 \\   \\ \cdots\text{Si} - \text{O} \cdots \\   \\ \text{CH}_3 \end{array} \right]_n$	Flexible and small joint replacements, breast implants, testicle implants, transfusion and catheter tubings, gastric bags, drains, endoscopic windows, bandages, contact lenses <sup>136,140</sup>

Except for some minor changes in the process temperature (*i.e.*, for all six additional materials, the temperature during the stabilization step is lowered to 60 °C – this requires an extension of this step duration to 4 h) and rinsing fluids (PMMA shows

a poor resistance towards organic solvents; thus, those samples are cleaned with ultrapure water instead of EtOH and 2-propanol), the coating protocol is the identical as described above.

All polymers were used as obtained from the distributor (IKS Schön GmbH, Neuss, Germany) except for PDMS. PDMS samples were prepared in different geometries from a commercially available PDMS system (Sylgard 184, Dow Corning, Midland, U.S.A.). Sylgard 184 is a very frequently used system in academic studies: its application ranges from microfluidic investigations<sup>141</sup> and surface functionalization studies<sup>142</sup> to cell culture and bacterial tests<sup>143</sup>. Furthermore, the Sylgard PDMS system used here was also used in previous publications in the field of biotribology<sup>20,89,144</sup>; therefore, this PDMS variant allows for good comparability of the obtained results with those from these previous studies. Samples were prepared by first mixing PDMS in a 10:1 ratio with the curing agent and exposing the mixture to vacuum for 1 h to remove air bubbles. The mixture was filled into a mold (the mold geometry varies according to the experimental setup the samples were used in) using a displacement pipette before curing the silicone at 80 °C for 1 h. Since other studies indicated that there might be unreacted low molecular weight residues left after curing the PDMS<sup>145</sup>, the samples were further tempered at 100 °C for 2 h. Prior to the surface modification, the specimens were cleaned with 80 % ethanol and ultrapure water.

~ ~ ~

## 2.4 Macrorheology

Most materials, especially those from biological origin, exhibit neither a pure viscous nor a pure elastic behavior. To describe such viscoelastic materials, the material response  $\sigma^*$  to an induced oscillating deformation  $\gamma^*$  is mapped. The corresponding modulus  $G^*(\omega)$  is a complex parameter and can be separated into a real and an imaginary part. Whereas the real part  $G'(\omega)$  describes the elastic response of a material, the imaginary part  $G''(\omega)$  describes its viscous properties:

$$G'(\omega) = \frac{\sigma_0}{\gamma_0} \cos(\delta)$$

$$G''(\omega) = \frac{\sigma_0}{\gamma_0} \sin(\delta)$$

Here,  $\sigma_0$  and  $\gamma_0$  denote the amplitude of the shear stress and the shear strain, respectively. The phase shift between the deformation of the material and its stress response is denoted with  $\delta$ , which is dependent on the angular frequency  $\omega$  of the stimulation. The viscoelastic properties of the different materials used in this thesis were determined using a research-grade shear rheometer (MCR302, Anton Paar, Graz, Austria). This device can be equipped with different commercial and custom-made measuring systems to allow for optimal measuring conditions in each scenario.

### Viscosity measurements

Viscous samples, *i.e.* those, which were expected to exhibit negligible elastic character) were probed with a cone/plate setup (measuring head: CP50, bottom plate: P-PTD200/Air, Anton Paar) in a rotational manner. The dynamic viscosity is typically measured in a logarithmic shear ramp to detect non-Newtonian behavior of the samples. For each measurement, a sample volume of 570  $\mu\text{L}$  was required. The viscosity was determined for shear rates between  $\dot{\gamma} = 1 \text{ s}^{-1}$  and  $\dot{\gamma} = 4000 \text{ s}^{-1}$ . Measurements were conducted at  $T = 21 \text{ }^\circ\text{C}$  or  $37 \text{ }^\circ\text{C}$  and a solvent trap was installed to avoid dehydration of the samples during measurements.

### Oscillatory shear measurements

The frequency-dependent viscoelastic parameters of the materials used here were determined in a plate/plate setup. Depending on the sample, the gap between the measuring head (PP25, Anton Paar) and the bottom plate (P-PTD200/Air, Anton Paar) was set to values between  $d = 100 \text{ } \mu\text{m}$  and  $d = 300 \text{ } \mu\text{m}$ . Oscillatory

measurements were performed in a logarithmic frequency ramp from  $f = 0.01$  Hz to  $f = 10$  Hz. To avoid exceeding the linear response regime, these measurements were preferably conducted in a torque-controlled manner. Depending on the sample, the torque was chosen as small as possible, typically between  $M = 0.5$  and  $10 \mu\text{Nm}$ . If the material exhibited time-dependent material properties, *e.g.* the material formed a gel after two components were mixed, it was necessary to fix the oscillation frequency to a certain level. This level was then chosen, such, that the storage modulus was probed in its plateau value (often  $f \approx 1$  Hz). However, to determine this plateau, it was first necessary to record a frequency spectrum of the sample in its final state prior to conducting the reaction kinetics measurement.

## 2.5 Biotribology

To investigate the lubricity of different solutions and coatings as well as their ability to protect surfaces from wear formation, tribological measurements were performed. During each tribological measurement, the coefficient of friction  $\mu$  was recorded as

$$\mu(v) = \frac{F_R(v)}{F_N}$$

where  $F_N$  denotes the normal force onto the tested surface and  $F_R(v)$  the friction force, *i.e.* the resistance a “rough” surface generates against the sliding movement. The friction force, and thus the coefficient of friction, are typically dependent on the sliding velocity  $v$ . Stribeck described three classical regimes that occur in any lubricated contact scenario, *i.e.* the boundary friction regime, the mixed regime, and the hydrodynamic regime.

The first one describes a typical scenario at low sliding velocities. Here, the opposing surfaces are in direct contact with each other. Consequently, the coefficient of friction is typically high here. With increasing sliding velocity, the lubricant generates buoyancy, and the surfaces start to separate, which is referred to as the mixed lubrication regime. Thus, the coefficient of friction drops in the mixed regime. The sliding velocity, where the two surfaces are totally separated for the first time, describes the turning point in the coefficient of friction curve. It also determines the start of the hydrodynamic regime. With further increasing sliding velocity, the surfaces separate even more and friction within the fluid (and eventually also turbulences) starts to occur, which leads to a slight but constant increase of the friction coefficient.

### Biopolymer lubrication mechanisms

Whereas simple aqueous or oil-based lubricants can only influence the coefficient of friction by adapting the viscosity to the desired working environment, (bio)-macromolecule-based lubricants have been shown to be able to allow for ultra-low friction coefficients over several decades of sliding velocities - even in the boundary lubrication regime<sup>4,12,89,93,146-148</sup>.

Two molecular processes are responsible for their ability to overcome the regimes described in the classic Stribeck theory, *i.e.* the sacrificial layer and the hydration lubrication mechanism. Both mechanisms require the macromolecule to be able to adsorb onto one or both surfaces of the friction partners. The sacrificial layer mechanism then describes the effect of cyclic shear-off and readsorption of the molecules, which allows for the dissipation of friction energy and thus the reduction of the friction coefficient (**Figure 8a**)<sup>11,149</sup>.

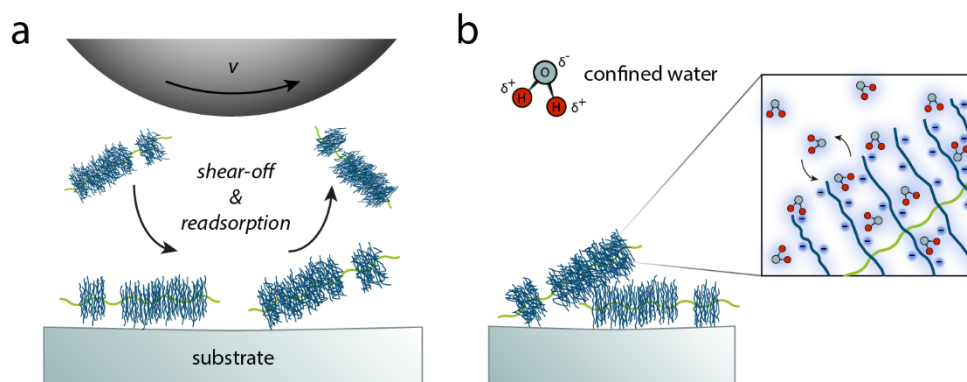


**Figure 8: Macromolecular lubrication mechanisms.** The outstanding lubrication of polymer-based lubricants originates from two effects, *i.e.* the continuous shear-off and readsorption of the polymers (a) and the ability of surface bound polymers to supply a water film to separate the opposing surfaces (b).

The second effect, *i.e.* the hydration lubrication mechanism, requires the molecule to be hygroscopic. When surface-bound polymers are also hydrated, they can form a thin water film between the friction partners that separates the opposing surfaces even at very low sliding velocities. Furthermore, under shear forces and pressure, water molecules between the polymer and surrounding fluid are exchanged, which further dissipates friction energy. The dissipation of energy increases with a stronger bonding of the water molecules to the polymer, *i.e.* when the polymer is charged and thus interacts with the electric dipole of the water molecules (**Figure 8b**)<sup>17-19,150,151</sup>.

### Stationary contact tribology

For friction measurements in a stationary contact mode, a commercial shear rheometer (MCR 302, Anton Paar) was equipped with a tribology unit (T-PTD 200, Anton Paar), and measurements were performed in a ball-on-cylinder geometry (Figure 9a).

As friction partners in the tribology setup, PDMS cylinders with a diameter of 6.2 mm (prepared as described above) and steel spheres with a diameter of 12.7 mm (1.4301, Kugel Pompel, Vienna, Austria) were chosen. This particular material pairing is selected, since both, steel and PDMS-based materials, are commonly used in various medical devices<sup>152,153</sup>. Moreover, such a hard-on-soft pairing involving both a hydrophilic and a hydrophobic surface is also frequently employed in biotribological studies to mimic, *e.g.*, the tongue-palate interface.

Measurements were performed at a constant normal load of  $F_N = 6$  N. This normal force is chosen such that friction in the boundary, mixed, and hydrodynamic regime can be probed within the accessible velocity range<sup>89,154</sup>. Based on the Hertzian contact theory<sup>155</sup>, the average contact pressure  $p_0$  was then estimated as follows:

$$p_0 = \frac{2}{3}p_{\max} = \frac{2}{3\pi} \sqrt[3]{\frac{6F_{N, \text{per pin}} \cdot E'^2}{R^2}} \quad \text{with} \quad \frac{1}{E'} = \frac{1 - \nu_1^2}{E_1} + \frac{1 - \nu_2^2}{E_2}$$

Using the Young's moduli and Poisson's ratios of steel ( $E_{\text{steel}} = 210$  GPa,  $\nu_{\text{steel}} \approx 0.30$ ) and PDMS ( $E_{\text{PDMS}} \approx 2$  MPa<sup>156</sup>,  $\nu_{\text{PDMS}} \approx 0.49$ <sup>156</sup>), the Hertzian contact theory returns an average contact pressure of approximately 0.31 MPa. The velocity-dependent friction behavior was evaluated by performing logarithmic velocity ramps from  $v \approx 700$  to 0.001 mm/s, and the friction coefficient was measured at 48 distinct velocity levels for 10 s each. Before acquiring the first measuring point, the system was allowed to stabilize at the highest rotational velocity for 30 s. For each measurement, 600  $\mu\text{L}$  of lubricant were required.

### Migrating contact tribology

The oscillatory tribology measuring system comprises a measuring head and a bottom plate, which are both mounted into a research-grade shear rheometer from the MCR302 series from Anton Paar (Graz, Austria). The design of the measuring head presented here is inspired by a commercially available system (T-PID/44) from Anton Paar (Graz, Austria). The basis of this measuring head is established by a circular disk. This disk allows for attaching the measuring head to a commercially

available adapter (D-CP/PP 7, Anton Paar, Graz, Austria) and offers space for three exchangeable pin holders. The center of each pin holder is placed 18 mm from the rotating axis and is regularly orientated. Each pin holder can be vertically adjusted by a fine thread (M8x1, ISO 261) to individually compensate for an unevenly distributed height of the probed specimens. Furthermore, two fitting surfaces (H7/f7, ISO 286) prevent the pin holder from nutating. Each pin holder comprises two main elements: first, a hollow, custom-made aluminum screw to fix the holder into the measuring head and, second, a brass pin. The brass pin carries the actual probing material (e.g., a steel ball) and is inserted and fixed into the hollow screw. A spring between the hollow screw and the brass pin protects the air bearing of the rheometer from possible lateral forces caused by strongly uneven samples.

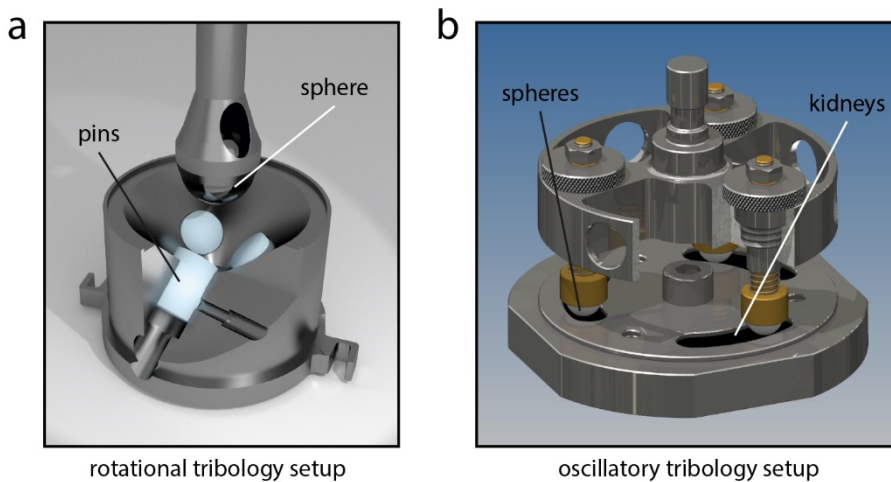


**Figure 9: Tribology setups.** The rotational tribology setup consists of a shaft that can hold a sphere and a sample holder unit, which allows for inserting three cylindrical samples (a). The measuring head of the oscillatory tribology setup offers space for three exchangeable and individually adjustable pin holders. The bottom plate allows for mounting either three cylindrical, kidney-shaped or hybrid samples (b).

The disk consists of austenitic stainless steel (material number: 1.4301) to avoid corrosion while working with water-based lubricants or in high humidity. To reduce weight and therefore the moment of inertia, cut-outs are placed where possible. This disk was fabricated by a workshop specialized in CNC technology (Volkmar Maschinenbau GmbH, Sennfeld, Germany). The holder for the counterparts can be mounted onto a commercial bottom plate (P-PTD 200, Anton Paar, Austria), which is equipped with a water-cooled temperature control unit ( $T = -20\text{ °C}$  to  $+70\text{ °C}$ ). The sample holder can be equipped with either three

cylindrical samples ( $d = 8$  mm), or three flat, kidney-shaped samples. Furthermore, this design allows for generating a lateral material interface by inserting a cylinder (made from a different material) into each kidney-shaped sample. An additional cover plate enables conducting measurements with submerged samples (filling volume: approximately 300  $\mu\text{L}$  per well) so that the influence of lubricating liquids can be probed (**Figure 9b**).

To determine the coefficient of friction, the friction torque was recorded over a deflection angle range of  $0 \leq \varphi \leq 16^\circ$  at sliding velocities between  $v = 0.01$  mm/s and  $v = 4$  mm/s. Around the turning points of each oscillation, artifacts – probably arising from the inertia of the measuring head – can occur. Thus, for further evaluation, only data points acquired between  $2^\circ$  and  $14^\circ$  are taken into account from each stroke. Furthermore, every first cycle of a multi-cycle measurement is discarded to minimize stick-slip-effects affecting the measured friction coefficients and to distribute the lubricant across the sample. To correct for the error caused by an inhomogeneous sample topography, an averaged friction trace  $\mu(\varphi)$  is calculated from the forward and backward stroke as:

$$\mu(\varphi) = \frac{\mu_f(\varphi) - \mu_b(\varphi)}{2}$$

Here,  $\varphi$  denotes the deflection angle, and  $\mu_f(\varphi)$  and  $\mu_b(\varphi)$  represent the friction traces obtained during the forward and backward stroke, respectively. Afterwards, the obtained function  $\mu(\varphi)$  is averaged with respect to  $\varphi$  to obtain an overall friction coefficient for such a multi-cycle friction measurement.

~ ~ ~

## 2.6 Fluorescence techniques

Different types of fluorescence techniques have been introduced decades ago with the purpose to allow for the visualization of typically invisible effects and processes. In this thesis, two of those techniques were adapted to visualize macromolecules and small proteins, *i.e.* fluorescence microscopy (to directly visualize fluorescently tagged molecules) and enzyme-linked immunosorbent assays, which allow for an indirect quantification *via* antibody labeling.

### Protein labeling

To allow for a visualization of either a mucin coating or the adsorption of small proteins (bovine serum albumin (BSA) and lysozyme were used as model proteins to test the antibiofouling properties of coated polymer surfaces), these proteins were labeled with three different fluorescent dyes (ATTO390 – blue, ATTO488 – green, ATTO594 – red, ATTO-TEC GmbH, Siegen, Germany). The carboxy modified ATTO dyes were linked to the proteins *via* carbodiimide coupling.

Therefore, the dye was first diluted to a concentration of  $c_{\text{ATTO}} = 1.0$  mg/mL in MES buffer (10 mM, pH = 5). Afterwards, 5 mM EDC and 5 mM sulfo-NHS were added to this solution and it was allowed to incubate light excluded at RT for 3 h. This prolonged incubation time ensured that the remaining free EDC was hydrolyzed before mucin was added (to avoid crosslinking of the mucin molecules). In parallel, 40 mg of either purified mucin, BSA (Albumin Fraction V, Carl Roth) or lysozyme (Sigma Aldrich) were dissolved in 19 mL PBS (10 mM, pH = 7). Then, both solutions were mixed thoroughly and again allowed to react at RT for 3 h. To remove unbound dye molecules, the mixture was dialyzed (MWCO = 300 kDa for mucin, MWCO = 6-8 kDa for BSA and lysozyme) against ultrapure water. The solution was then lyophilized and stored at -80 °C until further use.

### Enzyme-linked immunosorbent assay

To test the coated samples for the presence of mucin on the surface, indirect enzyme-linked immunosorbent assays (ELISA) were performed. Therefore, each sample was placed into a well of a 96 well cell culture plate and rinsed with PBS-Tween (containing 1 mg/mL Tween 20, Carl Roth, pH = 7.4) three times. Afterwards, all samples were incubated in a blocking buffer (comprising 5 % (w/v) milk powder dissolved in PBS-Tween) at 4 °C overnight.

For the following steps of the ELISA protocol, an empty well was filled with blocking buffer for each sample. On the next day, the blocked wells and the wells containing

the PDMS samples were again rinsed with PBS-Tween. Then, each sample was transferred into one of the blocked wells. Afterwards, the samples were incubated with a primary antibody (200  $\mu$ L per well) for 1 h while shaking (Promax 1020, Heidolph Instruments GmbH & Co. KG, Schwabach, Germany). For this step, a specific antibody for MUC5AC detection (ABIN966608, antibodies-online GmbH, Aachen, Germany), which targets the mucin in the C-terminus<sup>157</sup>, was used. The mucin antibody was diluted 1:400 in the blocking buffer. After incubation for 1 h, the wells were rinsed again with PBS-Tween.

A second antibody staining was then performed using a horseradish peroxidase (HRP) conjugated goat anti-mouse IgG antibody (ABIN237501, antibodies-online GmbH). This secondary antibody was diluted 1:5000 in blocking buffer. Incubation was allowed to take place at RT on a shaker for 2 h. Afterwards, the samples were washed in pure PBS (since Tween tends to interfere with the solutions used for the following steps). After washing the wells, 100  $\mu$ L of QuantaRed Working Solution were added into each well. The QuantaRed Working Solution consists of 50 parts QuantaRed Enhancer Solution, 50 parts QuantaRed Stable Peroxide and one part of QuantaRed ADHP Concentrate (QuantaRed Enhanced Chemifluorescent HRP Substrate Kit 15159, Thermo Fisher Scientific, Waltham, Massachusetts, USA). Since the Working Solution is light sensitive, direct light contact was avoided.

After 30 min of incubation at RT, the peroxidase activity was stopped by adding 20  $\mu$ L of QuantaRed Stop Solution to each well. The plate was incubated on the shaker again for 30 s before samples were removed from the wells and fluorescence of the converted substrate was measured with a multi-label plate reader (Viktor 3, PerkinElmer, Inc., Massachusetts, USA). Adsorption and fluorescence signals were measured at a wavelength of 570 nm using a data acquisition time of 0.1 s.

### 2.7 Liposomes

Liposomes are bi-layered hollow spheres that are frequently used as models as they are structurally very similar to cellular vesicles. By changing the composition of the lipid bilayer, the properties of the liposomes, *e.g.* stability, rigidity or the permeability can be tuned<sup>158-162</sup>. This versatility has caused a boom in liposomal research for drug delivery applications in recent years<sup>163-166</sup>; by now, some liposome based-therapies have already been FDA approved. In this thesis, liposomes with different net charges or surface features, *i.e.* streptavidin or biotin groups, are used to test for selective binding to functionalized surfaces. Furthermore,

thermoresponsive liposomes are used as smart switches that initiate a drug release event by liberating a specific ligand.

The liposomes used in this thesis were produced by lipid film hydration from a total of six different lipids: 1,2-dioleoyl-sn-glycero-3-phosphocholine (DOPC), 1,2-dioleoyl-3-trimethyl-ammonium-propane (DOTAP), 1,2-dioleoyl-sn-glycero-3-(phospho-rac-(1-glycerol)) (DOPG), 1,2-dipalmitoyl-sn-glycero-3-phosphocholine (DPPC) or 1,2-dioleoyl-sn-glycero-3-Phosphoethanolamine-N-(biotinyl) (Biotin-PE), and fluorescently labeled 1,2-dioleoyl-sn-glycero-3-phosphoethanolamine-N-(lissamine rhodamine B sulfonyl) (Rh-DOPE). The latter was added at a molar ration of 5 mol% to fluorescently tag liposomes used for selective binding studies. All lipids were obtained from Avanti Polar Lipids (Alabaster, AL, USA) and dissolved in chloroform.

To prepare liposomes the different lipids were mixed (see **Table 2** for the composition of the liposomes used in this thesis) to a final concentration of 0.5 mM (approximately  $10^{12}$  liposomes/mL). For preparing zwitterionic (“neutral”) DOPC liposomes, 90 mol% of DOPC and 5 mol% DOTAP were mixed to compensate for the negative charge introduced by the 5 mol% Rh-DOPE.

**Table 2: Composition of liposomes used in this thesis.** Liposomes mixtures comprising 5 mol% Rhod-PE as a fluorescent tag are marked with an asterisk.

Functionality	Component #1		Component #2		Component #3	
	Lipid	(mol%)	Lipid	(mol%)	Lipid	(mol%)
anionic*	DOPG	95	-		-	
zwitterionic*	DOPC	90	DOTAP	5	-	
cationic*	DOTAP	95	-		-	
biotinylated*	Biotin-PE	1	DOPC	89	DOTAP	5
thermoresponsive	DOTAP	6	DPPC	94	-	

Solvent evaporation was conducted overnight to generate a thin lipid film. The lipid film was resuspended in 0.5 mL of different aqueous solutions. The suspension was then sonicated in an ultrasonic bath for 5 min to produce small unilamellar vesicles followed three freeze-thaw cycles and extrusion through a polycarbonate membrane (pore sizes between 0.2 and 1.0  $\mu\text{m}$ ) using a mini extruder (Avanti Polar Lipids). Liposomes were stored at 4 °C for up to 8 weeks. To prepare streptavidin-functionalized liposomes, the biotinylated liposomes were diluted to a

concentration of 0.09 mM in PBS containing 2.5 mg/mL streptavidin (S4762, Sigma-Aldrich). The mixture was incubated at 4 °C on a shaker for 60 min. Afterwards, unbound streptavidin was removed from the liposome solution using size exclusion chromatography (PCR Kleen Purification Spin Columns, Bio-Rad). Prior to their use in filtration experiments, the streptavidin coated liposomes were extruded again to break up aggregates that might have formed during the functionalization process.

### **Liposome characterization**

Size and  $\zeta$  -potential of liposomes were determined with dynamic light scattering using a Zetasizer Nano ZS (Malvern Instruments, Herrenberg, Germany). For size and  $\zeta$  -potential measurements, lipids were resuspended in 20 mM TRIS buffer (pH = 7.3, 10 mM NaCl).

## **2.8 Drug release experiments from macromolecular coatings**

In the last part of this thesis, macromolecular coatings are used as drug depots that release their cargo in presence of a predefined trigger event. Here, two frequently used antibiotics, *i.e.* vancomycin hydrochloride (VAN, positively charged at neutral pH, Applichem, Darmstadt, Germany) or tetracycline hydrochloride (TCL, negatively charged at neutral pH, Applichem) are chosen as model drugs. To determine the drug release of either VAN or TCL from a coated surface, a spectroscopic detection method was employed: First, the bottom of cuvettes (polystyrene cuvettes, BrandTech™ macro, VWR, were used for TCL release, and UV transparent cuvettes (VWR) were used for VAN release) was covered with PDMS. To do so, PDMS was mixed and degassed as described above, and 300  $\mu$ L of the mixture were poured into the cuvette using a displacement pipette. This amount was chosen to ensure that the height of the PDMS layer does not interfere with the light sent into the cuvette by the UV spectrometer (**Figure 34a**). In the cuvette, the poured PDMS was allowed to crosslink at 60 °C overnight. Afterwards, this PDMS layer was coated with mucins as described above.

### **DNA-controlled mechanism**

For the DNA controlled release mechanism, thiol-modified single-stranded DNA sequences with self-complementary domains were used to crosslink mucins. These DNA strands are from now on referred to as crosslinker DNA (crDNA). Due to the sequence design, a crDNA/crDNA complex is stable until a displacement DNA (dDNA), which exhibits a higher affinity to crDNA than two crDNA molecules to

each other, is introduced to system. Then, a TCL solution (0.5 mg/mL) was added to the surface bound mucin layer and incubated at 4 °C for 4 h. Afterwards, lyophilized crDNA was first incubated with 100 mM DTT and then dissolved in 180 mM phosphate buffer (pH = 8). Next, the solution was added onto the mucin layer to a final crDNA concentration of 5 μM and incubated at 4 °C overnight. On the next day, the mucin layer was condensed by adding a 30 % (v/v) glycerol solution. Before starting a drug release experiment, excessive glycerol, drug, and DNA were removed by washing the cuvettes with ultrapure water.

Drug release from a condensed, crDNA-stabilized mucin layer was initiated by adding 20 μL of a 100 μM dDNA solution. The release of TCL was tracked spectroscopically with a specord210 spectral photometer (Analytikjena, Jena, Germany) at 360 nm. The amount of released drug was determined by matching the measured absorption values to a standard curve, which was prepared by characterizing the light absorption properties of serial dilutions of the respective drug solution (see *Appendix Figure C1*).

### **Ion-controlled mechanism**

Here, a surface bound mucin layer was created in cuvettes as described above. Then, a drug solution (TCL or VAC, 0.5 mg/mL each) was added to the surface bound mucin layer and incubated at 4 °C for 4 h. Then, a solution containing 30 % (v/v) glycerol was added to condense the mucin layer. Different from the DNA-based mechanism, here, stabilization of the condensed mucin layer was achieved by adding 100 mM MgCl<sub>2</sub> (dissolved in a 30 % glycerol solution) to the condensed mucin layer. After this addition step, the final Mg<sup>2+</sup> concentration was 50 mM, and the system was allowed to incubate for 2. Before starting a drug release experiment, excessive glycerol, drug, and ions were removed by washing the cuvettes with ultrapure water.

To initiate the drug release from Mg<sup>2+</sup>-stabilized mucin layers, 2 mL of a 150 mM NaCl solution were added as a trigger. The release of TCL was tracked spectroscopically at 360 nm. The release of VAN was also tracked spectroscopically, however in the UV-range, i.e. at 282 nm (see *Appendix Figure C2*). To determine the release efficiency of the process, Mg<sup>2+</sup>-stabilized mucin layers were opened by exposing the layer to a trypsin solution (50 μg/mL) for 12 h. Afterwards, the amount of released drug was determined spectroscopically to calculate the maximum loading capacity of the mucin layer.

### Multilayer coatings on PDMS

Mucin/Lectin multilayers were built according to Crouzier *et al.*<sup>167</sup> with small modifications. In brief, mucin coated PDMS samples were prepared as described in the previous section. Then, a second mucin layer was attached *via* lectin cross-linking, and the final, top mucin layer was added using dopamine as a connecting layer. In detail, the covalently mucin coated samples were incubated in a 0.2 mg/mL lectin solution (*triticum vulgare* lectin, Medicago) for  $\approx 1$  h. After washing twice with HEPES buffer (pH = 7), a second mucin layer was generated by submerging the lectin coated samples into a mucin solution (1.0 mg/mL) for  $\approx 1$  h. The top mucin layer was attached to the mucin-lectin-mucin construct using a dip-coating method. Dopamine hydrochloride (4 mg/mL, H8502, Sigma) was dissolved in 50 mM Tris buffer (pH = 8.5)<sup>168</sup>. Samples were incubated in this dopamine solution for  $\approx 2$  h, and then were rinsed thoroughly with ultrapure water to remove any unbound dopamine. Afterwards, the dopamine coated substrates were incubated in a mucin solution (0.1 % (w/v)) for  $\approx 1$  h, and then rinsed thoroughly with ultrapure water again.

### Antibiotic release experiments triggered by two distinct stimuli

To perform two-step release experiments using two distinct triggers, polystyrene cuvettes were filled with PDMS, coated with mucin and incubated in a TCL solution (0.5 mg/mL) as described above. Instead of condensing this initial mucin layer, a multilayer construct is created as described above. Thus, in the next step, the TCL solution was discarded, the cuvettes were filled with a lectin solution (0.2 mg/mL) and incubated for  $\approx 1$  h. Afterwards, the lectin solution was replaced by a mucin solution (1 mg/mL) containing 4 % (v/v) thermoresponsive liposomes (which were loaded with GlcNAc; empty, unloaded liposomes were used as a control), and the samples were again allowed to incubate for  $\approx 1$  h. This step created a second mucin layer loaded with liposomes. Then, a third mucin layer was attached on top as follows: first, a dopamine intermediate layer was generated (see above) and then the samples were incubated again in a mucin solution (0.1 % (w/v)) for  $\approx 1$  h. Then, the samples were covered with a TCL solution for  $\approx 1$  h to load to the uppermost mucin layer with this antibiotic as well. Subsequently, this top mucin layer was condensed with glycerol and stabilized with  $Mg^{2+}$  ions as described above.

Before conducting a release experiment, the multilayer samples were carefully rinsed with ultrapure water to remove any unbound molecules. Then, the samples were stored at physiological body temperature (37 °C). Release from the condensed top mucin layer was initiated by exposing the multilayer construct to a physiological

salt solution (150 mM NaCl), and the liberation of TCL was tracked spectroscopically with a spectral photometer at 360 nm. On the next day, the samples were heated up to 40 °C to mimic an inflammatory scenario, and this elevated temperature level initiated the leakage of the thermoresponsive liposomes, which – in turn – induced disassembly of the multilayer construct and release of TCL from the bottom mucin layer. Also, this second release cascade was followed using a photo spectrometer.

~ ~ ~

## 2.9 Adsorption measurements using quartz crystal microbalance with dissipation monitoring (QCM-D)

Quartz crystal microbalance with dissipation monitoring (QCM-D) is a technique that allows for detecting mass adsorption onto a substrate in ranges that are not accessible with a direct mass determination. Furthermore, in contrast to optical techniques such as surface plasmon resonance spectroscopy or ellipsometry, the QCM-D technique allows for accessing the wet mass of an adsorbed layer, *i.e.* the adsorbed molecules including an entrapped solvent.

To do so, a piezoelectric crystal with a defined resonance frequency  $\Delta f_0$  is set into oscillation, while the oscillating frequency is tracked. If the mass of this piezo crystal changes, *e.g.* through deposition of a molecular layer, the resulting change in mass affects the resonance frequency. For a thin, rigid layer adsorbed onto a substrate, the change in the resonance frequency  $\Delta f$  can be set in relation to the adsorbed mass  $\Delta m$  as described by the Sauerbrey equation<sup>169</sup>:

$$\Delta f = -\frac{f}{\rho \cdot A \cdot d} \cdot \Delta m = c \cdot \Delta m$$

Here  $\rho$ ,  $A$  and  $d$  refer to the density, the surface area and the thickness of the unloaded crystal, respectively. Those material parameters of the quartz crystal determine the sensitivity of the measurement and are typically summarized in the material parameter  $c$ .

If, however, the adsorbed layer becomes thicker and less rigid, which *e.g.* is the case if brush-like macromolecules adsorb to the substrates surface or multiple layers are deposited on the substrate, the simple linear Sauerbrey correlation holds not true anymore<sup>170,171</sup>. Such thick, soft layers additionally dampen the system through their moment of inertia or – in case of a liquid environment – interact with water molecules. Thus, the QCM-D device further records a so-called dissipation shift  $\Delta D$ , which allows for a better interpretation of the obtained data. The dissipation shift is defined as:

$$\Delta D = -\frac{E_{\text{dissipated}}}{2\pi E_{\text{stored}}} = \frac{1}{\pi f \cdot \tau}$$

where  $E_{\text{dissipated}}$  and  $E_{\text{stored}}$  refer to the dissipated and the stored energy, respectively,  $f$  to the recorded frequency and  $\tau$  to the decay time. Further, more complicated models have been developed, that – analogous to the Sauerbrey equation – allow for a quantification of the adsorbed mass of thick, soft layers<sup>172,173</sup>. However, those

models require additional input, *e.g.* overtone signals or the viscoelastic properties of the adsorbed layer, which are not directly measurable for typical resonance frequencies used in QCM-D measurements ( $f > 5$  MHz). Since here, the QCM-D technique is only used to support results or findings, which have been observed with other techniques, a precise quantification of the adsorbed mass is not required. Thus, data are qualitatively interpreted using the Sauerbrey equation and the recorded dissipation signal.

### Chip preparation

Here, adsorption measurements are exclusively performed with PDMS substrates. To obtain PDMS substrates usable for QCM-D measurements, commercially available gold sensor chips (piezo crystals as described above, which are coated with a thin layer of gold to attach electrodes for the oscillation stimulus,  $c = 0.23 \text{ Hz}\cdot\text{cm}^2/\text{ng}$ ) had to be coated with a thin PDMS film. Therefore, PDMS prepolymer and cross-linker (Sylgard 184, Dow Corning, Wiesbaden, Germany) were mixed in a ratio of 10:1, and further diluted with n-hexane to obtain a 1.0 % (v/v) polymer solution. Then, a blank gold sensor chip was placed onto the center of a spin coater (WS-400B-6NPP/LITE, Laurell, North Wales, USA), and 100  $\mu\text{L}$  of the prepared PDMS mixture were pipetted onto the gold chip. To distribute the PDMS solution, the spin-coater was set into rotation - first at 1500 rpm for 20 s and then at 3000 rpm for 60 s. Afterwards, the coated sensor chip was cured at 80 °C for 4 h.

### Mucin and PEG coatings

To obtain information on the coating density generated with PEG and mucin, a PDMS modified QCM-D sensor was precoated with TMS-EDTA as described above; however, some slight modifications in the coating procedure were introduced to avoid problems with the sensitive chips: first, the PDMS coated chips were placed into a plasma oven (Femto, Diener electronic GmbH & Co. KG) and treated with  $\text{O}_2$ -plasma (0.4 mbar, 30 W) for a reduced time of 30 s. Afterwards, the chips were immersed into acetate buffer (pH = 4.5) containing 0.1 % TMS-EDTA and incubated at 60 °C for 5 h. To avoid incompatibilities with the glue that is used to fix the gold sensors to their holder, the chips were then rinsed in Milli-Q water instead of ethanol and were placed into the oven again at 60 °C for 1 h.

The pre-coated chips were then inserted into the QCM-D device (QCM-D, qcell T-Q2, 3T-Analytik, Tuttlingen, Germany) and Milli-Q water was injected at a flow rate of 100  $\mu\text{L}/\text{min}$  until a stable baseline was obtained. Afterwards, the Milli-Q

water was replaced by 100 mM MES buffer (pH = 5) containing 5 mM EDC and 5 mM sulfo-NHS to activate the carboxyl groups on the PDMS surface. The activation reaction was allowed to take place for 30 min. Finally, a PBS solution (pH = 7.4) containing either 0.4 % (w/v) of mPEGa or 0.1 % of porcine gastric mucin was injected at a flow rate of 100  $\mu$ L/min for 60 min to generate an adsorption curve. The resulting frequency shift ( $\Delta f$ , Hz) is automatically recorded by the software “qGraph” (3T-Analytik, Tuttlingen, Germany).

### **Multilayer formation**

The successful generation of mucin multilayers on PDMS surfaces was also verified using the QCM-D technique. Therefore, a mucin (0.2 mg/mL) and lectin solution (0.1 mg/mL) were prepared in 20 mM HEPES buffer (pH = 7.4). Dopamine solution (4 mg/mL dopamine hydrochloride, Sigma Aldrich) was prepared in 50 mM Tris buffer (pH = 8). Layers were formed by injecting and leaving the tested solutions for 30 min of adsorption on PDMS-coated Au chips at a temperature of 30 °C. Chips were rinsed with a pure buffer between different solutions for 2 min.

### **2.10 Surface topography analysis**

To analyze surface alterations on artificial and biological surfaces as they can occur after a tribological treatment, surface topographies were determined using reflective confocal scanning microscopy. Reflective confocal scanning microscopy is based on the following measuring principle: For each  $x$ - $y$ -coordinate of the analyzed surface, the device (in this thesis a  $\mu$ surf custom white light profilometer (NanoFocus AG, Oberhausen, Germany) was used to perform all topography measurements) determines a reflection intensity curve over the height of the surface structures. This raw data is then usually fitted - the resulting curve is referred to as confocal curve - and the intensity maximum of the confocal curve is considered to be the material surface.

To allow for a quantification of the surface topography, the obtained raw data was typically processed in several steps: First, a macroscopic tilt or curvature of the surface was removed by applying a polynomial filter either of first or third degree. If the measurement contains non-measured points, which especially occur on steep flanks (since here, the reflection is not ideal), it was considered to either leave these points empty or to fill them by interpolating between surrounding height values. Whereas the first approach would be the more accurate way of processing, since only actual measured values are considered, some surface parameter calculations

(e.g. the surface development ratio) require a full set of data points making it necessary to fill invalid points.

Next, surface alterations and wear formation of the mechanically treated surfaces were quantified by calculating metrological parameters from those pre-processed topographical images. In principle, there is a broad set of parameters described in ISO norm 25178-2<sup>174</sup>. Here, the root mean square height  $S_q$  was the first parameter to be calculated:

$$S_q = \sqrt{\frac{1}{A} \iint_A (z(x, y))^2 dx dy}$$

This  $S_q$  value is a parameter that is commonly employed to characterize the topography of technical surfaces<sup>175-177</sup> and is defined as the standard deviation of the measured height values  $z$  in the  $x$ - $y$  plane. A parameter, that also depicts height information is the ten-point height  $S_{10z}$ , which is calculated as follows:

$$S_{10z} = \frac{\sum_{i=1}^5 |z_{pi}| + \sum_{i=1}^5 |z_{vi}|}{5}$$

The ten-point height considers the five highest peaks  $z_{pi}$  and the five deepest valleys  $z_{vi}$ , thus it is more sensitive towards extreme, local surface features compared to the  $S_q$  value.

To obtain additional information on a loss of material, volumetric parameters such as the material volume  $V_m(p)$  and the void volume  $V_v(q)$  can be calculated:

$$V_m(p) = \int_0^p (z(x) - z(p)) dx$$

$$V_v(q) = \int_q^{100\%} (z(q) - z(x)) dx$$

The material volume  $V_m(p)$  describes the total volume of all peaks exceeding a threshold line  $z(p)$ . This threshold line is chosen such that  $(1 - p)$  of all  $z$ -coordinates were below this line. Similarly, the void volume  $V_v(q)$  describes the total volume of valleys reaching below a threshold line  $z(q)$ .

Changes in surface complexity, however, can go along without changes in the surface roughness or the proportions of peaks and valleys. Therefore, the ISO norm

25178-2 offers another parameter, the developed interfacial area ratio,  $Sdr$ , which can be calculated as:

$$Sdr = \frac{1}{A} \iint_A \sqrt{1 + \left(\frac{\partial z(x, y)}{\partial x}\right)^2 + \left(\frac{\partial z(x, y)}{\partial y}\right)^2} - 1 \, dx dy$$

This value describes the complexity of a surface by comparing the actual surface and the projected surface.

Some surface alterations mostly comprise wear tracks, which are clearly visible but do not significantly change the previously described area surface parameters. These changes can be quantified by a spatial parameter: the isotropy of the surface  $Str$ , which can be determined based on the autocorrelation function (ACF):

$$Str = \frac{\min_{(\tau x, \tau y) \in R} \sqrt{\tau x^2 + \tau y^2}}{\max_{(\tau x, \tau y) \in Q} \sqrt{\tau x^2 + \tau y^2}} \quad \text{with} \quad \begin{aligned} R &= \{(\tau x, \tau y) : ACF(\tau x, \tau y) \leq 0.2\} \\ Q &= \{(\tau x, \tau y) : ACF(\tau x, \tau y) > 0.2\} \end{aligned}$$

$$ACF(\tau x, \tau y) = \frac{\iint_A z(x, y) z(x - \tau x, y - \tau y) \, dx dy}{\iint_A z^2(x, y) \, dx dy}$$

Here, a surface profile ( $z$ ) in one direction is compared with surface profile lines in the same direction at different positions ( $x, y$ ) and the correlation length between the profile lines is calculated. The isotropy of the surface is defined as the ratio of the minimum autocorrelation length in any direction divided by the maximum autocorrelation length in any direction. By integration of the Fourier spectrum of the autocorrelation length of each direction into polar coordinates, the principal direction of the surface structures can be determined, and the anisotropy quantified.

Deciding which surface parameters to choose is mostly driven by the type of sample that should be analyzed. Often it is appropriate to calculate more than one surface parameter to support findings and observations that can qualitatively be made with *e.g.* microscopical images. Statistical evaluation of the obtained surface parameters can help to identify a suitable set.

## 2.11 Data analysis and graphical representation

To detect significant differences between two examined groups, two-sample independent t-tests were conducted. Prior to testing, the normal distribution of the

measured values was verified with either the Shapiro-Wilk-test or the D'Agostino & Pearson test. Furthermore, homogeneity of variances was tested using the F-test. For non-normal distributed populations, the Wilcoxon-Mann-Whitney-test was used. For normal distributed populations with homogenous variances, Student's t-tests were performed, whereas Welch's t-test was used in case of unequal variances.

To detect statistical differences between more than two groups, one-way ANOVA (Analysis of Variances) and for multi-comparison Tukey Post Hoc tests were performed. Professional software (Prism 8, GraphPad Software, San Diego, CA, USA) was used to conduct all statistical calculations. The level for significant difference was set to  $p < 0.05$  and is marked with an asterisk where applicable.

The software Prism 8 was further used to generate all graphs shown in this work. If results are presented in boxplots, the bottom and top of the box represent the second and third quartiles. The band inside the box is the median. The length of the whiskers is based on data within the 1.5 interquartile range of the upper and lower quartile. Data points outside of this range are denoted as outliers (dots).

Graphical representations are designed using Adobe Illustrator CS6 (Adobe Inc., San José, Ca, USA).



### 3 Biomacromolecule enriched aqueous solutions as high-performance lubricants

In many fields of material science, development, and engineering - especially if the materials exhibit a persisting mechanical contact to a second material surface - friction and wear formation need to be considered<sup>178,179</sup>. As a consequence, there are a multitude of established tribological setups and characterization protocols that are commonly used to investigate the friction and wear properties of artificial materials<sup>180-185</sup>. However, friction and wear formation are not limited to technical materials but also occur for biological materials<sup>186-190</sup>. Whereas a replacement of defective parts is often possible in technical settings, biological materials as they are present in the human body, need to show excellent performance and wear resistance for several decades. Indeed, many biological tissues show very low friction and wear. Prominent examples of such biological surfaces include the cornea/eyelid interface and the articular cartilage layers in joints. Identifying the key components and understanding the underlying mechanisms that are responsible for the outstanding lubrication properties of biological systems is crucial to be able to transfer this knowledge into applications.

#### 3.1 Development of an oscillatory tribology setup\*

Owing to the complex shapes and the relatively low stiffness of biological materials compared to technical materials, characterizing their tribological properties is more challenging and requires dedicated setups<sup>189,191</sup>.

The most prominent example for a bio-tribological system is articular cartilage, which shows specific water release kinetics under load, and this behavior is responsible for a time-dependent coefficient of friction when the tissue is probed in a stationary contact geometry<sup>154</sup>. Whereas such a stationary contact may not be physiologically relevant, it is a very useful setup for quantifying the complex tribological behavior of cartilage and other water-containing materials. In contrast, physiological sliding is mimicked in measuring setups employing a migrating contact. Here, the probed material is temporarily unloaded before it is exposed

---

\* This section follows in part the publications Winkeljann *et al.*, *Biotribology* (2018) & Kiumarsi *et al.*, *Food Chemistry* (2019)

again to tribological shear<sup>192,193</sup>. In the case of cartilage, such unloading allows the tissue to re-absorb water thus providing a constantly low friction response. Typically, a migrating contact is achieved by a measuring head that slides across the surface of the material in a linear, reciprocating way with a defined stroke length and sliding velocity. However, the velocity range that can be explored by such linear tribometers is rather limited, which makes it difficult to explore the friction response of a material pairing over several orders of magnitude in sliding velocities. Vice versa, this is easily possible in rotational tribology setups, *e.g.* by probing a material pairing in a ball-on-pins geometry<sup>154</sup>. Yet, due to the sample tilt arising from the particular sample holder shape required for such a rotational tribology setup, it is not easily possible to image the treated material after tribological treatment without removing the samples from the sample holder. Such an imaging process, however, is necessary to quantify sample damage arising from tribological shear. Especially for soft, sensitive biological samples, their removal from the tribological setup and transfer to an imaging device can induce additional damage thus making wear analysis more complicated.

The technical requirements for a tribological setup become even more challenging when the friction response of a hybrid system is investigated, *i.e.* when a combination of a biological and an artificial surface is probed. Such hybrid systems are especially relevant in medical settings: examples for synthetic materials, which induce friction on biological tissues, include artificial joints, contact lenses, and catheters or intubation tubes<sup>189,194-197</sup>. Also, for such complex material pairings, both linear and rotational tribology measurements offer distinct advantages. However, those two measurement variants are typically implemented in different setups, and this often makes a direct, quantitative comparison of the obtained friction coefficients challenging. Using the same piece of equipment for both measurement types would improve this issue.

Thus, in a first step, a commercial research-grade shear rheometer is adapted to perform oscillatory tribology experiments. This is achieved by combining a custom-made measuring head with a dedicated sample holder (see *Materials and methods* for details).

### 3.1.1 Versatility of the custom-made measuring system

Different from commercial systems, this setup was designed to be highly versatile and flexible so that it can be used for various types of measurements from different

disciplines including mechanical engineering, biotribology and also food engineering.

### Validation of the oscillatory tribology setup

For validating the setup, first a steel/PDMS pairing is chosen since there are many previous studies reporting friction coefficients for different lubricants with this particular material pairing<sup>89,144,198-200</sup>. The measuring head is equipped with three steel spheres (Kugel Pompel, Austria, 1.4404,  $d = 5$  mm,  $S_q < 0.2$   $\mu\text{m}$ ), and kidney-shaped PDMS samples. The measuring head performs oscillations over a deflection angle range of  $0 \leq \varphi \leq 16^\circ$ . First, the setup is lubricated with a simple buffer solution (20 mM HEPES, pH = 7) devoid of any macromolecules.

Within a certain range, the velocity at which a cyclic friction measurement is performed can be varied. For the tested material pairing 'steel on PDMS', the friction coefficients obtained at different sliding velocities between 0.1 and 1 mm/s agree very well with the corresponding values obtained with a commercial rotational tribology setup operated at the same normal pressure (**Figure 10a**, black and cyan data). To obtain additional validation data, also a standard steel/steel pairing lubricated with standard motor oil (Formula Super 10W-40, Liqui Moly GmbH, Ulm, Germany) with a viscosity of  $\eta = 208 \pm 3$  mPas ( $n = 3$ ) is tested. Friction values are recorded at distinct velocities between 0.01 and 4 mm/s and it is found that these values, again, agree well with the values obtained with the commercial rotational tribology setup (**Figure 10a**, grey curve).

Since the moment of inertia of the measuring head sets an upper limit for the sliding velocity in oscillatory measurements, it is difficult to obtain a full Stribeck curve with this tribological system. However, changing the viscosity of the lubricant can shift the mode of lubrication thus switching the system from, *e.g.*, the boundary lubrication regime to the mixed lubrication regime. Thus, the tribological response of the steel-on-PDMS pairing when lubricated with Newtonian fluids of different viscosities is tested in the next step. As lubricants, different water/glycerol solutions (mixture ratios: 40/60, 25/75 and 10/90) are chosen with viscosities of  $12.8 \pm 0.9$  mPas,  $38.3 \pm 1.1$  mPas and  $182 \pm 1$  mPas, respectively ( $n = 3$ ). For each of those three Newtonian fluids, the coefficient of friction at four distinct velocities is measured and plotted as a function of the Sommerfeld Number  $S$ , where  $S = (v \cdot \eta)/p_0$ . The data points obtained with the different glycerol/water mixtures nicely overlap, and the typical shape of a Stribeck curve is obtained (**Figure 10b**). In the next step, the measurements conducted with both, the oscillating and the

rotating setup, are repeated using aqueous solutions containing different macromolecular lubricants, *i.e.*, hyaluronic acid (HA) or porcine gastric mucin.

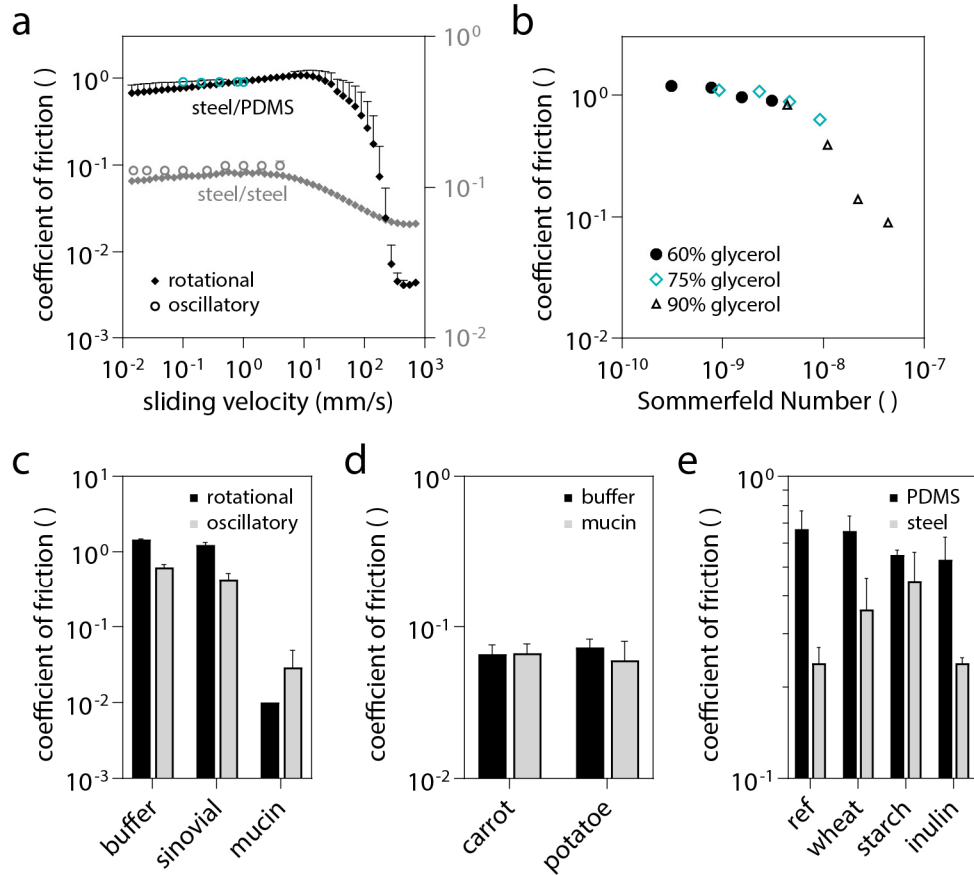


**Figure 10: Application examples of the oscillatory tribology setup.** The coefficients of friction determined by the oscillatory linear tribology setup are similar to those obtained with a rotational tribology setup both, for a steel/PDMS pairing (black) and for a steel/steel pairing lubricated with a synthetic oil (grey, different scaling) (a). Measurements with a steel/PDMS pairing lubricated with three different glycerol/water mixtures are conducted at four distinct sliding velocities and plotted as a function of the Sommerfeld Number (b). Measurements with two different macromolecular lubricants return similar values in rotational and oscillatory tribology (c). The friction values obtained for ‘food on PDMS’ pairings are similarly low, both for lubrication with mucin solutions and simple buffer (d). Friction values are further obtained with either PDMS or steel pins on four different types of bread formulations (e). Error bars denote the standard deviation as obtained from  $n \geq 3$  independent samples.

HA is diluted to a final concentration of 0.4 % (w/v) in HEPES buffer and mucin solutions are prepared at a concentration of 0.1 % (w/v) in the same HEPES buffer.

Based on previous experiments, HA is not expected to reduce friction considerably compared to a simple buffer. This expectation is based on the poor ability of HA to adsorb to surfaces carrying methoxy groups<sup>201</sup> (and such surfaces include those established by PDMS), and good surface adsorption is required for macromolecular lubricants to be efficient, *i.e.* for the formation of a sacrificial layer and subsequent hydration lubrication. In full agreement with this expectation, relatively high friction coefficients  $\mu_{\text{HA}} > 0.5$  are recorded with both setups. In contrast, purified porcine gastric mucin readily adsorbs to PDMS and – by employing a combination of sacrificial layer formation<sup>147</sup> and hydration lubrication<sup>18</sup> – reduces friction in the boundary regime by up to two orders of magnitude compared to buffer alone. Accordingly, with both setups, comparably low friction values  $\mu_{\text{mucin}} \approx 0.01 - 0.03$  can be obtained for the steel/PDMS pairing when lubricated with a mucin solution (**Figure 10c**).

### **Tribological investigations for food engineering**

Friction and wear formation in the oral cavity have, so far, only been addressed by a few studies and were often limited to investigating the lubricity of saliva or saliva substitutes using synthetic materials as counter parts<sup>4,202</sup>. Here, it is attempted to create a more physiological testing scenario to mimic oral tribology and replace the steel spheres in the oscillatory tribology measuring head by cylindrical food samples. Therefore, carrot and potato samples are chosen for those experiments since these vegetables are stiff enough to allow for the preparation of cylindrical pins ( $K_{\text{carrot}} = 2.8 \pm 0.7$  MPa and  $K_{\text{potatoe}} = 1.7 \pm 0.1$  MPa, as determined by unconfined compression tests,  $n = 3$ , see *Appendix B* for details). Friction measurements are conducted on kidney-shaped PDMS samples since PDMS is regularly used as a model material in soft biotribology to mimic the mechanical properties of the oral cavity surface. As lubricants, a simple buffer is compared to a 0.1 % (w/v) mucin solution - the latter mimics the presence of a mucosal lubricant in the esophagus. Both in the presence and absence of mucins in the lubricant, surprisingly low friction coefficients of  $\mu_{\text{carrot}} \approx \mu_{\text{potatoe}} \approx 0.07$  are obtained (**Figure 10d**).

Furthermore, in food engineering, it is often aimed at designing new types of food with the goal to *e.g.* reduce fat content or to remove unwanted components such as allergens or ingredients from animal origin. For consumer acceptance, these products, in general, have to be optimized regarding their perception and mouthfeel. To tune their perception, different parameters are considered depending on the type of product. The determination and optimization of the shear

dependent viscosity or the viscoelastic parameters *via* rheological methods is industrial standard for the development of many products including (low-fat) yogurt, chocolate, ketchup, and toothpaste. Characterization methods for more solid types of food are, however, less standardized and rely mostly on tests with human probands. Thus, it is asked now, if quantitative friction values – as they can be determined with the tribology setup introduced here - can be related to the subjective perception of human probands.

As an example-study, different types of gluten-free bread are chosen and evaluated regarding their perception in the oral cavity. For many people, especially patients suffering from celiac disease, it is necessary to remove gluten from their diet<sup>203,204</sup>. However, gluten plays an important role for the properties of flour in bakery industry and thus strongly affects the properties of bakery products. To mimic the oral perception of normal bread, a diverse range of dietary fibers has been investigated as gluten alternatives in the past decades, including inulin<sup>205</sup>, resistant starch<sup>206</sup>, and cereal brans<sup>204</sup>.

Here, the coefficient of friction is determined for three different types of dietary fiber fortified bread samples, *i.e.* inulin-fortified, wheat bran-fortified and resistant starch-fortified, and compared to a control sample containing gluten. The friction coefficients for those are found to be all in a similar range when treated with a PDMS probing pin. However, when treated with a steel sphere, clear differences between the different bread specimens can be detected. The corresponding friction values are determined to be 0.24, 0.36, 0.45 and 0.26 for inulin-fortified, wheat bran-fortified, resistant starch-fortified and the control sample, respectively. Compared to the control sample, higher friction coefficients are measured for bread containing either wheat bran or resistant starch fibers. This suggests that, compared to the control sample, those bread variants can be expected to trigger a different sensation in the oral cavity during chewing and swallowing (**Figure 10e**).

In contrast, inulin-enriched bread shows an almost identical friction behavior as the gluten-containing control sample. It is further observed that the obtained friction values are positively correlated with textural attributes from sensory tests with probands, *i.e.* bitterness, firmness, chewiness, and dryness (see *Appendix B* for details), which indicates that the friction coefficient might be a suitable predictor of these sensory attributes and a helpful tool in the development of various types of food products. The low error bars obtained with all those food-based tribology pairings demonstrate good reproducibility and underscore the high versatility of the custom-made measuring setup.

### 3.1.2 Tribology on lateral material interfaces

So far, friction and lubrication processes were studied, which occur at the contact area of a tribological interface established by two different materials only. However, in many settings, at least one of the surfaces involved in the tribological process consists of more than one material, and both friction and wear generation occurring at such an interface automatically become more complicated. Especially in such cases, where the mechanical properties of the two materials establishing one of the surfaces involved in the friction process differ, increased wear formation can be expected. For performing such interfacial tribology measurements with the setup developed here, a structured surface comprising a combination of PDMS and polytetrafluorethylene (PTFE) is chosen. The rationale for this choice is that PDMS and PTFE not only differ with respect to their Young's moduli ( $E_{\text{PDMS}} \approx 2 \text{ MPa}$ ,  $E_{\text{PTFE}} \approx 500 \text{ MPa}^{207}$ ), but they are also expected to show considerably different coefficients of friction when subjected to a tribological treatment with steel spheres.

To perform interfacial measurements with this material combination, kidney-shaped PDMS samples are prepared, and PTFE pins with a diameter of 8 mm are fabricated. To insert these PTFE pins into the PDMS samples, a cylindrical hole is generated in the silicone material and three PDMS samples containing a PTFE cylinder each are inserted into the sample holder (as depicted in the schematic top view shown in **Figure 11a**), and the vertical position of each PTFE cylinder is adjusted using screws on the bottom of the sample holder. With those composite samples, friction measurements are performed at a normal load of 1.35 N and at a sliding velocity of 0.1 mm/s for 3.5 h. As a lubricant, HEPES buffer is used. This time, the range of deflection angles is increased to  $0 \leq \varphi \leq 40^\circ$  to ensure that both lateral interfaces of the PDMS/PTFE composite sample are probed.

When analyzing the coefficient of friction as a function of the displacement angle (data obtained from backward strokes is corrected to obtain positive friction coefficients), a pronounced discontinuity is observed at both of the interfaces between PDMS and PTFE: here,  $\mu$  changes by almost two orders of magnitude, *i.e.* from  $\mu_{\text{PDMS}} \approx 0.80$  to  $\mu_{\text{PTFE}} \approx 0.02$  and vice versa. However, this change is less abrupt than one might anticipate; at either interface of the composite sample, a total variation in the angular deflection of  $\Delta\varphi \approx 4^\circ$  is required until a constant value of  $\mu$  is reached. This angular interval corresponds to a sliding distance of approximately 1.3 mm. It can be speculated that such a long sliding distance is necessary for the friction coefficient to reach a local plateau, since the two parts of the composite material have very different mechanical properties and, consequently, edge effects

are strong. Moreover, due to the manual punching process used to fabricate the PDMS samples, slight variations of the PTFE/PDMS hybrid samples are to be expected. As a consequence of those sample-to-sample variations, the three PTFE surfaces are probably not reached by the steel spheres located in the measuring head at exactly the same angles. However, the friction traces obtained from forward (**Figure 11a**, open symbols) and backward strokes (**Figure 11a**, closed symbols) are not only highly reproducible but also very similar to each other.

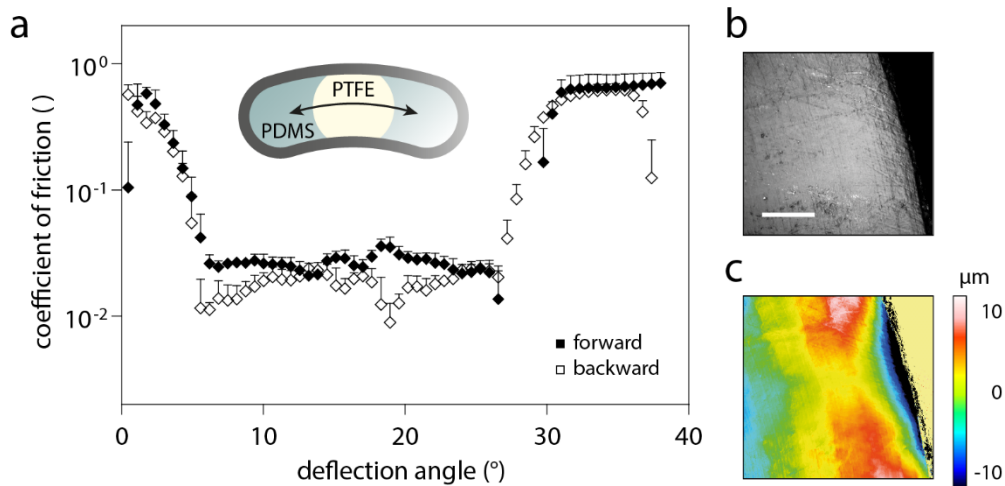


**Figure 11: Interfacial tribology.** The coefficient of friction drops almost two decades when the steel ball crosses the interface between PDMS and PTFE (a). Whereas microscopic images (b) hardly show any material alterations after the tribological testing, profilometric images (c) show that the material mismatch leads to serious wear generation directly at the interface. The scale bar represents 200  $\mu\text{m}$ .

After the tribological testing, the alterations in the sample surfaces are analyzed. Whereas images showing the intensity of reflected light reflection intensity are difficult to interpret (**Figure 11b**), topographical images clearly depict wear formation at the PDMS/PTFE interface (**Figure 11c**).

In principle, there are several metrological parameters described in ISO norm 25178 that can be calculated from such topographical data. Here, the first parameter to be calculated is the root mean square roughness  $S_q$ . Compared to the value obtained for untreated PTFE pins ( $S_q^{\text{untreated}} = 0.9 \mu\text{m}$ ), the  $S_q$  value obtained for the treated pin (**Figure 11c**) is increased by more than 300 % ( $S_q^{\text{treated}} = 4.0 \mu\text{m}$ ). This alteration in the total surface roughness is most likely caused by a loss of PTFE material at the lateral interface, *i.e.* at the location where the steel sphere has to switch from the soft

PDMS onto the stiffer PTFE. However, it is difficult to infer a loss of sample mass from analyzing the  $S_q$  value alone. Thus, also a volumetric parameter is calculated that describes such material loss, *i.e.* the void volume  $V_v$ . This volume parameter has been successfully applied before to profilometric images obtained from corneal tissue to quantify tribological damage<sup>26</sup>. It is found that, as a consequence of the tribological treatment, this void volume increases from  $V_v^{\text{untreated}} = 1.0 \cdot 10^{-4} \text{ mm}^3/\text{mm}^2$  to  $V_v^{\text{treated}} = 5.9 \cdot 10^{-4} \text{ mm}^3/\text{mm}^2$ .

This example depicts impressively how important it is to consider lateral interfaces in more-component materials when it comes to wear formation in a tribological contact. Compared to simple material pairings without a lateral interface, where wear formation is often investigated over thousands or millions of cycles, severe wear formation can occur very fast here. The setup shown here seems to be a promising tool for optimizing different types of material pairings by variation of surface and bulk material parameters to reduce both, friction and wear formation.

### 3.2 Friction and wear on articular cartilage lubricated with different biopolymer solutions\*

As discussed before, tribology on articular cartilage is an example, where it is especially critical to choose the correct measuring system for the question that is asked. A comparison of the friction values obtained in a glass-on-cartilage setup shows clearly, that friction values increase over time when the cartilage samples are exposed to a permanent load (**Figure 12a**, black curve), whereas cartilage is allowed to regenerate itself in a migrating contact, thus resulting in a constant low friction (**Figure 12a**, dashed line). Although, in most cases, a permanent contact might not represent the physiological load regimes articular cartilage is exposed to in the human body, the data obtained with such a stationary contact geometry can be indeed very useful to study certain material properties of cartilage. For example, the slope of the friction curve over time gives information about the water uptake and release kinetics of cartilage, which is a very important characteristic when it comes to the design of artificial cartilage replacement materials. Also, as discussed before, a rotational, stationary contact setup allows for probing the samples over several decades of sliding velocities. Thus, to compare the lubricating performance of different macromolecular lubricants in a glass-on-cartilage tribology pairing, a

---

\* This section follows in part the publications Boettcher *et al.*, *Biotribology* (2017) & Winkeljann *et al.*, *Biotribology* (2018)

rotational setup is chosen. As macromolecules, HA and lubricin are selected, since both naturally occur in mammalian joints and they are thought to be – at least in part – responsible for the ultralow friction and wear formation in joints. Furthermore, mucin is chosen as an additive for the lubricating fluid as mucin exhibits many structural similarities to the lubricin molecule, however, it is comparably easy to purify and thus available in a larger amount.

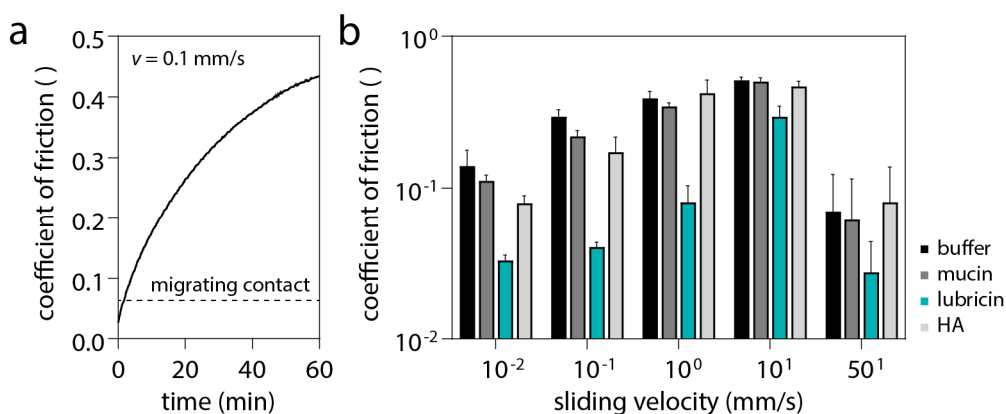


**Figure 12: Cartilage tribology.** The coefficient of friction obtained in a glass on cartilage pairing is dependent on the measuring method, *i.e.* stationary or migrating contact (a). The influence of different macromolecular substitutes to the lubricant is investigated over a wide range of sliding velocities in a rotational tribology setup (b).

Interestingly, neither hyaluronic acid nor mucin is able to reduce the coefficient of friction significantly compared to the values obtained, when the pairing is lubricated with a simple buffered solution. Only lubricin, although structurally very similar to mucin, is indeed able to reduce friction when added to the lubricant – and this occurs especially at low sliding velocities, *i.e.* between 0.01 and 1 mm/s (Figure 12b). However, studies on both artificial<sup>182,183,208,209</sup> and biological materials<sup>26,210,211</sup> have been shown, that friction and wear are not necessarily coupled and thus should be investigated separately. Therefore, first microscopical images are taken of the cartilage surface before and after the exposure to tribological stress. This optical examination of the cartilage surfaces by light microscopy clearly shows different wear features after lubrication with HA and lubricin solutions. Whereas the cartilage sample shows an increased amount of wear pits and asperities when lubricated with HA (Figure 13a), the surface exhibits rather orientated wear tracks when lubricated with lubricin (Figure 13b).

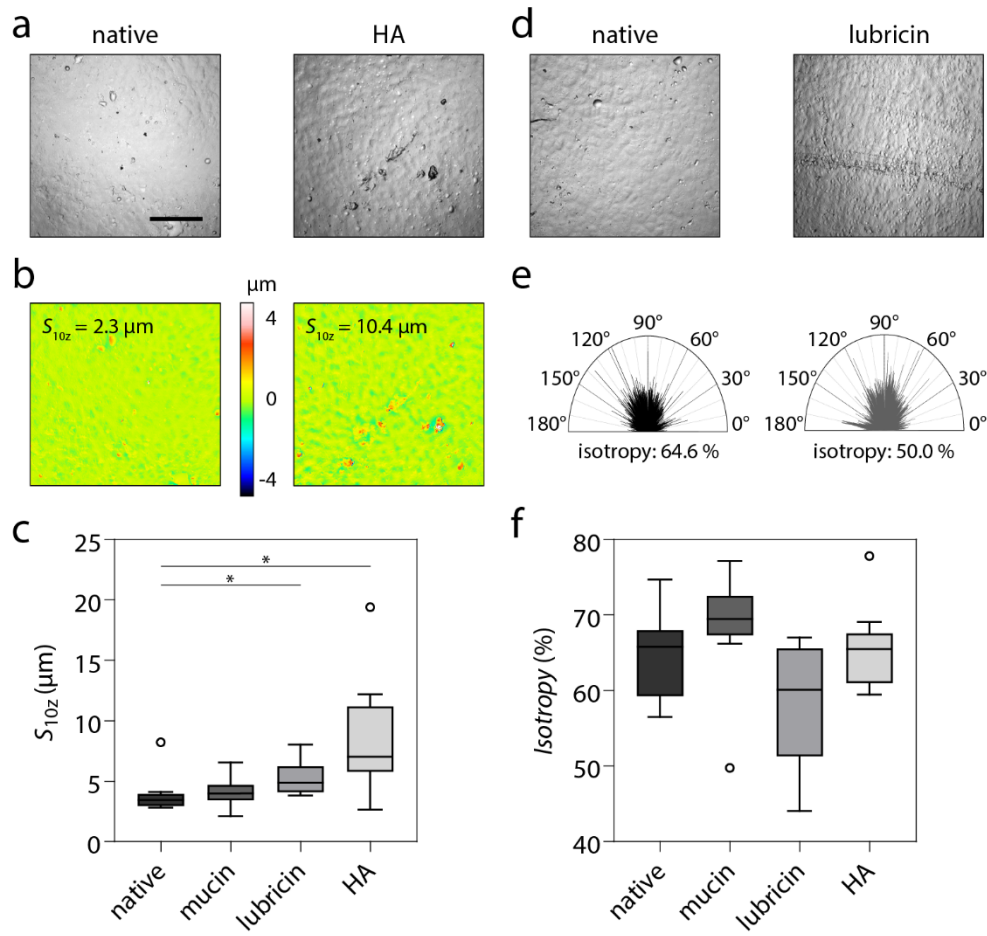


**Figure 13: Wear formation on articular cartilage.** In the surface images (a, d), and the topographical images (b) wear features are clearly visible. When HA or lubricin solutions are used as lubricants, the  $S_{10z}$  value is significantly increased compared to the surface of native cartilage (c). The determination of the isotropy parameter (e) reveals that, compared to the surface of native cartilage, lubrication with a lubricin solution reduces the surface isotropy (f). The scale bar represents 200  $\mu\text{m}$ . The boxes represent data as obtained from  $n=9$  independent samples.

If the tribological system, however, is lubricated with a mucin solution, virtually no changes in the cartilage surface can be observed (see *Appendix Figure C3*). To quantify the observations from microscopy images, 3D images are obtained from the cartilage surface *via* white light profilometry. Also here, the surface alterations observed in light microscopy images can be visualized clearly.

To quantitatively assess those damages, the first metrological parameter calculated is the root mean square roughness. However, it is found that employing this very simple parameter is not sufficient to depict the surface alterations which have been observed in the images. To assess those, further parameters are employed here, *i.e.* the ten-point height  $S_{10z}$  and the *surface isotropy* (see *Materials and methods* for details). Indeed, the  $S_{10z}$  values calculated from the topographical images are significantly increased compared to the native cartilage surface after the system had been lubricated with HA acid. In case of mucin or lubricin as an additive, the  $S_{10z}$  value is not significantly increased, which indicates that the wear tracks seen for lubricin lubricated samples cannot be resolved by calculating the ten-point height (**Figure 13c**).

Subsequently, to also quantify those wear tracks, the isotropy parameter is calculated. The isotropy of a surface can be nicely visualized in polar coordinate systems (**Figure 13e**). The exemplarily shown treated surface from **Figure 13d** exhibits a local maximum in the polar graphs at roughly  $180^\circ$  (which corresponds to the direction of the observed wear tracks), whereas the polar plot for the native sample is rather homogenous. The actual calculation of the *isotropy* parameter supports this finding, as the *isotropy* is lowered for samples that have been lubricated with lubricin during the tribological treatment compared to the value obtained for native samples. If other lubricants, *i.e.* mucin and hyaluronic acid are used, no considerable impact on the surface *isotropy* is observed after the tribological treatment (**Figure 13f**).

### 3.3 Lubricity of mucin in varying physiological conditions\*

As the results from cartilage tribology - and also a few other studies<sup>26,202,212,213</sup> - suggest, mucin seems to outperform other macromolecular lubricants either in terms of friction reduction and wear protection or simply in terms of availability (*e.g.* compared to lubricin). Thus, in the next step, the potential of mucin solutions as bio-lubricants for medical use is investigated more in detail. Therefore, several physiological parameters will be considered, which might affect mucin lubricity. Body fluids in general and mucosal tissues, in particular, can significantly differ in terms of pH, ionic strength and protein content, and each of those parameters might impact the performance of mucin-based lubricants.

---

\* This section follows in part the publication Song *et al.*, ACS Applied Bio Materials (2019)

### 3.3.1 Effect of mucin concentration

In the first step, it is investigated how strongly the mucin concentration affects the lubricity of mucin solutions. This question is motivated by two aspects: first, there might be an optimal mucin concentration above/below which the lubricant is less efficient; second, for economic reasons, identifying the minimal mucin concentration that yields good lubricity is important since the current purification process still only produces limited amounts of mucins. The concentration of a polymer in solution is directly linked to its dilution state and thus can heavily influence the properties of the solution, *e.g.* the shear dependent viscosity. The dilution of a polymer solution can be assessed by calculating the ratio of the volume fraction  $\Phi$

$$\Phi = \frac{c_{\text{polymer}}}{\rho_{\text{polymer}}} = c_{\text{polymer}} \cdot \frac{v_{\text{monomer}} \cdot N_{\text{AV}}}{M_{\text{monomer}}}$$

where  $c_{\text{polymer}}$  is the polymer mass concentration in the solution,  $\rho_{\text{polymer}}$  the polymer density,  $v_{\text{monomer}}$  is the occupied volume of a single monomer,  $N_{\text{AV}} = 6.022 \cdot 10^{23}$  1/mol the Avogadro Number and  $M_{\text{monomer}}$  the molecular weight of a single monomer. The overlap volume fraction  $\Phi^*$  is described by

$$\Phi^* = \frac{N \cdot v_{\text{monomer}}}{V_{\text{polymer}}}$$

where  $N$  represents the degree of polymerization, and  $V_{\text{polymer}}$  the pervaded volume, *i.e.* the volume of solution spanned by a single polymer. For a ratio of  $\Phi/\Phi^* < 1$ , the polymer solution is referred to as dilute, *i.e.* molecular interactions, such as entanglement play a minor role. In turn, if  $\Phi/\Phi^* > 1$ , the solution is referred to as semidilute, which means, that the polymer coils overlap in the solution and their interactions strongly govern the properties of the polymer solution<sup>214</sup> (**Figure 14a**).

In total, the backbone of porcine gastric mucin consists of 4192 amino acids<sup>215</sup>, which represents the degree of polymerization  $N$ . Within the backbone all 20 different amino acids can be found. Using the amino acid sequence of porcine gastric mucin<sup>215</sup> and the average volume occupied by every amino acid<sup>216</sup>, both, the number average of molecular weight and the occupied volume can be calculated as  $M_{\text{monomer}} \approx 123$  Da and  $v_{\text{monomer}} \approx 126 \text{ \AA}^3$ , respectively. Assuming the molecular weight of a mucin monomer to be  $M_{\text{mucin}} \approx 3$  MDa, the weight of a single mucin molecule can be calculated as

$$m_{\text{mucin}} = \frac{M_{\text{mucin}}}{N_{\text{AV}}}$$

The mass difference of mucin in its dry state, compared to its hydrated state has been determined to be  $\approx 0.046$ <sup>89</sup>.

Assuming a density of the hydrated mucin molecules to be similar to those of water, *i.e.*  $\rho_{\text{water}} \approx \rho_{\text{mucin, hydrated}} \approx 1 \text{ g/cm}^3$ , the occupied volume of the mucin molecule in an aqueous solution is calculated as:

$$V_{\text{mucin, hydrated}} = \frac{m_{\text{mucin}}}{0.046 \cdot \rho_{\text{mucin, hydrated}}}$$

Using these assumptions, the transition from dilute to semidilute for an aqueous solution containing porcine gastric mucins can be estimated to be at a mucin concentration of approximately 7.9 mg/mL (**Figure 14b**).

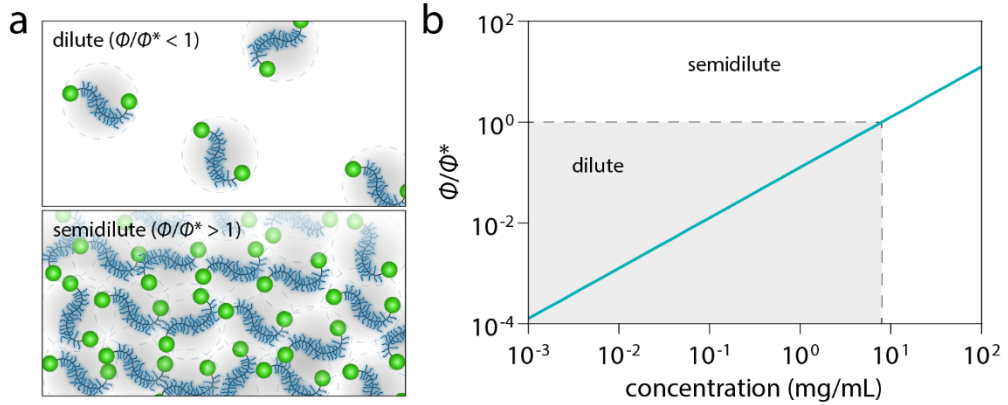


**Figure 14: Dilution of porcine gastric mucin.** The ratio of volume fraction  $\Phi$  and overlap volume fraction  $\Phi^*$  gives information, whether a polymer concentration is dilute, *i.e.* polymer interactions play an unimportant role, or semidilute, *i.e.* polymer interactions dominate the solution characteristics (a). For mucin solutions, the transition concentration can be estimated to be approximately 7.9 mg/mL (b).

First tribological measurements are performed at an intermediate mucin concentration of 0.1 % (w/v). Even considering that the assumptions for the estimation of the dilution state might be not perfectly accurate, the mucin solution should still be dilute at this concentration (**Figure 14b**). As observed in several studies before, a mucin solution at this concentration reduces the friction factor  $\mu$  by approximately two orders of magnitude, and this also holds true in the boundary lubrication regime, where  $\mu \approx 0.01$  (**Figure 15a**).

Interestingly, no perceivable improvement in lubricity can be observed, when the mucin concentration is increased to 1.0 % (w/v) (**Figure 15a**). At this higher mucin concentration, one would expect to have considerable interactions of the mucin molecules in solution as the ratio of volume fraction and overlap volume fraction indicates for this concentration (**Figure 14b**). Furthermore, the viscosity of the solution is already increased 8-fold (see *Appendix Table C1*). Thus – at least according to Stribeck theory – an increased lubricant viscosity should improve the lubricity of the system; however, this is not the case, which indicates that both, molecule interactions within the lubricants as well as lubricant viscosity are not a dominant factor for the tribological performance of mucin solutions. It also suggests that further increasing the mucin concentration will not be of much avail.

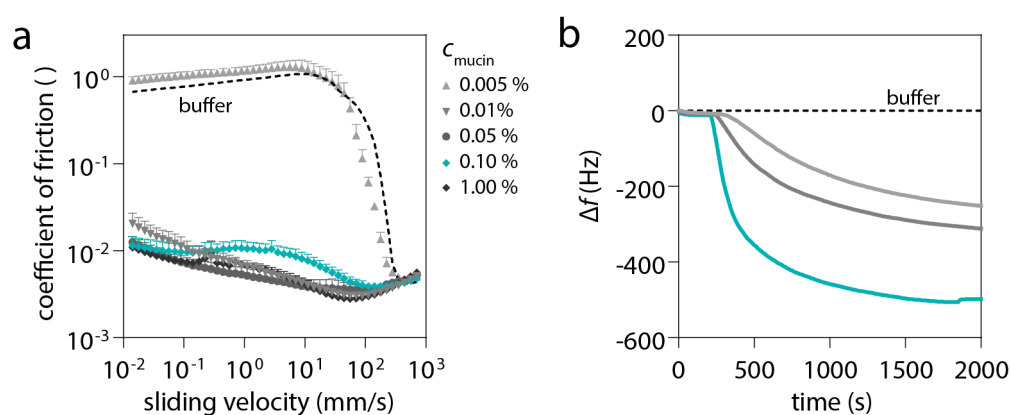


**Figure 15: Influence of the mucin concentration on the lubricity and adsorption behavior of mucin solutions.** (a) Tribological tests were carried out with a steel-PDMS pairing using 20 mM HEPES buffer at pH 7 with mucin concentrations ranging from 0 (pure HEPES buffer) to 1.0 % (w/v). The error bars denote the standard deviation as obtained from  $n \geq 5$  independent measurements. (b) Adsorption behavior of mucin solutions containing different concentrations of MUC5AC as assessed by QCM-D using PDMS-coated Au-chips. The results denote the average as obtained from  $n \geq 3$

Instead, when lowering the mucin concentration by a factor of ten it is found that, even at this reduced mucin content, the lubricity of the solution remains almost unaffected. However, this concentration of 0.01 % (w/v) seems to constitute a threshold: If the mucin solution is further diluted, *i.e.*, to 0.005 % (w/v), the obtained Stribeck curve closely resembles the one determined with buffer devoid of mucins (**Figure 15a**). This suggests that, at this low mucin concentration, some critical property of the solution is changed such that the lubricity of the system is suddenly and strongly compromised. However, molecular interactions are not

likely to be responsible for this effect, since at both concentrations the solution is already very dilute (**Figure 14b**).

However, it is known that, for macromolecular lubricants, the adsorption properties of the solubilized (bio)polymers are closely related to the lubricity of the solution<sup>89,217</sup>. Accordingly, the kinetics of mucin adsorption onto PDMS at different mucin concentrations is tested using QCM-D. At low mucin concentrations of 0.005 % (w/v), not only a roughly 2-fold reduction (compared to standard concentrations of 0.1 %) in the plateau value of the frequency shift can be detected, but also slower adsorption kinetics are observed (**Figure 15b**). By fitting an exponential decay to the QCM-D data, this impression is quantified:  $\Delta f \approx \exp(-t/\tau)$ . The decay time  $\tau$  changes from approximately 250 s (0.1 % mucin) to about 500 s (0.01 % mucin), and even further to 1000 s (0.005 % mucin). Since, in the last mucin dilution step, the adsorption kinetics seem to change more critically than the plateau value of  $\Delta f$ , it can be speculated that the velocity of mucin adsorption limits mucin lubricity at these low concentrations. In a model where sacrificial layer formation and hydration lubrication are the two key mechanisms governing the lubricity, this can be rationalized as follows: due to the tribological stress acting on the PDMS surface, adsorbed mucins are constantly sheared off and can only provide hydration lubrication when they re-adsorb quickly enough. If this re-adsorption process is too slow, *e.g.*, when the amount of available mucin macromolecules in the lubricant solution is below a sub-critical concentration, both sacrificial layer formation and hydration lubrication are compromised – resulting in drastically reduced lubricity as observed here.

### 3.3.2 Influence of pH conditions and salt concentrations

When used as a biomedical lubricant, mucin solutions might encounter a broad range of pH levels in the human body. Thus, in the next step, the lubrication and adsorption properties of mucin solutions at different physiological pH levels are evaluated.

Interestingly, decreasing the pH value does not have a considerable effect on the lubricity of mucin solutions, even when reaching strongly acidic pH levels around 2 as they occur in the human stomach. Increasing the pH slightly (pH 8), in turn, leads to a slight increase in the obtained friction values, however, even at slow sliding velocities the coefficient of friction still stays way below 0.1 (**Figure 16a**). Adsorption measurements show that there is also no major change in the adsorption kinetics of mucins. However, it can be observed that the final frequency

shift reaches its lowest level at pH 4 (**Figure 16b**) – and also at this value, the obtained friction values were lowest.

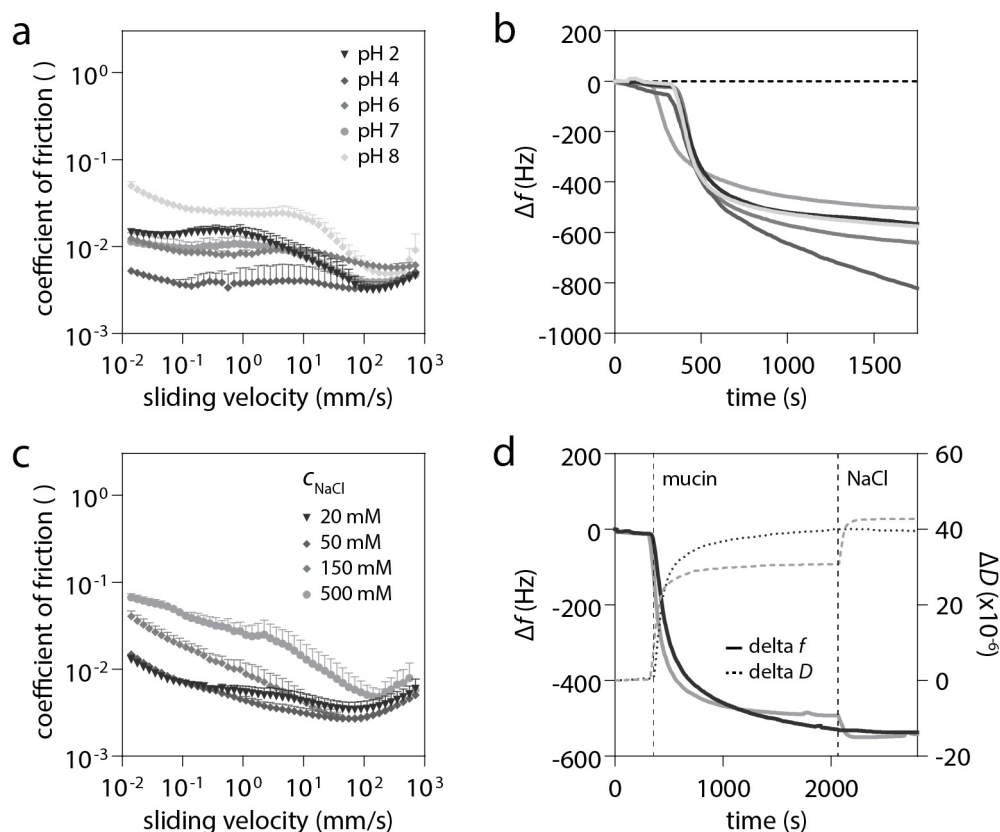


**Figure 16: Lubricity of mucin solutions in varying pH and salt conditions.** The lubricity (a) and adsorption kinetics (b) of mucin solutions are hardly affected by changes in pH levels from 2 to 8. The same counts for changing the ionic strength of the solution as long as the physiological level is not exceeded drastically (c). For high salt solutions (500 mM NaCl), both lubricity (c) and conformation (d) are altered. The results denote the average, while error bars denote the standard deviation as obtained from  $n = 3$  independent samples.

This indicates that, here, the adsorbed mucin layer assumes an optimal configuration. It was suggested that the conformation of gastric mucin changes at this pH<sup>218</sup>, and this alteration in mucin structure, also impacts the rheological properties of mucin solutions<sup>219</sup>. Thus, it can be speculated that more mucin molecules adsorb at this pH level than at higher/lower pH – and this would improve the efficiency of sacrificial layer formation.

The next physiological parameter to be explored regarding its influence on the lubricity of mucin solutions is the presence of salt ions. NaCl plays a vital role in the regulation of many body functions and is also an important part of the body's fluid balance control system. However, the NaCl concentration in those body fluids can change, *e.g.* as a result of electrolyte disturbance<sup>220</sup>. The same holds true for the ion concentration in mucosal layers, which can be affected by disease or after the consumption of food or beverages. When the NaCl content in a mucin solution is increased from low concentrations, *i.e.* 20 mM or 50 mM to 150 mM, only a slight increase of the friction coefficient is observed in the boundary and mixed lubrication regime. This effect becomes a bit more pronounced at high NaCl concentrations (*i.e.*, 500 mM). However, also here, friction coefficients are still well below 0.1 at all sliding velocities tested (**Figure 16c**). Even though the lubrication potential of mucin solutions is not strongly reduced by increasing salt concentrations, it is asked by which mechanism mucin lubricity is affected by NaCl.

Since mucins adsorb very well to PDMS by means of hydrophobic interactions<sup>89</sup>, it appears unlikely that simple NaCl can interfere with this process. Indeed, adsorption measurements demonstrate that the adsorption kinetics of mucins onto PDMS do not change much with increasing NaCl concentrations (see *Appendix Figure C4*). Thus in a next step, the physical properties of the adsorbed mucin layers are investigated by evaluating changes in both, the frequency shift  $\Delta f$  and the dissipation shift  $\Delta D$ : sequential exposure of PDMS-coated QCM-chips to mucin and high NaCl solutions induces a stronger alteration in both,  $\Delta D$  and  $\Delta f$ . (**Figure 16d**).

There are different possibilities to rationalize this observation: High ion concentrations induce Debye screening and thus reduce the number of charged groups available for ionic pairing<sup>221</sup>. In addition, it has been suggested that a shortened Debye-length can decrease the range and magnitude of the steric repulsion forces acting between mucin layers<sup>222</sup>. In salt solutions, mucins are reported to undergo a conformational change from a fully extended state to a collapsed state, and this behavior was explained to originate from a combination of two effects, electrostatic screening, and osmotic pressure acting on the mucin chains<sup>223</sup>. Together, those effects can influence the structure of an adsorbed mucin layer, thus reducing its thickness and, consequently, also its water content. Dehydration of mucin results in a decrease of the compatibility between mucin and an aqueous solution<sup>224</sup>, which is likely to limit the hydration lubrication abilities of a surface-bound mucin layer.

### 3.3.3 Interactions of small proteins with mucin molecules

When applied to mucosal surfaces of the human body, mucin solutions will not only encounter pre-existing pH conditions and NaCl concentrations, but also a variety of proteins. Thus, in the last step, it is evaluated how such proteins interfere with the lubricity and mucin solutions. Lysozyme, amylase, and serum albumin are prominent examples of proteins occurring in body fluids such as tears, saliva, synovial fluid, and vaginal fluid<sup>1225-228</sup>.

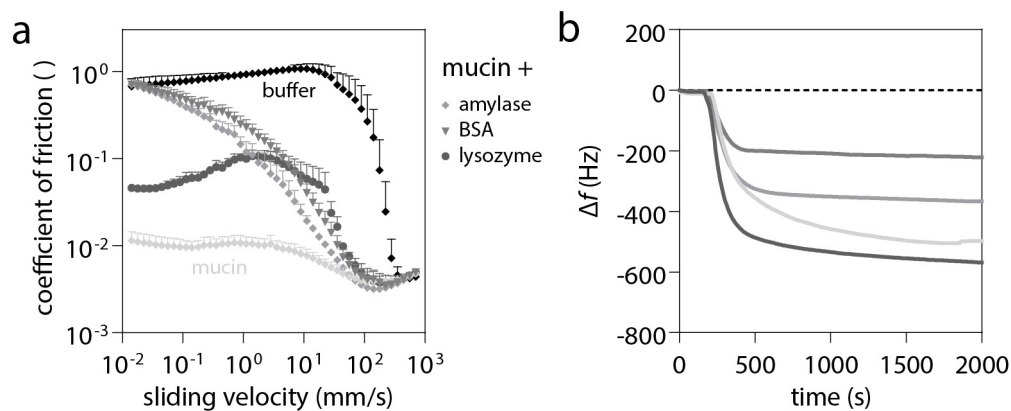


**Figure 17: Influence of small proteins on mucin lubricity.** The presence of small negatively charged proteins such as BSA and amylase strongly reduces the lubricity of a mucin solution. Also positively charged lysozyme has an effect on lubricity, however, less drastically (a). In contrast to BSA and amylase, the addition of lysozyme to a mucin solution even increases the frequency shift compared to pure mucin solution (b). The results denote the average, while error bars denote the standard deviation as obtained from  $n = 3$  independent samples.

For all protein/mucin mixtures tested here, higher friction coefficients are obtained compared to when a pure mucin solution is used for lubrication. If BSA or amylase is added to the mucin solution, the friction coefficients at very low sliding velocities are strongly increased and reach values almost as high as those obtained with simple buffer. For lysozyme, this effect is less drastic, and only an increase in friction by approximately one order of magnitude can be detected. In the mixed lubrication regime, still, a noticeable friction reduction compared to simple buffer can be found in all cases (**Figure 17a**). Whereas the presence of either BSA or amylase leads to a less pronounced frequency shift, the addition of lysozyme entails a stronger change in the resonance frequency. Interestingly, all protein/mucin mixtures reach a stable  $\Delta f$  signal more quickly than pure mucin solutions alone (**Figure 17b**). The molecular weight of BSA, amylase, and lysozyme is approximately 66 kDa, 51 kDa, and 14 kDa, respectively – all these proteins are much smaller than mucin.

Accordingly, the smaller protein molecules can diffuse through the aqueous solution more rapidly and might adsorb onto the PDMS surface more quickly than mucin. Then, the presence of this protein pre-coating could influence mucin adsorption differently – depending on the properties of this pre-coating layer.

Furthermore, at neutral pH conditions, the net charge of mucin, BSA and amylase are negative whereas lysozyme is positively charged<sup>229,230</sup>. For the negatively charged proteins, *i.e.* BSA and amylase, their adsorption onto PDMS would create a repulsive layer, thus impeding the adsorption of the negatively charged mucin. Indeed, similar behavior has already been reported for bovine submaxillary mucin in the presence of BSA<sup>231</sup>. As a consequence, both key mechanisms required for mucin lubricity, *i.e.* sacrificial layer formation and hydration lubrication, are compromised, which leads to highly increased friction coefficients.

In contrast to the results obtained with BSA and amylase, the observed frequency shift in the presence of lysozyme is stronger than for the pure mucin solution alone – but reduced lubricity occurs, nevertheless. However, also lysozyme molecules should be able to quickly diffuse through the lubricant and adsorb to the PDMS layer; the slightly accelerated kinetics of the frequency shift change would agree with this idea. Since lysozyme is positively charged, the pre-coated PDMS surface should still allow for the adsorption of mucins – albeit by means of electrostatic attraction instead of hydrophobic forces. It can be speculated, that such an electrostatically bound mucin layer might be less favorable for providing lubricity by means of sacrificial layer formation. How adsorbed mucin layers generated through different physical forces differ in this regard, *i.e.*, the binding strength of mucins to a surface, and how this translates into lubricity, remains to be investigated.

## 4 Covalently coupled macromolecules on clinically used polymer materials

It was demonstrated in *Chapter 3* that macromolecular lubricants have outstanding properties regarding lubrication and wear protection. However, since a rapid distribution of such aqueous lubricants in the human body can be expected, their application in biomedical applications is very limited. To compensate for a loss of the lubricant while maintaining lubricity, different strategies have been published in the last years on how to immobilize hydrated macromolecules onto a substrate<sup>20,28-30</sup>. Applying such lubricious coatings to medical devices appears to be a promising strategy to reduce friction and tissue damage whenever such devices challenge soft sensitive tissues through mechanical forces<sup>26</sup>. Possible scenarios include the insertion of a catheter into the urethra<sup>195</sup> or blood vessels<sup>194</sup> or the placement of an intubation tube into the trachea<sup>232,233</sup>. Of course, also more permanent placements of synthetic materials into the human body can cause irritations, *e.g.* braces in the oral cavity<sup>234-236</sup>, and thus those materials might as well benefit from a macromolecular coating to enhance their lubricity. Finally, as most body fluids contain lubricious macromolecules themselves, interactions between those and surface bound polymers might be used to further improve the lubricity of such devices.

Here, it is shown, how mucins can be covalently grafted onto a PDMS model surface and it is tested, how this coating affects the surface lubricity. Furthermore, the stability of such covalent mucin coatings towards mechanical, thermal and chemical stress is investigated. Moreover, the interactions between mucin coatings and solubilized macromolecules are studied. Those findings are then compared to other, frequently used macromolecular coatings, *i.e.* PEG, PLL, and hyaluronic acid coatings. Finally, it is demonstrated, that the coating process introduced here can easily be transferred to a set of six other clinically used polymer materials.

### 4.1 Covalent coatings with enhanced stability and surface lubricity\*

Even though hydrophobic PDMS surfaces can be quickly and easily coated with mucins by means of passive adsorption, such a passively adsorbed mucin layer is

---

\* This section follows in part the publications Winkeljann *et al.*, *Advanced Materials Interfaces* (2019) & Winkeljann *et al.*, *Advanced Materials Interfaces* (2020)

not very stable: after exposure to mechanical shear forces, which here are applied by using a rotational tribology setup, most of the mucin coating is eroded (Figure 18b, c). Consequently, also the lubricity of a PDMS surface coated with passively adsorbed mucins is comparable to uncoated samples (Figure 18a).

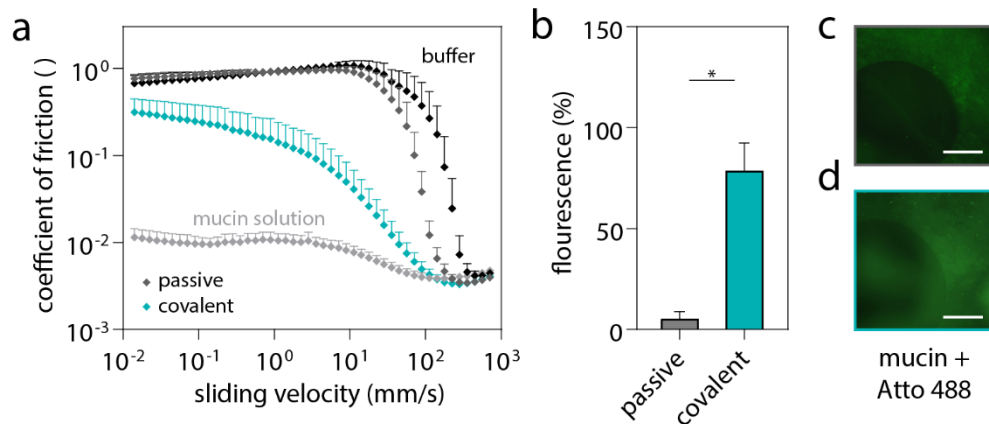


**Figure 18: Lubricity and mechanical stability of covalently bound mucin.** When lubricated with a simple buffer solution, the velocity-dependent coefficient of friction obtained for a steel-on-PDMS pairing shows the typical shape of a Stribeck curve (black). If mucin is added to the lubricant, this friction coefficient is reduced by almost two orders of magnitude (light grey). If mucins are attached to the PDMS surface *via* passive adsorption (grey), the obtained friction values almost overlap with those obtained for uncoated samples, whereas if mucins are covalently attached to the surface (cyan), the obtained friction values lie in between the two curves (a). The ELISA signal obtained from tribologically treated mucin coatings is compared to that obtained from freshly coated samples (*i.e.*, either passively or covalently coated ones) that were not mechanically challenged (b). PDMS pins carrying coatings comprising fluorescently labeled mucins are imaged with fluorescence microscopy after being subjected to tribological stress. Passively adsorbed mucins (c) are sheared off in the circular contact zone whereas covalently linked mucins (d) are still present. The scale bar represents 1 mm. Error bars depict the standard deviation as obtained from  $n = 9$  independent samples.

For a realistic medical application, *e.g.*, the insertion of an endotracheal tube, such a loosely attached coating would be insufficient for several reasons. First, if the coating is sheared off from some areas of the PDMS surface, these uncoated surface spots are highly prone to protein deposition or bacterial adhesion. Second, if a medical device “releases” molecules (here: mucins) into the human body in an uncontrolled way, obtaining approval for this device becomes more difficult as all possible side effects related to this release need to be considered<sup>237</sup>. Third, compared to mucin-functionalized surfaces, uncoated PDMS surfaces show inferior lubricity;

therefore, there will be a higher risk of tissue damage when a medical device, which has lost its coating, is removed again from the human body.

#### 4.1.1 Mucin coatings: lubricity and mechanical stability

To overcome these problems associated with insufficient mechanical stability of the coating, a process is introduced, how mucins can be covalently grafted onto a PDMS surface *via* a two-step coupling process: first, the PDMS surface is activated by oxygen plasma to prepare the surface for a silane-based pre-coating. Afterwards, mucin glycoproteins can be attached to this silane layer *via* carbodiimide chemistry. When first probing the tribological properties of such mucin-coated samples using a simple buffer solution as a lubricant, the obtained coefficient of friction is reduced by roughly a factor of 5 compared to the value obtained for uncoated PDMS (**Figure 18a**) tested at the same conditions. This indicates that the surface-bound mucins indeed form a hydration layer that separates the opposing surfaces from each other during the tribological treatment.

However, the lubrication potential of this mucin coating is less efficient compared to a situation when an uncoated PDMS surface is lubricated with a mucin solution. The outstanding lubrication ability of such mucin solutions has been demonstrated to originate from a combination of sacrificial layer formation<sup>11</sup> and hydration lubrication<sup>18</sup>. Here, the sacrificial layer mechanism is actively suppressed by covalently fixing the mucins to the PDMS surface. Thus, it can be concluded, that the remaining lubricity has to be based on the hydration lubrication mechanism alone. Furthermore, mucin detection methods based on antibody staining and fluorescence labeling (**Figure 18b, d**) demonstrate the excellent stability of the covalent mucin coating, which drastically outperforms the stability of the passively adsorbed mucin layer: this is indicated by the significantly higher amount of mucin molecules that remain after the tribological treatment (**Figure 18b**).

#### 4.1.2 Thermal and chemical stability of covalent mucin coatings

Of course, when used in the human body, medical devices are not only exposed to tribological shear stress but also to elevated temperatures around 37 °C. Moreover, during transport/shipping and storage of a medical device, the ambient conditions can vary and are not always precisely controlled. Thus, in a next step, the stability of the covalent mucin coating is analyzed at three different storage temperatures, *i.e.*, at 4 °C, 37 °C and 50 °C. After overnight incubation at these different temperatures, the presence of mucins is again assessed *via* antibody staining (ELISA) and these results are compared to freshly coated specimens. The amount

of surface-bound mucin remains stable after incubation and is hardly altered within the temperature range investigated here (**Figure 19a**).

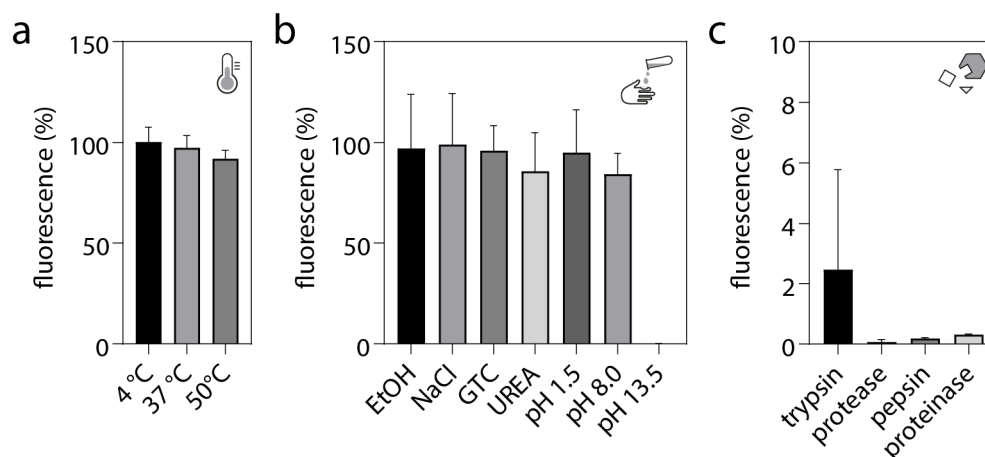


**Figure 19: Thermal and chemical stability of covalently coupled mucin coatings.** Mucin coatings generated on PDMS samples are exposed to (a) different temperatures, (b) selected chemical milieus (ethanol, chaotropic substances, high NaCl concentrations, and both, acidic and alkaline pH) as well as (c) different proteolytic enzymes. The bars display the ELISA signal obtained after the thermal/chemical challenge and indicate the amount of mucins present on the PDMS samples in comparison to freshly coated but unchallenged samples. All error bars denote the standard deviation as obtained from  $n = 3$  independent samples.

Since the covalent mucin coating shows promising results in terms of temperature resistance, the stability of the coating after challenging it with different environmental conditions relevant for a putative medical application is tested next: First, as medical devices are often treated with ethanol while handling them, the stability of the mucin layer is exposed to a high percentage (96 %) EtOH solution. Also here, the ELISA data show, that the mucin layer is extremely resistant towards ethanol exposure.

In the human body, medical devices would always be exposed to physiological NaCl concentrations around 150 mM. Thus, in the next step, the stability of the coating towards the influence of those salt ions is tested. To maximize the putative impact such NaCl ions could have, the coated samples are exposed to solutions containing 1 M of NaCl. However, even at those very high salt concentrations, the mucin coating again seems to be unaffected as the ELISA assay returns similarly high values as for unchallenged samples (**Figure 19b**). One possible application of such mucin coatings would be to use them on urinary catheters. In the urinary tract, medical devices are constantly exposed to urea, a chaotropic substance. Chaotropic

agents are able to reduce hydrophobic interactions, and such an effect may remove mucins from the PDMS surface that are not covalently attached but only passively adsorbed. Moreover, it may influence the conformation of surface-bound mucins and it can denature folded proteins if present at high enough concentrations<sup>238</sup>, which could affect the detectability of the coating *via* ELISA if the detection site for the antibody is compromised. However, even after exposure of mucin coated samples to high concentrations of urea (6 M solution) a significant reduction in the ELISA signal cannot be found. Similar results are obtained when the even stronger chaotropic agent guanidinium thiocyanate (GTC, 1 M solution) is used to challenge the coating. Together, these tests further confirm that that the mucins are indeed covalently attached to the PDMS surface and that denaturation of the (mostly unfolded) mucin glycoproteins plays a negligible role (**Figure 19b**).

Depending on the medical device the coating is supposed to be used on, also the pH value of the tissue fluid the device gets in contact with can vary: (strongly) acidic conditions are relevant for medical devices to be used, *e.g.*, in the stomach or the vaginal tract, and the small intestine exhibits a slightly alkaline pH value around 8. To test the influence of this pH range, some mucin coated samples are incubated in either 1 M formic acid (HCOOH, pH = 1.5) or 1  $\mu$ M sodium hydroxide (NaOH, pH 8). Importantly, the former treatment does not affect the intensity of the ELISA signal at all, and the slightly basic pH only has a minor influence on the antibody-based mucin detection test. Strongly alkaline conditions, however, (as realized by a 1 M NaOH solution, pH = 13.5) seem to fully remove or destroy the surface-bound mucin layer (**Figure 19b**), probably by alkaline hydrolysis<sup>239</sup>.

As the last group of physiologically relevant challenges, the influence of enzymatic degradation on the stability of the mucin coating is investigated. Proteolytic degradation of submaxillary bovine mucin by trypsin and pepsin has been reported previously<sup>240</sup>. Here, the mucin coating is expected to be somewhat vulnerable as not all parts of the mucin polypeptide chain are glycosylated thus leaving them exposed to enzymatic attack. Indeed, solubilized porcine gastric mucins are relatively resistant towards enzymatic degradation in their glycosylated areas, whereas the non-glycosylated terminal ends can be easily cleaved by trypsin<sup>89</sup>. To challenge the mucin coating, different variants of proteolytic enzymes are selected: trypsin, protease type XIV, pepsin, and proteinase K. Trypsin naturally occurs in the small intestine and thus has its pH optimum between 7 and 9, whereas pepsin occurs in the stomach and has its optimum at pH values between 1.5 and 3. Protease type XIV is a mixture of enzymes and combines at least three caseinolytic activities with one

aminopeptidase activity, and Proteinase K is a stable and highly reactive serine protease. The latter two enzymes exhibit their highest activity around neutral pH.

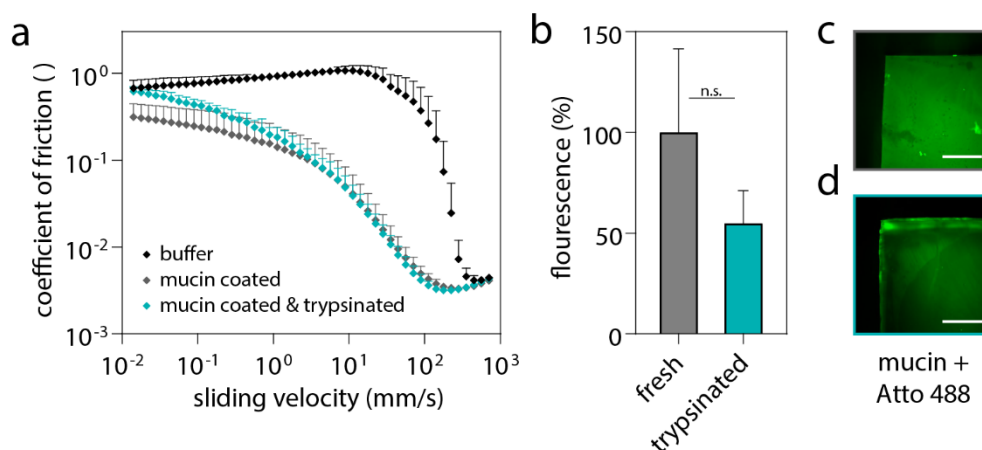


**Figure 20: Effect of trypsination on covalent mucin coatings.** The coefficient of friction obtained on uncoated PDMS samples (using simple buffer as a lubricant) shows the typical shape of a Stribeck curve (black). Covalently coupled mucins on the PDMS surface reduce the coefficient of friction, especially in the mixed lubrication regime (grey). After exposure to a trypsin solution (cyan), the mucin coating performs similarly well as the unchallenged coating although experiments with fluorescently labeled mucins show a reduction in surface-bound mucins after trypsination (c, d) compared to freshly coated samples (b, d). The scale bars represent 1 mm. Error bars depict the standard deviation as obtained from a minimum of  $n = 3$  independent sets of samples.

When the coating is exposed to any of those enzymes, a strong reduction in the ELISA signal can be observed in each case (**Figure 19c**). Among all enzymes tested, the Proteinase K treatment has the weakest effect. Nevertheless, also here, a clear decrease of the ELISA signal is observed. However, due to the antibody assay used here, it can be difficult to directly correlate a reduced fluorescence signal obtained with ELISA with a loss of surface-bound mucin (the antibody used to detect mucin targets the C-terminus of the mucin molecule<sup>157</sup>). Owing to the dense glycosylation pattern in the central region of the mucin glycoprotein, the polypeptide core is only accessible in the terminal regions of the macromolecule. Thus, enzymatic cleavage of these terminal regions could prevent the detection of the mucin *via* antibody staining although most of the molecule might still be present on the coated surface. To test this idea, the functionality of the mucin layer is assessed after its exposure to an enzyme solution. As shown above, when mucin coated PDMS pins are tested in a rotational tribology setup, they reduce the friction between those pins and the counter surface: this effect is most pronounced in the mixed lubrication regime

(**Figure 20a**, grey curve). If such mucin coated pins are exposed to degrading enzymes such as trypsin, it is found that the enzymatically challenged mucin coating still shows a good lubricating performance – especially in the mixed lubrication regime. Only at very low sliding velocities, a slightly increased coefficient of friction can be observed after enzymatic treatment (**Figure 20a**, cyan curve).

Also here, fluorescently labeled mucins are used again to visualize the effect of trypsination. Compared to freshly coated PDMS samples, trypsinated specimens indeed show a reduced ELISA signal, however, this reduction is not significant (**Figure 20b**). Fluorescent images support this finding as they give a similar visual impression for both, samples with and without exposure to trypsin treatment (**Figure 20c, d**). It can be concluded that indeed, trypsin does affect the mucin coating and at least the termini are cleaved after trypsin exposure. Furthermore, depending on the coating quality and density also the surface-bound termini could become accessible for enzymes.

#### 4.1.3 Lubricity of covalent PEG and PLL coatings

To be later (see *Section 4.2*) able to identify the mechanistic effects responsible for the lubricity of different coating/lubricant combinations, two other, differently charged macromolecules are used for the coatings, *i.e.* polyethylene glycol (PEG, neutral) and poly-L-lysine (PLL, polycationic).

Also, for PEG (**Figure 21a**) and PLL (**Figure 21b**), coatings can be generated that show nearly identical lubricity as described above for the mucin coating. Owing to their molecular structure and their ability to easily bind water molecules, it can be concluded that (in full analogy to the mucin coating) the observed lubricity of those PEG and PLL coatings is due to hydration lubrication as well – at least as long as there are no macromolecules in the lubricating fluid. For PEG and PLL, the grafting density might be different than for mucin (see *Appendix Figure C5*); however, for the remainder of this thesis, the lubricity of these coatings needs to be similar (and not necessarily the grafting density) since the friction level obtained with the coatings alone serves as a baseline, which later allows to compare the effect of different polymer-based lubricants.

~ ~ ~

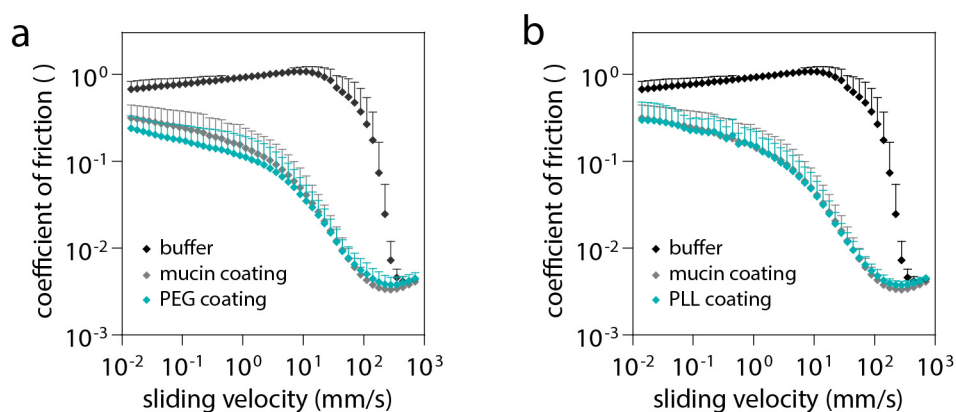


**Figure 21: Friction reduction by PEG and PLL coatings.** The velocity-dependent coefficient of friction recorded for PDMS specimens covalently coupled with either PEG (a) or PLL (b) against a steel sphere is virtually identical to those observed for mucin coating. The error bars depict the standard deviation as obtained from  $n = 9$  ( $n = 6$  in case of the PLL coating) independent samples.

## 4.2 Coating-lubricant interactions affect lubricity\*

If one of the presented macromolecular coatings were to be used in a (bio)medical application, *e.g.*, on catheters, intubation tubes or implants, they would get in contact with different fluids containing distinct molecular ingredients. Of course, those molecular components will interact with the surface coating and either improve or reduce its lubricity. Synergistic interaction of surface-bound molecules and biopolymers in solution is part of the tribological function of mammalian joints: Here, the opposing cartilage surfaces comprise surface-bound lubricin<sup>102</sup>. To reduce friction between these lubricin-coated surfaces to the outstandingly low levels observed for cartilage, the synovial fluid contains the polyanionic<sup>241</sup> biopolymer HA<sup>242</sup>. HA has been shown to interact with the surface-bound lubricin molecules; however, whether this occurs mainly through entanglement, *via* electrostatic forces or a combination of both, remains partially unclear<sup>102,148,243</sup>. Thus, in the next step, the three different macromolecular coatings introduced above are used to test different combinations of coatings/lubricants that might help to decide whether or not electrostatic interactions between the lubricant

\* This section follows in part the publication Winkeljann *et al.*, *Advanced Materials Interfaces* (2019)

macromolecule and the macromolecular coating are helpful for the tribological performance of a system.

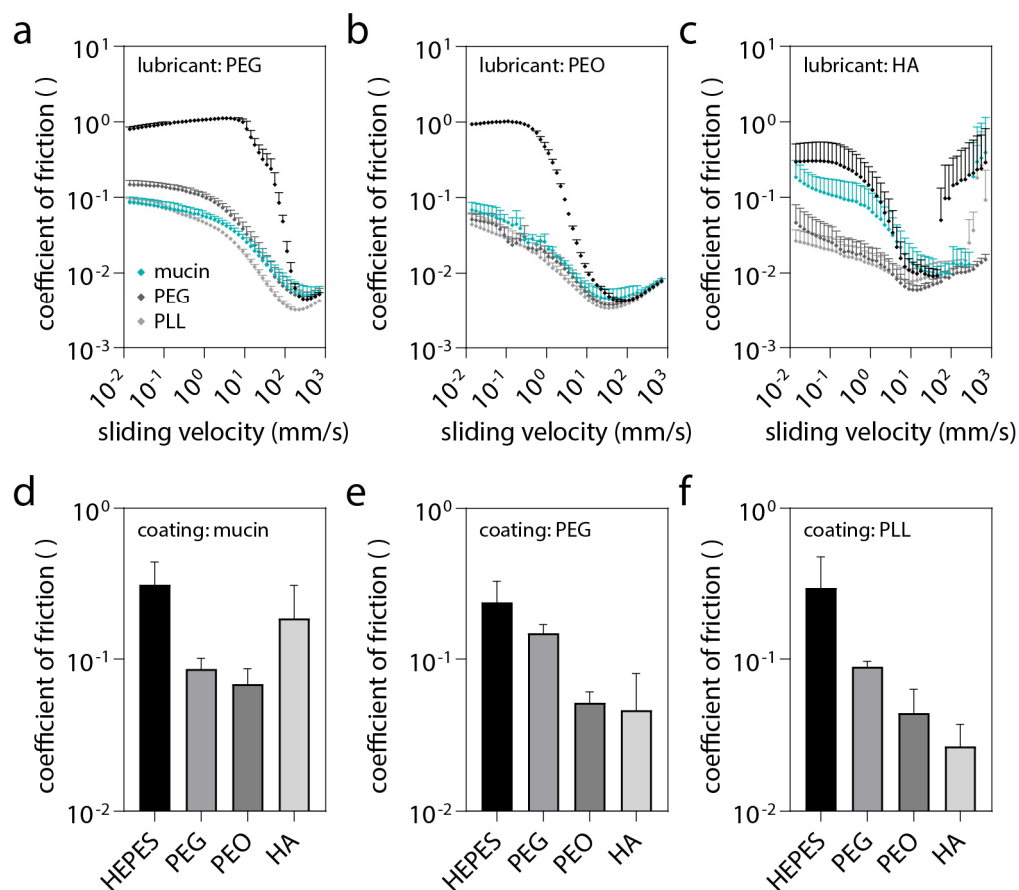


**Figure 22: Lubricant-coating interactions synergistically reduce friction.** In the absence of a macromolecular coating, aqueous solutions of PEG (a), PEO (b) and HA (c) show poor lubricity in a steel-on-PDMS pairing (black curves). However, in combination with a macromolecular coating, the lubricating potential of those solutions is improved (a-c). In turn, when a coated PDMS sample is lubricated with one of those macromolecular solutions, the obtained friction coefficients are almost lower than those obtained with the coatings alone (d-f). The error bars depict the standard deviation as obtained from at least  $n = 3$  independent samples.

As a first test-lubricant PEG is chosen, which – different from the polyanionic HA – does not carry any charged groups. Thus, a PEG-based lubricant should only be able to interact with the coatings *via* physical entanglement. Without such an entanglement interaction, solubilized PEG molecules lack the ability to adsorb to hydrophobic surfaces; thus, they can neither form a hydration layer on the PDMS

samples nor create a sacrificial layer. As a consequence, it is expected that the lubricating potential of a PEG solution on unmodified PDMS is negligible. Indeed, when a PEG-based lubricant solution is tested on unmodified PDMS, the obtained Stribeck curve resembles that obtained with pure buffer. However, when the PDMS surface is coated with one of the three different macromolecules, the friction response of the system is reduced by one order of magnitude (**Figure 22a**). To ensure that the lubricity of the combined coating/lubricant system indeed benefits from the macromolecular lubricant, it is focused on the friction coefficient obtained at low sliding velocities for the three coatings and, for each coating variant, the influence of the PEG lubricant compared to simple buffer is evaluated. It can be observed that the friction coefficient is significantly lowered when PEG is present in the lubricating fluid (**Figure 22d-f**). This indicates that, whereas unfunctionalized PDMS does not benefit from a simple macromolecular lubricant such as PEG, the coated samples do. This is in line with the expectation, that entanglement with the coating polymer enables sacrificial layer formation thus lowering the boundary friction response, and that such an entanglement is possible with each of the three different coatings.

To further support this idea, the rather small PEG ( $M_w = 10$  kDa) in the lubricant solution is replaced with a larger polymer variant. Here, it is expected that entanglement interactions between the lubricant polymer and the macromolecular surface coating should be more efficient if a larger lubricant polymer is chosen. To maintain the neutral, inert character of PEG, polyethylene oxide (PEO) with a molecular weight in the range of  $M_w = 1$  MDa is chosen. PEG and PEO are – in terms of chemistry - identical molecules that are historically referred to differently depending on the molecular weight range and the polymerization method used. Consistent with the results described before, when unmodified PDMS is lubricated with a PEO-based lubricant, a typical Stribeck curve emerges including all three lubrication regimes (**Figure 22b**). However, compared to when the smaller PEG is used, now the transitions from the hydrodynamic to the mixed lubrication regime as well as from the mixed to the boundary lubrication regime are shifted towards lower sliding velocities. This is not surprising considering the higher viscosity of the PEO solution ( $\eta_{\text{PEO}} = 26.4 \pm 0.3$  mPas) compared to the PEG solution ( $\eta_{\text{PEG}} = 1.2 \pm 0.1$  mPas) and buffer alone ( $\eta_{\text{buffer}} = 1.1 \pm 0.1$  mPas). When the PEO-based lubricant is tested in combination with the differently coated PDMS surfaces, a qualitatively similar result as obtained with the PEG solution can be observed, *i.e.* all three coating variants benefit from the macromolecular lubricant (**Figure 22d-f**). Moreover, the friction coefficients obtained at low sliding velocities are somewhat

lower for the PEO lubricant than for the PEG lubricant. At this point, it is important to realize that, in both cases, the macromolecular lubricant is applied at a similar concentration, *i.e.* 1.6 % (w/v) for PEG and 1.0 % (w/v) for PEO: due to the large differences in molecular weight, this corresponds to a more than 60-fold lower molar concentration of PEO compared to PEG. Nevertheless, the larger PEO molecule exhibits improved lubricity compared to PEG. Thus, it is concluded that this is due to enhanced entanglement of PEO with the surface coatings, which is enabled by the higher molecular weight of the PEO chains.

Of course, when the presented coatings were to be used in a medical application, the lubricating fluid will not only contain an inert, neutral molecule such as PEG but also a combination of differently charged molecules, *e.g.* proteins. Thus, it is possible that additional effects other than physical entanglement play a role in the interaction between the coating and the lubricant. Thus, the PEO based lubricant is now replaced with an artificial synovial fluid used for the non-invasive treatment of osteoarthritis. This model fluid is chosen as it contains primarily the polyanionic macromolecule HA (at a concentration of 1.6 % (w/v)) solubilized in a physiological salt solution together with small amounts of preservatives. For simplicity, this artificial synovial fluid is referred to as “HA solution” for the remainder of this thesis and this model fluid is used to assess the influence of electrostatic interactions as explained above.

Similar to PEG, HA is not expected to be able to form a sacrificial layer on the PDMS specimens<sup>201</sup>. Consequently, HA should not be able to act as a good lubricant on unmodified PDMS. Indeed, the obtained friction curves still exhibit a pronounced boundary lubrication regime with relatively high friction coefficients. Of course, due to the high viscosity of the HA solution ( $\eta_{\text{HA}} = 1.3 \text{ Pas}$ ) compared to simple buffer, the transitions of the different lubrication regimes are strongly shifted towards lower sliding velocities. Moreover, at high sliding velocities, a sudden loss of lubricity is observed which is likely to be attributed to fluid film rupture and internal fluid friction in the hydrodynamic regime – both consequences of the high lubricant viscosity.

In addition to those expected effects, one could expect a different lubricity of this HA solution on the three different coatings. For instance, the positively charged PLL coating might enhance HA adsorption and thus promote sacrificial layer formation. Indeed, strongly improved lubricity of HA solutions on PLL-coated PDMS is observed compared to mucin coated PDMS (**Figure 22c**); at low sliding velocities, the difference in friction response is up to one order of magnitude.

However, PDMS samples coated with uncharged PEG molecules perform equally well in combination with HA solutions as the PLL functionalized samples. This contradicts the expectation that electrostatic interactions might aid the lubrication process. Instead, it indicates that electrostatic repulsion forces might prevent the mucin coating from efficiently interacting with the HA molecules, thus rendering this particular combination less powerful than the other two. Together, those results motivate that electrostatic interactions still need to be considered; yet, they appear to interfere with physical entanglement rather than promoting it.

### 4.3 Macromolecular coatings improve wear resistance\*

When optimizing the tribological properties of a surface, wear prevention is equally important as friction reduction. However, as discussed above, friction and wear formation are not necessarily coupled, and thus should be assessed independently for any novel tribological system. Accordingly, it is aimed at analyzing if the additional lubricity provided by the synergistic interplay of a covalent macromolecular coating with a macromolecular lubricant also leads to increased resistance of the coated PDMS surface towards wear.

To answer this question, one type of macromolecular coating and macromolecular lubricant is selected exemplarily. Of course, pairing the mucin coating with an HA lubricant would be closest to physiological conditions in the synovial cleft; yet, as described above, the repulsive interactions between mucins and HA are probably not ideal for this purpose. Moreover, PEG molecules are routinely used in the context of cartilage replacement/repair strategies<sup>244</sup>, which is why it is decided to use a PEG coating in combination with an HA lubricant for this set of experiments. Since untreated PDMS is already quite resistant towards wear formation, the wear rate obtained in a short time tribological lab experiment is probably very low. Thus, wear formation is again quantified by employing a combination of white light profilometry and subsequent image analysis to quantify wear formation.

First, again the root mean square roughness,  $S_q$  is determined. To further support results obtained with this  $S_q$  parameter, the developed interfacial area ratio  $Sdr$  is analyzed. This  $Sdr$  value is a hybrid parameter that combines both height and spacing information; it compares the actual surface of a sample with its projected surface and calculates a percentage of surface development. Previously, this

---

\* This section follows in part the publication Winkeljann *et al.*, *Advanced Materials Interfaces* (2019)

parameter was successfully applied to differentiate between complex bacterial biofilm topographies.<sup>245</sup>

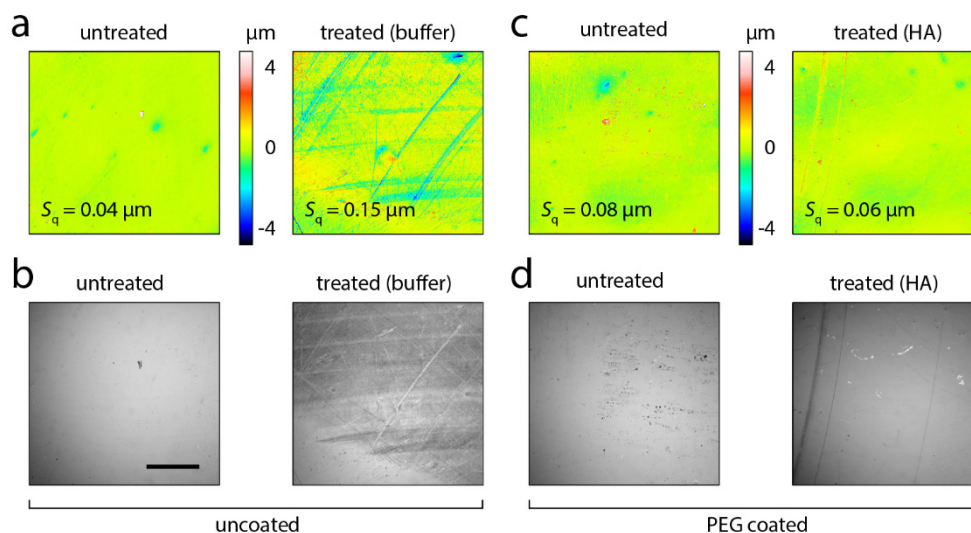


**Figure 23: Surface images of native and mechanically treated PDMS samples.** Exemplary 3D topographical images (a, c), as well as reflective microscopy images (b, d), depict the surfaces of uncoated and PEG-coated PDMS specimens before and after the exposure to tribological stress. The scale bar represents 200  $\mu\text{m}$ .

To assess wear formation, all tested samples are first imaged and subsequently exposed to tribological shear stress for approximately 12 h. Afterwards, the samples are imaged again to detect topographical differences that were caused by the treatment. As a positive control for wear formation, measurements with unfunctionalized PDMS pins are performed using simple buffer as a lubricant. Here, wear marks in the treated area are clearly visible in both, the profilometric images (**Figure 23a**), and the reflective microscopy images (**Figure 23b**). Consequently, both  $S_q$ , as well as  $S_{dr}$  parameters (**Figure 24a**), show a significant change of the surface structure after the tribological treatment. This wear formation could be attributed to two effects: first, the counterpart in the tribological system, *i.e.* the steel sphere, has been manufactured at very high-quality, yet still exhibits a rough surface on the microscale ( $S_q < 0.2 \mu\text{m}$ ), and this is considerably higher than the surface roughness of the casted PDMS pins (which is in the range of 50 nm). It is therefore expected that the roughness features of the steel sphere would generate abrasive wear on PDMS. Indeed, some of the wear tracks that are detected on the PDMS pins have a line-shaped morphology; this suggests that some of them are due

to local inhomogeneities on the steel sphere, which challenge the pin surface on every rotation thus creating linear wear motifs.

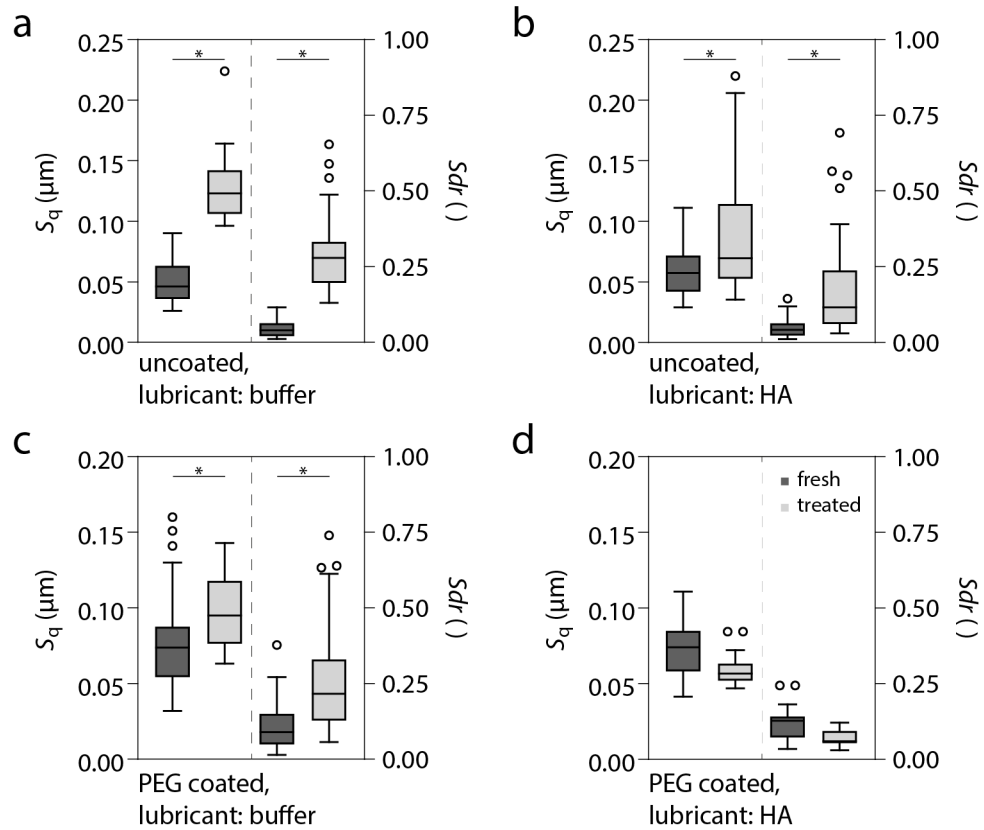


**Figure 24: Influence of a macromolecular coating and/or lubricant on the wear resistance of PDMS.** Two ISO parameters, the  $S_q$  and  $S_{dr}$  value are calculated from images of uncoated PDMS specimens are acquired before and after the tribological treatment (a). The formation of wear is less pronounced when uncoated PDMS is lubricated with an HA solution (b) or when PDMS is coated with PEG und lubricated with simple buffer (c). Wear-related surface alterations can be completely prevented by combining a PEG coating with a lubricating fluid containing HA (d). Boxplots represent pooled data from a minimum of 27 images obtained from 3 sets of individual PDMS pins.

Next, again uncoated pins are tested, this time, however, lubricated with HA. Also here, as a consequence of the tribological treatment, an increase in the surface roughness  $S_q$  and in the  $S_{dr}$  value can still be detected (**Figure 24b**), indicating that wear formation is still an issue - albeit reduced compared to lubrication with buffer only. In the third set of experiments the performance of PEG-coated PDMS pins lubricated with simple buffer is tested. Compared to uncoated pins, PEG-coated

PDMS pins initially exhibit slightly higher  $S_q$  and  $S_{dr}$  values, which are suspected to originate from the addition of the two molecular layers, *i.e.* the silane precursor and the grafted PEG. Furthermore, local inhomogeneities in the coating, as well as dust or other particles from the environment could be responsible for this. Although the lubricating fluid does not contain any macromolecules, still a slight reduction in wear formation can be observed, which is comparable to the results observed for the HA lubricated system (**Figure 24c**). The best results are obtained when the PEG-coated samples are lubricated with the HA solution. For this combination, neither an increase in the  $S_q$  value nor in the  $S_{dr}$  parameter can be found (**Figure 24d**), which indicates that wear formation is efficiently suppressed at the test conditions applied here. Moreover, even a slight decrease in the surface roughness parameters can be detected. The latter could be attributed to a mechanical smoothing of the surface, *i.e.* the local inhomogeneities created by the coating appear to be removed whereas the PDMS surface itself is not altered (**Figure 23c, d**). This illustrates that the synergistic interaction of a hydrating surface coating and a macromolecular lubricant entangling reduces not only friction but also wear.

#### 4.4 Applicability of the coating protocol to other polymers\*

Although silicone-based materials such as PDMS are very common for medical devices, there are many other polymer materials that are used in clinical applications. Here, six other polymers, *i.e.* PP, PU, PE, PVC, PET and PMMA (see *Materials and methods* for details), are chosen to test the applicability of the coating strategy introduced above. Since each of these polymers contains accessible hydrogen groups, they all can be activated by oxygen plasma in a similar manner as PDMS; thus, it is expected that the same two-step coating process can also be applied to those polymer materials.

This is tested in the next step. Indeed, the mucin coating procedure can be performed on these six different polymer materials in very similar ways: Except for some minor changes regarding the rinsing fluids (PMMA shows a poor resistance towards organic solvents; thus, those samples are cleaned with ultrapure water instead of EtOH and 2-propanol), the coating protocol is the same as described for PDMS specimens above. Afterwards, as for the PDMS samples, the successful deposition of mucin is analyzed by immunostaining. For all coated polymeric materials, these ELISA tests return a significantly higher fluorescence signal

---

\* This section follows in part the publication Winkeljann *et al.*, *Advanced Materials Interfaces* (2020)

compared to their uncoated counterparts (**Figure 25a**). This demonstrates that a considerable amount of mucin is present on all coated polymer surfaces.

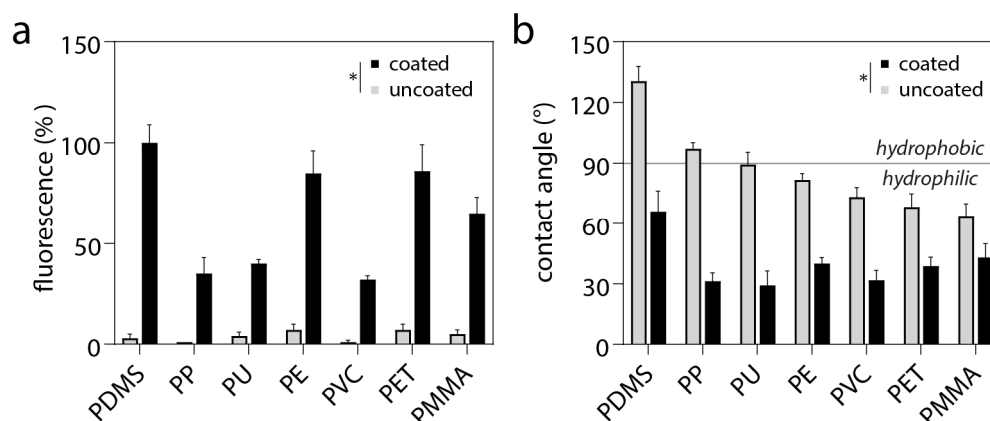


**Figure 25: Covalent mucin coatings on different polymer materials.** The presence of mucin on seven different medical polymer materials is verified *via* ELISA (a). Contact angle measurements compare the surface polarity of the polymer materials before and after mucin coating (b). The error bars depict the standard deviation as obtained from  $n = 3$  independent samples. As indicated by the asterisks in the two figure legends, the described properties of coated samples were always significantly different from their uncoated counterparts.

Since mucins are well hydrated and can bind a large amount of water molecules<sup>144</sup>, a mucin coating is expected to render the surfaces of all polymeric substrates more hydrophilic. Experimentally this expectation can be tested by comparing the contact angle of mucin-coated materials to the values obtained from their uncoated counterparts. The contact angle is a frequently used indicator for analyzing the wettability of a surface and thus the surface energy: materials with a contact angle above  $90^\circ$  are considered hydrophobic, whereas materials with a contact angle below  $90^\circ$  are referred to as hydrophilic. Indeed, for all tested materials, the mucin coating entails a significant reduction in contact angle – even the PDMS substrate, which shows an initial contact angle of roughly  $130^\circ$  (corresponding to a superhydrophobic surface), is rendered hydrophilic after mucin functionalization (**Figure 25b**). For PDMS samples, it was already shown above that the covalent coating procedure provides the mucin layer with good resistance towards mechanical stress. To confirm this finding for another polymeric substrate, PMMA, *i.e.*, the polymer material with the most hydrophilic surface properties before coating, is selected. However, PMMA ( $E_{\text{PMMA}} \approx 3 \text{ GPa}^{246}$ ) has a much higher stiffness than PDMS ( $E_{\text{PDMS}} \approx 2 \text{ MPa}^{156}$ ); thus, the tribological test used for PDMS samples would generate a very high (and unphysiological) contact pressure that can easily

induce wear on the PMMA substrate. Instead, ultrasonic treatment is chosen now as a gentler method to challenge the mechanical stability of the mucin coating on PMMA substrates. Indeed, this method is sufficient to reduce the surface fluorescence of the passively coated samples by approximately 40 % indicating that a significant amount of mucins is removed by the ultrasonic treatment (see *Appendix Figure C6*). In contrast, the covalently coupled mucin layer is completely unaffected by the ultrasonic treatment as indicated by the significantly higher fluorescence signals obtained from those samples compared to passively coated ones.



## 5 Biopolymer coatings with tunable functionalities

It was demonstrated in *Section 4* that macromolecular coatings are powerful tools to improve the lubricity and wear resistance of synthetic polymeric surfaces. Furthermore, it was shown how polymer-brush coatings interact with solubilized macromolecules as they occur in most body fluids. By introducing a method to covalently couple mucin glycoproteins to a set of polymer materials, the applicability and stability of such macromolecular coatings were significantly enhanced, thus providing a very promising tool to coat medical devices. However, up to now, these macromolecular coatings had a rather passive functionality, *i.e.* they reduce the contact of two opposing surfaces to reduce friction and wear at this particular interface. In the final part of this thesis, these macromolecular coatings will be tuned further to acquire an active character; they will act as selective binding partners to remove particular objects – either *via* passive forces or by specific interactions – from aqueous solutions. Furthermore, specialized coatings will be presented that allow for the immobilization of active components, such as enzymes, to perform non-consuming chemical reactions on the flow. In the last step, these coatings will be rendered smart, *i.e.* they will be supplied with drugs and trapped in semi-stable states that allow for the release of entrapped drugs in the presence of suitable physiological triggers.

### 5.1 Macromolecular coatings enable selective binding\*

Whether for laboratory use or clinical practice, many fields in Life Sciences require selective filtering. Furthermore, selective permeability and filtration are an essential feature of many biological processes, and technical filtration applications often make use of procedures which imitate biological strategies. For instance, the renal filtration mechanism of the human kidney is mimicked in cross-flow filtration and in purification processes for drinking water<sup>247</sup>.

Although there are several technical solutions for achieving selective filtration, these methods are often designed to sieve according to a certain parameter set and thus lack flexibility. Chromatographic methods, for example, provide the basis for a broad variety of filtration approaches<sup>248</sup>. However, a chromatography column designed for size exclusion filtration cannot filter molecules by means of affinity

---

\* This section follows in part the publication Winkeljann *et al.*, *Macromolecular Bioscience* (2017)

(which is implemented in, *e.g.*, ion exchange chromatography) as those techniques are based on different filtration mechanisms. Moreover, chromatographic filtration approaches typically require specific resins and thus can be cost-intensive<sup>249</sup>. Especially in lab-scale settings, where the need for versatile filtration and purification methods arises as research progresses, classical filtration options may not always be sufficient. Novel approaches to selectively sieve proteins (by shape or size) based on mesoporous structures<sup>250-252</sup> or to remove heavy metal ions from aqueous solutions<sup>253,254</sup> have been introduced in the last years; however, the flexibility of those novel methods is limited.

A porous PDMS matrix offers a suitable platform to test such an adaptable solid immobilization system, as it can be functionalized with a high number of molecules<sup>42,255-257</sup> which then can provide the desired selectivity properties. Additionally, a porous PDMS-based filtration system can be fabricated with a high surface-to-volume ratio, a feature that is essential for an efficient small-scale filtration process. However, commonly used porogens such as sugar, salt or air bubbles tend to give rise to insufficiently interconnected pores – unless they are added in very high concentrations<sup>258</sup>. As a consequence, the major part of the generated pores often constitutes dead ends, and non-leached porogens remain in the structure<sup>259</sup> which decreases the filtration efficiency. A comparably easy way of fabricating a well-interconnected porous PDMS system was presented before<sup>260</sup>, which is based on washing out embedded sugar fibers from a PDMS cube thus generating a PDMS structure containing a well-connected capillary system. Here, an optimization of this fabrication process is introduced (see *Appendix B* for methods). By coating, the inner surface of the capillaries with (bio)macromolecules, such as mucins or poly-L-lysine, various filtration profiles with the identical porous PDMS matrix are achieved. Depending on the macromolecule used for coating, filtration towards either positively or negatively charged particles– or both can be achieved. Further variation of the macromolecules used for filter coating enables filtration not only according to charge but also by means of specific binding to chemical motifs. In addition to the selective removal of particles, this highly versatile system can also be used to immobilize enzymes and to study the binding of test molecules to immobilized bio-macromolecules.

### 5.1.1 Selective filtering through electrostatic interactions

Although the PDMS model system used here offers the possibility to covalently link molecules through different coupling reactions<sup>42,255-257</sup>, performing such complicated, mostly multi-step coating processes in a fine capillary system can be

very challenging. However, since proteins and molecules can adhere strongly *via* unspecific binding to the hydrophobic PDMS<sup>5,261-265</sup>, performing a mucin coating by physisorption should be sufficient to test their performance as selective filters. As discussed before the mucin glycoprotein comprises densely glycosylated regions, and several carbohydrates found in this region (such as sialic acid or sulfated sugar residues) possess a strongly anionic character<sup>82</sup>. Consistently, mucins have been previously reported to bind cationic particles and molecules<sup>266-270</sup>.

To test different filter functionalizations liposomes appear to be a suitable platform, as the size and net charge of these particles can be easily and independently tuned, *i.e. via* extrusion and adjusting the lipid composition. Furthermore, lipids carrying specific binding motifs can be incorporated at adjustable concentrations.

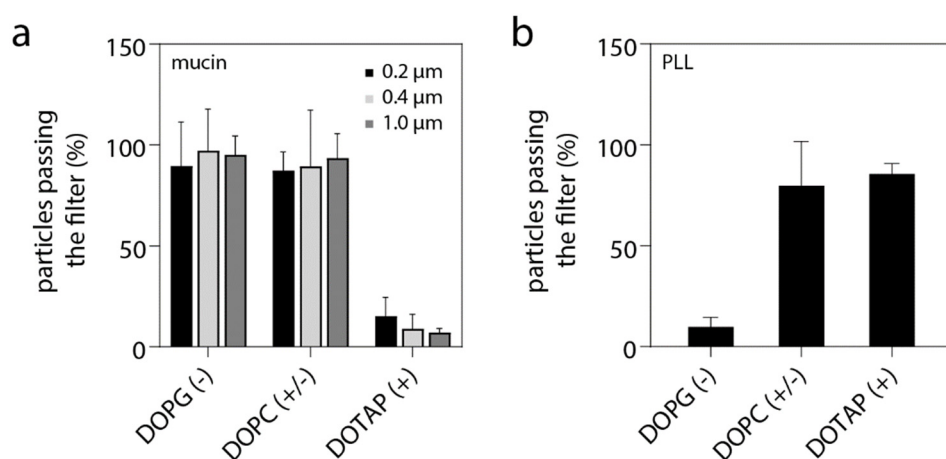


**Figure 26: Different macromolecular coatings of the PDMS-based capillary system lead to different selectivity profiles.** Depending on the molecule used for coating, the filter removes either (a) positively charged particles (electrostatic “low pass”), or (b) negatively charged particles (electrostatic “high pass”). The filtration outcome of a mucin coated filter is independent of the liposome size used here (a). Error bars denote the standard error of the mean as obtained from  $n = 3$  different filter realizations.

To test the interaction of immobilized mucins with such liposome test particles, different liposome solutions (*i.e.* negatively charged, zwitterionic/neutral, and positively charged liposomes - see *Appendix Table C2* for details) are flushed through a mucin-functionalized capillary system and the percentage of particles that were able to successfully pass the filter are determined. The mucin-coated capillary system allows anionic as well as zwitterionic liposomes to pass with high efficiency but retains a high fraction of cationic particles (**Figure 26a**). The virtually identical result is obtained when three variants of fluorescent dextrans are used to

determine the filtration profile: Although dextrans have hydrodynamic radii in the range of 8-9 nm and are thus roughly 20x smaller than the liposome particles, also here only the positively charged species, *i.e.* DEAE-functionalized dextrans, is removed (Appendix **Figure C7**). To support this finding, that indeed the mucin coating is responsible for the selective properties of the PDMS filter system, a coating with the polycationic poly-L-lysine (PLL) is tested. Based on the results obtained so far, the system should selectively filter out anionic particles only. In agreement with this expectation, a PLL coated filter removes up to 90 % of the anionic liposomes whereas positive and neutral liposomes can pass the capillary system (**Figure 26b**).

### 5.1.2 Site-specific binding

So far, it was described how electrostatic interactions can be used to provide the capillary PDMS filter with different selectivity properties. However, these interactions are rather nonspecific and can occur with numerous chemical motifs. Thus, it is now aimed at achieving a more precise filtration process by employing specific binding interactions.

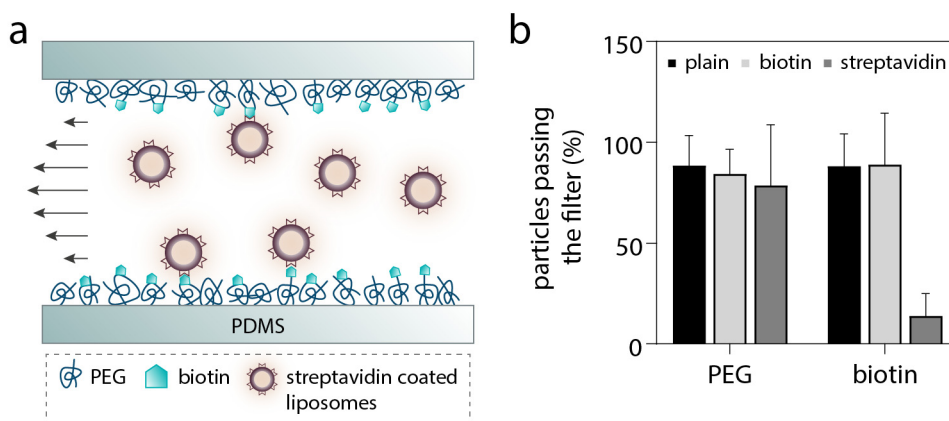


**Figure 27: Specific removal of liposomes by means of biotin-streptavidin binding.** Schematic illustration of a functionalized capillary modified to achieve specific filtering (a). Streptavidin-coated biotinylated DOPC-liposomes are filtered out since they can bind to the biotin groups on the functionalized capillary surface (a, b). Both, biotinylated and plain DOPC-liposomes lacking a streptavidin coat, however, can pass the filter unhindered. All three types of liposomes can pass a dopamine-PEG coated system when the biotin functionalization is omitted (b). Error bars denote the standard error of the mean as obtained from  $n = 3$  different filter realizations.

A well-known and thoroughly investigated specific binding interaction occurs between the vitamin biotin and the protein streptavidin<sup>271</sup>. To allow the capillary PDMS construct to selectively filter particles by means of biotin-streptavidin binding, streptavidin-coated biotinylated liposomes in combination with biotin-PEG coated capillary surfaces are used (**Figure 27a**). To functionalize the filter system with biotin, a dopamine-based coating strategy is chosen. The catecholamine dopamine is a molecule that can form strongly adherent polymer layers *via* self-polymerization on a wide variety of materials including PDMS surfaces<sup>272</sup>. Since dopamine reacts with thiols or amines *via* Michael addition or Schiff base reaction<sup>273-275</sup>, a dopamine coating can serve as a versatile platform for multiple secondary reactions, which is used here to attach a second layer of PEG and biotin onto the capillary surface (see *Appendix B* for methods).

And indeed, when such streptavidin liposomes are pumped through the functionalized filter, a removal efficiency of approximately 85 % can be observed. In contrast, biotinylated liposomes lacking streptavidin and simple DOPC liposomes as used above can pass this filter easily. To rule out unspecific binding, the filter is coated with simple PEG (lacking the biotin-terminus). As expected, all three liposome species can pass the filter nearly unhindered (**Figure 27b**).

### 5.1.3 Enzyme immobilization

Up to now, the capillary system was utilized to remove particles/molecules from a solution *via* specific and unspecific interactions with immobilized macromolecules. In a third step, it is aimed at utilizing the selective interaction of an immobilized enzyme and its corresponding substrate to enable enzymatic catalysis inside the capillary system.

As a model enzyme, horseradish peroxidase (HRP) is chosen. Using H<sub>2</sub>O<sub>2</sub> as an oxidizing agent, this protein can catalyze an oxidization reaction for several substrates. Whereas the substrate itself does not return a fluorescent signal, the converted substrates then can be detected *via* spectrophotometric methods. When the inner PDMS surface of our capillary system is coated with HRP *via* physisorption and the substrate ADHP (10-acetyl-3,7-dihydroxyphenoxazine) is pumped through the enzyme-coated filter (**Figure 28a**), an efficient substrate conversion can be observed (**Figure 28b**). This indicates that a significant fraction of the immobilized HRPs remained in an active conformation after adsorbing to the PDMS surface and that enough active sites of the adsorbed enzyme population (HRP possesses only one active site per protein) are accessible for the substrate.

Even when the filter is flushed with a high volume of water, subsequent injection of a substrate containing solution still returns a constantly high fluorescent signal after passing the filter.

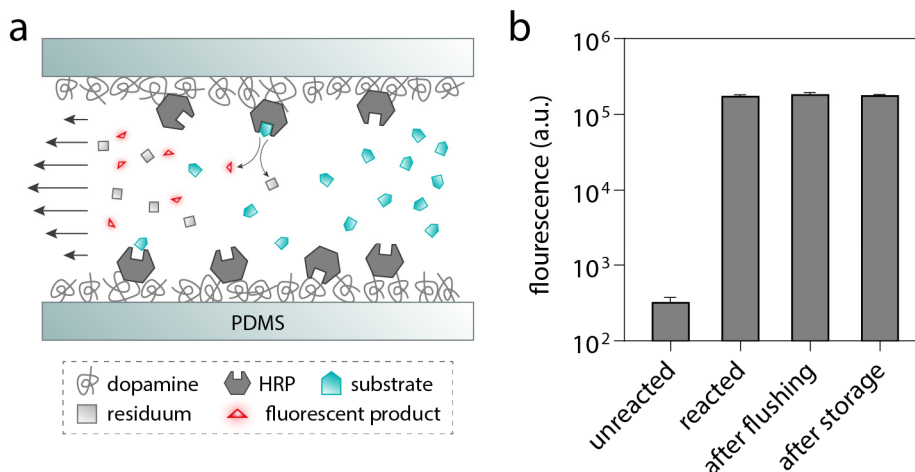


**Figure 28: Immobilization of enzymes onto the PDMS surface of the capillary system allows performing catalytic reactions with the filtration system.** Physisorption of the enzyme HRP leads to the conversion of a substrate which is pumped through the filter (a). The fluorescent intensity of the substrate solution is measured photospectrometrically before and after passing the filter and indicates enzymatic activity (b). After rinsing the capillary system with 500 mL of ultrapure water, no decrease in the enzymatic activity is observed. A similarly high enzymatic activity is obtained when the HRP coated filter is stored at room temperature for 48 hours prior to use. Error bars denote the standard deviation as obtained from  $n = 3$  different filter realizations.

After a total rinsing volume of 500 mL (which corresponds to more than 3000 filter volumes), the substrate conversion efficiency is equal to right after enzyme immobilization. Furthermore, the storage of an HRP coated filtration system at room temperature for 2 days returns similar catalytic activity (Figure 28b).

## 5.2 Covalent mucin coatings reduce the initial stages of biofouling\*

In a model setup, it was demonstrated, how macromolecular coatings can be used to provide surfaces with a tuneable selectivity. Especially in medical engineering, selectively binding surfaces are particularly interesting, as – depending on the application – a controllable selectivity can be used to promote tissue integration or

\* This section follows in part the publication Winkeljann *et al.*, *Advanced Materials Interfaces* (2020)

reduce the unwanted deposition of proteins, bacteria or fibrotic encapsulation. Furthermore, it was shown in *Section 4.1* that the covalent mucin coating introduced here is robust and resists both key requirements for use in medical implants - mechanical stress and several physiologically relevant environmental challenges.

Consequently, it is now aimed at verifying that this covalently coupled mucin layer shows similar anti-fouling properties as reported previously for mucin coatings generated *via* passive adsorption<sup>35,276-279</sup>.

### 5.2.1 Reduction of particle and protein adhesion

The following experiments are conducted with covalent mucin coatings generated on two different polymeric substrates. As for selective binding tests and mechanical stability tests, PDMS is selected again. Furthermore, PMMA is chosen as a second test substrate, which -in contrast to the relatively soft, hydrophobic PDMS - is stiff but hydrophilic. Whereas quite different regarding their material properties, those two polymer materials are very suitable for the following investigations as they are both transparent and thus allowing for optical microscopy tests in transmitted light mode.

First, the covalent mucin coating is exposed to two types of polystyrene (PS) nanoparticles; the first variant exhibits a carboxylated surface and thus carries an overall negative charge (as indicated by the negative zeta-potential  $\zeta_{\text{carboxy}} = -50.7 \pm 0.5$  mV), and the second one exhibits an aminated surface resulting in an overall positive net charge ( $\zeta_{\text{amine}} = +25.2 \pm 1.9$  mV). When analyzing the number of carboxylated particles adsorbed onto the different (coated *vs.* uncoated) PDMS specimens *via* fluorescence microscopy, a drastic reduction for mucin coated samples can be observed compared to uncoated PDMS (**Figure 29a**), which is in good agreement with the results obtained with the filtration model system.

For assessing the extent to which this effect is due to the mucin coating, also a PDMS surface carrying a silane pre-coating only is analyzed; also here, much fewer particles are detected than on uncoated PDMS, yet more than on mucin coated specimens. This result is not really surprising as both, the silane pre-coating and the mucin coating, introduce a high density of negative charges onto the PDMS surface thus repelling the anionic PS particles through electrostatic repulsion. Since the deposition of large, polyanionic mucins onto the PDMS surface is likely to create stronger repulsive forces than the small, weakly charged silane, the higher efficiency of the mucin coating towards the anionic PS particle appears reasonable.

Interestingly, also adsorption tests with positively charged PS particles return a similar result (**Figure 29a**). This finding seems to challenge the idea that the mucin coating was able to render the surface of the PDMS samples negatively charged – in this case, one would expect efficient adsorption of the cationic, amine-terminated PS particles. However, carboxyl- or amine-terminated PS particles both exhibit a strongly hydrophobic character. Thus, it appears likely that – for the weakly charged amine-terminated PS particles – their adsorption behavior onto PDMS is dominated by hydrophobic interactions, and that weak, attractive electrostatic forces between the mucin coating and the PS particles are still preferable to the strong hydrophobic forces present for uncoated PDMS.

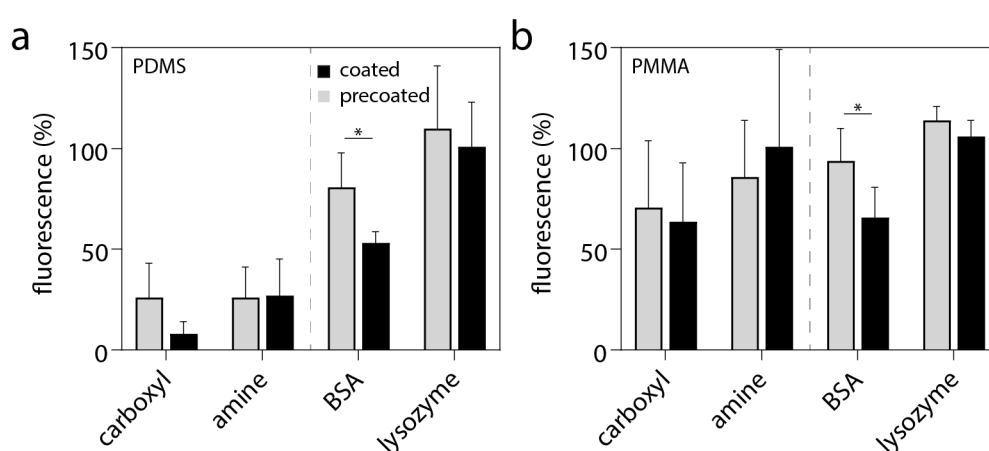


**Figure 29: Protein and particle adsorption onto mucin coated surfaces.** The adsorption behavior of carboxylated and amine-terminated polystyrene particles as well as BSA and lysozyme is determined for silane-precoatings and mucin coatings generated on PDMS (a) or PMMA (b) samples and compared to that obtained for uncoated specimens (horizontal lines in the respective subfigures). The error bars depict the standard deviation as obtained from  $n = 3$  independent samples each.

Consequently, the efficiency of the mucin coating can be expected to be less pronounced if the adsorption behavior of the same test particles is assessed on a hydrophilic substrate such as PMMA – and indeed, for those specimens, the adsorption of anionic PS particles is reduced whereas the adsorption behavior of cationic PS particles is mostly unaffected (**Figure 29b**). Of course, whereas giving mechanistic insight into the coating properties, polystyrene particles are a very crude model system for assessing anti-biofouling properties. Thus, in a second step, the anti-adhesive properties of the mucin coating are tested in a biomedically more relevant scenario. As the process of biofouling always starts with the formation of a

conditioning film, *i.e.*, the uncontrolled adsorption of proteins, the ability of the mucin coating to reduce the adsorption behavior of both, a negatively and a positively charged model protein is investigated; accordingly, fluorescent BSA (anionic at neutral pH) and lysozyme (cationic at neutral pH) are selected as test molecules. Since neither of those well-folded proteins should carry a large number of hydrophobic amino acids on their surface, it can be assumed that hydrophobic interactions do not play a major role regarding their adsorption behavior.

In full agreement with this expectation, it is found that the mucin coating returns comparable results on both materials, PDMS and PMMA: For the anionic BSA molecules, the mucin coating reduces the adsorption by roughly 40 % and is significantly more efficient than the silane precoating alone; for the cationic lysozyme molecules, the adsorption behavior is comparable to the uncoated polymer materials (**Figure 29a, b**). From those experiments, it can be concluded that the mucin coating can efficiently render hydrophobic materials resistant towards the adsorption of hydrophobic objects. Moreover, the mucin coating causes a significant reduction of the adsorption of anionic molecules on both, initially hydrophobic and hydrophilic materials.

### 5.2.2 Reduction of prokaryotic and eukaryotic cell adhesion

In the human body, the formation of a protein-based conditioning film on an artificial material is typically followed by the colonization of bacteria or the encapsulation by fibroblasts. It has previously been shown, that passively adsorbed mucin coatings have repelling properties towards different (pathogenic) bacteria, *e.g.*, *P. aeruginosa*, *S. epidermidis*, *S. aureus*, and *S. mutans*.<sup>276,278,280</sup>

Here, the mucin-coated surface is first exposed to *S. aureus* bacteria. *S. aureus* does not cause infections in healthy individuals; however, in patients with a weakened immune system, this bacterium can lead to pneumonia, endocarditis or even sepsis. When an uncoated PDMS surface is incubated with a solution of planktonic *S. aureus* bacteria, a very large number of bacteria adsorbs to the surface. However, when the same bacteria are brought into contact with a mucin coated PDMS surface, the number of adsorbed bacteria is reduced by approximately 35 % (this number represents the average reduction in adhered bacteria as obtained from  $n = 3$  independent samples with  $N = 3$  images each, see *Appendix B* for details) (**Figure 30a**). If the adhesion property of *S. aureus* is tested on PMMA surfaces, a qualitatively similar difference between coated and uncoated samples is observed (**Figure 30b**); however, now this difference is less pronounced ( $n = 3, N = 3$ ).

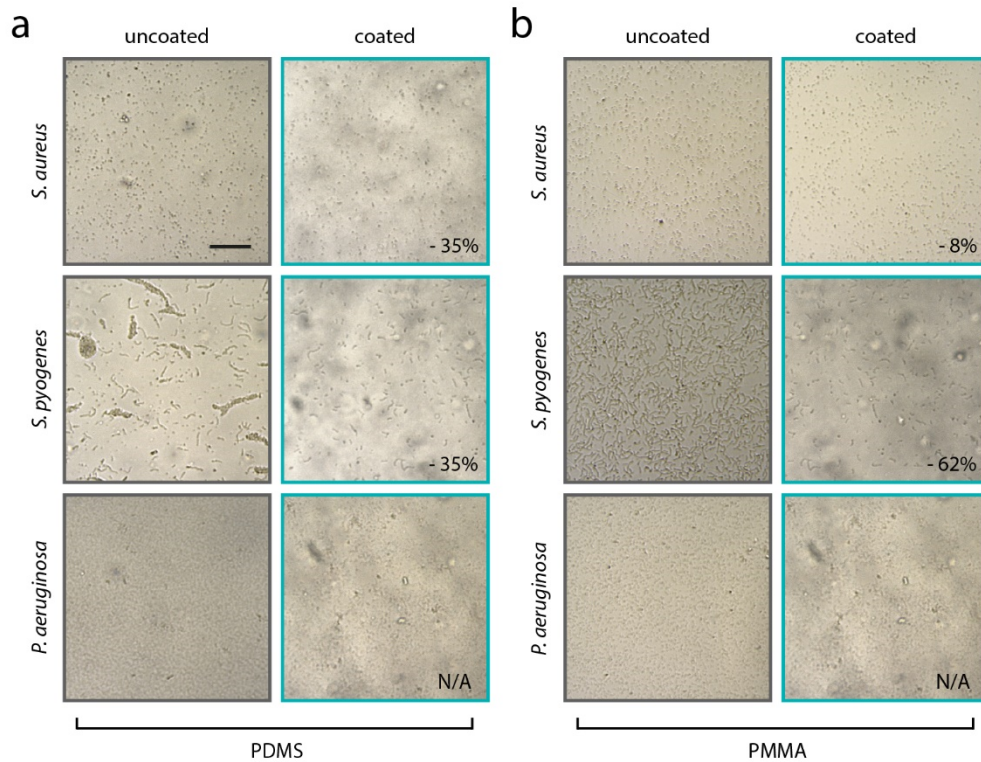


**Figure 30: Covalent mucin coatings can reduce the surface colonization by selected bacteria.** The adsorption of *S. aureus* and *S. pyogenes* onto PDMS and PMMA surfaces is reduced if a covalent mucin coating is applied previously to the bacterial exposure. *P. aeruginosa*, however, adheres similarly well to a mucin coated surface as to uncoated PDMS or PMMA surfaces. The scale bar represents 50  $\mu\text{m}$ .

Next, the two polymer materials are exposed to bacteria from the pathogenic strain *S. pyogenes*, which can, in addition to skin infections, be responsible for pharyngitis including severe forms of tonsillitis. Also here, light microscopy images of planktonic bacteria incubated on PDMS samples indicate, that the covalently coupled mucin layer can reduce bacterial adhesion to the polymer surface: on PDMS samples a 35 % reduction ( $n = 3, N = 3$ ) and on PMMA samples even a 62 % reduction ( $n = 3, N = 2$ ) is found. As a third pathogenic bacterium relevant in the context of biomedical devices *P. aeruginosa* is chosen. Also, *P. aeruginosa* is responsible for a multitude of nosocomial infections including pneumonia, skin infections or inflammations in the urinary tract. *P. aeruginosa* is a very resistant germ, that can survive in dry and humid conditions and has been shown to be mucoadhesive<sup>281-284</sup>. Consequently - as also shown before<sup>278</sup> - those pathogens

adhere very well to mucins and no difference between coated and uncoated surfaces can be observed – neither on PDMS nor on PMMA substrates. (Figure 30a, b).

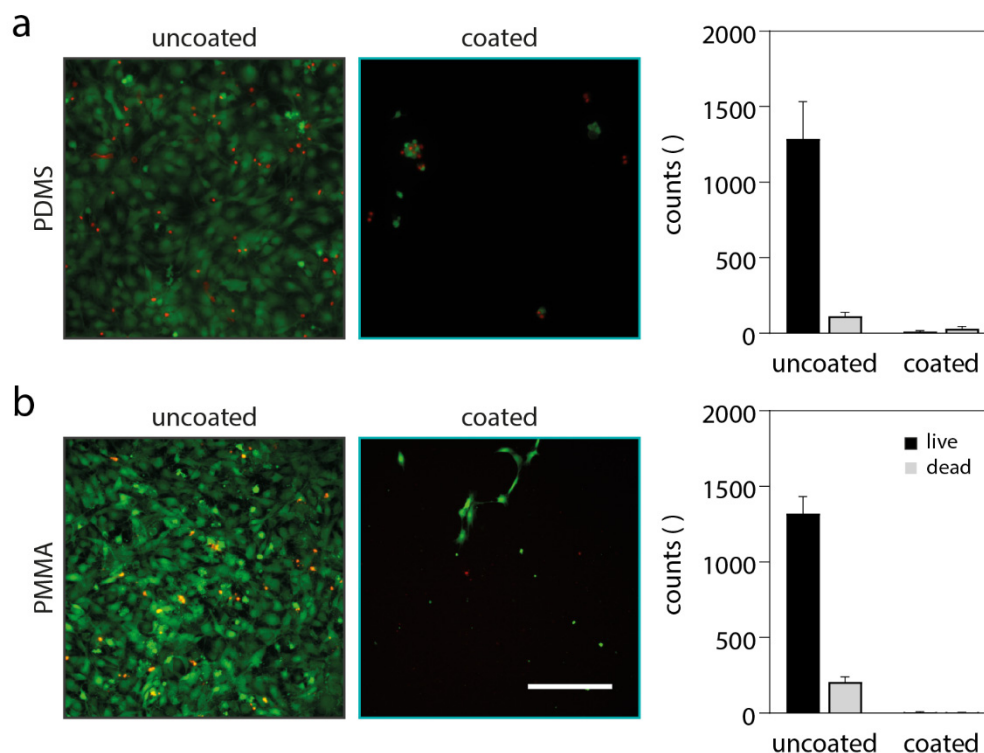


**Figure 31: Covalent mucin coatings reduce fibroblast adhesion.** The adsorption of NIH/3T3 fibroblasts onto both, PDMS and PMMA surfaces, is reduced when a covalent mucin coating is applied. The scale bar represents 400  $\mu\text{m}$ .

Having observed that mucin coatings can reduce the colonization of polymer surfaces by certain pathogenic bacteria, it is asked next, if the anti-adhesive properties of covalent mucin coatings also apply to eukaryotic cells. In detail, fibroblast adhesion is assed (see *Appendix B* for details), as unwanted colonization of implanted materials is mostly responsible for fibrous encapsulation of implants. Fibrous encapsulation compromises the efficiency of the device and, in the long term, frequently leads to device failure. To test this, an established fibroblast cell line (NIH/3T3 fibroblasts) is used here which was already reported to not adhere to mucin coatings generated by simple passive adsorption<sup>43</sup>. After incubation of those NIH/3T3 fibroblasts on uncoated and mucin-coated PDMS samples, respectively, a confluent cell layer has formed on blank PDMS, whereas the amount of adsorbed fibroblasts on mucin-coated surfaces is very low (Figure 31a). Additionally, the

adsorbed cells on the respective surfaces differ in terms of their morphology: On uncoated PDMS, the fibroblasts exhibit their typical well-spread morphology indicating strong adhesion; on mucin-coated surfaces, however, the few adherent cells exhibit a relatively round shape indicating weak adhesion. Still, most of the cells adsorbed onto mucin-coated surfaces are still alive, which is an important aspect as it means that the multi-step mucin-coating introduced here is not cytotoxic. When NIH/3T3 fibroblasts are cultivated on uncoated and mucin coated PMMA samples, respectively, a virtually identical result is obtained as on PDMS specimens (**Figure 31b**). This nicely illustrates that the ability of the covalent mucin coating to prevent fibroblast adhesion is independent of the carrier substrate the coating is generated on.

### 5.3 Switchable biopolymer-based coatings as smart drug delivery systems\*

Preventing and reducing biofouling is particularly important for medical implant devices such as catheters, stents, vascular grafts, and pacemakers, as both, biofilm formation and tissue infection have been identified as one of the most frequent reasons for device failure<sup>285,286</sup>. Furthermore, superficial or deep infections have been reported for 1-5 % of all hip and knee replacement operations<sup>287,288</sup>. However, when inserting an artificial implant material into the human body it is inevitable that also exogenous pathogens enter the surgical site<sup>289</sup>. Thus, even though antifouling strategies as mentioned above may be able to suppress biofouling events on the implant surface, bacterial infections around the implant can still occur – both, immediately after surgery and up to weeks after the operation.

In clinical practice, patients therefore receive systemic antibiotics during surgery and the following days to overcome early-stage infection. However, an oral administration limits the possibility of the drug to be delivered to the target region and comes with the risk of inducing antibiotic resistance<sup>290</sup>. In addition, local drug administration during the operation can cause an overly high antibiotic concentration in the plasma, and this can cause unwanted side effects such as nephrotoxicity. As an alternative, bactericidal or drug-loaded implant surfaces<sup>291-294</sup> and implant materials such as bone cements<sup>295,296</sup>, scaffolds<sup>297</sup> or nanoparticles<sup>298</sup> can offer local protection against bacterial infections; however, the drug release process

---

\* This section follows in part the publications Yan *et al.* (2018) & Kimna *et al.*, *Advanced Materials Interfaces* (2020) and the patent application Kimna *et al.*, (2019)

from such systems is typically not well controlled and mostly governed by the diffusive liberation of drugs.

Drug delivery systems based on polymeric coatings typically regulate the duration of a release event by either acting as a diffusive barrier or by serving as a degradable drug reservoir<sup>77-81</sup>. In some recent studies, it was possible to gain better control over the release of pharmaceuticals from such polymer coatings: there, pH-responsive, degradable structures were used, which were disassembled in the presence of bacteria thus triggering the release of an antibacterial agent<sup>299-302</sup>. However, once the drug load is released, those systems cannot offer any further protection of the surface. In particular, there is no controlled release mechanism yet, which establishes both, short- and long-term protection against bacterial infection by making use of specific trigger events as they occur as part of an infection event.

Also in this context, mucin-based biomaterials, either crosslinked or as blends together with other polymers, have been used previously to achieve a sustained and controlled release of molecules and active agents<sup>303-305</sup>. Therefore, it is now aimed at providing another functionality to the mucin coating introduced in *Chapter 4*, by adapting it to act as an intelligent drug delivery system.

### 5.3.1 Reversible condensation of mucin glycoproteins

The first step in designing a smart, drug supplying implant surface is to find a suitable way to immobilize the desired drug onto a surface. For macromolecules such as mucin, which are constantly secreted, the molecules are first synthesized in an extremely compacted form and then encapsulated in vesicles<sup>306</sup>. These vesicles are stored in the cell until an environmental change triggers the release of the cargo. Understanding how the cell manages to reversibly condense the gigantic mucin molecule into a compact form could open a way to use mucin molecules as dynamic carrier particles. Then, in the second step, the same mechanism could be applied to a surface-bound mucin layer to generate a triggerable drug depot.

Intact mucin-carrying vesicles are characterized by a low internal pH and a high calcium concentration. It has been shown that calcium solutions can stabilize de-membrated vesicles, possibly by shielding repulsive negative charges on the mucin glycans while acting as ionic cross-linkers that maintain the molecules in a compacted state<sup>307-309</sup>. In addition to those cross-linkers, the solvent quality was also shown to effectively mediate mucin condensation. Using glycerol as a stabilizing reagent, giant mucin vesicles extracted from the slug *Ariolimax columbianus* could expand up to 600-fold within seconds when glycerol was removed again<sup>309</sup>. The

unfolding of these compacted mucins is initiated once the vesicle is released into the extracellular environment. The increase in the pH value and the entry of sodium ions displace calcium ions and trigger the rapid unfolding of the molecules, which is driven by electrostatic and steric repulsions<sup>310,311</sup>. Mucin condensation and de-condensation have thus mostly been studied in the context of mucin vesicles, and only a few studies report about the response of individual mucins and mucin oligomer molecules to this environmental changes<sup>312,313</sup>.

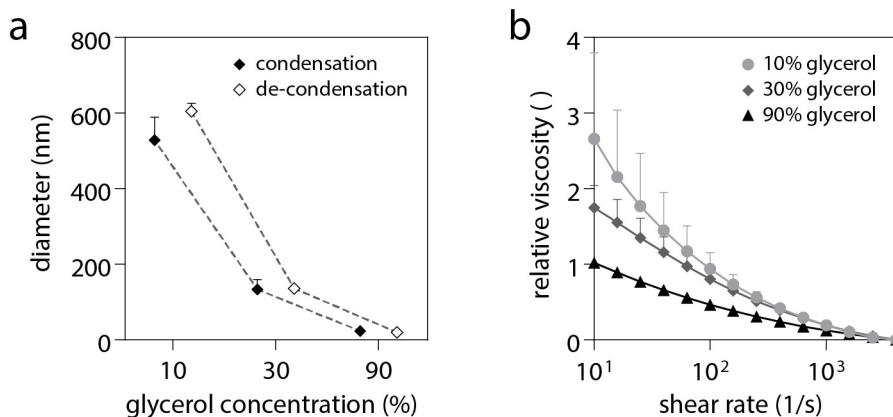


**Figure 32: Glycerol concentration affects mucin conformation.** The diameter of the mucin nanoparticles is gradually decreased as the glycerol concentration is increased. This condensation is fully reversible (a). The typical shear-thinning behaviour observed for solutions containing mucin molecules is also reduced as mucin molecules are further compacted (b). The error bars depict the standard deviation as obtained from  $n=3$  independent samples.

As it was shown that glycerol has a stabilizing effect on mucin particles, it is now tested if the same strategy can be applied for individual mucin molecules. And indeed, when glycerol is added to a mucin containing aqueous solution, the size of the mucin molecules is gradually decreased with increasing glycerol concentration. Furthermore, it can be observed, that the compaction of the glycoproteins is completely reversible as soon as glycerol is reduced or removed from the solution (**Figure 32a**). An explanation for the reversible condensation observed here can be found in two phenomena: the disaggregation of mucins driven by changes in intermolecular interactions and the compaction of the mucin molecules driven by insolubility. In the disaggregation model, it is assumed that the mucin solution is composed of multimeric structures, which are stabilized through hydrophobic interactions<sup>218</sup>. The addition of glycerol to aqueous protein solutions has been shown to stabilize proteins and prevent aggregation by forming an amphiphilic

interface between the hydrophobic domains of the protein and the polar solvent<sup>314</sup>. The second model suggests that the strong compaction of mucins is driven by the poor solubility of mucins in glycerol. Indeed, mucins are typically insoluble in nonpolar solvents such as hexane<sup>315</sup> and simple sugars are also less soluble in glycerol than in water<sup>316</sup>. Thus, increasing the glycerol concentration would promote mucin intramolecular interactions over mucin–solvent interactions, leading to a compaction of the molecular structure.

It can further be hypothesized, that the conformational change of mucins from a linear to a condensed state also affects macroscopic properties, *e.g.* the viscosity of mucin solutions. However, the use of highly viscous glycerol as a compaction reagent masks any effect of the mucin conformational changes on the absolute viscosity of the solutions. Yet, conformational changes of mucin induced by glycerol, even though occurring on the molecular level, could still be detected on the macroscale by comparing the dynamic viscosity of mucin solutions with different glycerol contents. Indeed, the classical drop of viscosity with increasing shear (*i.e.*, shear-thinning) rate seen for many polymer solutions is gradually reduced as the glycerol concentration is increased (**Figure 32b**). Indeed, the reversible condensation of mucins observed here seems to be an interesting mechanism, that could be used to temporarily entrap drug molecules.

### 5.3.2 DNA mediated drug release from a surface-bound mucin layer

Up to now, mucins were used as freely swimming molecules in an aqueous environment. Thus, it is now asked, if the same compaction strategy can be transferred to mucin molecules, that are immobilized on a substrate in a brush-like manner. Furthermore, triggering the de-condensation by removing glycerol is unfavorable for medical applications, as it already has to happen before the implant is brought in contact with the human body. To make this compaction of mucins applicable for implant coatings, another way has to be found to temporarily stabilize condensed mucin molecules on a device surface.

Single-stranded, partially self-complementary DNA sequences were previously used to act as temporary crosslinkers between nanoparticles (crDNA). There, the release of individual particles from those aggregates was achieved by introducing a fully-complementary displacement DNA (dDNA) sequence that can form a thermodynamically more stable complex with crDNA (dDNA/crDNA) than the cross-linking sequences do with each other (crDNA/crDNA)<sup>317,318</sup>.

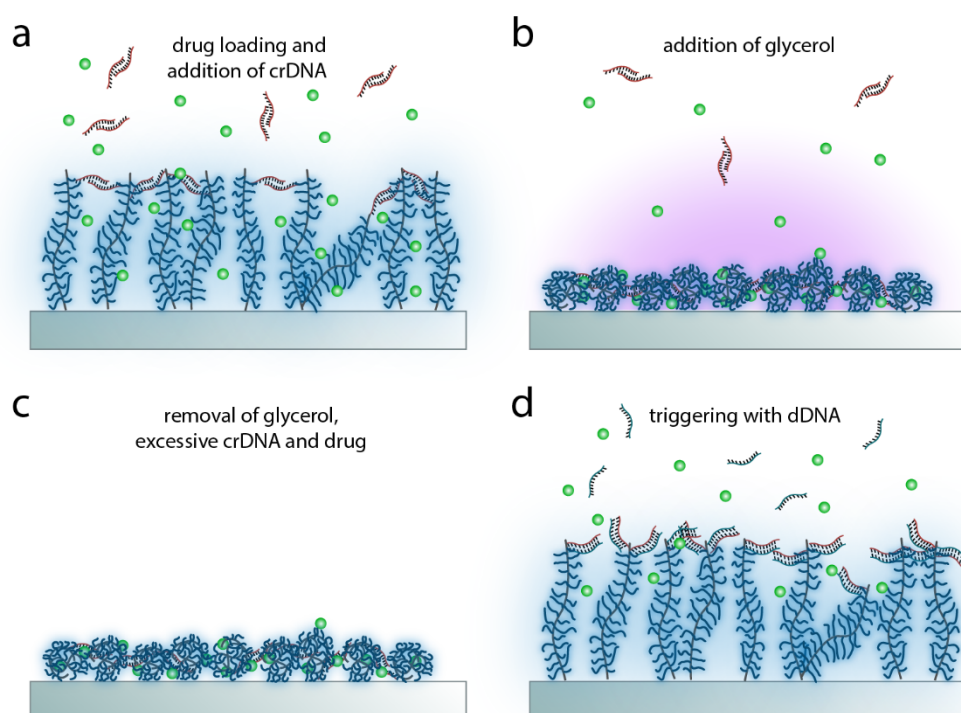


**Figure 33: DNA triggered release mechanism.** Self-complementary DNA strands are used to form a cage-like structure with surface-bound mucin molecules to entrap an antibiotic (a). By adding glycerol this cage can be further condensed (b) and stays stable after glycerol, excessive DNA and antibiotics are removed (c). With the exposure to a fully-complementary displacement DNA, the mucin layer returns its initial conformation and releases the antibiotic (d).

This mechanism was found to be precise, reproducible and highly efficient. Here, this DNA-mediated mechanism is adopted to temporarily stabilize a compacted surface-bound mucin layer that is loaded with drug molecules (**Figure 33** and **Appendix Figure C8a**). In brief, the strategy is as follows: a surface bound mucin layer is generated, and drug molecules are added. Thiol-functionalized crDNA strands are then added to this surface-bound mucin layer and spontaneously attach to cysteine-rich subdomains of mucins by forming disulfide bonds (**Figure 33a** and **Appendix Figure B1**)<sup>319</sup>. Next, the drug-loaded mucin layer is exposed to a glycerol solution, which condenses the mucin layer into a compacted state (**Figure 33b**); this compaction step enables the formation of crDNA/crDNA cross-links between neighboring mucin molecules and traps the drug molecules in the mucin layer. Glycerol, unbound crDNA strands and excess drug molecules are then removed by washing (**Figure 33c**), and the crDNA/crDNA cross-links maintain the compacted

state of the mucin layer. As a consequence, the drug molecules remain trapped in the mucin layer until release is triggered. This triggered release is achieved by exposing the mucin layer to dDNA strands, which open the stabilizing crDNA/crDNA cross-links; this event entails a de-condensation of the mucin layer, which returns into its initial conformation and releases the loaded drug (**Figure 33d**).

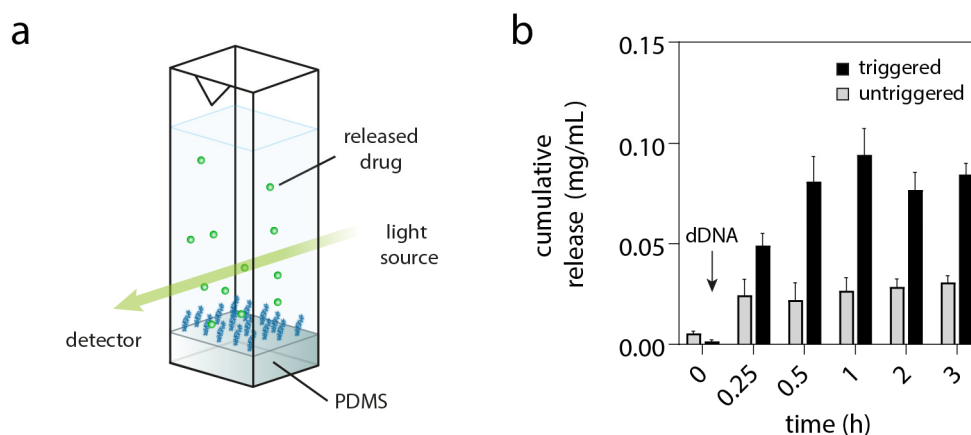


**Figure 34: DNA-based drug release from mucin coatings.** Self-complementary, thiolated DNA sequences are used to crosslink mucin polymers (a). By adding a suitable displacement DNA, the release of tetracycline can be triggered (b). The error bars represent the standard deviation as obtained from  $n = 3$  independent samples.

For a quantitative assessment of the drug release kinetics in macroscopic experiments, a spectroscopic detection method is employed (**Figure 34a**). Here, tetracycline (TCL), a broad-spectrum antibiotic, is selected as a model drug. Indeed, TCL release is successfully initiated by the DNA trigger (**Figure 34b**, black bars). Moreover, the release process is quite fast as we find a plateau in the release profile after 0.5-1 h.

In contrast, in the absence of this trigger (*i.e.*, when DNA strands with a ‘wrong’ sequence – so called control-DNA/coDNA – are added), only a small amount of initial TCL release is detected (**Figure 34b**, grey bars), which could be attributed to loosely bound TCL molecules that have not been entrapped well into the mucin layer. Further control measurements demonstrate both, the necessity of both, conducting the glycerol condensation step and stabilizing the condensed mucin layer (see *Appendix Table C3*).

### 5.3.3 A physiologically compatible trigger for large scale applications

Although the DNA triggered release mechanism discussed so far allows for a precisely defined starting point of the drug release, it is not very suitable for large scale applications: medical implants typically have a relatively large surface area that would need to be coated, which requires relatively large amounts of (rather costly) synthetic crDNA. Moreover, supplying suitable (synthetic) dDNA strands to trigger drug release is very difficult – if not impossible – *in situ*, *e.g.*, when a coated implant is inserted into the human body. In the next step, it is therefore aimed at replacing this DNA based release system with a practically more feasible and physiologically more compatible mechanism. In complete analogy to the strategy applied above, cationic cross-linkers, *e.g.*  $\text{Ca}^{2+}$ , could be used to stabilize the condensed mucin layer. However, in a biological context, calcium ions are not a good choice since cell signaling can be easily affected by this cation. Thus, it is crucial to find a different, suitable cationic cross-linker that stabilizes mucin particles even after glycerol is removed but allows for opening up the condensed mucin layer by a physiological trigger, *e.g.* exposure to a body fluid.

Magnesium ions appeared to be suitable for this purpose. Magnesium is the second most abundant cellular cation after potassium. Compared to other ions, the gradual release of low concentrations of  $\text{Mg}^{2+}$  ions into the human body should not influence physiological processes<sup>320-322</sup>; thus, this cationic cross-linker is a good candidate for a biocompatible delivery setting. Due to its small atomic radius, magnesium ions can compete with other divalent ions for specific binding sites and form bridges with negatively charged molecules<sup>323</sup>.

Using dynamic light scattering, it is found, that magnesium ions - similar to  $\text{Ca}^{2+}$  ions and PLL<sup>324</sup> – are able to stabilize condensed mucin particles even after glycerol is removed again. As increasing the ionic strength in the medium will induce Debye screening, it is hypothesized that the ensuing weakening of electrostatic interactions could be sufficient to induce de-condensation of the mucin particles. And indeed, if those ionically stabilized mucin particles are exposed to a physiological NaCl solution, it is observed that the stabilizing effect of  $\text{Mg}^{2+}$  diminishes and the mucin molecules turn back into a rather elongated conformation (**Table 3**). This magnesium induced semi-stable state has one crucial advantage, as it can be used as a smart trigger, that allows to open up those mucin particles when they come in contact with the human body.

**Table 3: Temporary stabilization of condensed mucins with magnesium ions.** The error depicts the standard deviation as obtained from  $n = 3$  independent samples.

solvent	peak 1		peak 2		peak 3		PDI
	size (nm)	(%)	size (nm)	(%)	size (nm)	(%)	
H <sub>2</sub> O	281 ± 60	96	55 ± 37	4	-	-	0.25
150 mM NaCl	546 ± 208	69	95 ± 50	27	> 1000	4	0.59

Consequently, in the next step, this approach is transferred to the surface-bound mucin layer, as introduced above. As observed for mucin particles, Mg<sup>2+</sup> ions are suitable for stabilizing a condensed mucin layer after glycerol removal and increasing the ionic strength in the medium induces de-condensation of the mucin layer (see *Appendix Figure C8b*). Indeed, when a TCL-loaded, condensed, and stabilized mucin layer (see *Methods* section for details) is exposed to the physiological trigger solution, a release of the therapeutical agent can be observed after approximately 30 min. After about 2 h, the drug concentration in the fluid reaches a plateau value (**Figure 35a**, black bars). The release efficiency was found to be > 90 %, which shows the surprisingly high efficiency of the trigger mechanism. Furthermore, with the coated surface covering over 100 mm<sup>2</sup> (= cross-sectional area of the cuvettes used here), the loading capacity of TCL of the functional coating is calculated to be around 4.5 µg/mm<sup>2</sup>.

Control experiments demonstrate that, in the absence of the NaCl trigger, the Mg<sup>2+</sup>-stabilized mucin layer shows only negligible leakage: If the drug loaded layer is exposed to ultrapure water instead of a NaCl solution (this is supposed to simulate storage of the drug-loaded coating), the drug remains well trapped: for the course of several hours, baseline release due to leakage is less than 2 % (**Figure 35a**, grey bars). This excellent stability significantly outperforms the comparable result obtained with crDNA-stabilized layers and might be due to a higher cross-linking density achieved with the small Mg<sup>2+</sup>, which can bind to all anionic groups along the mucin backbone. Compared to that, crDNA can only bind to cysteine residues in the terminal ends of the glycoprotein, and those accessible cysteines are (at neutral pH) approximately 6-times less frequent than the number of anionic residues along the mucin backbone<sup>325</sup>. As for the DNA-based strategy, also here, a control group created without glycerol condensation (see *Appendix Table C4*) shows little to no drug release at all – even if the correct trigger is used. Again, this can be rationalized by insufficient drug incorporation into the mucin layer, which

is a consequence of the missing condensation step. Tetracycline, the antibiotic used for drug loading so far, exhibits a negative net charge at pH = 7.4. However, drug molecules can – of course – also be cationic or zwitterionic/uncharged. Mucin glycoproteins, on the other hand, carry both, anionic and cationic motifs; at neutral pH, anionic residues dominate, which provides the glycoprotein with an overall anionic character<sup>89</sup>. Based on this information, it can be asked whether or not a drug molecule with a cationic net charge can be loaded into and released from mucin layers in a similar way. To test this, the same set of experiments is now performed with vancomycin hydrochloride (VAN), which is positively charged at neutral pH and widely used in implantation operations to prevent post-operative infections.

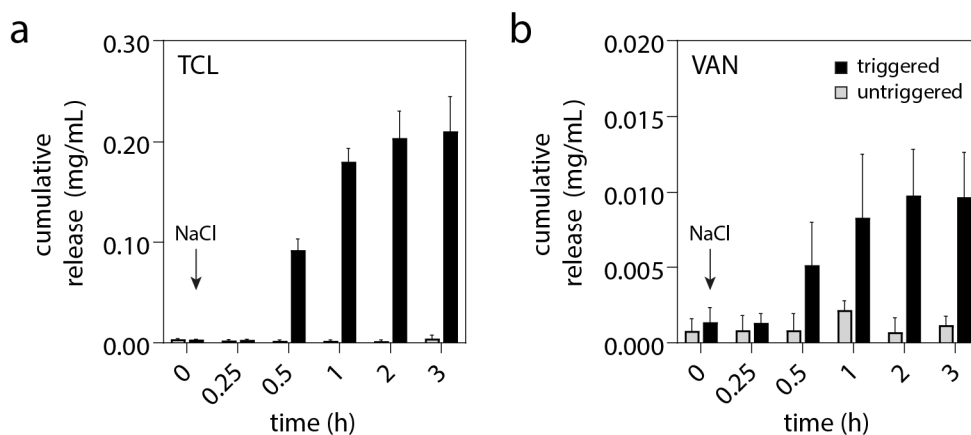


**Figure 35: Physiologically triggered release mechanism.** For TCL (a) and VAN (b), a release from the condensed mucin layer is observed as soon as the system is exposed to a physiological trigger. The error bars represent the standard deviation as obtained from  $n = 3$  independent samples.

Indeed, the results obtained with VAN-loaded mucin layers are similar to those obtained with TCL (**Figure 35b**). After exposing the system to the NaCl trigger, VAN release is observed within  $\approx 30$  min and saturates between 1-2 h (**Figure 35b**, black bars). From this data, the release efficiency of VAN can be determined to be  $\approx 47\%$ , which is lower than the corresponding value determined for TCL loaded surface coatings. This reduced release efficiency could be attributed to stronger electrostatic binding of the VAN molecules to the polyanionic mucin molecules than what could be expected for the anionic TCL. In the absence of the NaCl trigger, drug release is again very low (**Figure 35b**, grey bars). Also here, a similar control experiment as described above, *i.e.*, omitting the glycerol condensation step (see

*Appendix Table C5*) lead to layers where a stable drug loading is not achieved and – consequently – triggered drug release is not possible.

Together, the results discussed so far show that ionic cross-linking is a very efficient alternative for stabilizing condensed mucin layers, and that releasing both, cationic and anionic drug molecules from  $\text{Mg}^{2+}$ -stabilized mucin layers is very well possible by employing physiological salt solutions as a trigger. Similar to other local drug release strategies, the strategy applied introduced here may help reducing the application of systemic drug doses; this, in turn, would minimize the occurrence of unwanted side effects. For example, a conventional antibiotic treatment for tackling mild urinary tract infections induced by catheters comprises the systemic use of 500 mg of TCL every 6 h for a duration of 10 days<sup>326</sup>. Typical TCL serum and crevicular fluid concentrations that are achieved with such a systemic dosing are 3 – 4  $\mu\text{g}/\text{mL}$  and 5 – 12  $\mu\text{g}/\text{mL}$ , respectively<sup>327</sup>. Here, an antibiotic loading capacity on the coated surface of 4.5  $\mu\text{g}/\text{mm}^2$  was achieved. With this value, the local concentration of drug (released within 6 h after exposure of the coating to a body fluid) is estimated to be  $\approx 180 \mu\text{g}/\text{mL}$  (see *Appendix* for details). This concentration not only exceeds the serum levels achieved by a systemic drug administration – it is also well above the minimum inhibitory concentrations required to kill common bacterial pathogens responsible for urinary tract infections<sup>328</sup>.

#### 5.3.4 Variation of coating polymers and stabilizing ions

It seems, that three requirements are sufficient to obtain the controlled drug release mechanism described above: a surface-bound, charged macromolecule, the presence of a solvent, which promotes disaggregation of the polymer while also being a bad solvent, and an oppositely charged ionic crosslinker. To further challenge this hypothesis, it is now aimed to reproduce the same strategy applying other crosslinkers, condensation agents and coatings. When the same, mucin-based system is condensed with glycerol and subsequently stabilized with either zinc or iron (III) ions, a similar effect can be observed: Both coatings release their cargo immediately when they come in contact with a physiological salt solution (**Figure 36a, b**), however, the plateau value is reached notably faster compared to when the stabilizing step is performed using magnesium ions.

As both, zinc and iron (III) have the same or higher valence as magnesium, it is unlikely, that the charge density is responsible for the reduced stabilizing efficiency of those ions. However, it can be speculated that the larger radius of magnesium ions compared to zinc and iron (III) renders the bond between mucin and

magnesium slightly stronger as the increased distance might reduce electrostatic repulsion of the mucin molecules towards each other, thus retarding the release profile.

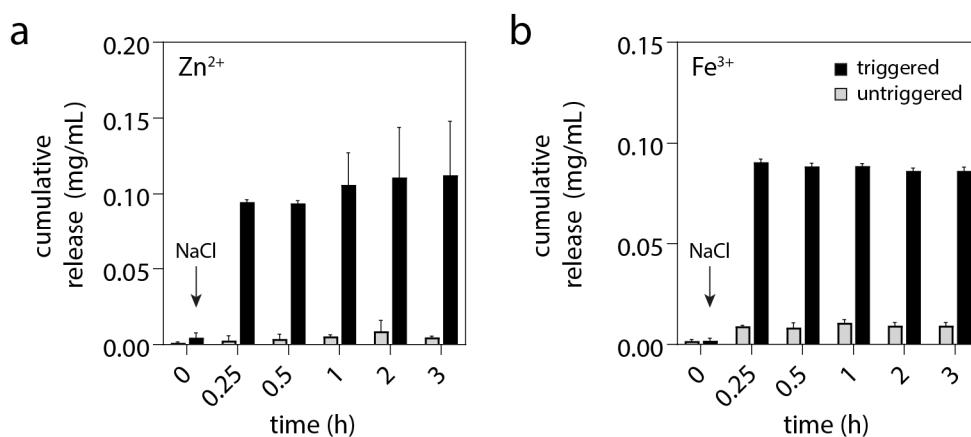


**Figure 36: Zinc and iron as stabilizing ions.** In both cases, when the condensed mucin layer is stabilized using zinc (a) or iron (III) ions (b), the release of entrapped TCL is initiated immediately when the system is exposed to a physiological trigger. The error bars represent the standard deviation as obtained from  $n = 3$  independent samples.

Having found, that also other ions can be used to stabilize the condensed mucin layer, it is now asked, whether or not also glycerol could be replaced by other, non-polar solvents. To test this, solubilized mucins are condensed using two other solvents, *i.e.* ethanol and hexane, and the hydrodynamic size and size distribution of the mucin particles is tracked *via* DLS.

As shown before, when mucin molecules are condensed in the presence of glycerol and magnesium, they form condensed nanoparticles with uniform hydrodynamic sizes (PDI = 0.25). When glycerol is replaced with either ethanol or hexane in the condensation step, mucin molecules still form condensed structures (approximately 65 % showed similar size distributions, see **Table 4**). However, the rest of the molecules formed large agglomerates and heterogeneous size distributions (PDI = 0.55 - 0.65, see **Table 4**). As mucins are poorly soluble in both, ethanol and hexane, it can be hypothesized, that those agglomerations rather arise from an insufficient disaggregation of the mucins in presence of the particular solvent. However, the details of the condensation process remain to be further investigated. In the case of immobilized mucins, disaggregation might play a minor role, thus – even if it might affect the release profile and the overall efficiency of the system – those other solvents could still serve as an alternative to glycerol.

**Table 4: Condensation of mucins using different non-polar solvents.** The error depicts the standard deviation as obtained from  $n = 3$  independent samples.

solvent	peak 1		peak 2		peak 3		PDI
	size (nm)	(%)	size (nm)	(%)	size (nm)	(%)	
glycerol	281 ± 60	96	55 ± 37	4	-	-	0.25
ethanol	360 ± 105	67	497 ± 765	23	> 1000	10	0.55
hexane	508 ± 295	66	521 ± 762	21	> 1000	13	0.65

In the third step, the mucin coating is replaced by other macromolecular coatings. Therefore, in addition to the glycoprotein mucin, an anionic polysaccharide (carboxymethyl dextran) and two polycationic molecules, *i.e.* chitosan (polysaccharide) and PLL (polypeptide) are chosen.

For carboxymethyl (CM) dextran and chitosan, a carbodiimide -based coupling strategy similar to mucin is chosen (see *Appendix B* for details). PLL is coupled *via* click chemistry reactions (see *Materials and methods* for details). As condensation agent, glycerol is used for all macromolecular coatings. The anionic CM dextran will – similar to mucin - be stabilized using magnesium ions, whereas divalent sulfate ions are chosen to stabilize the two polycationic molecules. Indeed, when a drug-loaded, condensed and stabilized CM-dextran layer is exposed to a physiological salt concentration, the release of the drug starts after approximately 30 min. The cumulative drug release reaches its plateau value after circa 1 h (**Figure 37a**).

Also for both cationic coatings, the mechanism seems to work perfectly fine. Both coatings release their cargo after exposure to a sodium chloride solution, and they also reach similarly high plateau values. Compared to the immediate burst release, that can be observed for the chitosan-based system (**Figure 37b**), the drug release is slightly retarded when PLL is used (**Figure 37c**). It can be speculated, that this effect is either due to the different charge densities of chitosan and PLL or originated in the slightly different composition of the pre-coatings. Nevertheless, those additional experiments (**Figure 37d**) show clearly the versatility and power of the mechanism developed here; as long as the three basic requirements (ionic polymer coating, condensation agent and oppositely charged ionic crosslinkers) are fulfilled, the strategy can easily be transferred to other systems.

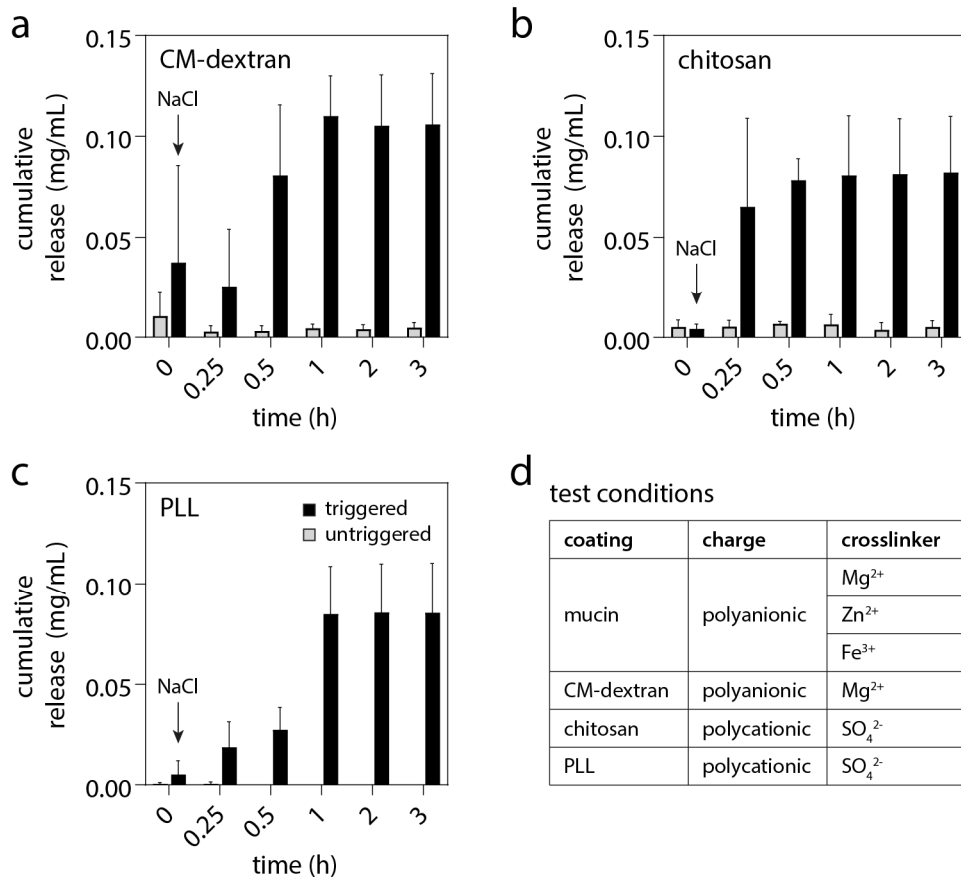


**Figure 37: Triggered antibiotic release from different surface-bound macromolecules.** The strategy applied for surface-bound mucins is transferred to three other macromolecular coatings, *i.e.* CM dextran (a), chitosan (b) and PLL (c). By stabilizing them in a condensed state using oppositely charged ionic crosslinkers (d), TCL can be entrapped in the polymer layer until a physiological salt concentration is introduced. The error bars represent the standard deviation as obtained from  $n = 3$  independent samples.

~ ~ ~

### 5.3.5 Controlled two-step release from a mucin multilayer construct

So far, the strategy presented here allows for the controlled release of a single dose of a given drug. To efficiently deal with a local infection after surgery, providing a single dose of an antibiotic may, however, not always be enough as infections can also reoccur at later time points. With the DNA-based strategy, it is in principle possible to program a system such that two consecutive release events occur<sup>318</sup>; yet, this release avalanche would then be initiated by the same trigger, *i.e.*, the second dose would always be provided if the first release process is triggered. Ideally, a “smart” release system would decide on its own, whether or not releasing a second dose of antibiotic is necessary and then provide the second dose only when required. Thus, for the remainder of this thesis, it is further aimed at adjusting the mucin-based release system such that exactly such a scenario is made possible.

In detail, a layer-by-layer approach is introduced where two different trigger strategies are combined such that they can lead to two distinct, independent release events: The NaCl-triggered drug release from a Mg<sup>2+</sup>-stabilized, condensed mucin layer is maintained but this particular mucin layer is relocated on top of a mucin-based multilayer system (**Figure 38a**, *drug reservoir 1*). Below this top mucin layer, two additional mucin layers are introduced, the lower of which is covalently attached to the substrate and loaded with the same drug as the top mucin layer (**Figure 38a**, *drug reservoir 2*). However, different from what was discussed so far, now, drug release from this bottom layer is prevented by covering it with several additional coatings. To gain access to these drug molecules, the upper layers need to be removed, and this event should only occur if the body requires a second drug dose. Mechanistically, it was aimed to employ a physiological stimulus associated with an inflammation event to serve as a trigger for this second, optional drug release event: an elevated temperature does not only occur globally in the human body as fever ( $\approx 40$  °C) but also locally as a typical body reaction to inflammation – and both phenomena can be triggered by an implant-mediated infection<sup>329,330</sup>. To construct such a temperature-sensitive system, the multilayer coating is designed in a way that it is disassembled when the local temperature is increased.

To construct a multilayer system which can be disassembled by a decrease in temperature, a combination of mucin/lectin interactions and thermoresponsive liposomes is chosen. Previous studies showed that lectin-stabilized mucin multilayers can resist a wide range of physiological pH and salt concentrations<sup>221,331</sup>, but can be disassembled very well by exposure to N-acetyl-D-glucosamine

(GlcNAc)<sup>167,332</sup>. Here, GlcNAc-loaded liposomes are incorporated into the system by storing them in a middle mucin layer, which is sandwiched between the drug-loaded bottom and top mucin layer. The liposome composition is chosen such that the liposome membrane becomes leaky at typical ‘fever’ temperature (see *Appendix Figure C9*)<sup>333</sup>. The central liposome-loaded mucin layer is connected to the bottom mucin layer *via* lectin cross-links, and to the top mucin layer *via* dopamine cross-links (**Figure 38a**). For this purpose, dopamine is a useful cross-linking agent as it can efficiently bind to various substrates; accordingly, it was already successfully employed in layer-by-layer assemblies<sup>334,335</sup>. Furthermore, its connection to the neighboring mucin layers is expected to be stable towards both, exposure to NaCl and elevated temperatures.

To verify the successful formation of this multilayered mucin system, the system is assembled from fluorescently labeled mucins using three different dyes, *i.e.* fluorophores emitting in the red, green and blue spectrum (see *Materials and Methods*). For the formation of each layer, a differently colored mucin is used – red for the covalently bound bottom layer, green for central mucin layer and blue for the top mucin layer, which will later be condensed by glycerol. Microscopy images obtained with those labelled mucins indeed confirm the presence of all three mucin layers when the complete assembly process is conducted (**Figure 38a**).

Moreover, the correct assembly of the full 5 -component multilayer is supported by QCM-D measurements (**Figure 38b**). Here, sequential injection of the different molecules entails a stepwise frequency shift indicating successful adsorption events. The recorded frequency signal shows, that indeed three mucin layers can be deposited onto the PDMS surface by connecting them to each other using either lectin or dopamine. Interestingly, exposing the multilayer construct to a physiological NaCl solution induces a slight frequency shift (**Figure 38b** and *Appendix Figure C10a*), which can be attributed to a conformational change of mucin molecules from a rather extended state to a more condensed state.

However, since this event is fully reversibly, this data demonstrates, that the full multilayer is still present when the NaCl is removed. In contrast, when the system is exposed to a GlcNAc solution, an irreversible increase in the recorded resonance frequency is detected (**Figure 38b** and *Appendix Figure C10b*) which indicates a permanent loss of adsorbed mass. This result is in full agreement with the expectation, that the lectin/mucin cross-links are opened by exposure to GlcNAc, and that the middle and top mucin layers (together with a fraction of the lectin

molecules used to connect them to the bottom mucin layer) are successfully detached.

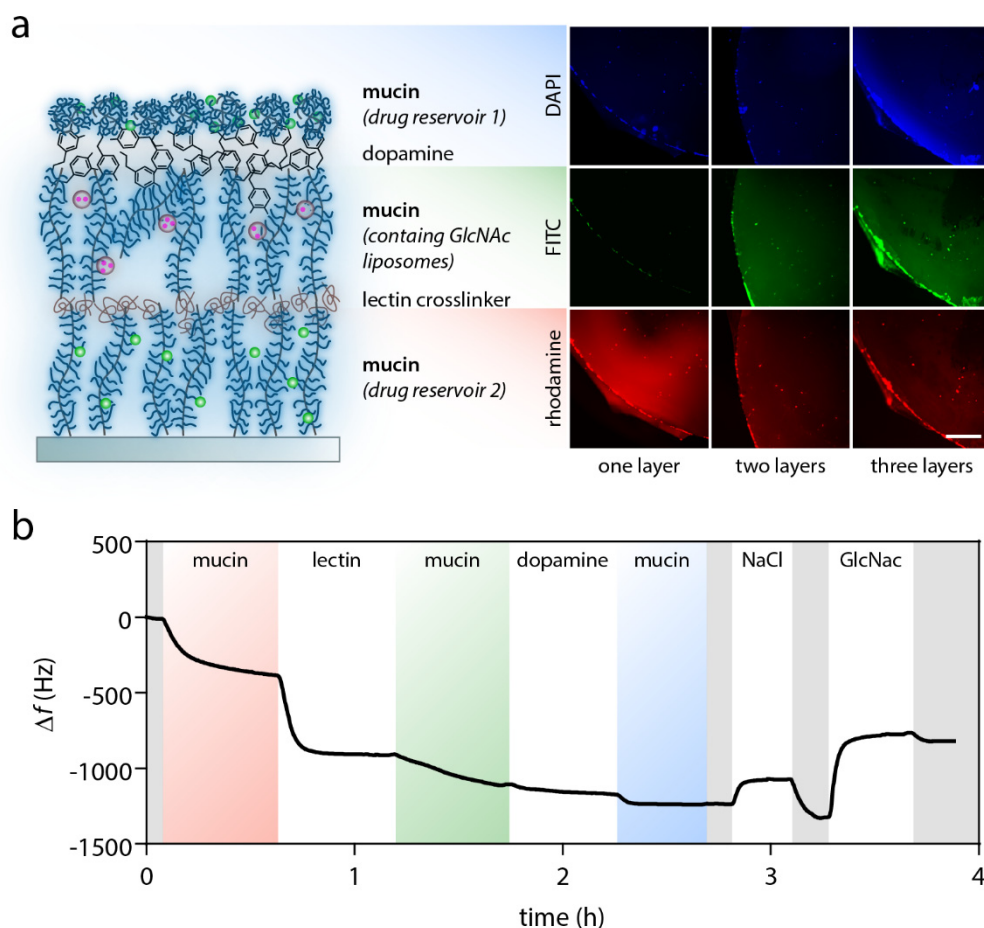


**Figure 38: Assembly of the mucin multilayer system.** The bottom mucin layer is covalently attached to the PDMS substrate via EDC chemistry and serves as a depot for an antibiotic. The second mucin layer is attached to the bottom mucin layer *via* lectin crosslinking and holds the third mucin layer (placed on top of the construct) *via* dopamine cross-links. This top layer is condensed and carries drug molecules again. Thermoresponsive liposomes loaded with GlcNAc are embedded into the middle mucin layer and release the GlcNAc at elevated temperatures (as they occur during inflammation). The released GlcNAc displaces the lectin cross-links thus inducing lift-off of the two upper mucin layers. The system was rinsed with the buffer in the time periods marked with the grey background.

Having verified both, the correct assembly and on-demand disassembly of the multilayer construct, in the last step the functionality of this multilayer system with regard to drug release is assessed. Before testing the whole construct, triggered drug

release experiments are conducted with simplified versions of the multilayer to ensure, that it is indeed the GlcNAc-mediated disassembly of the multilayer that leads to TCL release from the bottom mucin layer (see *Appendix Figure C11* and *C12*). To allow for an unambiguous interpretation of the results, those control experiments are conducted with multilayers where TCL is only incorporated in the bottom mucin layer. As expected, in both cases TCL release from the multilayer construct is observed once the GlcNAc trigger occurs – whether GlcNAc is added externally (see *Appendix Figure C11*) or released from embedded thermo-responsive liposomes upon temperature increase (see *Appendix Figure C12*).

Finally, a triggered release of two consecutive doses of TCL from a multilayer construct is attempted, where both, the bottom and top mucin layer are loaded with the drug. Now, TCL release from the top mucin layer should be triggered as soon as the construct is brought into contact with a physiological NaCl concentration whereas release from the bottom layer is supposed to occur only when a temperature increase occurs. And indeed the full construct shows the expected behavior: In the absence of the two triggers, virtually no drug leakage from the multilayer is detected and the system is stable for a three days (see *Appendix Figure C13*, black circles). Moreover, TCL release from the condensed top mucin layer can successfully be initiated by exposing the system to a physiological salt solution, and the release profile reaches a stable plateau after 2 h. Later, the second release event can be triggered by increasing the incubation temperature from 37 to 40 °C. Also here, the system reaches a stable release plateau after approximately 2 h (**Figure 39a**, full circles). In the control group, where thermo-responsive liposomes were incorporated into the multilayer construct without carrying a GlcNAc cargo, this second release event does not occur (**Figure 39a**, empty circles). This result further underscores that the multi-component system operates exactly as planned.

~ ~ ~

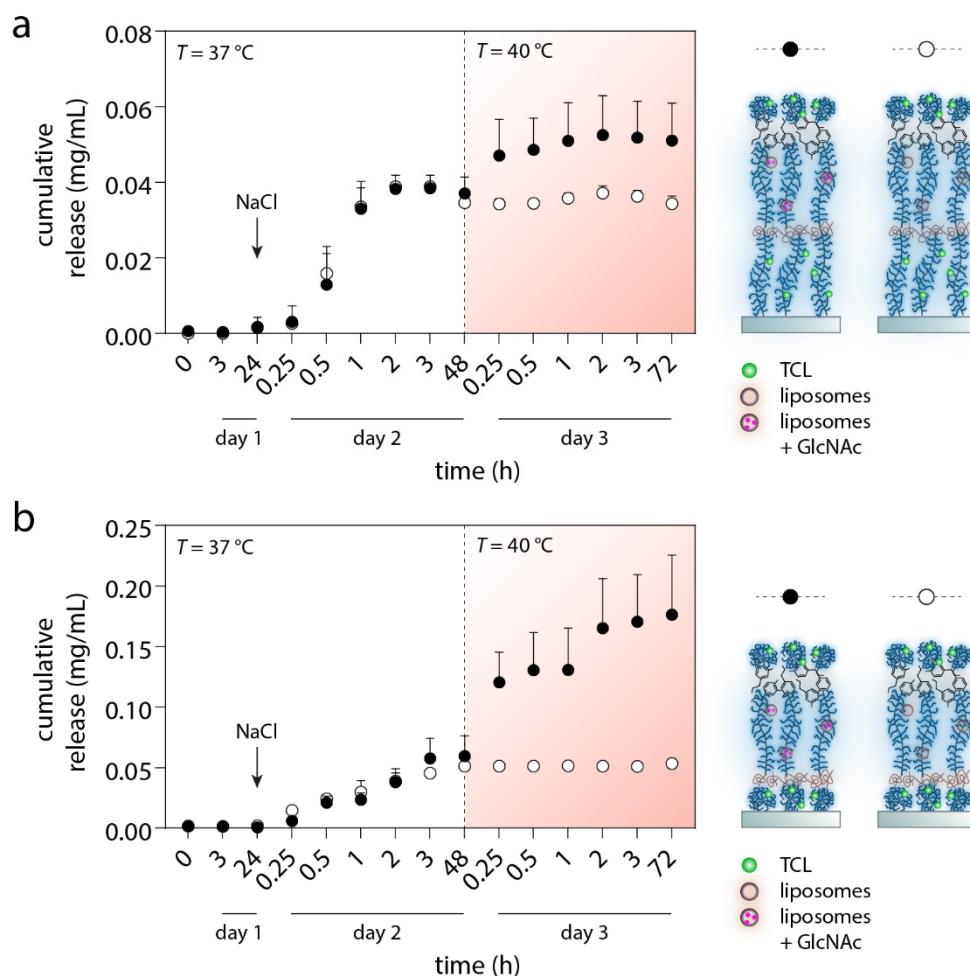


**Figure 39: Consecutive release of two TCL doses from the multilayer construct.** Multilayers are assembled in two variants, *i.e.*, with the bottom mucin layer in an uncondensed (a) and condensed state (b), respectively. Schematic representations of the respective multilayer systems including two TCL depots are shown on the right, time-dependent release of TCL from the multi-layer constructs on the left. Filled symbols represent samples comprising GlcNAc loaded thermoresponsive liposomes whereas empty symbols show data from a control group containing empty liposomes. Please note the different y-axis ranges in (a) and (b). Error bars denote the standard deviation as obtained from a minimum of  $n = 3$  independent samples.

However, compared to the first release event, the TCL dose released after the second trigger is rather small. This might be caused by insufficient trapping of TCL into the bottom mucin layer, which was not condensed. Thus, it is tested if this second release event can be improved by applying a last, small modification to the system, *i.e.*, by condensing the bottom mucin layer prior to generating the multilayer

system. Indeed, with this adjusted strategy, a remarkable increase in the temperature-triggered second TCL dose from  $\approx 0.02$  mg/mL to  $\approx 0.12$  mg/mL is achieved (**Figure 39b**, full circles). Again, a control group, where empty thermoresponsive liposomes (without a GlcNAc cargo) are incorporated into the system exhibits no drug release upon temperature increase (**Figure 39b**, empty circles). In the absence of the two triggers, TCL leakage is virtually absent (see *Appendix Figure C13*, grey circles). Together, these additional results demonstrate that the system we introduce here is very well reproducible, stable and allows for easily tuning the amount of stored/released drug.

## 6 Summary and outlook

The first part of this thesis pinpointed the outstanding properties of macromolecular lubricants in different scenarios. In the framework of those experiments, a custom-made oscillatory tribology setup was developed, that complements a commercial rotational measuring unit. Example studies in the fields of food engineering and cartilage tribology were conducted and the abilities of macromolecular lubricants to reduce both, friction and wear formation were highlighted. As one particular example, the possibilities and limitations of mucin solutions were further investigated in detail to gain a deeper understanding of the mechanisms that underlie macromolecular lubrication.

In the second part, macromolecules were immobilized onto technical polymer surfaces in the form of polymer-brush coatings. In this context, a multi-step coating process was developed that allows to covalently bind mucin glycoproteins onto a variety of medically relevant polymer materials. It was shown that this coating strategy is capable of creating mechanically stable mucin layers, which can further resist a broad range of physiologically relevant environmental conditions. Moreover, this thesis demonstrated that surface-bound macromolecules can interact with other solubilized macromolecules and that these interactions are mostly of steric nature, *i.e.* entanglement, and less governed by electrostatic effects.

The third part of this thesis continued in the field of macromolecular coatings; however, the viewpoint was shifted from lubrication to creating coatings, that interact directly with their environment. To underline the tuneability of macromolecular coatings, a platform was presented that allows for investigating the selective binding properties of macromolecules in a porous PDMS sponge. Furthermore, it was shown that the mucin coating presented before also exhibits intrinsic anti-biofouling properties, *i.e.* it reduces the undesirable deposition of proteins, bacteria and fibroblasts. Finally, a strategy is presented, how polymer-brush coatings can be loaded with antibiotic drugs and that the drugs remain entrapped inside the polymer layer until the layer is exposed to a physiological salt concentration. By applying a multilayer approach this strategy was complemented with a second antibiotic reservoir, which liberates antibiotics only as a response to reoccurring inflammations.

Combined, the three aspects of this approach, *i.e.* reduction of friction-induced inflammations, intrinsic anti-fouling properties, and the controlled release of anti-

inflammatory or antibacterial drugs build a strong foundation for controlling device and implant-associated health care-associated infections (HCAIs). Moreover, this approach is extremely versatile as all strategies presented here can also be applied using different macromolecules on different substrates or different drugs. Although the ideas and findings presented in this thesis show promising potential to be transferred from the level of academic research to clinical application, a few improvements and further ideas could still increase both, efficiency and applicability.

One question that typically arises when working with biomacromolecules is: “*Can they be totally replaced by synthetic polymers?*” This question is particularly important for two aspects; firstly, the production of synthetic molecules in industrial volumes is mostly less expensive than the purification of biological ones. Secondly, the ingredients can be better controlled; whereas purified biomolecules are typically assigned to the highest risk class for clinical approval<sup>336,337</sup> and often fail approval due to undefined amounts of impurities, these problems are less pronounced for synthetic molecules. Coming back to the question: “*yes or no?*”, it has to be answered with a disappointing: “*it depends*”. It depends on two points: Is it fully understood, which parts of the biomolecule are responsible for the effects observed, and can these parts be synthetically copied?

In the case of mucin, both questions have to be answered with “*no*”. Although this thesis sheds some additional light on the mechanisms that govern the multiple functionalities of the mucin molecule, many aspects still remain in the dark. Especially regarding their physiological activity and their immunomodulating properties, a lot more research needs to be conducted in the future. Creating a synthetic molecule, which exclusively comprises those components of mucin that are required for a particular application, has only been attempted for some specific applications<sup>338-340</sup>. However, synthetically recreating the whole mucin molecule is not possible yet. Until now, the only alternative to the purification of mucins from animal tissue is to express mucins recombinantly. Although a few attempts were made<sup>341,342</sup>, the use of expensive eukaryotic cell lines is required, which drastically lowers the applicability, yield and profitability of these processes.

For other cases than mucin, however, the two questions can often be answered with “*yes*”. For example, to obtain lubricious macromolecular coatings, it is known, that just a few requirements have to be fulfilled: To allow for efficient hydration lubrication, the macromolecules have to be highly hydrated and water should be bound strongly to the molecules; especially the latter requirement is very well

fulfilled for ionic or – in the best case – zwitterionic molecules<sup>17-19,21,343</sup>. Ideally, the molecule can be coated to the surface in a brush-like manner to achieve optimal coating density and surface separation<sup>17,150,151,343,344</sup>. This is in total agreement with the results presented in this thesis, as here two synthetic macromolecules, namely PEG and PLL, performed similarly well as lubricious coatings as the biomolecule mucin. Still, this is a rather one-sided point of view to look at this problem, since both molecules have their drawbacks: whereas PEG is rather prone to degradation in biological media<sup>116-122</sup>, PLL requires a more complex (and toxic) coupling chemistry to obtain a brush-like coating.

Assuming that the question of whether synthetic polymers can be used for the desired field of application, can be answered with a “yes”, are there further advances and developments that are imaginable? Two of the fields discussed in this thesis, *i.e.* the generation of a lubricious coating and achieving intrinsic anti-biofouling properties both critically depend on one parameter: the coating density. However, the use of charged, brush-like molecules, although favorable for a high water-binding affinity, causes limitations in the achievable coating density, as they tend to repel each other either *via* steric or electrostatic repulsion (or both). To tackle this problem, promising strategies have been developed before<sup>345</sup>. Instead of coupling the whole macromolecules directly to a surface (“*grafting to*”-method), small initiator molecules are attached to the surface, which, due to their small measures, do not repel each other that much. These initiators are then used to polymerize the macromolecule directly on the surface (“*grafting from*”-method). By ensuring a unidirectional growth, perfectly shaped brush coatings with a low polydispersity can be achieved. Using the “*grafting from*”-approach, macromolecular monolayers have already been generated with both, extremely high molecular weights of the brush polymers ( $M_w > 1$  MDa) and super high density (around 2 nm distance between the anchoring points<sup>346,347</sup>).

Although techniques to create polymer layers by the “*grafting from*”-approach have been initially designed for the development of new semiconductors, they have found their way into the field of biomedical engineering. In this context, PEG-based anti-biofouling coatings have been generated on different substrates *via* surface-initiated controlled radical polymerization (SI-CRP), including gold<sup>348</sup>, silicon<sup>349</sup>, titan<sup>350</sup> and PDMS<sup>351,352</sup>. Furthermore, some approaches exist, that generated zwitterionic anti-fouling brushes by using the same SI-CRP strategy. However, those have been limited to gold and silicon substrates<sup>353</sup>. A few studies even reported an application for low friction surfaces, but also those are limited to silicon

substrates and their applicability for a biomedical scenario still needs to be investigated<sup>354-357</sup>.

Further development of such “*grafting from*”-methods, seems to be promising to optimize the findings of this thesis. In one possible scenario, it could be hypothesized to use “*grafting from*”-methods to generate a super-dense and hydrated base-layer, which allows for the attachment of further functional groups in subsequent steps. Organic chemistry, therefore, offers a variety of functional groups including hydrocarbons, compounds containing oxygen as heteroatom, nitrogen-based groups, or carbonyl compounds. If it were possible to attach such reactive groups as a terminal group to the surface grown polymer brush, this would allow to specifically modify the base coating with other functional molecules, *e.g.* antimicrobial peptides, specific ligands or growth mediators.

However, several steps need to be accomplished and problems, such as (degradation) stability, applicability, or toxicity need to be solved. Until now, biomacromolecules like the mucin glycoprotein offer an extremely good trade-off. Also, as mucins can be purified from tissues which are typically not further processed as butchery products, the use of these waste products for protein purification can – at least to a certain degree – be considered an environmentally friendly and sustainable approach. Yet, the development of mucin-based biomaterials is far from having reached an end. Improvements in the purification of mucins<sup>93,315</sup>, the understanding of the influence of mucins on physiological processes<sup>358-363</sup>, and the chemical modification of mucins<sup>89,364</sup> keep pushing mucin-based materials forward towards clinical application – despite their biological origin – following the role model of hyaluronic acid.

## Appendix

### Appendix A: Purified porcine gastric mucin\*

As mucin glycoproteins play an important role in the context of this thesis, their origin, purification, and quality are discussed in detail in the following sections.

#### Comparison of manually purified and commercially available mucins

In principle, there are many options for harvesting crude mucus from which mucins can be purified. Traditionally, as commonly adopted for commercial purposes, pigs and cows have served as the main sources for harvesting mucus, and both porcine gastric mucin MUC5AC (PGM) as well as bovine submaxillary mucin MUC5B (BSM) have been extensively used in many studies.

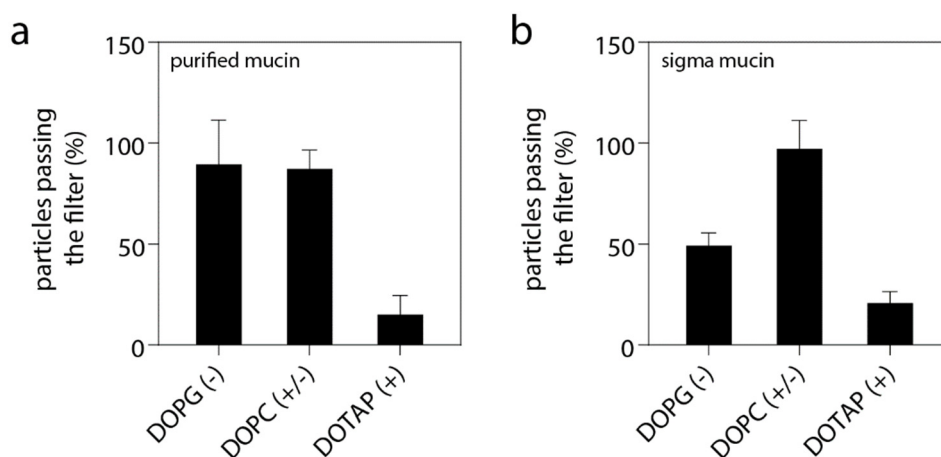


**Figure A1: Charge selectivity of commercial mucins.** Compared to manually purified mucins (a), commercial PGM exhibits not only a strong affinity towards positively charged test particles but also to negatively charged ones. Error bars denote the standard error of the mean as obtained from 3 independent filter realizations.

Unfortunately, mucin research is still limited by the availability of such functional mucins. Although the poor quality of commercial mucins has been documented<sup>193,94,365</sup>, commercial mucin products have been largely applied in

---

\* This section follows in part the publication Winkeljann *et al.*, *Macromolecular Bioscience* (2017), the book chapter: "Advances in Mucin Biopolymer Research: Purification, Characterization and Applications" by Marczynski *et al.* in "Advances in Biopolymers for Biomedical and Biotechnological Applications" by Rehm and Moradali, Wiley-VCH (2020) & the patent application Marczynski *et al.*, (2020)

numerous studies by different research groups. It is likely that harsh conditions during industrial purification processes can damage the mucin glycoproteins leaving corrupted molecules with altered physio-chemical properties. The important task of the mucus barrier, for example, is at least partially originated in its strongly polyanionic character. However, using the filtration device established here, it can be shown, that that commercial mucin, compared to manually purified mucin exhibits a strong affinity to negatively charged test particles (**Figure A1**). These observations suggest, that this difference in charge affinity is due to damages in the glycosylation pattern which are likely to result from the commercial purification process. If this glycosylation pattern were to be incomplete, the protein backbone of the commercial mucin glycoprotein would be exposed – and this backbone carries many amino acids, which can be positively (lysine, histidine, and arginine) or negatively (glutamic acid, aspartic acid) charged at neutral pH.

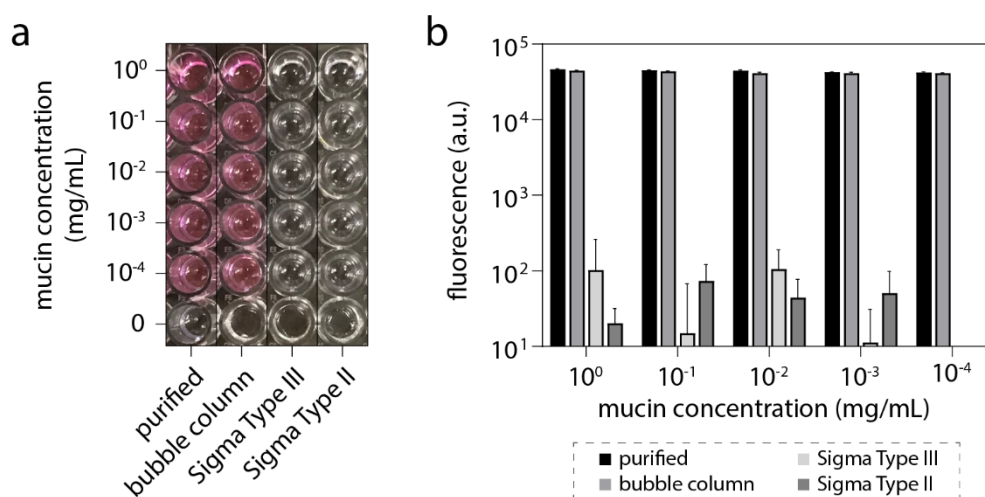


**Figure A2: Detection of mucin via antibody staining.** Manually purified mucins are clearly detectable via ELISA tests up to concentrations of 10<sup>-5</sup> % (w/v), whereas commercial mucin preparations only offer a weak noisy signal.

Furthermore, the detection of two commercial mucin variants (Type II and Type III, Sigma Aldrich) is tested via antibody staining (ELISA, as described in *Materials and methods*). Whereas the color reaction for manually purified mucins is clearly (even with bare eyes) detectable for mucin concentrations as low as 10<sup>-5</sup> % (w/v), commercial mucins hardly show more than a noise signal in the tested range of concentrations (**Figure A2**). Since the MUC5AC antibody used here specifically binds to a sequence in the non-glycosylated terminal region of the mucin backbone it can be assumed that those parts are either destroyed or – due to conformational

changes that might arise if the glycosylation is damaged – not accessible to the antibody. In either case, the results demonstrate, that commercial mucins useless as standards in molecular biological assays, *e.g.* in the analysis of clinical samples.

The most important property in regard to this thesis is the outstanding lubricity of manually purified mucin. Using the rotational tribology setup described in the *Materials and Methods* section, the lubrication performance of such manually purified mucins is compared to two types of commercial PGMs (Type II and Type III), to commercial BSM (Sigma Aldrich) as well as to a clinically used saliva substitute on mucin basis (*Saliva Orthana*). Whereas manually purified mucin can reduce the coefficient of friction in the boundary lubrication regime about two decades, commercial mucins hardly perform any better than simple buffer solution devoid of any macromolecules (**Figure A3a**).

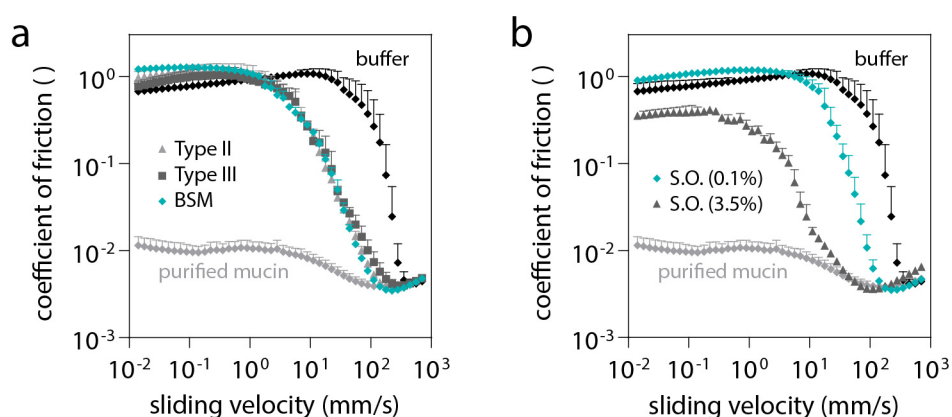


**Figure A3: Lubricity of commercial and purified mucins.** Manually purified mucins serve as excellent lubricants and can reduce the coefficient of friction in a steel on PDMS pairing about two decades. Different types of commercial mucins, however, hardly perform any better than an aqueous buffer.

Based on all the limitations of commercially available mucins, results obtained with such damaged molecules are questionable, at best.

### Optimization of the manual purification process for porcine gastric mucins

Although the purification process described by Schömig *et al.*<sup>93</sup> offers highly functional mucin glycoproteins, the yield is still rather low ( $\approx 100$  mg purified mucin per stomach) and the manual steps very time-consuming. All (medical) applications suggested in the context of this thesis, however, would require a scale-up for the purification of functional mucins to satisfy the demand. Thus, the

original purification process was further optimized to allow for a later commercialization.

The original protocol comprises a total of eight purification steps, including the mucus harvesting, homogenization, centrifugation, ultra-centrifugation, size exclusion chromatography (SEC), diafiltration and lyophilization (**Figure A4**).

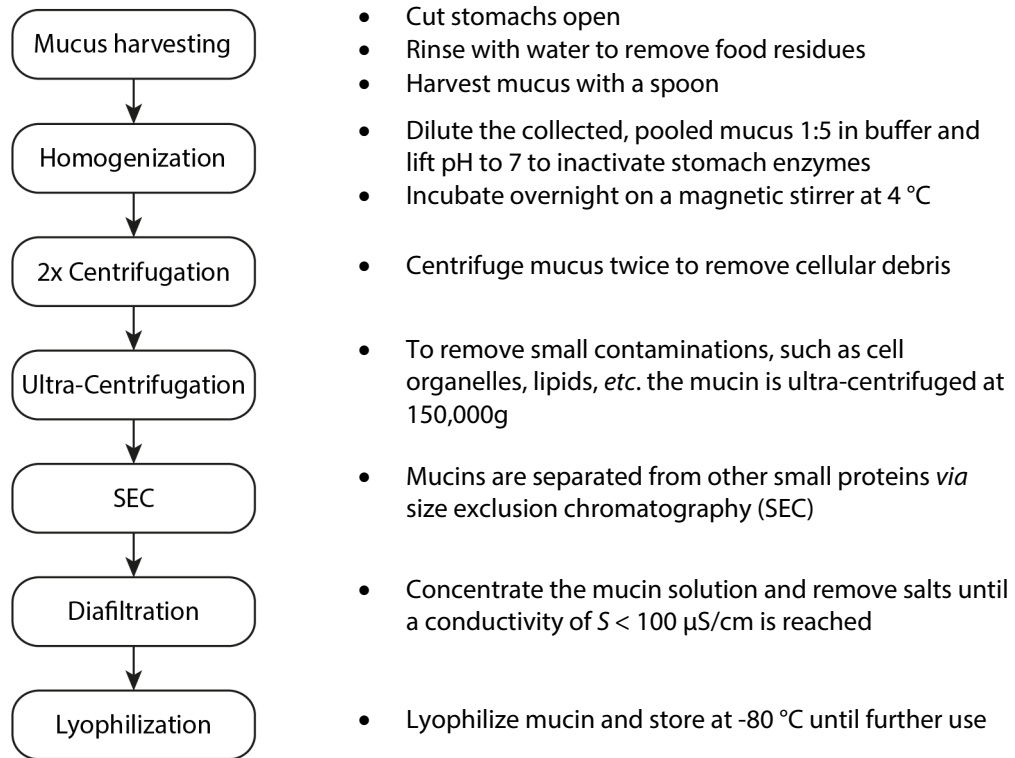


**Figure A4: Manual purification of porcine gastric mucins.** The manual purification process as described by Schömig *et al.*<sup>93</sup> comprises 8 steps until the final product is obtained.

Especially the harvesting, centrifugation and SEC are time and cost-intensive steps in the purification protocol. Therefore, it was aimed to reduce their impact on the whole purification process as much as possible. The first step was to replace the manual scraping of the stomachs with a semi-automatic system. Thus, a bubble column was established that allows for transferring the surface attached mucus in a buffered solution. The bubble column comprises a cylinder as main body element ( $h = 500 \text{ mm}$ ,  $d_i = 190 \text{ mm}$ ,  $d_a = 200 \text{ mm}$ ) with two flanges to attach bottom and top lid a bottom plate containing 5 regularly orientated holes ( $d = 3 \text{ mm}$ ) for gas supply

a bottom lid with a central G1/4 thread for gas supply a top lid containing a gas exit as well as a gas overflow filter with a collecting flask (**Figure A5**).

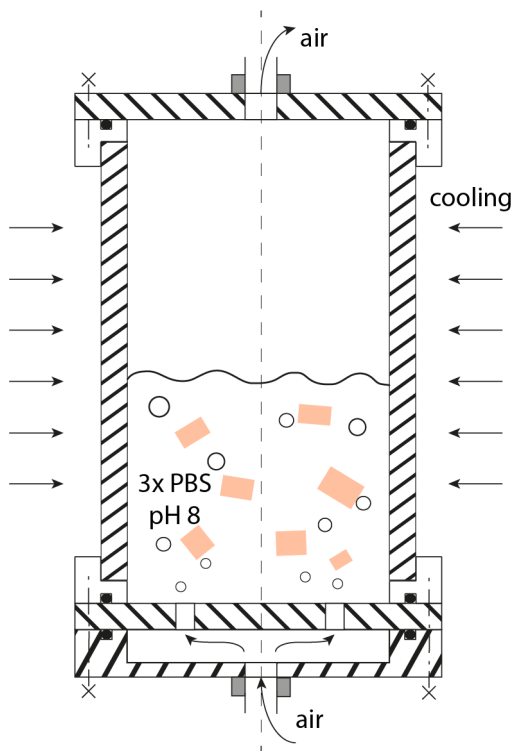


**Figure A5: Schematic illustration of the bubble column.**

An aerated bubble column comprising a cylindrical main body and bottom and lit with air supply and air outlet, respectively, was used to transfer mucus from the stomach internal surface into a buffered solution. The bubble column is cooled to 4 °C, while a continuous mixing of the stomach/buffer mixture allows for dissolving the mucus and, in parallel, a homogenization of the fluid. By decanting the fluid afterwards through a grid an easy separation of liquid and solid parts is achieved, which reduces the number of required centrifugation steps afterwards.

The bubble column was operated at 4 °C. Thus, the assembled bubble column was placed in a cold room and then connected to compressed air supply (oil-free, 10 bar) *via* a pneumatic clutch. Stomachs of freshly slaughtered pigs were cut into 6 pieces and placed into the bubble column. Then, pre-cooled (4 °C) 3xPBS (pH 8) was added to the porcine stomachs in a ratio of 2:1 (v/v) buffer to stomach pieces. The increased salt concentration of the buffer here was used for a better solving of the mucus since Debye Screening effects can reduce electrostatic interactions of the polyanionic mucin molecule with other charged contaminants. Furthermore, the pH level of the buffer was lifted to 8, since the aeration with carbon dioxide containing gases can lower the pH level over time. After the top lid of the bubble column was fixed and connected to the overflow flask *via* a pneumatic tubing, the gas flow was started carefully. The gas pressure was slowly adjusted to ≈ 3 bar using a manometer. Stomach pieces and buffer were mixed for ≈ 3 h before the gas supply was stopped. Then, the bubble column comprising the porcine stomachs and the mucin containing solution was decanted into a 10 L beaker using a grid to separate the liquid from the solid phase. However, the use of the bubble column not only

replaced the first and second step of the original purification protocol, it also drastically reduced the amount of cellular debris in the mucus homogenate. Thus, also the first two centrifugation steps can be omitted, and a single ultra-centrifugation step became sufficient to remove the remaining contaminants (also for the original protocol the two centrifugation steps can be replaced by simple filtration through a tea filter). In total, the amount of mucin purified using this method increased from initially 100 to about 300 mg per stomach. Further investigations also revealed that the crossflow filtration step of the original protocol was not sufficient to obtain a stable quality of mucins, especially regarding their lubricity. Therefore, first, the sodium chloride concentration was increased to 2 M to support the de-binding of contaminations attached to the mucin molecules *via* either hydrophobic or electrostatic interactions. Furthermore, the level for the minimum conductivity was lowered to  $S \leq 10 \mu\text{S}/\text{cm}$ . These additional modifications then led to a reproducibly high lubricity of those mucins. The detection by ELISA method returned similar results as for mucin purified according to the Schömig protocol (**Figure A2**), which suggests that the mucin molecule is intact.

However, since the development took place in parallel to the work of this thesis and it was difficult to obtain a reproducible lubricity of the bubble column purified mucins, the mucins used in this thesis were purified according to a modified version of the Schömig protocol, but without using the bubble column (see *Materials and methods*).

### **UV disinfection**

Since here it was not possible to purify mucins in a sterile environment, *e.g.* a clean room, the lyophilized mucins were often contaminated with bacteria or spores. Whereas these contaminations don't have a considerable impact when experiments are performed directly after the preparation of the mucin solution, experiments that include cells, are performed at elevated temperatures or are conducted over a long time can be significantly influenced. Thus, prior to every experiment, lyophilized mucin was disinfected using UV-light. Therefore, the lyophilized mucin was placed onto ice and then exposed under UV light for 30 to 60 min before it was dissolved in the water. To test the effect of the UV treatment on the contamination of the mucin samples mucin was UV treated for 30 min. Afterwards it was dissolved to a concentration of 0.1 % (w/v) in sterile PBS. Then, 200  $\mu\text{L}$  of mucin solution were pipetted onto either a minimal medium (MSgg) or a lysogeny broth (LB) growth medium enriched with glycerol and manganese (LBGM) agar plate and distributed

using a Drigalski spatula. The mucin solution was allowed to dry for 15 min before the agar plate was incubated at 37 °C for 4 days. After incubation plates were analyzed for the growth of bacterial colonies. For testing in a liquid environment, 200 µL of mucin solution were pipetted into a tube containing 10 mL of CASO liquid medium. The mixture was inoculated at 37 °C for two days and contamination was quantified *via* OD<sub>600</sub> measurement.

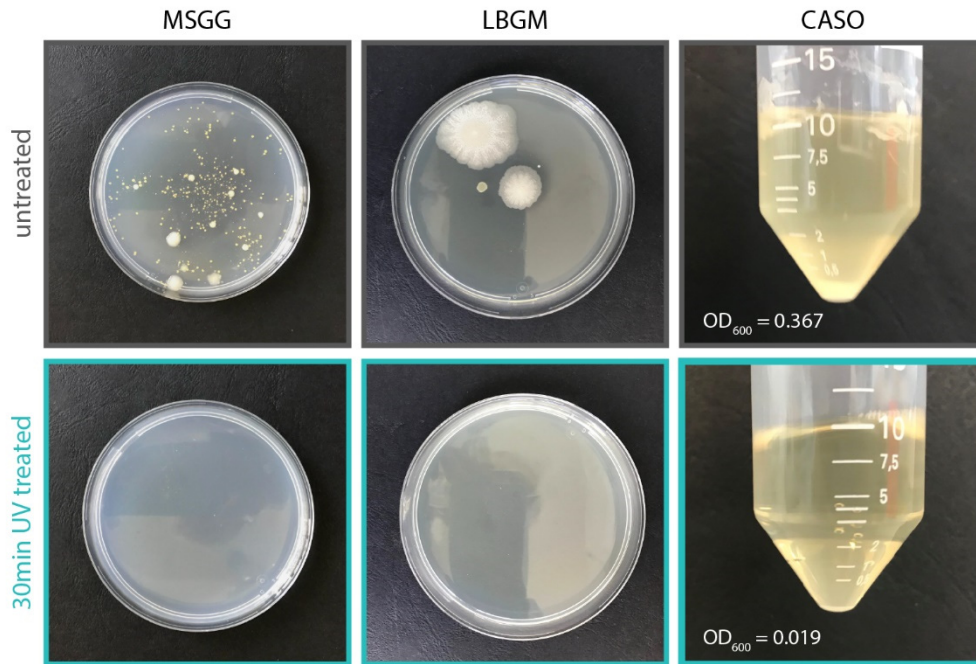


**Figure A6: UV treatment of purified mucins.** After 30 min of UV treatment, mucin samples show virtually no sign of bacterial contamination anymore neither when incubated on MSGG or LBGM agar plates, nor when inoculated in CASO liquid medium.

When agar plates are incubated with mucin solutions that haven't been exposed to UV light before they are strongly contaminated as indicated by a multitude of bacterial colonies grown on the agar plates. However, when mucins are exposed to a UV treatment that can be as short as 30 min virtually no sign of bacterial contamination can be detected on the agar plates. Also, when unsterilized mucin is inoculated in a liquid medium the medium turns turbid, indicating bacterial contamination. This observation is supported by an increased OD<sub>600</sub> value. In comparison, when mucin is UV treated before inoculation, the medium remains clear (**Figure A6**). These findings suggest that UV treatment indeed is a very effective tool to reduce contamination in mucin samples for laboratory tests.

However, it is clear, that further steps in the development of mucin-based medical products, *e.g. in vivo* studies, clinical trials *etc.*, will require a more detailed investigation of the sterilization.

## Appendix B: Additional methods\*

### Unconfined Compression tests

By means of unconfined compression using a cylindrical steel measuring head (PP8, Anton Paar), we determine compression moduli  $K$  of  $K_{\text{carrot}} = 2.8 \pm 0.7$  MPa and  $K_{\text{potatoe}} = 1.7 \pm 0.1$  MPa, respectively ( $n = 3$  for each sample type).

### Bread preparation

The ingredients for all bread samples were mixed at 25 °C for 5 min at 100 rpm in a laboratory mixing machine (DIOSNA, Dierks & Söhne GmbH, Germany). A basic formula for gluten-free batter was prepared by mixing 100 g of gluten-free flour, 120 mL water, 1.65 g of sucrose, 1.25 g salt and 2.10 g dried active bakery yeast. The time for mixing the flour was chosen such that the dough consistency reached a value of 500 Brabender units. Brabender units were determined using a Farinograph (Brabender Inc., Duisburg, Germany).

To prepare dietary fiber-fortified batters, 7.5 % (w/w) modified inulin, 7 % (w/w) resistant starch and 7 % (w/w) modified wheat bran were separately added to the gluten-free flour basis. 130, 145 and 150 g water per 100 g flour was added to the bread formulations containing inulin, wheat bran, and resistant starch, respectively.

All prepared batters were then transferred to the proofer and fermented for 180 min in a fermentation cabinet (250×10×10) mm<sup>3</sup> at 30 °C and a relative humidity of 86 %. For each bread sample, 100 g of the fermented batter was poured into a cylindrical shape mold made out of stainless steel ( $d = 50$  mm,  $h = 50$  mm) and baked in an oven at 200 °C for 30 min. After baking, the fresh bread loaves were sliced and placed in a sealed container for further analysis.

---

\*The methods presented here follow in part the publications Winkeljann *et al.*, *Biotribology* (2018), Kiumarsi *et al.*, *Food Chemistry* (2019), Winkeljann *et al.*, *Advanced Materials Interfaces* (2020), Winkeljann *et al.*, *Macromolecular Bioscience* (2017), Yan *et al.*, *Langmuir* (2018) & Kimna *et al.*, *Advanced Materials Interfaces* (2020)

## Food perception

Time-intensity (TI) evaluation was performed under normal lightening conditions at RT. The crumb slices were presented (1 cm thickness) on plastic dishes and served in a randomized order. Water was provided to drink between each sample for palate cleansing. The TI evaluation was carried out by ten trained panelists (5 males and 5 females, aged 20-35 years).<sup>366</sup> The attributes were evaluated using references (**Table B1**) and discussed with the panel group.

The TI determination of bread attributes, *i.e.* bitterness, firmness, chewiness, and dryness (see **Table B1** for description) was carried out 2 h after baking in four different sessions. The panelists were asked to move the cursor along the intensity scale (1-10 points) as the sensation evolved in the mouth until the end of perception. Then, the sensory parameters including  $I_{\max}$  (maximum intensity determined by the panelist),  $T_{i_{\max}}$  (time in which the maximum intensity was determined) and total duration time of perception ( $T_{\text{tot}}$ ) were extracted from the TI-curves.

**Table B1: Definition and references of perception parameters used in food engineering.**

Attribute	Definition	Reference
<b>Taste</b>		
Bitterness	Refers to caffeine in aqueous solution	Caffeine (0.3 g/dL)
<b>Texture/Mouthfeel</b>		
Firmness	Force required by the molar teeth to compress the food	Hard candy
Chewiness	Number of chews necessary for food to be swallowed	Hard taffy
Dryness	Dry property of a food bolus that causes a feeling of dryness in the mouth	Cracker

### **Contact angle measurements**

To determine the surface polarities of the different synthetic polymer materials before and after the mucin coating, contact angle measurements were conducted. Therefore, samples were first cleaned with 80 % ethanol and Millipore water. After drying the samples, a droplet of 8  $\mu$ L Millipore water was placed onto each sample, and a transversal image of the liquid-solid interface was captured using a high-resolution camera (Point Gray Research, Richmond, Canada). Then, the static contact angle value was determined using the software Image J and the “drop snake” plug-in.

### **Protein and particle adsorption**

Adsorption tests were conducted on samples inspired by so-called Janus's particles: For the experiments conducted here, cuboid samples (2 mm x 4 mm x 18 mm) were separated into three different zones each of which was coated differently. The top area remained uncoated, the central area was precoated with the silane precursor, and the bottom area received the full two-layer coating, i.e., precursor and mucin. To test the antiadhesive properties of the coatings, a set of 5 to 7 Janus inspired plates (JIPs) was inserted into a 5 mL laboratory tube filled up with a 20 mM HEPES solution containing either 0.1 % (w/v) of fluorescent proteins (BSA, lysozyme) or red fluorescent polystyrene (PS) nanoparticles ( $d = 300$  nm, either aminated or carboxylated, Invitrogen, Thermo Fisher Scientific).

While protected from light, the tube containing the JIPs was placed onto an orbital shaker (10-15 rpm, Polymax 2040, Heidolph Instruments GmbH & CO. KG, Schwabach, Germany) for 20-30 min. After this incubation, the samples were rinsed with Millipore water. The JIPs were placed onto a microscope slide and left to dry for 2-3 min. Once the JIPs were completely dry, images were acquired on a fluorescent microscope (Axioskop 2 MAT mot, Carl Zeiss AG, Oberkochen, Germany) equipped with a mercury arc lamp as a light source (HBO 103 W/2, Osram, Munich, Germany) and a digital camera (C10600 ORCA-R2, Hamamatsu Photonics Europe GmbH, Herrsching, Germany). For images of samples incubated with nanoparticles (NPs), 10x magnification and an appropriate filter set (excitation: BP 546/12 nm, filter block: 580 nm, emission: LP 590 nm) was chosen. Protein treated samples were examined with a different filter set (excitation: BP 450-490 nm, filter block: 510 nm, emission: LP 515 nm), and a magnification of 10x was chosen for tests with BSA and 20x for tests with lysozyme. On every sample, 3-5

images were taken from each zone; this ensures that the obtained results are representative for the whole zone. Images within one JIP were always taken with identical camera settings, *i.e.*, using the same exposure time, gain and offset values. These images were evaluated with ImageJ by either counting the number of fluorescent points (in case of NPs) or by measuring the average fluorescence intensity (in case of proteins).

### **Bacterial adhesion tests**

Bacterial attachment to mucin coatings was evaluated for *S. aureus*, *S. pyogenes*, and *P. aeruginosa*. *S. pyogenes* strain ATCC 700294 was cultured in Brain Heart Infusion Broth (Carl Roth), *S. aureus* USA300 in Lysogeny Broth (Carl Roth) supplemented with 0.1 % dibasic potassium phosphate (Acros Organics) and *P. aeruginosa* PAO1 in pure Lysogeny Broth. The three strains were grown during shaking at 37 °C. Bacteria were directly diluted from overnight culture to an OD<sub>600</sub> of 0.2 (*S. aureus* and *S. pyogenes*) or grown to logarithmic phase (*P. aeruginosa*) and subsequently diluted to an OD<sub>600</sub> of 0.2. Bacteria were incubated under static conditions at 37 °C and 5 % CO<sub>2</sub> for 1.5 h in wells containing uncoated or mucin coated PDMS/PMMA samples. Unattached bacteria were aspirated by removing the supernatant, and samples were washed with sterile PBS (1 mL) 1 to 4 times. Images were acquired at 20x magnification using the Zeiss microscope Primovert equipped with a Zeiss AxioCam ERc 5s. Adhesion of bacteria (*S. aureus*) or bacterial colonies (*S. pyogenes*) were quantified with the software ImageJ using the 'find maxima'-command. The boxes for 'exclude edge maxima' and 'light background' were checked and the noise tolerance was set between 10 and 30 depending on the image. Images were preprocessed by adjusting brightness and contrast. If images were too noisy for a proper quantification, a Gaussian smoothing algorithm (smoothing radius was set to 5.0 px) was applied to the images using the software gimp 2.8 (GNU Image Manipulation Program, The gimp team) prior to image analysis.

### **Fibroblast adhesion**

NIH/3T3 fibroblasts were maintained at subconfluency in T75 flasks with Dulbecco's modified Eagle medium (DMEM; Sigma-Aldrich) supplemented with 10 % (v/v) fetal bovine serum (Sigma Aldrich) and 1 % (v/v) antibiotics solution (25 U/mL penicillin, 25 µg/mL streptomycin; both Sigma Aldrich). The cells were detached using trypsin/EDTA (Sigma Aldrich), and the cells were seeded at a

density of 120,000 cells/cm<sup>2</sup> on uncoated and mucin coated PDMS surfaces, respectively. After 24 h of incubation at 37 °C and 5 % CO<sub>2</sub>, the surfaces were washed twice with PBS. Cell viability was assessed by a live/dead assay employing a double-stain: 1 μM calcein AM (Invitrogen, Carlsbad, CA, USA) and 2 μM ethidium homodimer 1 (Invitrogen) were dissolved in serum-free DMEM, and cells were incubated with this solution for 1 h before they were imaged on a DMI8 Leica microscope (Leica, Wetzlar, Germany) in fluorescence mode. Images were acquired with a digital camera (Orca Flash 4.0 C11440, Hamamatsu, Japan) using the software Leica Application Suite X (Leica).

### **Production of the PDMS filter system**

The capillary system was created by modifying a protocol described in Bellan *et al.*<sup>260</sup>. PDMS (Sylgard 184 Silicone Elastomer, Dow Corning, Midland MI, USA) prepolymer and cross-linker were mixed in a 10:1 ratio. Air bubbles were removed from the mixture by applying a vacuum for a minimum of 30 min. An aluminum cavity with dimensions of 35 mm x 35 mm was filled with 4 g of mixed PDMS to generate a continuous bottom layer and cured at 80 °C for 60 min. Sacrificial sugar structures were produced using a modified cotton candy machine (ZVM 3478, Clatronic International GmbH, Kempen, Germany), and 600 mg of these fibers were added into a second aluminum mold with smaller dimensions (*i.e.* 20 mm x 20 mm) to a height of ≈ 8 mm and covered with 4 g of mixed PDMS. Again, a vacuum was applied to remove air bubbles before curing this PDMS/cotton candy composite.

The cured PDMS/sugar block was then placed into the center of the larger aluminum mold, *i.e.* on top of the previously generated PDMS layer and, fixed with two copper wires ( $d = 1.5$  mm) with a length of 10 mm each. The cavity around this PDMS/sugar block was filled with PDMS and cured once more. The copper wires were removed, and the remaining two channels were extended to reach all the way through the PDMS/sugar block by using a 1.3 mm HSS spiral drill to create an in- and an outlet. The whole PDMS/sugar block was then placed into hot water (70 °C) for several days to dissolve the sugar fibers.

Finally, two brass tubes with an outer diameter of 2 mm were placed into the drilled in- and outlet to enable a connection of the porous PDMS structure to tubings (cross-linked silicone peroxide, inner diameter = 1 mm, outer diameter = 3 mm, VWR, Darmstadt, Germany). The amount of cotton candy used in our protocol

represents a compromise between obtaining a high surface area, good capillary interconnectivity and maintaining easy handling during the filter production process.

### **Filter functionalization**

Three different biological polymers were used to coat the inner surface of the filter: manually purified mucin, commercially purified porcine gastric mucin (M2378, Sigma-Aldrich, Schnelldorf, Germany) and poly-L-lysine (P8920, Sigma-Aldrich). Each macromolecule was dissolved in PBS (pH 7.3, DPBS, Lonza, Verviers, Belgium) at a concentration of 0.1 % (w/v). The filter was then filled with one of those solutions and incubated at room temperature for 90 min (in case of mucins) or for 180 min (in case of poly-L-lysine), respectively. After this incubation step, the capillaries were rinsed with 2 mL of PBS.

To functionalize the filter with artificial molecules, the capillaries were coated with dopamine first. 4 mL of dopamine solution (0.2 % (w/v) in 10 mM TRIS buffer, pH 8.5) were pumped through the filter at a flow rate of 1 mL/min to generate a dopamine surface coating and flushed afterwards with 2 mL TRIS buffer. The pre-coated filter was then filled with either 6-aminohexanoic acid or polyethyleneimine (0.1 % (w/v) or 10.0 % (w/v), respectively, both in TRIS buffer) and for probing specific filtering with streptavidin/biotin with amine-PEG-biotin (2.3 kDa) or bis-amine-PEG (1.5 kDa) (both dissolved 0.2 % (w/v) in TRIS buffer). The incubation period was 90 min and afterwards the filter was rinsed with 2 mL of PBS. All substances mentioned above were obtained from Sigma Aldrich.

### **Characterizing the filtration behavior of functionalized filters**

For testing the selective properties of the filters with liposomes, the liposome stock solutions were diluted to a concentration of  $\approx 1.2 \cdot 10^9$  liposomes/mL in PBS and 4 mL were flushed through the filter at a flow rate of 1 mL/min using a syringe pump. The first mL of a solution, which had passed the filter, was discarded. Then, three drops of the filtrate were collected at three time-intervals of 1 min each. The difference in liposome quantity before and after flushing through the filter was determined by counting using the 'Find Maxima' command implemented into the analysis tool ImageJ (version 1.49v). For this counting procedure, 1.5  $\mu$ L of each sample were filled into a Thoma Cell Counting Chamber (Poly-Optik GmbH, Bad Blankenburg, Germany). Fluorescence images were acquired on an Axioskop 2 Mat

mot microscopic (Zeiss, Oberkochen, Germany) using a 50x lens (EC Epiplan-Neofluar 50x/0.8 HD DIC M27, Zeiss, Oberkochen, Germany). Each filter was tested with three sets of liposome solutions: DOPG, DOPC and DOTAP. In between each filtration test, the capillary system was rinsed with 2 mL PBS. Control experiments showed that the filtration efficiency did not depend on the order in which the liposomes were flushed through the filter.

For testing the selective properties of the filters with fluorescently labeled dextrans, either unmodified FITC-dextrans ( $M_w = 150$  kDa, Sigma Aldrich) or chemically modified FITC-dextrans with carboxymethyl (CM) groups or diethylaminoethyl (DEAE) groups were diluted at a concentration of  $10 \mu\text{g/mL}$  in PBS buffer. 4 mL of this solution were flushed through the filter at a flow rate of 1 mL/min, and the filtered solution was collected as described above for liposomes. The fluorescence intensity of the collected solutions was measured using a plate reader (VICTOR X3 Multilabel Plate Reader, Perkin-Elmer, Waltham, MA, USA) at an excitation wavelength of  $\lambda_{485 \text{ nm}}$  and an emission wavelength of  $\lambda_{535 \text{ nm}}$ .

#### **Enzymatic catalysis by immobilized horseradish peroxidase (HRP)**

Horseradish peroxidase (HRP) was obtained from Sigma Aldrich. For coating, the inner capillary surface, 100  $\mu\text{g}$  HRP were dissolved in 1 mL ultrapure water. The enzyme solution was injected into the filter and incubated for 30 minutes. Afterwards, the filter was rinsed with 5 mL ultrapure water to remove excess HRP. To measure enzymatic activity, the substrate ADHP (10-acetyl-3,7-dihydroxyphenoxazine) from a commercial kit (QuantaRed™ Enhanced Chemifluorescent HRP Substrate Kit, Thermo Fisher, MA, USA) was used. The substrate solution was freshly prepared by adding ADHP to a mix of buffer and enhancer solution as provided by the commercial kit and pumped through the filter at a flow rate of 1 mL/min. The successful conversion of the substrate was indicated by the solution acquiring a pink color. The converted substrate solution was collected at the filter outlet and the change in color was quantified spectrophotometrically in a 96-well plate with a Victor<sup>3</sup> plate reader (PerkinElmer, MA, USA) at an excitation wavelength of  $\lambda_{570 \text{ nm}}$  and an emission wavelength of  $\lambda_{642 \text{ nm}}$ .

For assessing the stability of the physisorbed HRP, the coated capillary system was rinsed with up to 500 mL of ultrapure water. At distinct time points of this rinsing procedure, 1 mL of the substrate was injected to test for enzymatic activity. For

testing the influence of filter storage, HRP coated filter systems were either filled with PBS, covered in Parafilm and incubated at room temperature for 48 hours or dried and incubated at room temperature for 72 hours. Afterwards, the enzyme activity was determined as described above.

### **Nanoparticle Tracking Analysis**

A NTA setup (Nanosight NS300 instrument, Malvern, Uppsala, Sweden) with a 405 nm laser was used to evaluate the size of condensed mucin (diameters) in situ. Latex beads having a size of 100 nm (ThermoFisher) in ultrapure water were used to confirm the correct size measurements by NTA (within 5% error). The samples were diluted in different glycerol/water mixtures to a final mucin concentration of 0.2 mg/mL. Then, three 60 s NTA captures were taken at 20 °C. Between each sample, the sample chambers were washed with 16.4 mM sodium dodecyl sulfate (adjusted to pH = 2.9), followed by 5 % ethanol. Chambers were dried by nitrogen flow. The data of the average size and diffusion coefficient was processed by using NTA 3.2 software. The diameters estimated by NTA measurements are calculated based on the Stokes Einstein equation.

### **DNA design**

The DNA sequences were designed according to a previous study<sup>317</sup>. Briefly, single-stranded DNA strands, which do not form any secondary structures at the working temperature used here, were designed to form complexes with each other; thus, they are able to form cross-links when attached to mucins and – consequently – are referred to as ‘crDNA’ (cross-linking DNA, see **Figure B1**). Additionally, ‘displacement DNA’ (dDNA) is designed (see **Figure B1**); this DNA variant is made such that a dimerization with crDNA sequences (dDNA/crDNA) is more favorable than dimerization between two crDNA strands (crDNA/crDNA). Therefore, addition of dDNA to a crDNA/crDNA-crosslinked mucin layer can break the crDNA/crDNA as thermodynamically more favorable crDNA/dDNA complexes are formed. In addition, a control DNA sequence (coDNA) was used that does not form a stable structure with crDNA; this control molecule was used to demonstrate that displacement effect obtained with dDNA is specific to the designed nucleotide sequence.

All designed DNA sequences were analyzed with the OligoAnalyzer 3.1 software using the following parameters<sup>367</sup>: target type, DNA; oligo concentration, 300  $\mu$ M;



Prior to experiments, lyophilized crDNA was dissolved in 180 mM phosphate buffer (pH = 8) containing 100 mM DTT and incubated at RT for 1 h to reduce disulfide bonds. Protection groups were reduced and DTT is removed from solution using NAP-25 Sephadex G-25 column (GE Healthcare, Freiburg, Germany). Here, buffer was exchanged to 180 mM phosphate buffer and the concentration of crDNA is adjusted to 500  $\mu$ M.

### **Preparation of mucin nanoparticles and Dynamic Light Scattering**

To prepare mucin nanoparticles (NPs), lyophilized mucin was dissolved at a concentration of 5 mg/mL in ultrapure and stirred at 4 °C overnight. The mucin solution was added to a 30 % (w/v) glycerol (alternatively ethanol or hexane) solution in a ratio of 1:4 (v/v) and vortexed for 30 s to form condensed mucin nanoparticles. Afterwards a 30 % (w/v) glycerol (or ethanol or hexane, respectively) solution containing 100 mM MgCl<sub>2</sub> is added in a ratio of 1:1 (v/v) and again vortexed for 30 s to obtain a final mucin concentration of 0.5 mg/mL. To remove glycerol and unbound ions, the mixture was finally transferred to dialysis tubes (Spectrum™ Spectra/Por™ Float-A-Lyzer™ G2, MWCO: 300 kDa, Roth) and dialyzed against a physiological sodium chloride solution overnight. The hydrodynamic size of mucin NPs was determined with a zeta sizer (Nano ZS, Malvern Instruments, Herrenberg, Germany) using a backscatter angle of 173°.

### Estimating the local drug concentration released from a mucin layer

We estimate the local drug concentration that can be achieved in proximity of a mucin-coated surface by assuming free diffusive spreading of the drug in an aqueous environment ( $\eta_{\text{water}} = 1 \text{ mPa}\cdot\text{s}$ ). Here, free diffusion mimics the ‘*worst case scenario*’ as it describes the fastest possible way drug molecules could escape from the surface of the coating (e.g., an implant surface).

For tetracycline (TCL), we estimate (based on the molecular structure of the molecule) a size (= radius) of  $r_{\text{TCL}} = 0.5 \text{ nm}$ . According to the Stokes-Einstein relation, we can then calculate the diffusion coefficient for a TCL molecule,  $D_{\text{TCL}}$ , at a physiological body temperature of  $T = 37 \text{ }^\circ\text{C}$  (310 K) as follows:

$$D_{\text{TCL}} = \frac{k_{\text{B}} \cdot T}{6\pi \cdot \eta_{\text{water}} \cdot r_{\text{TCL}}}$$

Where  $k_{\text{B}} = 1.380649 \cdot 10^{-23} \text{ J/K}$  denotes the Boltzmann-constant. By further assuming a one-dimensional diffusional escape process orthogonal to the implant surface ( $d = 1$ , again mimicking the worst-case scenario), we can further estimate the maximal (average) distance a drug molecule can escape as a function of time  $t$  to be  $R$  with:

$$\langle R(t)^2 \rangle = 2 \cdot d \cdot D_{\text{TCL}} \cdot t$$

To be able to compare the local drug concentration to a typical systemic dosing applied during the day (i.e., within 6 h), we then calculate the diffusive escape distance  $R(t)$  for  $t = 6 \text{ h}$ . With the other parameters given above, we obtain an average escape distance of  $R = 1 \text{ mm}$  (measured from the surface of the coating).

With the mucin monolayer coating discussed in Fig. 3 of the main paper, we obtained an antibiotic loading capacity on the model surface of  $4.5 \mu\text{g}/\text{mm}^2$  (see main paper for details). With this value, we can estimate the concentration of released TCL in a cuboid volume above the coated surface to be  $180 \mu\text{g}/\text{mL}$  after 6 h.

### Coating process for CM dextran

PDMS was prepared and activated with oxygen plasma as described above (see *Chapter 2.2*). Afterwards an amine-functionalized silane (3-Aminopropyltriethoxysilane, APTES, Sigma Aldrich) was diluted to 0.1 % in 2-propanol and the cuvettes were incubated with this solution at  $60 \text{ }^\circ\text{C}$  for 5 h. Afterwards, the samples

were washed in 80 % ethanol (Carl Roth) for 1 h to remove unbound residues before they were placed in the oven at 60 °C for another 60 min to stabilize the bond between the PDMS and the silane.

In parallel, carboxy modified dextran (150 kDa, TdB Consultancy AB, Uppsala Sweden) was dissolved to a concentration of 1 % (w/v) in 10 mM MES buffer (pH = 5) and 5 mM EDC and 5 mM sulfo-NHS were added to activate the carboxyl groups. The solution was incubated for at RT for 3 h to make sure that unreacted EDC and NHS were hydrolyzed before the solution was diluted 1:10 in PBS (pH = 7.4) to obtain a final dextran concentration of 0.1 % (w/v). The solution was filled into the cuvettes and allowed to react at 4 °C overnight. Amine groups of the silane molecule then react with the EDC activated groups of the dextran and form a stable covalent bond.

### **Coating process for chitosan**

The coupling reaction was performed as described for the coupling of porcine gastric mucin (see *Chapter 2.2*) except for the last step: After the carboxyl groups of the silane had been activated, the EDC-NHS solution was replaced by 2 % acetic acid containing 0.1 % (w/v) of chitosan (95/3000, Heppe Medical Chitosan GmbH, Halle, Germany) and stored overnight at 4 °C. Amine groups of the chitosan molecule then react with the EDC activated groups of the silane and form a stable covalent bond.

## Appendix C: Supplementary data\*

### Drug quantification

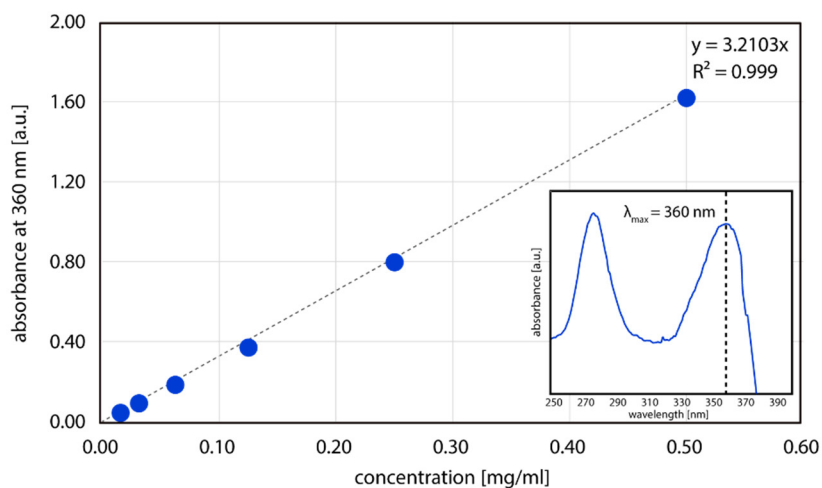


**Figure C1: Tetracycline standard curve.** TCL standard curve is prepared by measuring the absorbance values of serially diluted TCL solutions at 360 nm. This wavelength was determined by scanning the TCL solution in a wavelength range of 250 – 400 nm (inset).

---

\* This section follows in part the publications Kimna *et al.*, *Advanced Materials Interfaces* (2020), Boettcher *et al.*, *Biotribology* (2017), Song *et al.*, *ACS Applied Bio Materials* (2019), Winkeljann *et al.*, *Advance Materials Interfaces* (2019), Winkeljann *et al.*, *Advanced Materials Interfaces* (2020) & Winkeljann *et al.*, *Macromolecular Bioscience* (2017)

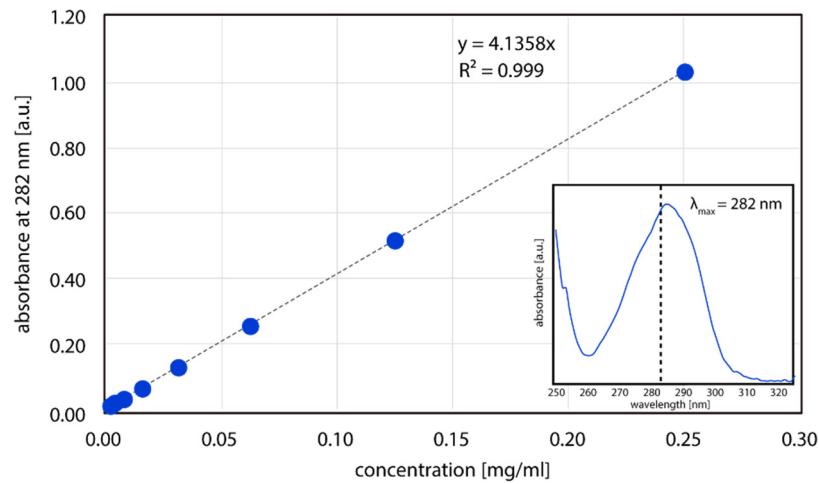


**Figure C2: Vancomycin standard curve.** VAN standard curve is prepared by measuring the absorbance values of serially diluted VAC solutions at 282 nm. This wavelength was determined by scanning the VAN solution in a wavelength range of 250 – 330 nm (inset).

### Mucin as a lubricant in cartilage tribology

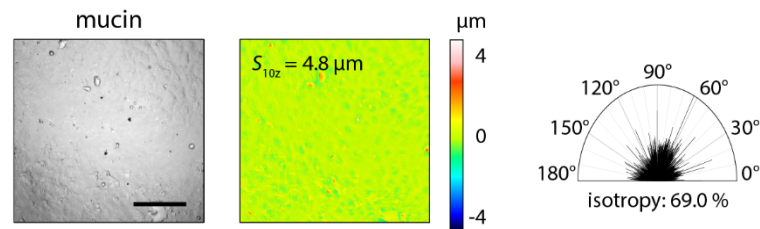


**Figure C3: Wear formation on articular cartilage.** When a class on cartilage pairing is lubricated with mucin solutions neither surface images nor topographical images show any sign of wear formation. Consequently, the  $S_{10z}$  value is not significantly increased compared to the surface of native cartilage. The determination of the isotropy parameter further supports the observation, that also no unidirectional wear tracks can be found. The scale bar represents 200  $\mu\text{m}$ .

## Viscosity of aqueous solutions containing purified mucins

**Table C1: Viscosities of different mucin-based solutions.** The error values shown depict the standard deviation as obtained from  $n = 3$  independent measurements.

Buffer	pH	Components	Viscosity (mPa-s)
HEPES	7.0	0.005 % mucin	$0.99 \pm 0.01$
HEPES	7.0	0.01 % mucin	$0.99 \pm 0.01$
HEPES	7.0	0.05 % mucin	$1.07 \pm 0.01$
HEPES	7.0	0.1 % mucin	$1.24 \pm 0.18$
HEPES	7.0	1.0 % mucin	$8.30 \pm 0.05$
UB	2.0	0.1 % mucin	$1.04 \pm 0.10$
UB	4.0	0.1 % mucin	$0.92 \pm 0.11$
UB	6.0	0.1 % mucin	$1.13 \pm 0.42$
UB	8.0	0.1 % mucin	$1.23 \pm 0.05$
HEPES	7.0	0.1 % mucin + 20 mM NaCl	$1.22 \pm 0.05$
HEPES	7.0	0.1 % mucin + 50 mM NaCl	$1.38 \pm 0.11$
HEPES	7.0	0.1 % mucin + 150 mM NaCl	$1.23 \pm 0.07$
HEPES	7.0	0.1 % mucin + 500 mM NaCl	$1.19 \pm 0.01$

## Mucin adsorption in varying salt conditions

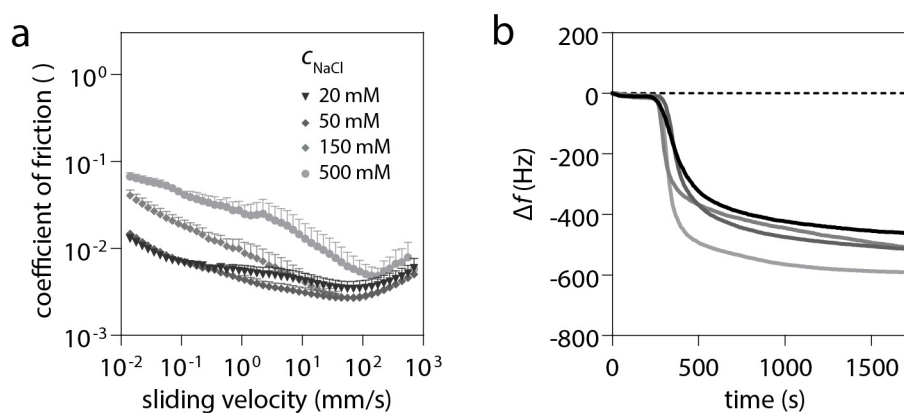


**Figure C4: Lubricity of mucin solutions in varying salt conditions.** The lubricity (a) and adsorption kinetics (b) of mucin solutions are hardly affected by changes in the ionic strength of the solution as long as the physiological level is not exceeded drastically. For high salt solutions (500 mM NaCl), both lubricity (c) and adsorption (d) are altered. The results denote the average, while error bars denote the standard deviation as obtained from  $n = 3$  independent samples.

## Coating density of covalent mucin and PEG coatings

To obtain information on the coating density generated with PEG and mucin, the mass of bound macromolecules was studied by using QCM-D. Therefore, gold sensor chips were coated with a thin PDMS film as described in the *Methods* section. Next, the sensor was pre-coated with TMS-EDTA as described in the *Methods* section; however, some slight modifications in the coating procedure were introduced to avoid problems with the sensitive chips: first, the PDMS coated chips were placed into a plasma oven and treated with  $O_2$ -plasma (0.4 mbar, 30 W) for 30 s. Afterwards, the chips were immersed into acetate buffer (pH = 4.5) containing 0.1 % TMS-EDTA and incubated at 60 °C for 5 h. To avoid incompatibilities with the glue that is used to fix the gold sensors to their holder, the chips were then rinsed in Milli-Q water instead of ethanol and were placed into the oven again at 60 °C for 1 h. The pre-coated chips were then inserted into the QCM-D device and Milli-Q water was injected at a flow rate of 100  $\mu$ L/min until a stable baseline was obtained. Afterwards, the Milli-Q water was replaced by 100 mM MES buffer (pH = 5) containing 5 mM EDC and 5 mM sulfo-NHS to activate the carboxyl groups on the PDMS surface. The activation reaction was allowed to take place for 30 min. Finally,

a PBS solution (pH = 7.4) containing either 0.4 % (w/v) of mPEGa or 0.1 % of porcine gastric mucin was injected at a flow rate of 100  $\mu\text{L}/\text{min}$  for 60 min to generate an adsorption curve.

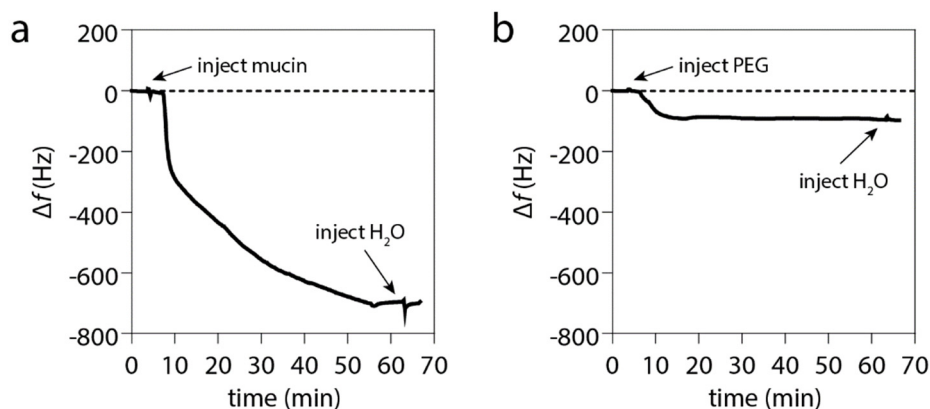


**Figure C5: Macromolecule adsorption to activated PDMS surfaces.** QCM-D measurements were performed on PDMS-coated Au-chips which were pre-coated with a TMS-EDTA layer activated with EDC. Due to the large difference in molecular weight, mPEGa adsorption (b) induces a much weaker alteration in the frequency shift than mucin adsorption (a). In both cases, the added macromolecule layer is stable as indicated by the constant signal which is maintained during rinsing with water.

For both, mPEGa and MUC5AC, we detected a clear frequency drop, which is in line with our expectation that the macromolecules are being coupled to the activated PDMS surface (**Figure C5**). As the frequency drop is – according to Sauerbrey (see *Methods* section) – directly proportional to the amount of the adsorbed mass, mPEGa ( $M_{W, \text{PEG}} = 20 \text{ kDa}$ ) was expected to induce a much less pronounced frequency shift than the way larger mucin ( $M_{W, \text{mucin}} = \text{up to a few MDa}$ ). And indeed, the frequency shift obtained for porcine gastric mucin was considerably larger than the one detected for mPEGa, *i.e.*  $\approx 700 \text{ Hz}$  (a) compared to  $\approx 100 \text{ Hz}$  (b). Using the Sauerbrey equation the density of surface-bound molecules to be approximately  $43.5 \mu\text{g}/\text{mm}^2$  for mPEGa and  $304 \mu\text{g}/\text{mm}^2$  for mucin, respectively. This seems to suggest, that a somewhat higher coating density was achieved with mPEGa compared to mucin; however, one needs to be aware, that – especially for thick, non-rigid layers – the Sauerbrey equation underestimates the adsorbed mass due to dissipation effects. Thus, the coating densities of the mucin and mPEGa layers might be more similar than the numbers suggest, and they should be just seen as an orientation. As mentioned before, the main goal was to obtain a similar friction response from the macromolecular coatings and not a

similar coating density; the idea was that the friction response obtained with the coatings alone would serve as a baseline which would later allow for comparing the effect of different polymer-based lubricants. Within the framework of the hydration lubrication model, both, the total bound mass of macromolecules as well as their density can contribute to the amount of surface-bound water and thus the reduction of friction. Consequently, for the third coating, *i.e.* PLL, it was also aimed at a similar friction performance and not necessarily an identical coating density.

### Mechanical stability of covalent mucin coatings on PMMA

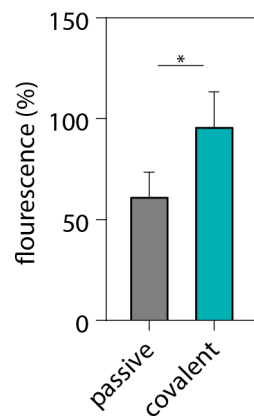


**Figure C6: Coating stability on PMMA.**

Passively adsorbed and covalently linked mucin coatings generated on PMMA are exposed to ultrasonic treatment. Mucins are detected *via* ELISA, and the obtained signal is compared to freshly coated samples (*i.e.*, either passively and covalently coated ones) that were not challenged with ultrasound. Error bars denote the standard deviation as obtained from  $n = 5$  independent samples.

## Characteristics of the liposomes used for filtration studies

**Table C2:** Diameter and  $\zeta$ -potential of all liposome species were determined in 20 mM TRIS buffer at pH 7.3 and 10 mM NaCl. The error values represent the standard deviation as obtained from three different measurements.

liposome species	diameter (nm)	PDI ( )	$\zeta$ -potential at pH 7.3 (mV)
DOPG	199 $\pm$ 35	0.16 $\pm$ 0.03	-55.8 $\pm$ 1.3
DOPC 200	235 $\pm$ 31	0.17 $\pm$ 0.04	+5.4 $\pm$ 0.3
DOPC 400	529 $\pm$ 39	0.38 $\pm$ 0.03	+1.4 $\pm$ 0.1
DOPC 1000	836 $\pm$ 43	0.41 $\pm$ 0.03	+5.4 $\pm$ 0.3
DOTAP	230 $\pm$ 46	0.17 $\pm$ 0.04	+48.6 $\pm$ 0.9
DOPC-biotin	203 $\pm$ 2	0.26 $\pm$ 0.02	-4.7 $\pm$ 0.4

## Filtration of differently charged dextrans

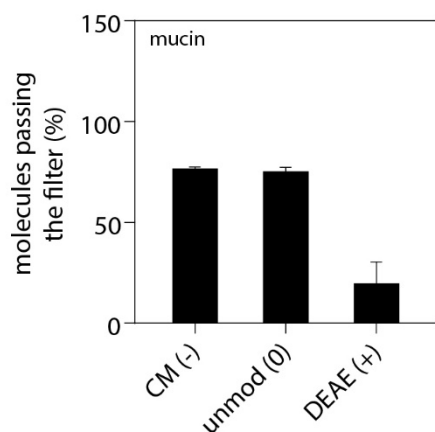


**Figure C7: Filtration of a mucin-coated PDMS-filter when flushed with different dextran variants.** FITC-labeled dextrans ( $M_w = 150$  kDa) – modified with either carboxymethyl (CM) groups, diethyl-aminoethyl (DEAE) groups or unmodified – were pumped through the capillary system. The fluorescence intensity of the dextran solution prior to and after passing the filter was measured to determine the fraction of molecules that have passed the filter. The error bars denote the standard deviation as obtained from  $n=3$  independent filter realizations.

### Conformational change of surface bound mucin layers

To assess if the conformational change a surface bound mucin layer is expected to undergo from its native to condensed state (or, *vice versa*, from its condensed to its original state following a decondensation trigger), the thickness of a fluorescently labelled mucin coating determined with confocal laser scanning microscopy (CLSM) before condensation, after condensation and after triggered decondensation.

To prepare specimens suitable for CSLM, microscopy glass cover slips (24 mm x 24 mm, Thermo Fisher Scientific) were first coated with a thin layer of PDMS using a spin coater (WS-400B-6NPP/LITE, Laurell, North Wales, USA). To obtain this coating, PDMS prepolymer and cross-linker (Sylgard 184, Dow Corning, Wiesbaden, Germany) were mixed in a ratio of 10:1, and further diluted with *n*-hexane to obtain a 1% (v/v) polymer solution. Then, a bare glass cover slip was placed onto the center of the spin coater, and 300  $\mu$ L of the prepared PDMS mixture were pipetted onto the cover slip. To distribute the PDMS solution, the spin-coater was set into rotation - first at 1500 rpm for 20 s and then at 3000 rpm for 60 s. Afterwards, the coated cover slip was cured at 80 °C for 4 h. Afterwards, the PDMS surface was coated with mucins as described in the main paper with a slight modification: First, to avoid damaging the thin PDMS film, the exposure time for the plasma activation step was reduced from 90 to 30 s. Furthermore, 10 % (w/w) of fluorescently labelled mucins (label: ATTO488, see *Materials and Methods* for details of the labelling procedure; the remaining 90% (w/w) of mucins were used without a label) were used in the last step of the coating procedure to allow for imaging the mucin layer with CLSM while avoiding too intense fluorescence signals.

From those mucin coated PMDS/glass cover slips, five different variants were prepared: uncondensed samples, condensed and stabilized (both for DNA and ion-based mechanism) samples, and decondensed/triggered samples (also for both stabilization strategies). Condensation and decondensation was achieved as described for the drug release experiments in *Materials and Methods*.

Imaging was performed using a Leica TCS SP5 II setup (Leica, Wetzlar, Germany) equipped with a DMI6000 microscope corpus (Leica) and a 40x oil immersion objective (HCX PL APO; NA = 1.25, Leica). An argon laser was used to excite fluorescence from the tagged mucin layer at 488 nm and a laser power of 40 %. Emission was detected in a window ranging from 500 to 527 nm. The thickness of the fluorescently tagged mucin layers was then determined by scanning through the

$z$ -levels of the samples and subtracting the  $z$ -value where fluorescence started to occur from the  $z$ -level where the signal diminished again. This procedure was repeated on five randomly chosen spots for each of the five conditions described above.

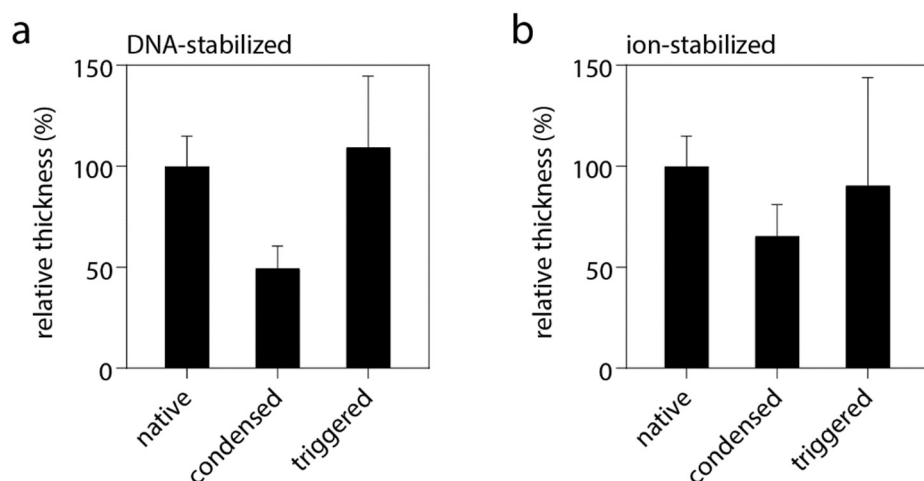


**Figure C8: Conformational changes of surface bound mucin layers.** If a surface bound mucin layer is condensed with glycerol and stabilized with crDNA (a) or  $Mg^{2+}$  ions (b) it is compacted to 50 % (or 66 %, respectively) of its original thickness, even after glycerol removal. If the compacted system is then exposed to the correct trigger, *i.e.* dDNA (a) or 150 mM NaCl solution, it returns to its original conformation. The error bars represent the standard deviation as measured at  $n = 5$  random spots for each condition.

For freshly coated, uncondensed samples, an average thickness of  $26.6 \pm 4 \mu\text{m}$  is obtained. This value is reasonable considering the following two aspects: first, when grafted onto a surface using carbodiimide chemistry (which targets the termini of the mucin glycoprotein), it is likely that the mucins are attached to the surface in an elongated, brush-like conformation. The peptide backbone of a porcine gastric mucin macromolecule comprises 4192 amino acids<sup>325</sup>. With an average length of 35 pm per amino acid, a total length of a single mucin molecule of  $\approx 15 \mu\text{m}$  can be estimated (by assuming a fully elongated structure; this is a bit of an overestimation as minor parts of the peptide chain are folded). Actually, electron microscopy images of porcine gastric mucins indicated molecule lengths up to  $\approx 5 \mu\text{m}$ <sup>369</sup>. Second, mucins can form oligomers through disulfide bridges, with molecular weights up to 50 MDa, and the mucins used here are expected to be present in oligomeric form.

As described above, the compaction of the mucin layer is achieved by exposure to glycerol, and the compacted mucin layers are stabilized with either crDNA or Mg<sup>2+</sup>. After glycerol removal, it is found that the mucin layer is compacted to 50 % (for DNA-stabilized layers, **Figure C8a**) or 66 % (for ion-stabilized, **Figure C8b**) of its original thickness. If the condensed layer is then exposed to the correct trigger (i.e., dDNA for DNA-stabilized samples and 150 mM NaCl for Mg<sup>2+</sup>-stabilized samples), the compaction is reversed.

### Control groups for release from single layer construct

**Table C3: Tetracycline cumulative release from DNA-crosslinked mucin layers.**

	<b>Group 1</b>	<b>Group 2</b>	<b>Group 3</b>	<b>Group 4</b>
condensation	glycerol	glycerol	glycerol	-
stabilization	crDNA	crDNA	coDNA	crDNA
trigger	dDNA	coDNA	dDNA	dDNA
time (h)	c <sub>TCL</sub> (µg/mL)	c <sub>TCL</sub> (µg/mL)	c <sub>TCL</sub> (µg/mL)	c <sub>TCL</sub> (µg/mL)
0	1.6 ± 1	5.4 ± 1	1.2 ± 1	0.4 ± 1
0.25	49.0 ± 6	24.4 ± 8	2.9 ± 1	0.5 ± 1
0.5	81.1 ± 12	22.0 ± 9	3.6 ± 1	0.3 ± 1
1	97.0 ± 12	29.6 ± 9	4.8 ± 2	0.1 ± 1
2	94.2 ± 13	26.6 ± 7	6.9 ± 2	0.0 ± 1
3	76.4 ± 8	26.1 ± 4	8.1 ± 2	0.1 ± 1

**Table C4: Tetracycline cumulative release from Mg<sup>2+</sup> stabilized mucin layers.**

	<b>Group 1</b>	<b>Group 2</b>	<b>Group 3</b>
condensation	glycerol	glycerol	-
stabilization	Mg <sup>2+</sup>	Mg <sup>2+</sup>	Mg <sup>2+</sup>
trigger	150 mM NaCl	water	150 mM NaCl
time (h)	c <sub>TCL</sub> (µg/mL)	c <sub>TCL</sub> (µg/mL)	c <sub>TCL</sub> (µg/mL)
0	3.4 ± 0	3.5 ± 1	7.2 ± 4
0.25	2.9 ± 1	2.5 ± 1	6.9 ± 4
0.5	92.0 ± 11	2.1 ± 1	9.5 ± 6
1	196.3 ± 8	2.1 ± 1	12.6 ± 10
2	180.5 ± 13	2.0 ± 1	17.5 ± 19
3	180.7 ± 15	1.4 ± 1	17.3 ± 19

**Table C5: Vancomycin cumulative release from Mg<sup>2+</sup> stabilized mucin layers.**

	<b>Group 1</b>	<b>Group 2</b>	<b>Group 3</b>
condensation	glycerol	glycerol	-
stabilization	Mg <sup>2+</sup>	Mg <sup>2+</sup>	Mg <sup>2+</sup>
trigger	150 mM NaCl	water	150 mM NaCl
time (h)	c <sub>VAN</sub> (µg/mL)	c <sub>VAN</sub> (µg/mL)	c <sub>VAN</sub> (µg/mL)
0	1.4 ± 1	0.8 ± 1	1.8 ± 1
0.25	1.3 ± 1	0.8 ± 1	2.2 ± 1
0.5	5.1 ± 3	0.8 ± 1	2.4 ± 1
1	5.7 ± 1	2.4 ± 1	3.5 ± 1
2	8.3 ± 4	2.2 ± 1	3.4 ± 1
3	8.4 ± 3	1.4 ± 1	3.6 ± 0

### The phase transition temperature of different liposome compositions

The phase transition temperature of four different liposome compositions, *i.e.* 16 %, 10 %, 6 % and 3 % DOTAP/DPPC was determined by measuring the changes in the scattering intensity of these liposomes<sup>370</sup> using a Nano ZS zeta sizer (Malvern Instruments, Herrenberg, Germany). The minimum of the mean count rate, *i.e.* the average number of photons detected per second, was determined over a temperature interval of 32 °C to 42 °C (temperature step = 1 °C). The change of the count rate indicates the gel-to-liquid crystalline phase transition temperature of the different liposome compositions.

In agreement with previously shown data on DOTAP-DPPC liposomes<sup>371</sup>, a shift of the transition temperature to higher temperatures was observed when the concentration of DOTAP is lowered (**Figure C9**).

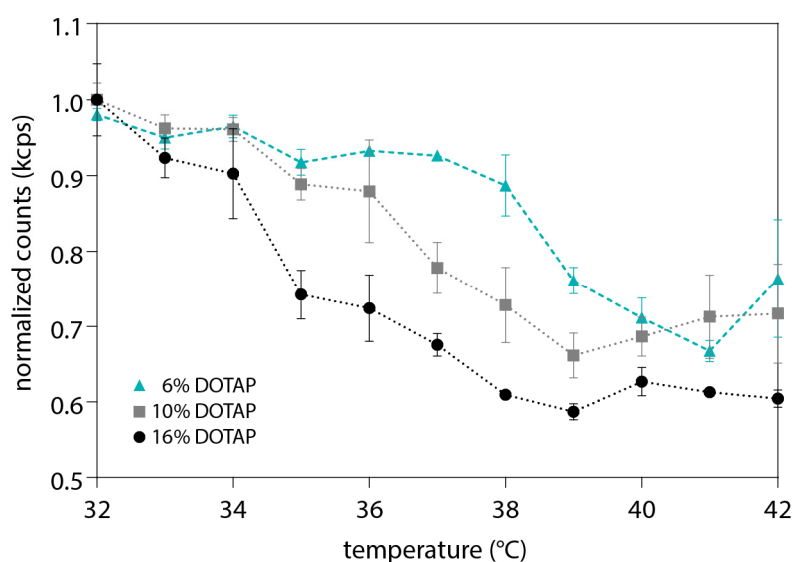


**Figure C9: Thermoresponsive liposomes.** The phase transition temperature of liposomes can be adjusted by changing the DOTAP concentration. Error bars depict the standard deviation as obtained from  $n = 3$  independent samples.

With 16 % DOTAP, the phase transition takes place in a temperature range between roughly 33 °C and 39 °C. However, if the DOTAP content is decreased to only 3 % the phase transition temperature becomes less clear since liposomes prepared from DPPC exclusively are known to be less stable<sup>371</sup>.

### Layer by layer assembly of mucins

The formation of mucin double layers is successful in both cases, *i.e.* when dopamine is used as a crosslinker (**Figure C10a**) and when lectin WGA is used as a crosslinker (**Figure C10b**) as indicated by the corresponding shifts in the resonance frequency. The dopamine crosslinked mucin construct was then exposed to a physiological salt solution to mimic the scenario when the implant comes in contact with the human body. The observed frequency shift is fully reversible when the multilayer is again exposed to salt-free simple water, indicating that this effect is caused by conformational changes of the mucin layers (**Figure C10a**).

The controlled disintegration of the mucin/lectin/mucin multilayers is tested by exposing the system to the lectin ligand *N*-acetyl-D-glucosamine (GlcNAc). Therefore, the coated chip was flushed with a 100 mM GlcNAc solution. The strong, irreversible increase in the resonance frequency supports the finding that indeed, the mucin/lectin bound is opened and the upper mucin layer is taken off (**Figure C10b**).

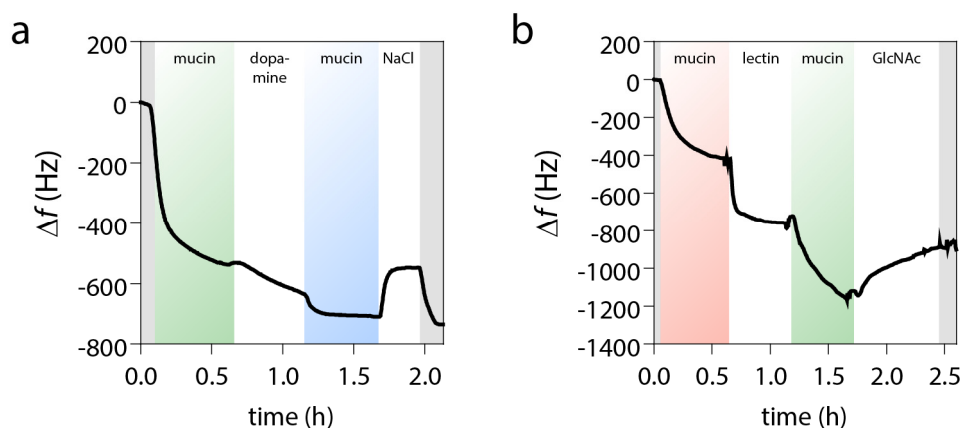


**Figure C10: Layer by layer assembly visualized using QCM.** Mucin double layers are generated on a QCM-D chip by either using dopamine (a) or lectin WGA (b) as a crosslinker. Mucin-dopamine interactions show a reversible frequency shift after the addition of 150 mM NaCl (a). The mucin lectin bound is irreversibly disrupted by the addition of GlcNAc (b). Grey areas depict time intervals where the system is rinsed with ultrapure water.

### Control groups for the release of TCL from mucin multilayer constructs

a) Verifying that the successful disassembly of the mucin multilayer by GlcNAc results in a release of TCL from the bottom mucin layer

First, the covalently bound mucin layer was incubated with a TCL solution (0.5 mg/mL) for 2 h to load this layer with the drug. Then, a mucin-based multilayer (comprising 5 layers, *i.e.*, mucin/lectin/mucin/dopamine/mucin) was generated as described in *Materials and Methods*. The samples were incubated at 40 °C to be consistent with the data shown in **Figure 38**, but without integrating liposomes into the middle mucin layer. The purpose of this control is to show, that adding the top four layers onto the bottom mucin layers is sufficient to stably trap the TCL in the bottom mucin layer and, that the external addition of GlcNAc to the system triggers release of TCL from the bottom mucin layer by lifting off the top layers

Drug release from the multilayer construct was initiated by adding 2 mL of the trigger solution (which now was a combination of 150 mM NaCl and 100 mM GlcNAc in 20 mM HEPES buffer, pH = 7.4) to the multilayer system.

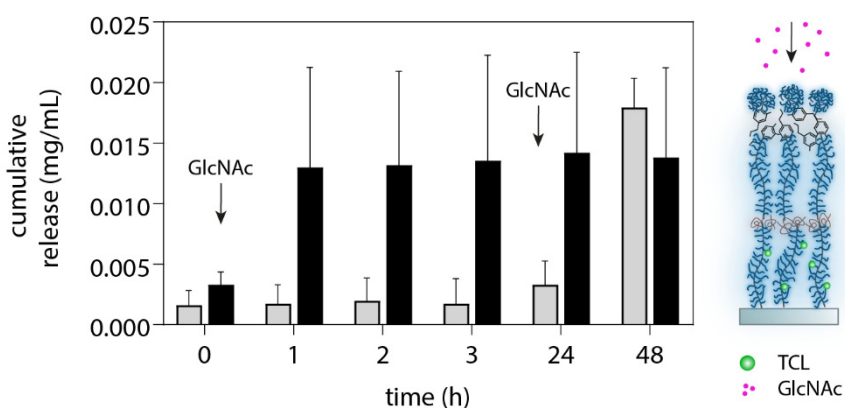


**Figure C11: TCL release from the bottom mucin layer of the multilayer construct triggered by the external supply of GlcNAc.** The mucin multilayer system is loaded with TCL in the bottom layer only. The addition of GlcNAc to the outside buffer efficiently triggers the release of the entrapped drug. Error bars depict the standard deviation as obtained from  $n = 3$  independent samples.

Indeed, as expected, the addition of free GlcNAc induces release of TCL, which reaches a plateau after approximately 1 h (**Figure C11**). In contrast, in the absence of GlcNAc addition (*i.e.*, if only 150 mM NaCl is used as a ‘trigger’ solution), there was only a low baseline level of drug release which is attributed to minor leakage

events. However, when the trigger is added at later time points, *i.e.* after 24 h of storage, similarly high final release levels occurred as when drug release was triggered at the beginning of the experiment.

*b) Verifying that a temperature increase triggers lift-off of the top mucin layers (and thus release from the bottom mucin layer) by inducing leakage of the embedded thermoresponsive liposomes*

Here, a very similar multilayer system as described above was assembled; the only difference was that the GlcNAc trigger molecules were now encapsulated into thermoresponsive liposomes as described in *Materials and Methods*, and those liposomes were embedded into the middle mucin layer of the construct.

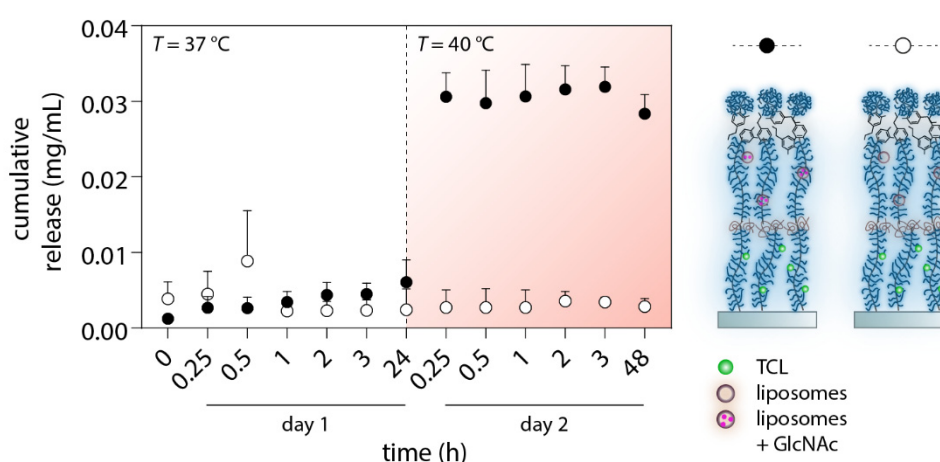


**Figure C12: TCL release from the bottom mucin layer of the multilayer construct triggered by an increase in temperature.** Drug release is only observed when GlcNAc loaded, thermoresponsive liposomes are embedded into the multilayer construct, but not when empty liposomes are used. Error bars represent the standard deviation as obtained from  $n = 3$  independent samples.

The purpose of this experiment was to verify the efficiency of drug release from the bottom mucin layer when lift-off of the two upper mucin layers is triggered by a temperature increase that induces GlcNAc leakage from liposomes; as a control, the same multilayer was constructed, but empty liposomes were added. Both sample variants were incubated at 37 °C for 24 h. Afterwards, the incubation temperature was increased to 40 °C (which exceeds the phase transition temperature of the

liposomes). The temperature driven drug release was then followed photo-spectrometrically as described before.

For both sample variants almost no drug release is detected, when incubated at 37 °C, (**Figure C12**). However, when the incubation temperature is increased to 40 °C, TCL is released from the samples carrying GlcNAc-loaded liposomes – but not from the control. This result demonstrates that the envisioned release mechanism operates as planned.

*c) Verifying the storage stability of completely assembled but untriggered samples.*

To verify the storage stability of the multilayer system two different variants of the fully assembled system, *i.e.* with an uncondensed (**Figure C13**, black circles) and with a condensed bottom layer (**Figure C13**, grey circles) were incubated at 37 °C in absence of both triggers. As expected, both variants showed only little drug leakage from the multilayer, and the system is stable for three days.

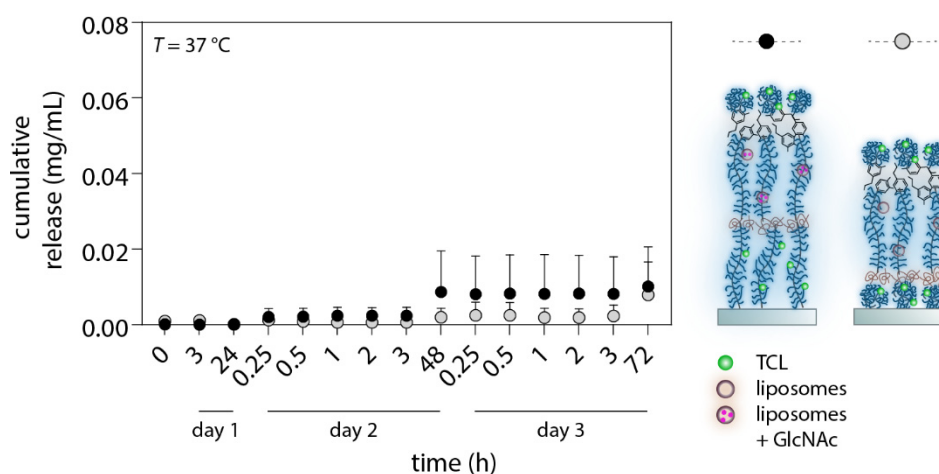


**Figure C13: Leakage from untriggered multilayer systems.** Multilayers are assembled in two variants, *i.e.*, with the bottom mucin layer in an uncondensed (black circles) and condensed state (grey circles), respectively. Schematic representations of the respective multilayer systems including two TCL depots are shown on the right, time-dependent release of TCL from the multi-layer constructs on the left. Error bars denote the standard deviation as obtained from a minimum of  $n = 3$  independent samples.

## Bibliography

- 1 McNaught, A. D. & McNaught, A. D. *Compendium of chemical terminology*. Vol. 1669 (Blackwell Science Oxford, 1997).
- 2 Klein, J. Molecular mechanisms of synovial joint lubrication. *Proceedings of the Institution of Mechanical Engineers, Part J: Journal of Engineering Tribology* **220**, 691–710 (2006).
- 3 Schmidt, T. A., Gastelum, N. S., Nguyen, Q. T. *et al.* Boundary lubrication of articular cartilage: Role of synovial fluid constituents. *Arthritis & Rheumatism* **56**, 882–891 (2007).
- 4 Bongaerts, J. H. H., Rossetti, D. & Stokes, J. R. The Lubricating Properties of Human Whole Saliva. *Tribology Letters* **27**, 277-287 (2007).
- 5 Coles, J. M., Chang, D. P. & Zauscher, S. Molecular mechanisms of aqueous boundary lubrication by mucinous glycoproteins. *Current Opinion in Colloid & Interface Science* **15**, 406-416 (2010).
- 6 Klein, J. Polymers in living systems: from biological lubrication to tissue engineering and biomedical devices. *Polymers for Advanced Technologies* **23**, 729-735 (2012).
- 7 Jay, G. D. Lubricin and surfacing of articular joints. *Current Opinion in Orthopaedics* **15**, 355–359 (2004).
- 8 Katta, J., Pawaskar, S. S., Jin, Z. M. *et al.* Effect of load variation on the friction properties of articular cartilage. *Proceedings of the Institution of Mechanical Engineers, Part J: Journal of Engineering Tribology* **221**, 175–181 (2007).
- 9 Schmidt, T. A. & Sah, R. L. Effect of synovial fluid on boundary lubrication of articular cartilage. *Osteoarthritis Cartilage* **15** (2007).
- 10 Kwiecinski, J. J., Dorosz, S. G., Ludwig, T. E. *et al.* The effect of molecular weight on hyaluronan's cartilage boundary lubricating ability – alone and in combination with proteoglycan 4. *Osteoarthritis and Cartilage* **19**, 1356–1362 (2011).

- 11 Chan, S. M. T., Neu, C. P., DuRaine, G. *et al.* Tribological altruism: A sacrificial layer mechanism of synovial joint lubrication in articular cartilage. *Journal of Biomechanics* **45**, 2426–2431 (2012).
- 12 Majd, S. E., Kuijer, R., Köwitsch, A. *et al.* Both Hyaluronan and Collagen Type II Keep Proteoglycan 4 (Lubricin) at the Cartilage Surface in a Condition That Provides Low Friction during Boundary Lubrication. *Langmuir* **30**, 14566–14572 (2014).
- 13 Lieleg, O. & Ribbeck, K. Biological hydrogels as selective diffusion barriers. *Trends in Cell Biology* **21**, 543–551 (2011).
- 14 Rivera, J., Cordero, J. R., Furumoto, Y. *et al.* Macromolecular protein signaling complexes and mast cell responses: a view of the organization of IgE-dependent mast cell signaling. *Molecular Immunology* **38**, 1253–1258 (2002).
- 15 Reitsma, S., Slaaf, D. W., Vink, H. *et al.* The endothelial glycocalyx: composition, functions, and visualization. *Pflügers Archiv - European Journal of Physiology* **454**, 345–359 (2007).
- 16 Lieleg, O., Baumgartel, R. M. & Bausch, A. R. Selective filtering of particles by the extracellular matrix: an electrostatic bandpass. *Biophys J* **97**, 1569–1577 (2009).
- 17 Klein, J. Hydration lubrication. *Friction* **1**, 1–23 (2013).
- 18 Ma, L., Gaisinskaya-Kipnis, A., Kampf, N. *et al.* Origins of hydration lubrication. *Nature Communications* **6**, 6060 (2015).
- 19 Jahn, S. & Klein, J. Hydration Lubrication: The Macromolecular Domain. *Macromolecules* **48**, 5059–5075 (2015).
- 20 Pradal, C., Yakubov, G. E., Williams, M. A. K. *et al.* Responsive polysaccharide-grafted surfaces for biotribological applications. *Biotribology* **18**, 100092 (2019).
- 21 Chen, M., Briscoe, W. H., Armes, S. P. *et al.* Lubrication at Physiological Pressures by Polyzwitterionic Brushes. *Science* **323**, 1698–1701 (2009).
- 22 Seror, J., Zhu, L., Goldberg, R. *et al.* Supramolecular synergy in the boundary lubrication of synovial joints. *Nat Commun* **6** (2015).

- 23 Yarimitsu, S., Moro, T., Kyomoto, M. *et al.* Influences of dehydration and rehydration on the lubrication properties of phospholipid polymer-grafted cross-linked polyethylene. *Proceedings of the Institution of Mechanical Engineers, Part H: Journal of Engineering in Medicine* **229**, 506–514 (2015).
- 24 Kyomoto, M., Moro, T., Saiga, K. *et al.* Biomimetic hydration lubrication with various polyelectrolyte layers on cross-linked polyethylene orthopedic bearing materials. *Biomaterials* **33**, 4451–4459 (2012).
- 25 Han, L., Xiang, L., Zhang, J. *et al.* Biomimetic lubrication and surface interactions of dopamine-assisted zwitterionic polyelectrolyte coatings. *Langmuir* **34**, 11593-11601 (2018).
- 26 Winkeljann, B., Boettcher, K., Balzer, B. N. *et al.* Mucin Coatings Prevent Tissue Damage at the Cornea–Contact Lens Interface. *Advanced Materials Interfaces* **4**, 1700186 (2017).
- 27 Zhang, C., Liu, Y., Wen, S. *et al.* Poly (vinylphosphonic acid)(PVPA) on titanium alloy acting as effective cartilage-like superlubricity coatings. *ACS Applied Materials & Interfaces* **6**, 17571-17578 (2014).
- 28 Li, S., An, Y., Zhao, X. *et al.* Bioinspired Smart Coating with Superior Tribological Performance. *ACS Applied Materials & Interfaces* **9**, 16745-16749 (2017).
- 29 Dobryden, I., Steponavičiūtė, M., Klimkevičius, V. *et al.* Bioinspired Adhesion Polymers: Wear Resistance of Adsorption Layers. *Langmuir* **35**, 15515-15525 (2019).
- 30 Chawla, K., Lee, S., Lee, B. P. *et al.* A novel low-friction surface for biomedical applications: Modification of poly(dimethylsiloxane) (PDMS) with polyethylene glycol(PEG)-DOPA-lysine. *Journal of Biomedical Materials Research Part A* **90A**, 742-749 (2009).
- 31 Harding, J. L. & Reynolds, M. M. Combating medical device fouling. *Trends in Biotechnology* **32**, 140-146 (2014).
- 32 Donlan, R. M. Problems of biofilms associated with medical devices and implants. *Medical Biofilms: Detection, Prevention and Control*, 29-49 (2003).
- 33 Shirtliff, M., Leid, J. G. & Shirtliff, M. *The role of biofilms in device-related infections*. Vol. 2 (Springer, 2009).

- 34 Wei, Y., Hung, H.-C., Sun, F. *et al.* Achieving low-fouling surfaces with oppositely charged polysaccharides via LBL assembly. *Acta Biomaterialia* **40**, 16-22 (2016).
- 35 Labeed, F. H., Sear, R. P. & Keddie, J. L. Adhesion of microorganisms to bovine submaxillary mucin coatings: effect of coating deposition conditions AU - Bushnak, Ibraheem A. *Biofouling* **26**, 387-397 (2010).
- 36 Lewis, A. L. Phosphorylcholine-based polymers and their use in the prevention of biofouling. *Colloids and Surfaces B: Biointerfaces* **18**, 261-275 (2000).
- 37 Yebra, D. M., Kiil, S. & Dam-Johansen, K. Antifouling technology—past, present and future steps towards efficient and environmentally friendly antifouling coatings. *Progress in Organic Coatings* **50**, 75-104 (2004).
- 38 Chambers, L. D., Stokes, K. R., Walsh, F. C. *et al.* Modern approaches to marine antifouling coatings. *Surface and Coatings Technology* **201**, 3642-3652 (2006).
- 39 Bixler, G. D. & Bhushan, B. Biofouling: lessons from nature. *Philosophical Transactions of the Royal Society A: Mathematical, Physical and Engineering Sciences* **370**, 2381-2417 (2012).
- 40 Kurpinski, K. T., Stephenson, J. T., Janairo, R. R. R. *et al.* The effect of fiber alignment and heparin coating on cell infiltration into nanofibrous PLLA scaffolds. *Biomaterials* **31**, 3536-3542 (2010).
- 41 Bumgardner, J. D., Wiser, R., Gerard, P. D. *et al.* Chitosan: potential use as a bioactive coating for orthopaedic and craniofacial/dental implants. *Journal of Biomaterials Science, Polymer Edition* **14**, 423-438 (2003).
- 42 Kuddannaya, S., Chuah, Y. J., Lee, M. H. *et al.* Surface chemical modification of poly(dimethylsiloxane) for the enhanced adhesion and proliferation of mesenchymal stem cells. *ACS Appl Mater Interfaces* **5**, 9777-9784 (2013).
- 43 Crouzier, T., Jang, H., Ahn, J. *et al.* Cell Patterning with Mucin Biopolymers. *Biomacromolecules* **14**, 3010-3016 (2013).
- 44 Schmidt, C. E. & Leach, J. B. Neural tissue engineering: strategies for repair and regeneration. *Annual review of biomedical engineering* **5**, 293-347 (2003).

- 45 Mistry, A. S. & Mikos, A. G. in *Regenerative medicine II* 1-22 (Springer, 2005).
- 46 Huang, B. J., Hu, J. C. & Athanasiou, K. A. Cell-based tissue engineering strategies used in the clinical repair of articular cartilage. *Biomaterials* **98**, 1-22 (2016).
- 47 Skin Tissue Engineering for Tissue Repair and Regeneration. *Tissue Engineering Part B: Reviews* **14**, 105-118 (2008).
- 48 Kim, B. S., Kwon, Y. W., Kong, J.-S. *et al.* 3D cell printing of in vitro stabilized skin model and in vivo pre-vascularized skin patch using tissue-specific extracellular matrix bioink: a step towards advanced skin tissue engineering. *Biomaterials* **168**, 38-53 (2018).
- 49 Ho, S. T. B., Hutmacher, D. W., Ekaputra, A. K. *et al.* The evaluation of a biphasic osteochondral implant coupled with an electrospun membrane in a large animal model. *Tissue Engineering. Part A* **16**, 1123–1141 (2010).
- 50 Unterman, S. A., Gibson, M., Lee, J. H. *et al.* Hyaluronic Acid-Binding Scaffold for Articular Cartilage Repair. *Tissue Engineering Part A* **18**, 2497–2506 (2012).
- 51 Yuan, Z., Huang, S., Lan, S. *et al.* Surface engineering of titanium implants with enzyme-triggered antibacterial properties and enhanced osseointegration in vivo. *Journal of Materials Chemistry B* **6**, 8090-8104 (2018).
- 52 Shi, Y., Wang, L., Niu, Y. *et al.* Fungal Component Coating Enhances Titanium Implant-Bone Integration. *Advanced Functional Materials* **28**, 1804483 (2018).
- 53 Hasani-Sadrabadi, M. M., Sarrion, P., Nakatsuka, N. *et al.* Hierarchically Patterned Polydopamine-Containing Membranes for Periodontal Tissue Engineering. *ACS nano* **13**, 3830-3838 (2019).
- 54 Block, M. S., Kent, J. N. & Kay, J. F. Evaluation of hydroxylapatite-coated titanium dental implants in dogs. *Journal of Oral and Maxillofacial Surgery* **45**, 601-607 (1987).

- 55 Le Guéhennec, L., Soueidan, A., Layrolle, P. *et al.* Surface treatments of titanium dental implants for rapid osseointegration. *Dental materials* **23**, 844-854 (2007).
- 56 Koch, S., Flanagan, T. C., Sachweh, J. S. *et al.* Fibrin-poly lactide-based tissue-engineered vascular graft in the arterial circulation. *Biomaterials* **31**, 4731-4739 (2010).
- 57 De Visscher, G., Mesure, L., Meuris, B. *et al.* Improved endothelialization and reduced thrombosis by coating a synthetic vascular graft with fibronectin and stem cell homing factor SDF-1 $\alpha$ . *Acta Biomaterialia* **8**, 1330-1338 (2012).
- 58 Kim, D., Chung, J. J., Jung, Y. *et al.* The effect of Substance P/Heparin conjugated PLCL polymer coating of bioinert ePTFE vascular grafts on the recruitment of both ECs and SMCs for accelerated regeneration. *Scientific Reports* **9**, 17083 (2019).
- 59 Lahann, J., Balcells, M., Lu, H. *et al.* Reactive polymer coatings: a first step toward surface engineering of microfluidic devices. *Analytical Chemistry* **75**, 2117-2122 (2003).
- 60 Chaubey, A. & Malhotra, B. D. Mediated biosensors. *Biosensors and Bioelectronics* **17**, 441-456 (2002).
- 61 Ronkainen, N. J., Halsall, H. B. & Heineman, W. R. Electrochemical biosensors. *Chemical Society Reviews* **39**, 1747-1763 (2010).
- 62 Pinto, V., Minas, G. & Correia-Neves, M. in *2015 IEEE 4th Portuguese Meeting on Bioengineering (ENBENG)*. 1-5 (IEEE).
- 63 Moon, J., Byun, J., Kim, H. *et al.* Surface-Independent and Oriented Immobilization of Antibody via One-Step Polydopamine/Protein G Coating: Application to Influenza Virus Immunoassay. *Macromolecular Bioscience* **19**, 1800486 (2019).
- 64 Thakur, B., Amarnath, C. A. & Sawant, S. N. Pectin coated polyaniline nanoparticles for an amperometric glucose biosensor. *RSC Advances* **4**, 40917-40923 (2014).
- 65 Kownacka, A. E., Vegelyte, D., Joosse, M. *et al.* Clinical evidence for use of a noninvasive biosensor for tear glucose as an alternative to painful finger-

- prick for diabetes management utilizing a biopolymer coating. *Biomacromolecules* **19**, 4504-4511 (2018).
- 66 Xie, X., Doloff, J. C., Yesilyurt, V. *et al.* Reduction of measurement noise in a continuous glucose monitor by coating the sensor with a zwitterionic polymer. *Nat Biomed Eng* **2**, 894-906 (2018).
- 67 Chen, Z., Mao, X., Tan, L. *et al.* Osteoimmunomodulatory properties of magnesium scaffolds coated with  $\beta$ -tricalcium phosphate. *Biomaterials* **35**, 8553-8565 (2014).
- 68 Hachim, D., LoPresti, S. T., Yates, C. C. *et al.* Shifts in macrophage phenotype at the biomaterial interface via IL-4 eluting coatings are associated with improved implant integration. *Biomaterials* **112**, 95-107 (2017).
- 69 Dias, F. G. F., Prudente, A., Siniscalchi, R. T. *et al.* Can highly purified collagen coating modulate polypropylene mesh immune-inflammatory and fibroblastic reactions? Immunohistochemical analysis in a rat model. *International Urogynecology Journal* **26**, 569-576 (2015).
- 70 Kroll, A. V., Fang, R. H. & Zhang, L. Biointerfacing and Applications of Cell Membrane-Coated Nanoparticles. *Bioconjugate Chemistry* **28**, 23-32 (2017).
- 71 Yeh, C.-Y., Hsiao, J.-K., Wang, Y.-P. *et al.* Peptide-conjugated nanoparticles for targeted imaging and therapy of prostate cancer. *Biomaterials* **99**, 1-15 (2016).
- 72 Gao, C., Lin, Z., Jurado-Sánchez, B. *et al.* Stem cell membrane-coated nanogels for highly efficient in vivo tumor targeted drug delivery. *Small* **12**, 4056-4062 (2016).
- 73 Zhu, J.-Y., Zheng, D.-W., Zhang, M.-K. *et al.* Preferential Cancer Cell Self-Recognition and Tumor Self-Targeting by Coating Nanoparticles with Homotypic Cancer Cell Membranes. *Nano Letters* **16**, 5895-5901 (2016).
- 74 Zhang, C., Qu, X., Li, J. *et al.* Biofabricated Nanoparticle Coating for Liver-Cell Targeting. *Advanced Healthcare Materials* **4**, 1972-1981 (2015).
- 75 Gao, W., Fang, R. H., Thamphiwatana, S. *et al.* Modulating Antibacterial Immunity via Bacterial Membrane-Coated Nanoparticles. *Nano Letters* **15**, 1403-1409 (2015).

- 76 Clemente-Casares, X., Blanco, J., Ambalavanan, P. *et al.* Expanding antigen-specific regulatory networks to treat autoimmunity. *Nature* **530**, 434-440 (2016).
- 77 Gulati, K., Ramakrishnan, S., Aw, M. S. *et al.* Biocompatible polymer coating of titania nanotube arrays for improved drug elution and osteoblast adhesion. *Acta Biomaterialia* **8**, 449-456 (2012).
- 78 Zhou, J., Cai, X., Cheng, K. *et al.* Release behaviors of drug loaded chitosan/calcium phosphate coatings on titanium. *Thin Solid Films* **519**, 4658-4662 (2011).
- 79 Wakerly, Z., Fell, J. T., Attwood, D. *et al.* Pectin/Ethylcellulose Film Coating Formulations for Colonic Drug Delivery. *Pharmaceutical Research* **13**, 1210-1212 (1996).
- 80 Gollwitzer, H., Ibrahim, K., Meyer, H. *et al.* Antibacterial poly(D,L-lactic acid) coating of medical implants using a biodegradable drug delivery technology. *Journal of Antimicrobial Chemotherapy* **51**, 585-591 (2003).
- 81 Lee, B.-J., Ryu, S.-G. & Cui, J.-H. Controlled release of dual drug-loaded hydroxypropyl methylcellulose matrix tablet using drug-containing polymeric coatings. *International journal of pharmaceutics* **188**, 71-80 (1999).
- 82 Bansil, R. & Turner, B. S. Mucin structure, aggregation, physiological functions and biomedical applications. *Current Opinion in Colloid & Interface Science* **11**, 164-170 (2006).
- 83 Davidson, H. J. & Kuonen, V. J. The tear film and ocular mucins. *Vet Ophthalmol* **7**, 71-77 (2004).
- 84 Johansson, M. E. V., Sjovall, H. & Hansson, G. C. The gastrointestinal mucus system in health and disease. *Nat Rev Gastroenterol Hepatol* **10**, 352-361 (2013).
- 85 Lagow, E., DeSouza, M. & Carson, D. Mammalian reproductive tract mucins. *Human Reproduction Update* **5**, 280-292 (1999).
- 86 Linden, S. K., Sutton, P., Karlsson, N. G. *et al.* Mucins in the mucosal barrier to infection. *Mucosal Immunol* **1**, 183-197 (2008).

- 87 McGuckin, M. A., Linden, S. K., Sutton, P. *et al.* Mucin dynamics and enteric pathogens. *Nat Rev Microbiol* **9**, 265-278 (2011).
- 88 Caldara, M., Friedlander, R. S., Kavanaugh, N. L. *et al.* Mucin biopolymers prevent bacterial aggregation by retaining cells in the free-swimming state. *Curr Biol* **22**, 2325-2330 (2012).
- 89 Käs Dorf, B. T., Weber, F., Petrou, G. *et al.* Mucin-Inspired Lubrication on Hydrophobic Surfaces. *Biomacromolecules* **18**, 2454-2462 (2017).
- 90 Mejías-Luque, R. & Cobler, L. MUC5AC (mucin 5AC, oligomeric mucus/gel-forming). *Atlas of Genetics and Cytogenetics in Oncology and Haematology* (2010).
- 91 Stürmer, R., Harder, S., Schlüter, H. *et al.* Commercial Porcine Gastric Mucin Preparations, also Used as Artificial Saliva, are a Rich Source for the Lectin TFF2: In Vitro Binding Studies. *ChemBioChem* **19**, 2598-2608 (2018).
- 92 Kočev ar-Nared, J., Kristl, J. & Šmid-Korbar, J. Comparative rheological investigation of crude gastric mucin and natural gastric mucus. *Biomaterials* **18**, 677-681 (1997).
- 93 Schö mig, V. J., Käs Dorf, B. T., Scholz, C. *et al.* An optimized purification process for porcine gastric mucin with preservation of its native functional properties. *RSC Advances* **6**, 44932-44943 (2016).
- 94 Svensson, O. & Arnebrant, T. Mucin layers and multilayers - Physicochemical properties and applications. *Current Opinion in Colloid & Interface Science* **15**, 395-405 (2010).
- 95 Celli, J., Gregor, B., Turner, B. *et al.* Viscoelastic Properties and Dynamics of Porcine Gastric Mucin. *Biomacromolecules* **6**, 1329-1333 (2005).
- 96 Dédinaité, A. Biomimetic lubrication. *Soft Matter* **8**, 273-284 (2012).
- 97 Greene, G. W., Banquy, X., Lee, D. W. *et al.* Adaptive mechanically controlled lubrication mechanism found in articular joints. *Proceedings of the National Academy of Sciences* **108**, 5255-5259 (2011).
- 98 Steele, B. L., Alvarez-Veronesi, M. C. & Schmidt, T. A. Molecular weight characterization of PRG4 proteins using multi-angle laser light scattering (MALLS). *Osteoarthritis and Cartilage* **21**, 498-504 (2013).

- 99 Blewis, M., Nugent-Derfus, G., Schmidt, T. *et al.* A model of synovial fluid lubricant composition in normal and injured joints. *European Cells and Materials* **13**, 26-39 (2017).
- 100 Abubacker, S., Dorosz, S., Ponjevic, D. *et al.* Full-Length Recombinant Human Proteoglycan 4 Interacts with Hyaluronan to Provide Cartilage Boundary Lubrication. *Annals of Biomedical Engineering*, 1–10 (2015).
- 101 Seror, J., Merkher, Y., Kampf, N. *et al.* Articular Cartilage Proteoglycans As Boundary Lubricants: Structure and Frictional Interaction of Surface-Attached Hyaluronan and Hyaluronan–Aggrecan Complexes. *Biomacromolecules* **12**, 3432–3443 (2011).
- 102 Bonnevie, E. D., Galesso, D., Secchieri, C. *et al.* Elastoviscous Transitions of Articular Cartilage Reveal a Mechanism of Synergy between Lubricin and Hyaluronic Acid. *PLOS ONE* **10**, e0143415 (2015).
- 103 Gomes, J. A. P., Amankwah, R., Powell-Richards, A. *et al.* Sodium hyaluronate (hyaluronic acid) promotes migration of human corneal epithelial cells in vitro. *British Journal of Ophthalmology* **88**, 821-825 (2004).
- 104 Inoue, M. & Katakami, C. The effect of hyaluronic acid on corneal epithelial cell proliferation. *Investigative Ophthalmology & Visual Science* **34**, 2313-2315 (1993).
- 105 Neuman, M. G., Nanau, R. M., Oruña-Sanchez, L. *et al.* Hyaluronic acid and wound healing. *Journal of Pharmacy & Pharmaceutical Sciences* **18**, 53-60 (2015).
- 106 Sun, C., Miao, J., Yan, J. *et al.* Applications of antibiofouling PEG-coating in electrochemical biosensors for determination of glucose in whole blood. *Electrochimica Acta* **89**, 549-554 (2013).
- 107 Ito, Y., Hasuda, H., Sakuragi, M. *et al.* Surface modification of plastic, glass and titanium by photoimmobilization of polyethylene glycol for antibiofouling. *Acta Biomaterialia* **3**, 1024-1032 (2007).
- 108 Tacar, O., Sriamornsak, P. & Dass, C. R. Doxorubicin: an update on anticancer molecular action, toxicity and novel drug delivery systems. *Journal of pharmacy and pharmacology* **65**, 157-170 (2013).

- 109 Torchilin, V. P. Recent advances with liposomes as pharmaceutical carriers. *Nat Rev Drug Discov* **4**, 145-160 (2005).
- 110 Blümmel, J., Perschmann, N., Aydin, D. *et al.* Protein repellent properties of covalently attached PEG coatings on nanostructured SiO<sub>2</sub>-based interfaces. *Biomaterials* **28**, 4739-4747 (2007).
- 111 Muszanska, A. K., Rochford, E. T. J., Gruszka, A. *et al.* Antiadhesive Polymer Brush Coating Functionalized with Antimicrobial and RGD Peptides to Reduce Biofilm Formation and Enhance Tissue Integration. *Biomacromolecules* **15**, 2019-2026 (2014).
- 112 Nejadnik, M. R., van der Mei, H. C., Norde, W. *et al.* Bacterial adhesion and growth on a polymer brush-coating. *Biomaterials* **29**, 4117-4121 (2008).
- 113 Krishnan, S., Weinman, C. J. & Ober, C. K. Advances in polymers for anti-biofouling surfaces. *Journal of Materials Chemistry* **18**, 3405-3413 (2008).
- 114 Nakanishi, T., Fukushima, S., Okamoto, K. *et al.* Development of the polymer micelle carrier system for doxorubicin. *Journal of Controlled Release* **74**, 295-302 (2001).
- 115 Zalipsky, S. Chemistry of polyethylene glycol conjugates with biologically active molecules. *Advanced Drug Delivery Reviews* **16**, 157-182 (1995).
- 116 Ostuni, E., Chapman, R. G., Holmlin, R. E. *et al.* A survey of structure–property relationships of surfaces that resist the adsorption of protein. *Langmuir* **17**, 5605-5620 (2001).
- 117 Harder, P., Grunze, M., Dahint, R. *et al.* Molecular conformation in oligo (ethylene glycol)-terminated self-assembled monolayers on gold and silver surfaces determines their ability to resist protein adsorption. *The Journal of Physical Chemistry B* **102**, 426-436 (1998).
- 118 Weinhart, M., Grunwald, I., Wyszogrodzka, M. *et al.* Linear poly (methyl glycerol) and linear polyglycerol as potent protein and cell resistant alternatives to poly (ethylene glycol). *Chemistry–An Asian Journal* **5**, 1992-2000 (2010).
- 119 Thomas, A., Müller, S. S. & Frey, H. Beyond poly (ethylene glycol): linear polyglycerol as a multifunctional polyether for biomedical and pharmaceutical applications. *Biomacromolecules* **15**, 1935-1954 (2014).

- 120 Herold, D. A., Keil, K. & Bruns, D. E. Oxidation of polyethylene glycols by alcohol dehydrogenase. *Biochemical pharmacology* **38**, 73-76 (1989).
- 121 Gaberc-Porekar, V., Zore, I., Podobnik, B. *et al.* Obstacles and pitfalls in the PEGylation of therapeutic proteins. *Current Opinion in Drug Discovery and Development* **11**, 242 (2008).
- 122 Li, L., Chen, S. & Jiang, S. Protein interactions with oligo (ethylene glycol)(OEG) self-assembled monolayers: OEG stability, surface packing density and protein adsorption. *Journal of Biomaterials Science, Polymer Edition* **18**, 1415-1427 (2007).
- 123 Khademhosseini, A., Suh, K. Y., Yang, J. M. *et al.* Layer-by-layer deposition of hyaluronic acid and poly-l-lysine for patterned cell co-cultures. *Biomaterials* **25**, 3583-3592 (2004).
- 124 Hahn, S. K. & Hoffman, A. S. Preparation and characterization of biocompatible polyelectrolyte complex multilayer of hyaluronic acid and poly-l-lysine. *International Journal of Biological Macromolecules* **37**, 227-231 (2005).
- 125 Hahn, S. K. & Hoffman, A. S. Characterization of biocompatible polyelectrolyte complex multilayer of hyaluronic acid and poly-l-lysine. *Biotechnology and Bioprocess Engineering* **9**, 179-183 (2004).
- 126 Orive, G., Tam, S. K., Pedraz, J. L. *et al.* Biocompatibility of alginate-poly-l-lysine microcapsules for cell therapy. *Biomaterials* **27**, 3691-3700 (2006).
- 127 Ai, H. Layer-by-layer capsules for magnetic resonance imaging and drug delivery. *Advanced Drug Delivery Reviews* **63**, 772-788 (2011).
- 128 Strand, B. L., Ryan, L., Veld, P. I. t. *et al.* Poly-L-Lysine Induces Fibrosis on Alginate Microcapsules via the Induction of Cytokines. *Cell Transplantation* **10**, 263-275 (2001).
- 129 Fischer, D., Li, Y., Ahlemeyer, B. *et al.* In vitro cytotoxicity testing of polycations: influence of polymer structure on cell viability and hemolysis. *Biomaterials* **24**, 1121-1131 (2003).
- 130 Zhang, F. & Srinivasan, M. P. Self-Assembled Molecular Films of Aminosilanes and Their Immobilization Capacities. *Langmuir* **20**, 2309-2314 (2004).

- 131 Sam, S., Touahir, L., Salvador Andresa, J. *et al.* Semiquantitative Study of the EDC/NHS Activation of Acid Terminal Groups at Modified Porous Silicon Surfaces. *Langmuir* **26**, 809-814 (2010).
- 132 Padwa, A. a. P., W. H.,. *Synthetic Applications of 1,3-Dipolar Cycloaddition Chemistry Toward Heterocycles and Natural Products.* (John Wiley & Sons, 2003).
- 133 Bock, V. D., Hiemstra, H. & van Maarseveen, J. H. CuI-Catalyzed Alkyne–Azide “Click” Cycloadditions from a Mechanistic and Synthetic Perspective. *European Journal of Organic Chemistry* **2006**, 51-68 (2006).
- 134 Meldal, M. & Tornøe, C. W. Cu-Catalyzed Azide–Alkyne Cycloaddition. *Chemical Reviews* **108**, 2952-3015 (2008).
- 135 Sarode, P. B., Bahekar, S. B. & Chandak, H. S. DABCO/AcOH Jointly Accelerated Copper(I)-Catalysed Cycloaddition of Azides and Alkynes on Water at Room Temperature. *Synlett* **27**, 2681–2684 (2016).
- 136 Wintermantel, E., Ha, S. *Medizintechnik.* 1379 (Springer-Verlag Berlin Heidelberg, 2009).
- 137 Kaiser, W. *Kunststoffchemie für Ingenieure.* (Hanser, 2006).
- 138 Abts, G. *Kunststoff-Wissen für Einsteiger.* (Carl Hanser Verlag GmbH Co KG, 2016).
- 139 Hellerich, W. & Harsch, G. *Werkstoff-Führer Kunststoffe.*
- 140 Puoci, F. *Advanced polymers in medicine.* (Springer, 2015).
- 141 Beal, J. H. L., Bubendorfer, A., Kemmitt, T. *et al.* A rapid, inexpensive surface treatment for enhanced functionality of polydimethylsiloxane microfluidic channels. *Biomicrofluidics* **6**, 36503-36503 (2012).
- 142 Bodas, D. & Khan-Malek, C. Formation of more stable hydrophilic surfaces of PDMS by plasma and chemical treatments. *Microelectronic Engineering* **83**, 1277-1279 (2006).
- 143 Song, F. & Ren, D. Stiffness of Cross-Linked Poly(Dimethylsiloxane) Affects Bacterial Adhesion and Antibiotic Susceptibility of Attached Cells. *Langmuir* **30**, 10354-10362 (2014).

- 144 Crouzier, T., Boettcher, K., Geonnotti, A. R. *et al.* Modulating Mucin Hydration and Lubrication by Deglycosylation and Polyethylene Glycol Binding. *Advanced Materials Interfaces* **2**, 1500308 (2015).
- 145 Kim, J., Chaudhury, M. K. & Owen, M. J. Hydrophobic Recovery of Polydimethylsiloxane Elastomer Exposed to Partial Electrical Discharge. *Journal of Colloid and Interface Science* **226**, 231-236 (2000).
- 146 Zappone, B., Ruths, M., Greene, G. W. *et al.* Adsorption, Lubrication, and Wear of Lubricin on Model Surfaces: Polymer Brush-Like Behavior of a Glycoprotein. *Biophysical journal* **92**, 1693-1708 (2006).
- 147 Yakubov, G. E., McColl, J., Bongaerts, J. H. H. *et al.* Viscous Boundary Lubrication of Hydrophobic Surfaces by Mucin. *Langmuir* **25**, 2313-2321 (2009).
- 148 Abubacker, S., Dorosz, S. G., Ponjevic, D. *et al.* Full-Length Recombinant Human Proteoglycan 4 Interacts with Hyaluronan to Provide Cartilage Boundary Lubrication. *Annals of Biomedical Engineering* **44**, 1128-1137 (2016).
- 149 Hsu, S. M. Boundary lubrication: current understanding. *Tribology Letters* **3**, 1-11 (1997).
- 150 Klein, J., Briscoe, W. H., Chen, M. *et al.* Polymer brushes and surface forces. *Polymer Adhesion, Friction, and Lubrication*, 135-176 (2013).
- 151 Lee, S. & Spencer, N. D. Sweet, hairy, soft, and slippery. *Science* **319**, 575-576 (2008).
- 152 Goda, T., Konno, T., Takai, M. *et al.* Biomimetic phosphorylcholine polymer grafting from polydimethylsiloxane surface using photo-induced polymerization. *Biomaterials* **27**, 5151-5160 (2006).
- 153 Hanawa, T. In vivo metallic biomaterials and surface modification. *Materials Science and Engineering: A* **267**, 260-266 (1999).
- 154 Boettcher, K., Grumbein, S., Winkler, U. *et al.* Adapting a commercial shear rheometer for applications in cartilage research. *Rev Sci Instrum* **85**, 093903 (2014).
- 155 Hertz, H. Über die Berührung fester elastischer Körper. *Journal für die reine und angewandte Mathematik* **92**, 156-171 (1882).

- 156 Johnston, I. D., McCluskey, D. K., Tan, C. K. L., Tracey, M. C. Mechanical characterization of bulk Sylgard 184 for microfluidics and microengineering. *Journal of Micromechanics and Microengineering* **24** (2014).
- 157 Bara, J., Chastre, E., Mahiou, J. *et al.* Gastric M1 mucin, an early oncofetal marker of colon carcinogenesis, is encoded by the MUC5AC gene. *International journal of cancer* **75**, 767-773 (1998).
- 158 De Gier, J., Mandersloot, J. G. & Van Deenen, L. L. M. Lipid composition and permeability of liposomes. *Biochimica et Biophysica Acta (BBA) - Biomembranes* **150**, 666-675 (1968).
- 159 Barza, M., Stuart, M. & Szoka, F. Effect of size and lipid composition on the pharmacokinetics of intravitreal liposomes. *Investigative Ophthalmology & Visual Science* **28**, 893-900 (1987).
- 160 Li, J., Wang, X., Zhang, T. *et al.* A review on phospholipids and their main applications in drug delivery systems. *Asian journal of pharmaceutical sciences* **10**, 81-98 (2015).
- 161 Mouritsent, O. G. & Jørgensen, K. Micro-, nano-and meso-scale heterogeneity of lipid bilayers and its influence on macroscopic membrane properties. *Molecular membrane biology* **12**, 15-20 (1995).
- 162 Ueno, M., Yoshida, S. & Horikoshi, I. Characteristics of the membrane permeability of temperature-sensitive liposome. *Bulletin of the Chemical Society of Japan* **64**, 1588-1593 (1991).
- 163 Peer, D., Karp, J. M., Hong, S. *et al.* Nanocarriers as an emerging platform for cancer therapy. *Nature nanotechnology* **2**, 751 (2007).
- 164 Huynh, N. T., Roger, E., Lautram, N. *et al.* The rise and rise of stealth nanocarriers for cancer therapy: passive versus active targeting. *Nanomedicine* **5**, 1415-1433 (2010).
- 165 Torchilin, V. P. Multifunctional nanocarriers. *Advanced Drug Delivery Reviews* **58**, 1532-1555 (2006).
- 166 Allen, T. M. & Cullis, P. R. Liposomal drug delivery systems: from concept to clinical applications. *Advanced Drug Delivery Reviews* **65**, 36-48 (2013).

- 167 Crouzier, T., Beckwitt, C. H. & Ribbeck, K. Mucin multilayers assembled through sugar-lectin interactions. *Biomacromolecules* **13**, 3401-3408 (2012).
- 168 Ponzio, F., Payamyar, P., Schneider, A. *et al.* Polydopamine films from the forgotten air/water interface. *The journal of physical chemistry letters* **5**, 3436-3440 (2014).
- 169 Sauerbrey, G. Verwendung von Schwingquarzen zur Wägung dünner Schichten und zur Mikrowägung. *Zeitschrift für Physik* **155**, 206-222 (1959).
- 170 Rodahl, M. & Kasemo, B. On the measurement of thin liquid overlayers with the quartz-crystal microbalance. *Sensors and Actuators A: Physical* **54**, 448-456 (1996).
- 171 Keiji Kanazawa, K. & Gordon, J. G. The oscillation frequency of a quartz resonator in contact with liquid. *Analytica Chimica Acta* **175**, 99-105 (1985).
- 172 Iruthayaraj, J., Olanya, G. & Claesson, P. M. Viscoelastic Properties of Adsorbed Bottle-brush Polymer Layers Studied by Quartz Crystal Microbalance — Dissipation Measurements. *The Journal of Physical Chemistry C* **112**, 15028-15036 (2008).
- 173 Voinova, M. V., Rodahl, M., Jonson, M. *et al.* Viscoelastic acoustic response of layered polymer films at fluid-solid interfaces: continuum mechanics approach. *Physica Scripta* **59**, 391 (1999).
- 174 ISO 25178-2: 2012 Geometrical product specification (GPS) - Surface texture: Areal - Part 2: Terms, definitions and surface texture parameters.
- 175 Reizer, R., Pawlus, P., Galda, L. *et al.* Modeling of worn surface topography formed in a low wear process. *Wear* **278-279**, 94-100 (2012).
- 176 Vulliez, M., Gleason, M. A., Souto-Lebel, A. *et al.* Multi-scale Curvature Analysis and Correlations with the Fatigue Limit on Steel Surfaces after Milling. *Procedia CIRP* **13**, 308-313 (2014).
- 177 Berglund, J., Brown, C. A., Rosén, B. G. *et al.* Milled die steel surface roughness correlation with steel sheet friction. *CIRP Annals* **59**, 577-580 (2010).
- 178 Biswas, S. K. & Vijayan, K. Friction and wear of PTFE — a review. *Wear* **158**, 193-211 (1992).
- 179 Kato, K. Wear in relation to friction — a review. *Wear* **241**, 151-157 (2000).

- 180 Song, J. & Schinow, V. Correlation between friction and wear properties and electrical performance of silver coated electrical connectors. *Wear* **330–331**, 400-405 (2015).
- 181 Bhushan, B., Israelachvili, J. N. & Landman, U. Nanotribology: friction, wear and lubrication at the atomic scale. *Nature* **374**, 13 (1995).
- 182 Rahaman, M. L., Zhang, L., Liu, M. *et al.* Surface roughness effect on the friction and wear of bulk metallic glasses. *Wear* **332–333**, 1231-1237 (2015).
- 183 Sawyer, W. G., Freudenberg, K. D., Bhimaraj, P. *et al.* A study on the friction and wear behavior of PTFE filled with alumina nanoparticles. *Wear* **254**, 573-580 (2003).
- 184 Xiong, D. & Ge, S. Friction and wear properties of UHMWPE/Al<sub>2</sub>O<sub>3</sub> ceramic under different lubricating conditions. *Wear* **250**, 242-245 (2001).
- 185 Dufils, J., Wimmer, M. A., Kunze, J. *et al.* Influence of molybdate ion and pH on the fretting corrosion of a CoCrMo – Titanium alloy couple. *Biotribology* **11**, 20-28 (2017).
- 186 Kienle, S., Boettcher, K., Wiegleb, L. *et al.* Comparison of friction and wear of articular cartilage on different length scales. *Journal of Biomechanics* **48**, 3052–3058 (2015).
- 187 McGann, M. E., Vahdati, A. & Wagner, D. R. Methods to assess in vitro wear of articular cartilage. *Proceedings of the Institution of Mechanical Engineers, Part H: Journal of Engineering in Medicine* **226**, 612–622 (2012).
- 188 Klaassen, M., Schipper, D. J. & Masen, M. A. Influence of the relative humidity and the temperature on the in-vivo friction behaviour of human skin. *Biotribology* **6**, 21-28 (2016).
- 189 Trevino, R. L., Stoia, J., Laurent, M. P. *et al.* Establishing a live cartilage-on-cartilage interface for tribological testing. *Biotribology* **9**, 1-11 (2017).
- 190 Yin, W., Liu, Z., Tian, P. *et al.* Tribological properties of wood as a cellular fiber-reinforced composite. *Biotribology* **5**, 67-73 (2016).
- 191 Dunn, A. C., Uruena, J. M., Puig, E. *et al.* Friction Coefficient Measurement of an In Vivo Murine Cornea. *Tribology Letters* **49**, 145-149 (2013).
- 192 Shi, L., Sikavitsas, V. I. & Striolo, A. Experimental Friction Coefficients for Bovine Cartilage Measured with a Pin-on-Disk Tribometer: Testing

- Configuration and Lubricant Effects. *Annals of Biomedical Engineering* **39**, 132–146 (2011).
- 193 Caligaris, M. & Ateshian, G. A. Effects of sustained interstitial fluid pressurization under migrating contact area, and boundary lubrication by synovial fluid, on cartilage friction. *Osteoarthritis and Cartilage* **16**, 1220–1227 (2008).
- 194 Bostan, L. E., Noble, C., Smulders, N. *et al.* Measurement of Friction-induced Changes in Pig Aorta Fibre Organization by Non-invasive Imaging as a Model for Detecting the Tissue Response to Endovascular Catheters. *Biotribology* **12**, 24-32 (2017).
- 195 Dellimore, K. H. J., Mank, A. J. G., Wojnowski, J., Noble, C., Franklin, S. E. Evaluation of catheter-induced tribological damage to porcine aorta using infra-red spectroscopy. *Biotribology* (2016).
- 196 Hofmann, G., Jubin, P., Gerligand, P., Gallois-Bernos, A., Franklin, S., Smulders, N., Gerhardt, L., Valster, S. In-vitro method for determining corneal tissue friction and damage due to contact lens sliding. *Biotribology* **5**, 23-30 (2016).
- 197 Roba, M., Duncan, E. G., Hill, G. A. *et al.* Friction Measurements on Contact Lenses in Their Operating Environment. *Tribology Letters* **44**, 387-397 (2011).
- 198 Li, J., Zhou, F. & Wang, X. Modify the friction between steel ball and PDMS disk under water lubrication by surface texturing. *Meccanica* **46**, 499-507 (2011).
- 199 Myant, C., Spikes, H. A. & Stokes, J. R. Influence of load and elastic properties on the rolling and sliding friction of lubricated compliant contacts. *Tribology International* **43**, 55-63 (2010).
- 200 Menezes, P. L., Kishore, Kailas, S. V. *et al.* Friction and transfer layer formation in polymer–steel tribo-system: Role of surface texture and roughness parameters. *Wear* **271**, 2213-2221 (2011).
- 201 Chang, D. P., Abu-Lail, N. I., Guilak, F. *et al.* Conformational Mechanics, Adsorption, and Normal Force Interactions of Lubricin and Hyaluronic Acid on Model Surfaces. *Langmuir* **24**, 1183-1193 (2008).

- 202 Biegler, M., Delius, J., Käs Dorf, B. T. *et al.* Cationic astringents alter the tribological and rheological properties of human saliva and salivary mucin solutions. *Biotribology* **6**, 12-20 (2016).
- 203 Gallagher, E., Gormley, T. & Arendt, E. K. Recent advances in the formulation of gluten-free cereal-based products. *Trends in Food Science & Technology* **15**, 143-152 (2004).
- 204 Sabanis, D., Lebesi, D. & Tzia, C. Effect of dietary fibre enrichment on selected properties of gluten-free bread. *LWT-Food Science and Technology* **42**, 1380-1389 (2009).
- 205 Ziobro, R., Korus, J., Juszcak, L. *et al.* Influence of inulin on physical characteristics and staling rate of gluten-free bread. *Journal of Food Engineering* **116**, 21-27 (2013).
- 206 Ziobro, R., Korus, J., Witczak, M. *et al.* Influence of modified starches on properties of gluten-free dough and bread. Part II: Quality and staling of gluten-free bread. *Food Hydrocolloids* **29**, 68-74 (2012).
- 207 Dielectric Corporation Product Information: <http://www.dielectriccorp.com/downloads/thermoplastics/teflon.pdf>, 22.03.2018.
- 208 Borruto, A., Crivellone, G. & Marani, F. Influence of surface wettability on friction and wear tests. *Wear* **222**, 57-65 (1998).
- 209 Wieleba, W. The statistical correlation of the coefficient of friction and wear rate of PTFE composites with steel counterface roughness and hardness. *Wear* **252**, 719-729 (2002).
- 210 Eguiluz, R. C. A., Cook, S. G., Brown, C. N. *et al.* Fibronectin mediates enhanced wear protection of lubricin during shear. *Biomacromolecules* **16**, 2884–2894 (2015).
- 211 Lee, D. W., Banquy, X. & Israelachvili, J. N. PNAS Plus: Stick-slip friction and wear of articular joints. *Proceedings of the National Academy of Sciences* **110**, E567–E574 (2013).
- 212 Steiger-Ronay, V., Tektas, S., Attin, T. *et al.* Comparison of Profilometric and Microindentation Analyses for Determining the Impact of Saliva on the Abrasion of Initially Eroded Enamel. *Caries Res* **53**, 33-40 (2019).

- 213 Sweeney, M. P., Bagg, J., Baxter, W. P. *et al.* Clinical trial of a mucin-containing oral spray for treatment of xerostomia in hospice patients. *Palliat Med* **11**, 225–232 (1997).
- 214 Rubinstein, M. & Colby, R. H. *Polymer physics*. Vol. 23 (Oxford university press New York, 2003).
- 215 UniProt. a worldwide hub of protein knowledge. *Nucleic acids research* **47**, D506-D515 (2018).
- 216 Harpaz, Y., Gerstein, M. & Chothia, C. Volume changes on protein folding. *Structure* **2**, 641-649 (1994).
- 217 Stokes, J. R., Macakova, L., Chojnicka-Paszun, A. *et al.* Lubrication, adsorption, and rheology of aqueous polysaccharide solutions. *Langmuir* **27**, 3474-3484 (2011).
- 218 Cao, X., Bansil, R., Bhaskar, K. R. *et al.* pH-Dependent Conformational Change of Gastric Mucin Leads to Sol-Gel Transition. *Biophysical Journal* **76**, 1250-1258 (1999).
- 219 Celli, J. P., Turner, B. S., Afdhal, N. H. *et al.* Rheology of gastric mucin exhibits a pH-dependent sol-gel transition. *Biomacromolecules* **8**, 1580–1586 (2007).
- 220 Noakes, T. D. Fluid and electrolyte disturbances in heat illness. *International journal of sports medicine* **19**, S146-S149 (1998).
- 221 Crouzier, T., Beckwitt, C. H. & Ribbeck, K. Mucin Multilayers Assembled through Sugar–Lectin Interactions. *Biomacromolecules* **13**, 3401-3408 (2012).
- 222 Pettersson, T., Feldötö, Z., Claesson, P. M. *et al.* in *Surface and Interfacial Forces – From Fundamentals to Applications*. (eds Günter K. Auernhammer, Hans-Jürgen Butt, & Doris Vollmer) 1-10 (Springer Berlin Heidelberg).
- 223 Zhang, C., Liu, Y., Liu, Z. *et al.* Regulation Mechanism of Salt Ions for Superlubricity of Hydrophilic Polymer Cross-Linked Networks on Ti6Al4V. *Langmuir* **33**, 2133-2140 (2017).
- 224 Jhon, Y. K., Bhat, R. R., Jeong, C. *et al.* Salt-induced depression of lower critical solution temperature in a surface-grafted neutral thermoresponsive polymer. *Macromolecular rapid communications* **27**, 697-701 (2006).

- 225 Beltzer, E. K., Fortunato, C. K., Guaderrama, M. M. *et al.* Salivary flow and alpha-amylase: collection technique, duration, and oral fluid type. *Physiology & behavior* **101**, 289-296 (2010).
- 226 Nasioudis, D., Beghini, J., Bongiovanni, A. M. *et al.*  $\alpha$ -Amylase in vaginal fluid: association with conditions favorable to dominance of Lactobacillus. *Reproductive Sciences* **22**, 1393-1398 (2015).
- 227 Bonavida, B. & Sapse, A. T. Human tear lysozyme: II. Quantitative determination with standard Schirmer strips. *American journal of ophthalmology* **66**, 70-76 (1968).
- 228 Roba, M., Naka, M., Gautier, E. *et al.* The adsorption and lubrication behavior of synovial fluid proteins and glycoproteins on the bearing-surface materials of hip replacements. *Biomaterials* **30**, 2072-2078 (2009).
- 229 Sriamornsak, P., Wattanakorn, N. & Takeuchi, H. Study on the mucoadhesion mechanism of pectin by atomic force microscopy and mucin-particle method. *Carbohydrate polymers* **79**, 54-59 (2010).
- 230 Haghtalab, A., Mokhtarani, B. & Maurer, G. Experimental Results and Thermodynamic Modeling of the Partitioning of Lysozyme, Bovine Serum Albumin, and  $\alpha$ -Amylase in Aqueous Two-Phase Systems of PEG and (K<sub>2</sub>HPO<sub>4</sub> or Na<sub>2</sub>SO<sub>4</sub>). *Journal of Chemical & Engineering Data* **48**, 1170-1177 (2003).
- 231 Feiler, A. A., Sahlholm, A., Sandberg, T. *et al.* Adsorption and viscoelastic properties of fractionated mucin (BSM) and bovine serum albumin (BSA) studied with quartz crystal microbalance (QCM-D). *Journal of colloid and interface science* **315**, 475-481 (2007).
- 232 Ito, S., Shimohata, N., Iwanaga, S. *et al.* Prevention of intubation-induced mucosal damage using a tube coated with 2-methacryloyloxyethyl phosphorylcholine polymer. *European Journal of Anaesthesiology (EJA)* **29**, 100-104 (2012).
- 233 Bishop, M. J. Mechanisms of laryngotracheal injury following prolonged tracheal intubation. *Chest* **96**, 185-187 (1989).
- 234 Travess, H., Roberts-Harry, D. & Sandy, J. Orthodontics. Part 6: Risks in orthodontic treatment. *British dental journal* **196**, 71-77 (2004).

- 235 Kvam, E., Gjerdet, N. R. & Bondevik, O. Traumatic ulcers and pain during orthodontic treatment. *Community dentistry and oral epidemiology* **15**, 104-107 (1987).
- 236 Scheurer, P. A., Firestone, A. R. & Bürgin, W. B. Perception of pain as a result of orthodontic treatment with fixed appliances. *The European Journal of Orthodontics* **18**, 349-357 (1996).
- 237 ISO 10993-1:2018 Biological evaluation of medical devices Part 1: Evaluation and testing within a risk management process.
- 238 Rose, G. D., Fleming, P. J., Banavar, J. R. *et al.* A backbone-based theory of protein folding. *Proceedings of the National Academy of Sciences of the United States of America* **103**, 16623-16633 (2006).
- 239 Argüeso, P. & Sumiyoshi, M. Characterization of a carbohydrate epitope defined by the monoclonal antibody H185: sialic acid O-acetylation on epithelial cell-surface mucins. *Glycobiology* **16**, 1219-1228 (2006).
- 240 Madsen, J. B., Svensson, B., Abou Hachem, M. *et al.* Proteolytic Degradation of Bovine Submaxillary Mucin (BSM) and Its Impact on Adsorption and Lubrication at a Hydrophobic Surface. *Langmuir* **31**, 8303-8309 (2015).
- 241 Ruoslahti, E. & Yamaguchi, Y. Proteoglycans as modulators of growth factor activities. *Cell* **64**, 867-869 (1991).
- 242 Mazzucco, D., Scott, R. & Spector, M. Composition of joint fluid in patients undergoing total knee replacement and revision arthroplasty: correlation with flow properties. *Biomaterials* **25** (2004).
- 243 Seror, J., Merkher, Y., Kampf, N. *et al.* Articular cartilage proteoglycans as boundary lubricants: structure and frictional interaction of surface-attached hyaluronan and hyaluronan--aggrecan complexes. *Biomacromolecules* **12**, 3432-3443 (2011).
- 244 Samaroo, K. J., Tan, M., Andresen Eguiluz, R. C. *et al.* Tunable Lubricin-mimetics for Boundary Lubrication of Cartilage. *Biotribology* **9**, 18-23 (2017).
- 245 Werb, M., García, C. F., Bach, N. C. *et al.* Surface topology affects wetting behavior of *Bacillus subtilis* biofilms. *npj Biofilms and Microbiomes* **3**, 11 (2017).

- 246 Ishiyama, C. & Higo, Y. Effects of humidity on Young's modulus in poly(methyl methacrylate). *Journal of Polymer Science Part B: Polymer Physics* **40**, 460-465 (2002).
- 247 Wah, T. Y. Nature-inspired membrane set to reduce purification costs. *Membrane Technology* **2016**, 7 (2016).
- 248 Issaq, H. J. *A century of separation science*. (CRC Press, 2001).
- 249 Lundanes, E. *Chromatography : Basic Principles, Sample Preparations and Related Methods*. (2013).
- 250 El-Safty, S. & Shenashen, M. A. Size-selective separations of biological macromolecules on mesocylinder silica arrays. *Analytica Chimica Acta* **694**, 151-161 (2011).
- 251 El-Safty, S. A., Shenashen, M. A., Ismael, M. *et al.* Mesocylindrical Aluminosilica Monolith Biocaptors for Size-Selective Macromolecule Cargos. *Advanced Functional Materials* **22**, 3013-3021 (2012).
- 252 Yiu, H. H. P., Botting, C. H., Botting, N. P. *et al.* Size selective protein adsorption on thiol-functionalised SBA-15 mesoporous molecular sieve. *Physical Chemistry Chemical Physics* **3**, 2983-2985 (2001).
- 253 Hu, J., Chen, G. & Lo, I. M. C. Selective Removal of Heavy Metals from Industrial Wastewater Using Maghemite Nanoparticle: Performance and Mechanisms. *Journal of Environmental Engineering* **132**, 709-715 (2006).
- 254 Sdiri, A., Khairy, M., Bouaziz, S. *et al.* A natural clayey adsorbent for selective removal of lead from aqueous solutions. *Applied Clay Science* **126**, 89-97 (2016).
- 255 Zhou, J., Ellis, A. V. & Voelcker, N. H. Recent developments in PDMS surface modification for microfluidic devices. *ELECTROPHORESIS* **31**, 2-16 (2010).
- 256 Muck, A. & Svatoš, A. Chemical modification of polymeric microchip devices. *Talanta* **74**, 333-341 (2007).
- 257 Diaz-Quijada, G. A. & Wayner, D. D. M. A Simple Approach to Micropatterning and Surface Modification of Poly(dimethylsiloxane). *Langmuir* **20**, 9607-9611 (2004).

- 258 Mikos, A. G., Thorsen, A. J., Czerwonka, L. A. *et al.* Preparation and characterization of poly(l-lactic acid) foams. *Polymer* **35**, 1068-1077 (1994).
- 259 Thomson, R. C., Yaszemski, M. J., Powers, J. M. *et al.* Fabrication of biodegradable polymer scaffolds to engineer trabecular bone. *Journal of Biomaterials Science, Polymer Edition* **7**, 23-38 (1996).
- 260 Bellan, L. M., Singh, S. P., Henderson, P. W. *et al.* Fabrication of an artificial 3-dimensional vascular network using sacrificial sugar structures. *Soft Matter* **5**, 1354-1357 (2009).
- 261 Kim, D. & Herr, A. E. Protein immobilization techniques for microfluidic assays. *Biomicrofluidics* **7**, 041501 (2013).
- 262 Mao, H., Yang, T. & Cremer, P. S. Design and Characterization of Immobilized Enzymes in Microfluidic Systems. *Analytical Chemistry* **74**, 379-385 (2002).
- 263 Toepke, M. W. & Beebe, D. J. PDMS absorption of small molecules and consequences in microfluidic applications. *Lab on a Chip* **6**, 1484-1486 (2006).
- 264 Shi, L. & Caldwell, K. D. Mucin Adsorption to Hydrophobic Surfaces. *Journal of Colloid and Interface Science* **224**, 372-381 (2000).
- 265 Lee, S., Muller, M., Rezwan, K. *et al.* Porcine gastric mucin (PGM) at the water/poly(dimethylsiloxane) (PDMS) interface: influence of pH and ionic strength on its conformation, adsorption, and aqueous lubrication properties. *Langmuir* **21**, 8344-8353 (2005).
- 266 Lieleg, O., Vladescu, I. & Ribbeck, K. Characterization of particle translocation through mucin hydrogels. *Biophys J* **98**, 1782-1789 (2010).
- 267 Olmsted, S. S., Padgett, J. L., Yudin, A. I. *et al.* Diffusion of macromolecules and virus-like particles in human cervical mucus. *Biophys J* **81**, 1930-1937 (2001).
- 268 Nowald, C., Penk, A., Chiu, H. Y. *et al.* A Selective Mucin/Methylcellulose Hybrid Gel with Tailored Mechanical Properties. *Macromol Biosci* (2016).
- 269 Lai, S. K., O'Hanlon, D. E., Harrold, S. *et al.* Rapid transport of large polymeric nanoparticles in fresh undiluted human mucus. *Proc Natl Acad Sci U S A* **104**, 1482-1487 (2007).

- 270 Norris, D. A. & Sinko, P. J. Effect of size, surface charge, and hydrophobicity on the translocation of polystyrene microspheres through gastrointestinal mucin. *Journal of Applied Polymer Science* **63**, 1481-1492 (1997).
- 271 Green, N. M. Avidin. *Adv Protein Chem* **29**, 85-133 (1975).
- 272 Lee, H., Dellatore, S. M., Miller, W. M. *et al.* Mussel-inspired surface chemistry for multifunctional coatings. *Science* **318**, 426-430 (2007).
- 273 Burzio, L. A. & Waite, J. H. Cross-Linking in Adhesive Quinoproteins: Studies with Model Decapeptides. *Biochemistry* **39**, 11147-11153 (2000).
- 274 LaVoie, M. J., Ostaszewski, B. L., Weihofen, A. *et al.* Dopamine covalently modifies and functionally inactivates parkin. *Nat Med* **11**, 1214-1221 (2005).
- 275 Sugumaran, M., Dali, H. & Semensi, V. Chemical- and cuticular phenoloxidase- mediated synthesis of cysteinyl-catechol adducts. *Archives of Insect Biochemistry and Physiology* **11**, 127-137 (1989).
- 276 Shi, L., Ardehali, R., Caldwell, K. D. *et al.* Mucin coating on polymeric material surfaces to suppress bacterial adhesion. *Colloids and Surfaces B: Biointerfaces* **17**, 229-239 (2000).
- 277 Sandberg, T., Carlsson, J. & Ott, M. K. Mucin Coatings Suppress Neutrophil Adhesion to a Polymeric Model Biomaterial. *Microscopy Research and Technique* **70**, 864-868 (2007).
- 278 Co, J. Y., Crouzier, T. & Ribbeck, K. Probing the Role of Mucin-Bound Glycans in Bacterial Repulsion by Mucin Coatings. *Advanced Materials Interfaces* **2**, 1500179 (2015).
- 279 Janairo, R. R. R., Zhu, Y., Chen, T. *et al.* Mucin Covalently Bonded to Microfibers Improves the Patency of Vascular Grafts. *Tissue Engineering. Part A* **20**, 285-293 (2014).
- 280 Frenkel, E. S. & Ribbeck, K. Salivary mucins in host defense and disease prevention. *Journal of Oral Microbiology* **7**, 10.3402/jom.v3407.29759 (2015).
- 281 Arora, S. K., Ritchings, B. W., Almira, E. C. *et al.* The *Pseudomonas aeruginosa* Flagellar Cap Protein, FliD, Is Responsible for Mucin Adhesion. *Infection and Immunity* **66**, 1000-1007 (1998).

- 282 Lillehoj, E. P., Kim, B. T. & Kim, K. C. Identification of *Pseudomonas aeruginosa* flagellin as an adhesin for Muc1 mucin. *American Journal of Physiology-Lung Cellular and Molecular Physiology* **282**, L751-L756 (2002).
- 283 Scharfman, A., Arora, S. K., Delmotte, P. *et al.* Recognition of Lewis x Derivatives Present on Mucins by Flagellar Components of *Pseudomonas aeruginosa*. *Infection and Immunity* **69**, 5243-5248 (2001).
- 284 Reddy, M. S. Human tracheobronchial mucin: purification and binding to *Pseudomonas aeruginosa*. *Infection and Immunity* **60**, 1530-1535 (1992).
- 285 Tang, L. & Eaton, J. W. Inflammatory Responses to Biomaterials. *American Journal of Clinical Pathology* **103**, 466-471 (1995).
- 286 Mahmoudi, M., Zhao, M., Matsuura, Y. *et al.* Infection-resistant MRI-visible scaffolds for tissue engineering applications. *BioImpacts : BI* **6**, 111-115 (2016).
- 287 Nathens, A. & Dellinger, E. Surgical site infections. *Current Treatment Options in Infectious Diseases* **2**, 347-358 (2000).
- 288 Zimmerli, W., Trampuz, A. & Ochsner, P. E. Prosthetic-joint infections. *N Engl J Med* **351**, 1645-1654 (2004).
- 289 Ahmed, W., Zhai, Z. & Gao, C. Adaptive antibacterial biomaterial surfaces and their applications. *Materials Today Bio* **2**, 100017 (2019).
- 290 Gao, P., Nie, X., Zou, M. *et al.* Recent advances in materials for extended-release antibiotic delivery system. *The Journal Of Antibiotics* **64**, 625 (2011).
- 291 Li, D., Li, Y., Shrestha, A. *et al.* Effects of Programmed Local Delivery from a Micro/Nano-Hierarchical Surface on Titanium Implant on Infection Clearance and Osteogenic Induction in an Infected Bone Defect. *Advanced Healthcare Materials* **8**, 1900002 (2019).
- 292 Yuan, P., Qiu, X., Wang, X. *et al.* Substrate-Independent Coating with Persistent and Stable Antifouling and Antibacterial Activities to Reduce Bacterial Infection for Various Implants. *Advanced Healthcare Materials* **8**, 1801423 (2019).
- 293 Li, J., Mutreja, I., Hooper, G. J. *et al.* Combined Infection Control and Enhanced Osteogenic Differentiation Capacity on Additive Manufactured

- Ti-6Al-4V are Mediated via Titania Nanotube Delivery of Novel Biofilm Inhibitors. *Advanced Materials Interfaces* **7**, 1901963 (2020).
- 294 Escobar, A., Muzzio, N. E., Andreozzi, P. *et al.* Antibacterial Layer-by-Layer Films of Poly(acrylic acid)–Gentamicin Complexes with a Combined Burst and Sustainable Release of Gentamicin. *Advanced Materials Interfaces* **6**, 1901373 (2019).
- 295 Jiranek, W. A., Hanssen, A. D. & Greenwald, A. S. Antibiotic-loaded bone cement for infection prophylaxis in total joint replacement. *JBJS* **88**, 2487-2500 (2006).
- 296 Wu, K., Chen, Y.-C., Hsu, Y.-M. *et al.* Enhancing drug release from antibiotic-loaded bone cement using porogens. *JAAOS-Journal of the American Academy of Orthopaedic Surgeons* **24**, 188-195 (2016).
- 297 Ezazi, N. Z., Shahbazi, M.-A., Shatalin, Y. V. *et al.* Conductive vancomycin-loaded mesoporous silica polypyrrole-based scaffolds for bone regeneration. *International journal of pharmaceutics* **536**, 241-250 (2018).
- 298 Zhang, Y., Liang, R.-j., Xu, J.-j. *et al.* Efficient induction of antimicrobial activity with vancomycin nanoparticle-loaded poly (trimethylene carbonate) localized drug delivery system. *International journal of nanomedicine* **12**, 1201 (2017).
- 299 Wei, T., Yu, Q. & Chen, H. Responsive and Synergistic Antibacterial Coatings: Fighting against Bacteria in a Smart and Effective Way. *Advanced Healthcare Materials* **8**, 1801381 (2019).
- 300 Xu, Q., Li, X., Jin, Y. *et al.* Bacterial self-defense antibiotics release from organic–inorganic hybrid multilayer films for long-term anti-adhesion and biofilm inhibition properties. *Nanoscale* **9**, 19245-19254 (2017).
- 301 Albright, V., Zhuk, I., Wang, Y. *et al.* Self-defensive antibiotic-loaded layer-by-layer coatings: Imaging of localized bacterial acidification and pH-triggering of antibiotic release. *Acta Biomaterialia* **61**, 66-74 (2017).
- 302 Hu, J., Quan, Y., Lai, Y. *et al.* A smart aminoglycoside hydrogel with tunable gel degradation, on-demand drug release, and high antibacterial activity. *Journal of Controlled Release* **247**, 145-152 (2017).

- 303 Ofokansi, K., Adikwu, M. & Okore, V. Preparation and evaluation of mucin-gelatin mucoadhesive microspheres for rectal delivery of ceftriaxone sodium. *Drug development and industrial pharmacy* **33**, 691-700 (2007).
- 304 Builders, P. F., Kunle, O. O., Okpaku, L. C. *et al.* Preparation and evaluation of mucinated sodium alginate microparticles for oral delivery of insulin. *European Journal of Pharmaceutics and Biopharmaceutics* **70**, 777-783 (2008).
- 305 Duffy, C. V., David, L. & Crouzier, T. Covalently-crosslinked mucin biopolymer hydrogels for sustained drug delivery. *Acta Biomaterialia* **20**, 51-59 (2015).
- 306 Verdugo, P. Goblet cells secretion and mucogenesis. *Annual review of physiology* **52**, 157-176 (1990).
- 307 Espinosa, M., Noe, G., Troncoso, C. *et al.* Acidic pH and increasing [Ca<sup>2+</sup>] reduce the swelling of mucins in primary cultures of human cervical cells. *Human Reproduction* **17**, 1964-1972 (2002).
- 308 Verdugo, P., Deyrup-Olsen, I., Aitken, M. *et al.* Molecular mechanism of mucin secretion: I. The role of intragranular charge shielding. *Journal of Dental Research* **66**, 506-508 (1987).
- 309 Verdugo, P., Deyrup-Olsen, I., Martin, A. W. *et al.* in *Mechanics of swelling* 671-681 (Springer, 1992).
- 310 Holstein, T. & Tardent, P. An ultrahigh-speed analysis of exocytosis: nematocyst discharge. *Science* **223**, 830-833 (1984).
- 311 Pollack, G. H. The cell as a biomaterial. *Journal of Materials Science: Materials in Medicine* **13**, 811-821 (2002).
- 312 Varma, B., Demers, A., Jamieson, A. *et al.* Light scattering studies of the effect of Ca<sup>2+</sup> on the structure of porcine submaxillary mucin. *Biopolymers: Original Research on Biomolecules* **29**, 441-448 (1990).
- 313 Bastardo, L., Claesson, P. & Brown, W. Interactions between mucin and alkyl sodium sulfates in solution. A light scattering study. *Langmuir* **18**, 3848-3853 (2002).

- 314 Vagenende, V., Yap, M. G. & Trout, B. L. Mechanisms of protein stabilization and prevention of protein aggregation by glycerol. *Biochemistry* **48**, 11084-11096 (2009).
- 315 Schoemig, V., Isik, E., Martin, L. *et al.* Solid liquid liquid extraction of porcine gastric mucins from homogenized animal material. *RSC Advances* **7**, 39708-39717 (2017).
- 316 Segur, J. & Miner, C. Sugar solubility, sucrose and dextrose in aqueous glycerol. *Journal of Agricultural and Food Chemistry* **1**, 567-569 (1953).
- 317 Nowald, C., Käs Dorf, B. & Lieleg, O. Controlled nanoparticle release from a hydrogel by DNA-mediated particle disaggregation. *Journal of Controlled Release* **246**, 71-78 (2017).
- 318 Kimna, C. & Lieleg, O. Engineering an orchestrated release avalanche from hydrogels using DNA-nanotechnology. *Journal of Controlled Release* **304**, 19-28 (2019).
- 319 Islam, M. A., Firdous, J., Choi, Y.-J. *et al.* Design and application of chitosan microspheres as oral and nasal vaccine carriers: an updated review. *International journal of nanomedicine* **7**, 6077 (2012).
- 320 Li, L., Gao, J. & Wang, Y. Evaluation of cyto-toxicity and corrosion behavior of alkali-heat-treated magnesium in simulated body fluid. *Surface and Coatings Technology* **185**, 92-98 (2004).
- 321 Zhang, E., Xu, L., Yu, G. *et al.* In vivo evaluation of biodegradable magnesium alloy bone implant in the first 6 months implantation. *Journal of Biomedical Materials Research Part A* **90A**, 882-893 (2009).
- 322 Windhagen, H., Radtke, K., Weizbauer, A. *et al.* Biodegradable magnesium-based screw clinically equivalent to titanium screw in hallux valgus surgery: short term results of the first prospective, randomized, controlled clinical pilot study. *BioMedical Engineering OnLine* **12**, 62 (2013).
- 323 Wolf, F. I. & Trapani, V. Cell (patho) physiology of magnesium. *Clinical science* **114**, 27-35 (2008).
- 324 Yan, H., Chircov, C., Zhong, X. *et al.* Reversible Condensation of Mucins into Nanoparticles. *Langmuir* **34**, 13615-13625 (2018).

- 325 UniProt. A worldwide hub of protein knowledge. *Nucleic acids research* **47**, D506-D515 (2019).
- 326 Rosenstock, J., Smith, L., Gurney, M. *et al.* Comparison of single-dose tetracycline hydrochloride to conventional therapy of urinary tract infections. *Antimicrobial agents and chemotherapy* **27**, 652-654 (1985).
- 327 Winkelhoff, A. J. V., Rams, T. E. & Slots, J. Systemic antibiotic therapy in periodontics. *Periodontology 2000* **10**, 45-78 (1996).
- 328 *The European Committee on Antimicrobial Susceptibility Testing, Breakpoint tables for interpretation of MICs and zone diameters, version 9.0*, <[http://www.eucast.org/clinical\\_breakpoints/](http://www.eucast.org/clinical_breakpoints/)> (2019).
- 329 Schierholz, J. & Beuth, J. Implant infections: a haven for opportunistic bacteria. *Journal of Hospital Infection* **49**, 87-93 (2001).
- 330 Wardlow, R., Bing, C., VanOsdol, J. *et al.* Targeted antibiotic delivery using low temperature-sensitive liposomes and magnetic resonance-guided high-intensity focused ultrasound hyperthermia. *International Journal of Hyperthermia* **32**, 254-264 (2016).
- 331 Polak, R., Crouzier, T., Lim, R. M. *et al.* Sugar-mediated disassembly of mucin/lectin multilayers and their use as pH-Tolerant, on-demand sacrificial layers. *Biomacromolecules* **15**, 3093-3098 (2014).
- 332 Schwefel, D., Maierhofer, C., Beck, J. G. *et al.* Structural basis of multivalent binding to wheat germ agglutinin. *Journal of the American Chemical Society* **132**, 8704-8719 (2010).
- 333 Nowald, C., Penk, A., Chiu, H. Y. *et al.* A selective mucin/methylcellulose hybrid gel with tailored mechanical properties. *Macromolecular bioscience* **16**, 567-579 (2016).
- 334 Lynge, M. E., van der Westen, R., Postma, A. *et al.* Polydopamine--a nature-inspired polymer coating for biomedical science. *Nanoscale* **3**, 4916-4928 (2011).
- 335 Lee, H., Dellatore, S. M., Miller, W. M., Messersmith, P. B., Mussel-Inspired Surface Chemistry for Multifunctional Coatings. *Science* (2007).
- 336 Regulation (EU) 2017/745 of the European Parliament and of the Council. (2017).

- 337 Food and Drug Administration (FDA) Title 21 CFR Parts 800-1299.
- 338 Rabuka, D., Parthasarathy, R., Lee, G. S. *et al.* Hierarchical Assembly of Model Cell Surfaces: Synthesis of Mucin Mimetic Polymers and Their Display on Supported Bilayers. *Journal of the American Chemical Society* **129**, 5462-5471 (2007).
- 339 Godula, K. & Bertozzi, C. R. Density Variant Glycan Microarray for Evaluating Cross-Linking of Mucin-like Glycoconjugates by Lectins. *Journal of the American Chemical Society* **134**, 15732-15742 (2012).
- 340 Godula, K., Rabuka, D., Nam, K. T. *et al.* Synthesis and Microcontact Printing of Dual End-Functionalized Mucin-like Glycopolymers for Microarray Applications. *Angewandte Chemie International Edition* **48**, 4973-4976 (2009).
- 341 An, J., Dédinaité, A., Nilsson, A. *et al.* Comparison of a Brush-with-Anchor and a Train-of-Brushes Mucin on Poly(methyl methacrylate) Surfaces: Adsorption, Surface Forces, and Friction. *Biomacromolecules* **15**, 1515-1525 (2014).
- 342 Li, F., Wilkins, P. P., Crawley, S. *et al.* Post-translational modifications of recombinant P-selectin glycoprotein ligand-1 required for binding to P-and E-selectin. *Journal of Biological Chemistry* **271**, 3255-3264 (1996).
- 343 Klein, J., Kumacheva, E., Mahalu, D. *et al.* Reduction of frictional forces between solid surfaces bearing polymer brushes. *Nature* **370**, 634 (1994).
- 344 Giasson, S. & Spencer, N. D. Aqueous lubrication with polymer brushes. *Aqueous Lubrication: Natural And Biomimetic Approaches* **3**, 183 (2014).
- 345 Marshall, N., Sontag, S. K. & Locklin, J. Surface-initiated polymerization of conjugated polymers. *Chemical Communications* **47**, 5681-5689 (2011).
- 346 Bialk, M., Prucker, O. & Rühle, J. Grafting of polymers to solid surfaces by using immobilized methacrylates. *Colloids and Surfaces A: Physicochemical and Engineering Aspects* **198**, 543-549 (2002).
- 347 Prucker, O. & Rühle, J. Mechanism of radical chain polymerizations initiated by azo compounds covalently bound to the surface of spherical particles. *Macromolecules* **31**, 602-613 (1998).

- 348 Ma, H., Wells, M., Beebe Jr, T. P. *et al.* Surface-initiated atom transfer radical polymerization of oligo (ethylene glycol) methyl methacrylate from a mixed self-assembled monolayer on gold. *Advanced Functional Materials* **16**, 640-648 (2006).
- 349 Tugulu, S., Arnold, A., Sielaff, I. *et al.* Protein-functionalized polymer brushes. *Biomacromolecules* **6**, 1602-1607 (2005).
- 350 Fan, X., Lin, L. & Messersmith, P. B. Cell fouling resistance of polymer brushes grafted from Ti substrates by surface-initiated polymerization: effect of ethylene glycol side chain length. *Biomacromolecules* **7**, 2443-2448 (2006).
- 351 Xiao, D., Zhang, H. & Wirth, M. Chemical modification of the surface of poly (dimethylsiloxane) by atom-transfer radical polymerization of acrylamide. *Langmuir* **18**, 9971-9976 (2002).
- 352 Tugulu, S. & Klok, H. A. in *Macromolecular symposia*. 103-109 (Wiley Online Library).
- 353 Barbey, R., Lavanant, L., Paripovic, D. *et al.* Polymer brushes via surface-initiated controlled radical polymerization: synthesis, characterization, properties, and applications. *Chemical Reviews* **109**, 5437-5527 (2009).
- 354 Kobayashi, M. & Takahara, A. Synthesis and frictional properties of poly (2, 3-dihydroxypropyl methacrylate) brush prepared by surface-initiated atom transfer radical polymerization. *Chemistry letters* **34**, 1582-1583 (2005).
- 355 Kobayashi, M., Terayama, Y., Hosaka, N. *et al.* Friction behavior of high-density poly (2-methacryloyloxyethyl phosphorylcholine) brush in aqueous media. *Soft Matter* **3**, 740-746 (2007).
- 356 Nomura, A., Okayasu, K., Ohno, K. *et al.* Lubrication mechanism of concentrated polymer brushes in solvents: effect of solvent quality and thereby swelling state. *Macromolecules* **44**, 5013-5019 (2011).
- 357 Sakata, H., Kobayashi, M., Otsuka, H. *et al.* Tribological properties of poly (methyl methacrylate) brushes prepared by surface-initiated atom transfer radical polymerization. *Polymer journal* **37**, 767 (2005).
- 358 Marczyński, M., Käsdorf, B. T., Altaner, B. *et al.* Transient binding promotes molecule penetration into mucin hydrogels by enhancing molecular partitioning. *Biomaterials Science* **6**, 3373-3387 (2018).

- 359 Yan, H., Hjorth, M., Winkeljann, B. *et al.* Mucin hydrogel glyco-modulation to investigate immune activity of mucin glycans. *bioRxiv*, 2019.2012.2018.880757 (2019).
- 360 Johansson, M. E. & Hansson, G. C. Immunological aspects of intestinal mucus and mucins. *Nature Reviews Immunology* **16**, 639 (2016).
- 361 Shan, M., Gentile, M., Yeiser, J. R. *et al.* Mucus enhances gut homeostasis and oral tolerance by delivering immunoregulatory signals. *Science* **342**, 447-453 (2013).
- 362 Wheeler, K. M., Cárcamo-Oyarce, G., Turner, B. S. *et al.* Mucin glycans attenuate the virulence of *Pseudomonas aeruginosa* in infection. *Nature Microbiology* **4**, 2146-2154 (2019).
- 363 Pinzón Martín, S., Seeberger, P. H. & Varón Silva, D. Mucins and Pathogenic Mucin-Like Molecules Are Immunomodulators During Infection and Targets for Diagnostics and Vaccines. *Frontiers in Chemistry* **7** (2019).
- 364 Yan, H., Seignez, C., Hjorth, M. *et al.* Immune-Informed Mucin Hydrogels Evade Fibrotic Foreign Body Response In Vivo. *Advanced Functional Materials*, 1902581 (2019).
- 365 Kocevar-Nared, J., Kristl, J., Smid-Korbar, J. Comparative rheological investigation of crude gastric mucin and natural gastric mucus. *Biomaterials* **18**, 677-681 (1997).
- 366 de Moraes, E. C., Cruz, A. G. & Bolini, H. M. A. Gluten-free bread: multiple time-intensity analysis, physical characterisation and acceptance test. *International journal of food science & technology* **48**, 2176-2184 (2013).
- 367 Owczarzy, R., Tataurov, A. V., Wu, Y. *et al.* IDT SciTools: a suite for analysis and design of nucleic acid oligomers. *Nucleic acids research* **36**, W163-W169 (2008).
- 368 Zadeh, J. N., Steenberg, C. D., Bois, J. S. *et al.* NUPACK: analysis and design of nucleic acid systems. *Journal of computational chemistry* **32**, 170-173 (2011).

- 369 Sheehan, J., Oates, K. & Carlstedt, I. Electron microscopy of cervical, gastric and bronchial mucus glycoproteins. *Biochemical Journal* **239**, 147-153 (1986).
- 370 Michel, N., Fabiano, A.-S., Polidori, A. *et al.* Determination of phase transition temperatures of lipids by light scattering. *Chemistry and Physics of Lipids* **139**, 11-19 (2006).
- 371 Cinelli, S., Onori, G., Zuzzi, S. *et al.* Properties of Mixed DOTAP–DPPC Bilayer Membranes as Reported by Differential Scanning Calorimetry and Dynamic Light Scattering Measurements. *The Journal of Physical Chemistry B* **111**, 10032-10039 (2007).

## Acknowledgements

At this final point of my time as a doctoral candidate, I want to express my deep gratitude towards everyone who helped to make this project a success.

Of course, my supervisor Prof. Oliver Lieleg is the first one who should be mentioned here: Thank you, Oliver, for guiding me through this important part of my career. Thank you for all the exciting projects I was able to contribute during my time here. Thank you for giving me the freedom to develop new projects, for discussing and providing ideas, for improving my writing, and for accepting my (sometimes) unconventional approach to working. I am grateful for everything I learned from you. *P.S.* I had never been responsible for the surprising occurrence of the unicorn, however, I significantly ( $p < 0.05$ ) contributed to its rapid spreading within the group and the institute :P

Second, I want to say thank you to all my collaborators and colleagues, which directly had an impact on the results of this thesis. I want to thank Prof. Thomas Crouzier and Dr. Hongji Yan from the KTH in Sweden for several exciting collaborations, which led to three publications. Thank you, guys, it was a pleasure to meet and work with you! Furthermore, I want to thank Rudolf Lehrhuber from the workshop of the physics department. Thank you, Rudi, not only for all my constructions that you put from paper to reality but also for the helpful input regarding their development. Also here, I want to thank Christian Ramoser for assisting me in the construction of my oscillatory tribology setup and Iris König-Decker for providing some really awesome illustrations. Finally (clap!), a huge thanks goes to all my students – no matter if Intern or Master - who I was allowed to supervise during my PhD time. I learned so much from each of you and I hope that you enjoyed our time together as much as me. Without you, many of my publications (and the purification patent) wouldn't have been possible. Thank you, Agnes, Philippe, Theresa, Maria, Robert, and Max!

The third in the row are all my precious friends. Without you, PhD life would have been a boring duty, but with you, it became an amazing road trip full of exciting experiences and memorable stories. Firstly, I want to thank you Mr. Käs Dorf. You n00ty n00ty m#!%\$&!?!\*&r. Thank you for all the joy and good vibes you brought into this group every day until you graduated. Thank you for our weekly extreme hardcore morning boulder sessions at f?&%!\* n 7 a.m.! Thank you for our inglorious insult battles throughout the whole institute, for sharing a common love to fabulous noises of the animal kingdom and legendary gin tastings. Also thank you for

everything I learned from you in the lab – but screw that professional shiat :P Secondly, I want to thank you, Tin. Thank you for these inappropriate jokes, for stories that made double up with laughter. Thank you for the awesome barbecue events at your place and for sharing my love for the juniper juice. As all good things come in threes it's now your turn, Dr. Falcón; not just once your sarcastic but on-point comments to everyday situations made my day. I want to thank you for all your support in whatever topic and for your ear which was always open for a talk. Thank you for all the awesome barbecue and night-out events in and around Munich city. n00t n00t Caro :D Next, I want to thank you, Jian. Thank you for being the only truly nice person I ever met, for your precisely selected jokes that always hit the nail. Thank you for introducing me to the authentic Chinese cuisine but also for the expertise you shared with me during our shared projects. I am happy to consider you my friend. I also want to thank you, Matthias, not only for everything I learned from you about protein purification but mostly for our regular walks through the beautiful nature of the Garching Campus with lots of scientific-philosophical conversations. Finally, I want to thank my friend and mentor of this dissertation project Katharina Düregger. Thank you, Kat, for all the experiences you shared with me. Thank you for your always positive and supportive character and that I always had the chance to talk to you. Also thank you for all the great time we spent together outside the campus, *e.g.* for barbecue, birthday parties, or the awesome sailing trip in Croatia three years ago.

I furthermore want to thank Dr. Elisabeth Pinker. Without you Dr. Pinker this time of my life might have failed. Thank you for scratching me up from the floor when I fell. You managed to unleash new energy in me. I will always be grateful for that. Also, a huge thanks goes to Marshall Mathers. Listening to the artistic intonation of your poetic texts was always a source of energy and motivation for me. No matter, whether I was sad, angry, bored, or cheerful, I could always find a suitable artwork in your collection to fit the ambiance. The freshest member among here – but of course no less important – is my new bro Hopfen. By stepping into my life at the beginning of 2020s quarantine time you made these days unforgettable. I loved the times we were sitting together in the garden and philosophizing about the birds flying. Maaaa!

The last section of this work is dedicated to the most important people in my life: Ceren, my brother Joshua, my dad Toni and my mom Gitti. Ceren, thank you for everything, for being my patao, my bok kafalı bebek, my mimo. You are my motivation to give the best every day. Thank you for reinventing the way I see science. Thank you for all the time we shared and will share in the future – immer

ZWEI! Joshua, thank you for critically proofreading this whole f?&%!\*n document. Thank you for introducing me to the art of typography. I hope I could fulfill most of your high standards, however, I have to apologize for not using quarter spaces where appropriate. I know I can always count on you. Thank you! Finally, I thank you for everything, dad and mom. Without you, this journey would obviously not have been possible. Your endless support throughout my whole life is the foundation for everything I did. No text, no document could summarize how grateful I am to be born as your son.



## Author Contributions

This thesis follows a total number of 9 research articles, 1 review article, 1 book chapter and 2 European patent applications to which I contributed during my time as doctoral candidate. Those publications, which built the fundament for the individual chapters, are marked in the beginning of every sub-chapter in a footnote. My individual contribution to these publications is listed below:

- 1 K. Boettcher, **B. Winkeljann**, T. A. Schmidt and O. Lieleg, *Quantification of cartilage wear morphologies in uni-directional sliding experiments: Influence of different macro-molecular lubricants*  
**Individual contribution:** I contributed to the design and performance of some experiments, the data analysis, and writing of the article.
- 2 **B. Winkeljann**, B. Käsdorf, J. Boekhoven and O. Lieleg, *Macromolecular coating enables tunable selectivity in a porous PDMS matrix*  
**Individual contribution:** I contributed to the conception of this study, the design and performance of the experiments, the data analysis, and writing of the article.
- 3 **B. Winkeljann**, A. B. Bussmann, M. G. Bauer and O. Lieleg, *Oscillatory tribology performed with a commercial shear rheometer*  
**Individual contribution:** I contributed to the conception of this study, the design and performance of the experiments, the data analysis, and I wrote the article.
- 4 H. Yan, C. Chircov, X. Zhong, **B. Winkeljann**, I. Dobryden, H.E. Nilsson, O. Lieleg, P.M. Claesson, Y.S. Hedberg, and T. Crouzier, *Reversible condensation of mucins into nanoparticles*  
**Individual contribution:** I contributed to the design and performance of some experiments and the data analysis.

- 5 M. Kiumarsi, M. Shahbazi, S. Yeganehzad, D. Majchrzak, O. Lieleg and **B. Winkeljann**, *Relation between structural, mechanical and sensory properties of gluten-free bread as affected by modified dietary fibers*  
**Individual contribution:** I contributed to the design and performance of some experiments and the data analysis.
- 6 **B. Winkeljann**, P. A. Leipold and O. Lieleg, *Macromolecular coatings enhance the tribological performance of polymer-based lubricants*  
**Individual contribution:** I contributed to the conception of this study, the design and performance of the experiments, the data analysis, and I wrote the article.
- 7 J. Song, **B. Winkeljann** and O. Lieleg, *Lubricity of manually purified porcine gastric mucin on hydrophobic surfaces at different physiologically relevant conditions*  
**Individual contribution:** I contributed to the design and performance of some experiments and the data analysis.
- 8 **B. Winkeljann**, M. G. Bauer, M. Marczyński, T. Rau, S. Sieber and O. Lieleg, *Covalent mucin coatings form stable anti-biofouling layers on a broad range of medical polymer materials*  
**Individual contribution:** I contributed to the conception of this study, the design and performance of the experiments, the data analysis, and I wrote the article.
- 9 J. Song, **B. Winkeljann** and O. Lieleg, *Biopolymer-based coatings: promising strategies to improve the biocompatibility and functionality of materials used in biomedical engineering*  
**Individual contribution:** I contributed to the conception, the literature review and writing of the review article.

- 10 C. Kimna, **B. Winkeljann**, J. Song and O. Lieleg, *Smart biopolymer-based multilayers enable consecutive drug release events on demand*  
**Individual contribution:** I contributed to the conception of this study, the design and performance of the experiments, the data analysis, and writing of the article.
- 11 M. Marczyński, **B. Winkeljann** and O. Lieleg, *Advances in mucin biopolymer research: purification, characterization and applications*  
**Individual contribution:** I contributed to the conception, the literature review and writing of the book chapter.
- 12 M. Marczyński, **B. Winkeljann**, M. Weber-Hohengrund and O. Lieleg, *Method of the effective extraction of highly functional mucin from mucin containing tissue*  
**Individual contribution:** I contributed to the conception of this invention, the design and performance of some experiments and the data analysis.
- 13 C. Kimna, **B. Winkeljann** and O. Lieleg, *Controlled release of therapeutical agents from polymer brush coatings by employing reversible polymer condensation using ionic cross-linkers*  
**Individual contribution:** I contributed to the conception of this invention, the design and performance of some experiments and the data analysis.



## List of publications

- 1 K. Boettcher, **B. Winkeljann**, T. A. Schmidt and O. Lieleg, Quantification of cartilage wear morphologies in uni-directional sliding experiments: Influence of different macromolecular lubricants, *Biotribology* **12**, 43–51 (2017)
- 2 **B. Winkeljann**, K. Boettcher, B. Balzer and O. Lieleg, Mucin coatings prevent tissue damage at the cornea-contact lens-interface, *Advanced Materials Interfaces* **19** (4) 1700186 (2017)
- 3 **B. Winkeljann**, B. Käsdorf, J. Boekhoven and O. Lieleg, Macromolecular coating enables tunable selectivity in a porous PDMS matrix, *Macromolecular Bioscience* **18** (2) 1700311 (2017)
- 4 **B. Winkeljann**, A. B. Bussmann, M. G. Bauer and O. Lieleg, Oscillatory tribology performed with a commercial shear rheometer, *Biotribology* **14**, 11-18 (2018)
- 5 H. Yan, C. Chircov, X. Zhong, **B. Winkeljann**, I. Dobryden, H.E. Nilsson, O. Lieleg, P.M. Claesson, Y.S. Hedberg, and T. Crouzier, Reversible condensation of mucins into nanoparticles, *Langmuir* **34** (45) 13615-13625 (2018)
- 6 M. Kiumarsi, M. Shahbazi, S. Yeganehzad, D. Majchrzak, O. Lieleg and **B. Winkeljann**, Relation between structural, mechanical and sensory properties of gluten-free bread as affected by modified dietary fibers, *Food Chemistry* **30**, 664-673 (2019)
- 7 **B. Winkeljann**, P. A. Leipold and O. Lieleg, Macromolecular coatings enhance the tribological performance of polymer-based lubricants, *Advanced Materials Interfaces* **6** (16) 1900366 (2019)
- 8 J. Lang, **B. Winkeljann**, O. Lieleg and C. Zollfrank, Continuous synthesis and application of novel, archaeo-inspired tackifiers from birch bark waste, *ACS Sustainable Chemistry and Engineering* **7** (15) 13157-13166 (2019)
- 9 J. Song, **B. Winkeljann** and O. Lieleg, Lubricity of manually purified porcine gastric mucin on hydrophobic surfaces at different physiologically relevant conditions, *ACS Applied Bio Materials* **2** (8) 3448-3457 (2019)

- 10 H. Yan, C. Seignez, M. Hjorth, **B. Winkeljann**, O. Lieleg, M. Phillipson and T. Crouzier, Immune-informed mucin hydrogels evade fibrotic foreign body response *in vivo*, *Advanced Functional Materials* **29** (46) 1902581 (2019)
- 11 **B. Winkeljann**, M. G. Bauer, M. Marczynski, T. Rau, S. A. Sieber and O. Lieleg, Covalent mucin coatings form stable anti-biofouling layers on a broad range of medical polymer materials, *Advanced Materials Interfaces* **7** (4) 1902069 (2020)
- 12 H. Yan, M. Hjorth, **B. Winkeljann**, I. Dobryden, O. Lieleg and T. Crouzier, Glyco-modification of mucin hydrogels to investigate their immune activity, *ACS Applied Materials and Interfaces* **12** (17) 19324–19336 (2020)
- 13 J. Song, **B. Winkeljann** and O. Lieleg, Biopolymer-based coatings: promising strategies to improve the biocompatibility and functionality of materials used in biomedical engineering, *Advanced Materials Interfaces* **7** (14) 2000850 (2020)
- 14 K. Dai, J. Rodon-Fores, C. Wanzke, **B. Winkeljann**, A. Bergmann, O. Lieleg and J. Boekhoven, Regulating chemically fueled peptide assemblies by molecular design, *Journal of the American Chemical Society* **142** (33) 14142–14149 (2020)
- 15 C. Kimna, **B. Winkeljann**, J. Song and O. Lieleg, Smart biopolymer-based multilayers enable consecutive drug release events on demand, *Advanced Materials Interfaces* **7** (19) 2000735 (2020)
- 16 M. Marczynski, **B. Winkeljann** and O. Lieleg, Advances in mucin biopolymer research: purification, characterization and applications *in* B. H. A. Rehm and M. F. Moradali, *Advances in biopolymers for biomedical and biotechnological applications*, Wiley-VCH, in press (2020)
- 17 C. Kimna, **B. Winkeljann**, J. Hoffmeister and O. Lieleg, Biopolymer-based nanoparticles with tunable mucoadhesivity efficiently deliver therapeutics across the corneal barrier, *Materials Science and Engineering: C*, accepted
- 18 F. Schnitter, A. M. Bergmann, **B. Winkeljann**, J. Rodon Fores, O. Lieleg and J. Boekhoven, Synthesis and characterization of dissipative supramolecular materials driven by carbodiimide-based fuels, *Nature Protocols*, in revision

## List of patents

- 1 M. Marczyński, **B. Winkeljann**, M. Weber-Hohengrund and O. Lieleg, Method of the effective extraction of highly functional mucin from mucin containing tissue, *EP19197142.3*, European patent application (2019)
- 2 C. Kimna, **B. Winkeljann** and O. Lieleg, Controlled release of therapeutical agents from polymer brush coatings by employing reversible polymer condensation using ionic cross-linkers, *EP19217921.6*, European patent application (2019)